UQAR
Université du Québec
à Rimouski

DYNAMIQUE SÉDIMENTAIRE ET PALÉOCÉANOGRAPHIE LE LONG DES MARGES CONTINENTALES DES MERS DE BEAUFORT ET DES TCHOUKTCHES (OCÉAN ARCTIQUE) DEPUIS LA DERNIÈRE DÉGLACIATION

Thèse présentée

dans le cadre du programme de doctorat en océanographie

en vue de l'obtention du grade de Philosophiae Doctor

PAR

©CHARLES-EDOUARD DESCHAMPS

Avril 2018

Composition du jury :

Gwénaëlle Chaillou, présidente du jury, UQAR

Jean-Carlos Montero-Serrano, directeur de recherche, ISMER-UQAR

Guillaume St-Onge, codirecteur de recherche, ISMER-UQAR

Christophe Colin, examinateur externe, département des sciences de la Terre - université Paris-Sud

Dépôt initial le 26 Avril 2018 Dépôt final le 10 Août 2018

["Personally, I regard alcohol, used in moderation, as a medicine in the Polar regions. (...) Two men who have fallen out a little in the course of the week are reconciled at once by the scent of rum." Roald Amundsen, 1872-1927.]

REMERCIEMENTS

Je tiens tout particulièrement à remercier mon directeur de thèse qui m'a offert l'opportunité de faire cette thèse. Un grand merci à **Jean-Carlos Montero-Serrano**, pour cette aventure qui a duré quatre ans et demi. Je remercie aussi mon co-directeur **Guillaume St-Onge** pour son soutien et son optimisme à toute épreuve. Le doctorat c'est toute une aventure. C'est une aventure incluant le déménagement de la chambre froide un nombre incalculable de fois, la réalisation de cartes et de graphiques sans trop de couleurs mais finalement il faut mettre plein de couleur mais aussi un magnétomètre très capricieux. Merci à eux deux pour leurs disponibilités, leurs conseils et leurs supervisions et pour les opportunités que vous m'avez offerte. Une école d'été à Minneapolis, trois missions en mer sur l'Amundsen et le Pourquoi Pas et de nombreux voyages, euh congrès... Je remercie également les autres personnes avec qui j'ai pu également travailler et échanger tout au long de mon doctorat : **André Rochon**, **André Poirier** et aussi **Leonid Polyak**. Le doctorat c'est aussi beaucoup de labo et qui dit labo dit aussi protocole et utilisation de machine complexe. Un grand merci aux auxiliaires de recherche qui baby-sit tous ces petits étudiants. Merci à **Jacques Labrie**, **Marie-Pier St-Onge** pour leur apprentissage sur le MSCL, magnétomètre et sur l'ouverture des carottes au début de mon doctorat. Un grand merci aussi à **Mathieu Babin** pour m'avoir laissé faire joujou avec le LA-ICP-MS et sa confiance pour l'utilisation de l'appareil. Pour finir, merci à **Quentin Beauvais** pour son aide constante au cours de mon doctorat, ses conseils pertinents que ce soit pour le magnétomètre, les carottes, et la paperasse administrative.

Un doctorat c'est aussi quatre ans partagé avec une équipe, un laboratoire donc avec d'autres personnes qui sont en maîtrise et au doctorat. Merci à tous les gens du labo pour leurs aides constantes, leurs bonnes humeurs : **Pierre-Arnaud Desiage, Quentin Duboc, Julie Heggdal Velle, Marie Casse, Arthur Bieber, Myriam Caron, Adriana Gamboa, Édouard Philippe, Omain Kurtos, Naïs Sirdeys et Sarah Letaïef.**

Un doctorat c'est aussi 4 ans d'une vie en dehors de la fac notamment avec une équipe

de frisbee qui s'est formée avec **Alex, Dave, Gab, PAD et philou**. C'est aussi un groupe d'ami qui s'est formé avec des gâteaux pour le midi, des soirées jeux à ne plus finir avec des gens plus ou moins frustrés quand ils perdent (je ne dirais pas de nom, mais on sait tous de qui je parle), des restos avec le succulent Gor Gin, des parties de FIFA et des soirées séries pour GoT, Westworld etc... Pour tous ces moments merci à **Paul, Éva, Mél, PAD, Quentin**. Parmi ces personnes il y a aussi mes colocs avec qui j'ai partagé de merveilleux moments durant ces 3 dernières années avec des feux de maison lorsque **Noémi**e tentait de faire du caramel, des cheveux roux qui bouchent la salle de bain. Les fameux saucisse-salade de notre Franco-hispano-canadien communiste préféré : **Enrique**. Merci Enrique de nous avoir payé Netflix et l'abonnement à la playstation. Merci à **Gab** pour tous les jeux vidéo et toutes ces parties de civilisation jouées. Pour finir merci à **Mathilde** (Matouuuuuu ! ! !) qui partage ma vie depuis plus de 3 ans maintenant qui subit chaque jour mon mauvais caractère et qui m'a aidé dans les moments difficiles de la thèse. Tout à commencer par une soirée et de nombreuse pause-café à l'auriculaire et jusqu'où cela va-t-il finir... Au final, il a fallu vivre à Rimouski pour que deux Charentais puissent se rencontrer...

Finalement je remercie le **CRSNG**, le **GEOTOP**, l'**UQAR** et **la chaire de recherche en géologie marine** pour avoir contribué au financement de mon doctorat, les voyages pour les congrès et les expéditions sur l'Amundsen.

RÉSUMÉ

Dans l'océan Arctique, la rétroaction de l'albédo de la glace de mer est un paramètre clé pour le climat des hautes latitudes de l'hémisphère Nord, tout comme le climat global et la circulation océanique. Au cours des dernières décennies, les données instrumentales démontrent une augmentation de température et une réduction accélérée de la couverture mais aussi du volume et de l'épaisseur de la glace de mer en Arctique. Dans ce contexte, les données sédimentologiques, géochimiques, minéralogiques, et magnétiques extraites des enregistrements sédimentaires peuvent donner des indices pour documenter les cycles climatiques naturels et comprendre les processus contrôlant la circulation océanique et la variabilité des sources sédimentaires. Ainsi, le but principal de cette thèse consiste à caractériser les propriétés sédimentologiques, physiques, magnétiques, minéralogiques (fraction totale et argileuse) et géochimiques (éléments majeurs, traces et rapports isotopiques du Nd et du Hf) d'un ensemble de carottes sédimentaires recueillies sur les marges continentales de la mer de Beaufort canadienne et de la mer des Tchouktches. Ces données serviront à mieux documenter les processus contrôlant la variabilité des sources sédimentaires et la circulation océanique dans l'ouest de l'océan Arctique depuis la dernière déglaciation.

Dans le chapitre 1, les variations du champ magnétique terrestre (inclinaison, déclinaison et paléointensité relative) ont été utilisées pour établir la chronostratigraphie de trois carottes sédimentaires dont la carotte 01JPC située en mer des Tchouktches et les carottes 02PC et 03PC situées en mer de Beaufort canadienne. La comparaison des variations séculaires du champ magnétique terrestre avec des enregistrements datés indépendamment dans la même zone ont permis d'établir la chronostratigraphie des carottes sédimentaire. Les carottes 01JPC, 03PC et 02PC couvrent les derniers 6, 10 et 14 cal ka BP avec des vitesses de sédimentation allant de 10 cm.ka^{-1} à 70 cm.ka^{-1}. Les modèles d'âge ont été vérifiés indépendamment par téphrochronologie, datation radiocarbone et ^{210}Pb. La compilation des données magnétiques des carottes de cette étude et les données précédemment publiées ont été utilisées pour étudier les changements dans les propriétés magnétiques le long de la marge nord-américaine. La magnétite est le minéral magnétique dominant dans les sédiments, il s'agit de l'un des critères les plus importants pour les reconstructions paléomagnétiques. Au cours de la déglaciation, les deux marges sont sous l'influence de la fonte et de l'écoulement des icebergs de la calotte laurentidienne apportant des grains magnétiques plus grossiers. Les grains magnétiques sont généralement plus fins pendant l'Holocène dans les deux marges, ce qui pourrait être associés à l'arrêt de l'écoulement de l'eau de fonte de la calotte laurentidienne. Les résultats montrent l'utilité du paléomagnétisme pour améliorer la datation de matériel géologique arctique.

Dans le chapitre 2, des analyses granulométriques, minéralogiques (fraction totale et argileuse), et géochimiques (éléments majeurs, traces et terres-rares) réalisées sur deux carottes sédimentaires prélevées sur la marge continentale canadienne de la mer de Beaufort (02PC) et de la marge d'Alaska (05JPC) ont permis de reconstituer des changements de

provenance et de transport des sédiments en tenant compte de la variabilité climatique et océanographique depuis la dernière déglaciation. L'algorithme de modélisation par mélange de pôles "EMMA" appliqué aux données de granulométrie montre trois pôles de taille des grains qui sont centrés à 2 μm (glace de mer), 5 μm (transport néphéloïde et fleuve Mackenzie) et 13 μm (vêlage d'icebergs). Les assemblages minéralogiques en conjonction avec le programme SedUnMixMC montrent que les sédiments de la carotte 02PC sont principalement dérivés du fleuve Mackenzie tandis que pour la carotte 05JPC, il s'agit d'un mélange de sédiments provenant du fleuve Mackenzie, de la marge Eurasienne et du détroit de Béring durant l'Holocène. Au cours de la déglaciation, les couches contenant des débris délestés par les icebergs (IRD) riches en dolomite sont reliés aux différentes phases des décharges d'icebergs provenant du golfe d'Amundsen vers 12,8 et 11 cal ka BP. Cependant, les IRD riches en quartz et en feldspath résultent des événements de fonte des eaux provenant de la calotte Laurentidienne (13 cal ka BP) pour la carotte 02PC et de la chaîne de Brooks (10.6 cal ka BP) pour la carotte 05JPC. Nous concluons que l'apport d'eau de fonte provenant du lac Agassiz et la débacle d'icebergs provenant de la langue glaciaire du golfe d'Amundsen sont responsable de la période froide du Drays récent. Les résultats géochimiques montrent un contrôle granulométrique et minéralogique sur la concentration totale en terres-rares. En effet les terres-rares sont principalement enrichis dans les sédiments dérivés de roches felsiques et logent principalement dans la structure des phyllosilicates et plus spécifiquement dans l'illite et la kaolinite. Finalement, la concentration totale en terres-rares de la carotte 02PC résulte d'apports de matériel felsique provenant du fleuve Mackenzie et de l'archipel Arctique canadien depuis la dernière déglaciation. Pour la carotte 05JPC, la concentration totale en terres-rares est plus élevée durant la déglaciation compte tenu de l'apport de matériel felsique provenant du fleuve Mackenzie. Cependant, au cours de l'Holocène, la concentration totale en terres-rares diminue avec l'apport de matériel mafique provenant du détroit de Béring.

Dans le chapitre 3, les isotopes radiogéniques du Sr, Nd et Hf ainsi que la concentration en terres-rares ont été analysés sur les encroutements ferromagnésiens des sédiments de deux carottes sédimentaires, 02PC (mer de Beaufort canadienne) et 01JPC (mer des Tchouktches). Le but de ce chapitre a été de tracer les variations de la circulation profonde et le régime d'altération continentale dans l'Arctique de l'ouest depuis la dernière déglaciation. Les signatures εNd et εHf dans les marges canadiennes de Beaufort et des Tchouktches changent vers des valeurs plus radiogéniques au cours de l'Holocène. D'après les enregistrements εNd et εHf, les valeurs moins radiogéniques ne sont pas contrôlées par la provenance et le mélange des masses d'eau, mais plutôt par la provenance et un changement du régime d'altération dans les bassins versants des fleuves Mackenzie et du Yukon au début et au milieu de l'Holocène. Cependant, les valeurs plus radiogéniques en εNd et εHf, couplées avec les enregistrements minéralogiques à la fin de l'Holocène, sont principalement contrôlés par une augmentation de l'afflux d'eau via le détroit de Béring, résultant des changements des modes de variabilité climatique du Pacifique (tels que PNA/PDO/ENSO)

Dans l'ensemble, la contribution principale de cette thèse est l'établissement d'une nou-

velle banque de données grâce à laquelle il est possible (1) d'améliorer la chronostratigraphie régionale en Arctique de l'ouest, et (2) de mettre en évidence l'évolution de la dynamique sédimentaire le long des marges continentales de la mer de Beaufort canadienne et de la mer des Tchouktches depuis la dernière déglaciation. En outre, il s'agit de la première étude incluant des données minéralogiques (fraction totale et argileuse), géochimiques et isotopiques (Nd-Hf) sur un ensemble de carottes sédimentaires dans l'océan Arctique de l'ouest. Enfin, l'ensemble de données contribue à mieux comprendre les changements dans la provenance des sédiments, le changement de la circulation de surface et la circulation profonde de l'Arctique depuis la dernière déglaciation.

Mots clés : Arctique, Holocène, déglaciation, dynamique sédimentaire, paléomagnétisme, minéralogie, géochimie, terres rares, isotopes radiogéniques.

ABSTRACT

In the Arctic Ocean, ice-albedo feedback is a key factor controlling climate in high latitude in the northern hemisphere, oceanic circulation and global climate. Monitoring data over the last decades have recorded a rise in surface temperature and a decrease in surface and thickness of sea-ice in the Arctic Ocean. In this context, sedimentological, geochemical, mineralogical and magnetic data from marine cores can be used to better document natural climate variability and understand the processes controlling oceanic circulation and sediment provenance. Thus, the main purpose of this thesis consisted in characterizing the physical, magnetic, mineralogical (bulk and clay fractions) and geochemical (majors, traces, rare earth elements and Nd-Hf isotopes) properties of a set of cores recovered along the Canadian Beaufort and Chukchi Alaskan margins. The gathered data will be used better understand the processes that control changes in sediment provenance and oceanic circulation in the Western Arctic Ocean since the last deglaciation.

In chapter 1, the Earth magnetic field's variations (inclination, declination and relative paleointensity) were used to establish the chronostratigraphy of three sedimentary cores including core 01JPC in the Chukchi Sea, as well as cores 03PC and 02PC located in the Canadian Beaufort Sea. The comparison of the paleomagnetic secular variation with other independently dated records from the same area allowed us to establish the chronostratigraphy of these cores. The records span the last 6, 10 and 14 cal ka BP respectively with sedimentation rates from 10 cm.ka^{-1} to 60 cm.ka^{-1}. The age models were verified by AMS radiocarbon dating, tephrochronology and ^{210}Pb-based sedimentation rate. The compilation of the magnetic data of the cores in this study and previously published data were used to study changes in magnetic properties along the North American margin. Based on the compilation, magnetite was found to be the dominant magnetic mineral in sediments, and is the most important criterion for paleomagnetic reconstructions. During late deglacial, both margins are under the influence of the melting and iceberg discharge of the Laurentide Ice Sheet carrying coarser magnetic grain. The overall magnetic grains are finer during the Holocene in both margins which could be associated with the end of the meltwater discharge from the Laurentide Ice Sheet. Overall, this study illustrates the usefulness of palaeomagnetism to improve the dating of Arctic geological material.

In chapter 2, grain size, bulk mineralogy, clay mineralogy and geochemical (trace, rare and rare earth elements) compositions of two sediment piston cores recovered in the Chukchi-Alaskan (core HLY01-05JPC) and Beaufort (core AMD0214-02PC) margins were investigated to reconstruct changes in detrital sediment provenance and transport related to climate variability since the last deglaciation. An end-member modelling analysis (EMMA) of grain-size data and sediment-unmixing models (SedUnMixMC) were used to investigate sediment transport conditions and determine down-core changes in sediment provenance, respectively. EMMA displays three grain size end-member models in both margins which are centered at

2 μm (anchor ice), 5 μm (nephloid transport and Mackenzie River) and 13 μm (ice rafted debris). Unmixing of the sediment composition based on five potential source regions indicates that sediments in 02PC are mainly derived from the Mackenzie River, whereas for core 05JPC the sediment are a mix from the North Pacific, the Eastern Sea and the Mackenzie River during the Holocene. The IRD dated at ~ 12.8 cal ka BP and ~ 11 cal ka BP, respectively, with high dolomite content can be related to the different phases of meltwater and icebergs discharges from the Amundsen Gulf Ice Stream. Quartz and feldspar-rich IRD dated at 13 and 10.6 ka cal BP are related to the Lake Agassiz outburst in core 02PC and meltwater discharge from the Brooks Range glaciers in core 05JPC. Our detrital proxies in core 02PC support the hypothesis that large meltwater and iceberg discharges from the Lake Agassiz outburst and Amundsen Gulf ice stream to the Arctic Ocean may have triggered the Younger Dryas. REE content showed a clear granulometric control and further suggests that REE were enriched in felsic material and are lodging in phyllosilicates structures and more specifically in the illite and kaolinite. Finally, the trace and REE variations though the cores indicate that core 02PC is related to input of felsic material coming from the Mackenzie River and from the Banks Island since the last deglacial. The REE content and trace element in core 05JPC displayed several variations since the last deglacial varying from more mafic sources material with lower REE content derived from the Eurasian margin and Bering Strait and more felsic sources material during the late deglacial coming from the north Canadian margin linked to an intensified Beaufort Gyre.

In chapter 3, radiogenic isotopes (Sr-Nd-Hf) and REE concentration were retrieved from the authigenic Fe-Mn oxyhydroxides of two cores located in the Beaufort (02PC) and Chukchi Seas (01JPC). The main objective of this chapter was to investigate changes in dissolved weathering inputs and deep water circulations in the Western Arctic Ocean since the last deglacial.The εNd and εHf signatures in the Canadian Beaufort and Chukchi-Alaskan margins reveal changes towards more radiogenic values from the early- to late-Holocene. Based on the εNd and εHf records, we suggest that the unradiogenic values are not controlled by water mass provenance and mixing but rather by provenance and a change in the weathering regime over the Mackenzie and Yukon drainage basins during the early- to mid-Holocene. However, more radiogenic εNd and εHf, combined with mineralogical records in the late-Holocene, has primarily been controlled by an increase in the Bering Strait inflow, which is likely related to major changes in the atmospheric climate mode (such as PNA/PDO/ENSO).

Globally, the major contribution of this thesis is the rich dataset improving (1) the regional chronostratigraphy in the Western Arctic Ocean and (2) the sedimentary dynamics along the continental margin of the Canadian Beaufort and Alaska-Chukchi Seas. Moreover, this is the first study including mineralogical (bulk and clay fractions), geochemical and isotopic (Nd-Hf) composition on a set of sedimentary cores in the Western Arctic Ocean. Finally, the rich data set contributes to better understanding changes in sediment origin, change in surface and deep circulation since the last deglacial.

Keywords : Arctic, Holocene, deglaciation, paleomagnetism, geochemistry, rare

earth elements mineralogy, radiogenic isotope.

TABLE DES MATIÈRES

LISTE DES TABLEAUX

LISTE DES FIGURES

LISTE DES ABRÉVIATIONS

AAC : *Alaska coastal current*, courant côtier d'Alaska

AF : *Alternating field*, champ altérnatif

AIW : *Arctic intermediate water*, eau Arctique intermédiaire

AL : *Aleutian Low*, dépression des Aléoutiennes

AO : *Arctic oscillation*, oscillation arctique

AODW : *Arctic Ocean deep water*, eau Arctique profonde

ARM : *anhysteretic remanent magnetisation*, aimantation rémanente anhystérétique

AW : *Atlantic water*, eau Atlantique

BG : *Beaufort gyre*, gyre de Beaufort

BSI : *Bering Strait inflow*, entrée d'eau pacifique

CAA : *Canadian Arctic Archipelago*, archipel Arctique canadien

CAIR : Centre d'Appuie à l'Innovation de la Recherche

ChRM :*characteristic remanent magnetisation*, magnétisation caractéristique rémanente

CHUR :*Chondritic Uniform Reservoir*,Réservoir Uniforme Chondritique

CIA :*Chemical Index of Alteration*, indice d'altération chimique

ENSO :*El Niño Southern Oscillation*, oscillation australe El Niño

GAD : *geocentric axial dipole*, dipole axial géocentré

Hc :*coercive force*, coercivité

Hcr : *remanent coercive force*, coercivité rémanente

IML : Institut Maurice Lamontagne

INRS-ETE : Institut National de Recherche Scientifique – Centre eau, terre et environnement

IRD : *ice rafted debris*, velâge d'iceberg

IRM : *isothermal remanent magnetisation*, aimantation rémanente isothermale

ISMER : Insitut des Sciences de la Mer à Rimouski

$\mathbf{k}_{ARM}$: *susceptibility of the anhysteretic remanent magnetisation*, susceptibilité de l'aimantation rémanente anhystérétique

$\mathbf{k}_{LF}$: *low field magnetic susceptibility*, susceptibilité magnétique dans un champ faible

LIS : *Laurentide ice sheet*, calotte Laurentidienne

MAD : *maximum angular deviation*, déviaton angulaire maximum

MD : *multidomain*, domaines multiples

MDF : *median destructive field*, champ médian destructif

Mr : *saturation remanence*, rémanence à saturation.

Ms : *saturation magnetisation*, aimantation à saturation

MSCL : *multi-sensor core logger*, banc de mesures

NRM : *natural remanent magnetisation*, aimantation naturelle rémanente

PAAS : *Post-Archaean Average Shale*, schiste moyen post-archéen

PDO : *Pacifif decadal oscillation*, oscillation Pacifique décénale

PNA : *Pacific North American*, Pacifique nord-américain

PSD : *pseudo-single domain*, pseudo-mono-domaine

PSV : *paleomagnetic secular variation*, variation séculaire du champ magnétique

PSW : *polar surface water*, eau de surface polaire

PW : *Pacific water*, eau Pacifique

REE : *Rare earth elements*, terres-rares

RPI : *relative paleointensity*, paléointensité relative

SCC : *Siberian coastal current*, courant côtier sibérien

SD : *single domain*, domaine unique

SIRM : *saturation isothermal remanent magnetisation*, aimantation rémanente isothermale à saturation

TPD : *transpolar drift*, courant transpolaire

UQAM : Université du Québec à Montréal

UQAR : Université du Québec à Rimouski

XRD : *X-ray diffraction*, diffraction des rayons X

XRF : *X-ray fluorescence spectrometry*, La spectrométrie de fluorescence des rayons X

LISTE DES SYMBOLES

$\Delta\mathbf{R}$: Age reservoir local.

σ : erreur sur les mesures.

ε : notation de la composition isotopique correspondant à l'écart relatif d'un ratio isotopique d'un échantillon à celui d'un standard.

INTRODUCTION GÉNÉRALE

L'introduction générale de cette thèse présente la problématique globale du projet de recherche dans un contexte sédimentologique, paléoenvironnementale et paléoclimatique. Dans un premier temps, une revue de littérature sera présentée introduisant la géographie de l'océan Arctique et plus particulièrement les deux sites d'études : les mers de Beaufort et des Tchouktches. Dans un second temps, les notions de masses d'eau, la circulation profonde, la circulation océanique de surface, les oscillations climatiques, le couvert de glace et les sources sédimentaires seront énoncés. Ensuite, les objectifs et les questions de recherches abordés pour chacun des chapitres seront exposés. Enfin, la méthodologie utilisée pour répondre aux différents objectifs sera présentée. Cette introduction générale sera suivie par la présentation détaillée des trois chapitres de la thèse, exposant les réalisations majeures obtenues au cours du projet de recherche.

L'océan Arctique

Avec les changements climatiques actuels, de nouveaux enjeux environnementaux et économiques apparaissent en Arctique. Le changement climatique induit par les activités anthropiques en Arctique est deux fois plus rapide que la moyenne globale et il est appelé « amplification polaire » (Screen et Simmonds, 2010; Screen et Francis, 2016; Serreze et al., 2000, 2007; Vihma, 2014). Ce phénomène a pour conséquence une diminution de l'extension, de l'épaisseur et de la longueur de la saison de la glace de mer. En outre, au cours des dernières décennies, les glaciers en Arctique ont perdu de leurs masses (Meier et al., 2007). Les eaux de surface de l'Arctique ayant une faible salinité sont exportées vers l'océan nord Atlantique via le détroit de Fram (70 %) et un plus petit volume vers la mer du Labrador via l'archipel arctique canadien (30 % ; Dyke et al., 1997; Miller et al., 2010). Cette exportation d'eau peu salée contrôle la circulation méridienne de retournement Atlantique et donc la circulation thermohaline dans sa totalité (Dickson et al., 2007). De plus, la réduction du couvert

de glace entraine l'apparition de nouvelles voies navigables facilitant le transport commercial et l'exploitation des ressources naturelles tel que les gisements de minerai, mais aussi des énergies fossiles (ex. le pétrole et le gaz naturel). Le nombre de navire traversant l'archipel arctique canadien est ainsi passé de 80 à 140 par année depuis 1990 (Pizzolato et al., 2014). L'augmentation du trafic maritime peut avoir pour conséquence l'introduction d'espèces non indigènes en milieu arctique (Chan et al., 2015). De plus le retrait de la glace de mer va accélérer l'érosion côtière et augmenter l'action des vagues (Polyak et al., 2010). Le retrait de la glace de mer a aussi des conséquences sur les réseaux trophiques incluant les grands prédateurs tels que les ours polaires ou les phoques dépendants de la couverture de glace de mer (Polyak et al., 2010). De ce fait, l'océan Arctique est au milieu des discussions et des problématiques actuelles touchant une grande partie de la communauté scientifique.

Physiographie

L'océan Arctique est un bassin semi-fermé. La taille de l'océan Arctique est comprise entre 4000 km de long pour 2400 km de large et représente 15 % des plateaux continentaux mondiaux (Woodgate, 2013). L'océan Arctique est découpé en différents bassins par des dorsales océaniques (Fig. 1). Dans la partie eurasienne, les bassins d'Amundsen et de Makarov sont séparés par la dorsale de Lomonosov. Dans l'océan Arctique central, la dorsale de Mendeleïev marque la séparation entre les bassins de Makarov et du Canada. L'ensemble de ces bassins peuvent atteindre une profondeur de 4 500 m. Les connexions au système d'échange *via* les masses d'eau vers les autres océans se font à travers le détroit de Béring, l'archipel arctique canadien et les détroits de Fram et de Strait. L'océan Arctique est formé par différentes mers incluant les mers de Laptev, Kara et Sibérie orientale pour la partie eurasienne.

Cette étude se concentre sur les deux mers situées sur la marge nord-américaine que sont la mer de Beaufort canadienne et celle des Tchouktches. La marge de la mer de Beaufort canadienne correspond à une région rectangulaire de 120 km de largeur pour 530 km de

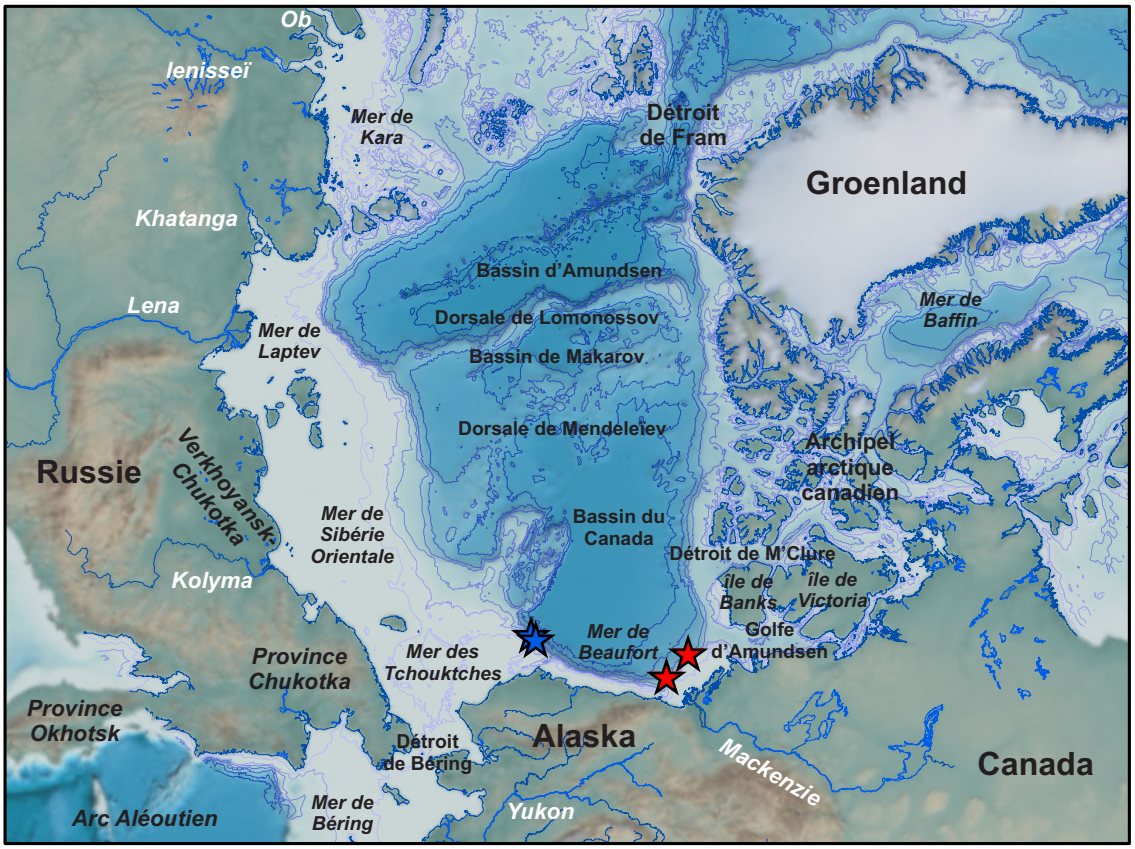

Figure 1: Carte physiographique de l'océan Arctique. La localisation des carottes 02PC et 03PC (étoiles rouges) ainsi que les carottes 01JPC et 05JPC (étoiles bleues) sont aussi montrées.

longueur (Richerol et al., 2008). Elle est bordée par le golfe d'Amundsen à l'est, le bassin du Canada au nord, le delta du fleuve Mackenzie au sud et la mer des Tchouktches à l'ouest (Fig.1). La mer des Tchouktches se trouve à la limite entre la marge eurasienne et la marge nord-américaine située entre la mer de Beaufort et la mer de Sibérie orientale. Au sud de la mer des Tchouktches se trouve le détroit de Béring formant une connexion vers l'océan Pacifique et plus précisément vers la mer de Béring.

Circulation océanique profonde

L'océan Arctique est stratifié par cinq masses d'eau principales : les eaux de surface polaire (PSW ; Polar surface water), les eaux pacifiques (PW ; Pacific water), les eaux atlantiques (AW ; Atlantic water), les eaux arctiques intermédiaires (AIW ; Arctic intermediate water) et les eaux profondes arctiques (AODW ; Arctic Ocean deep water) (Poirier et al., 2012 ; Fig.2-3).

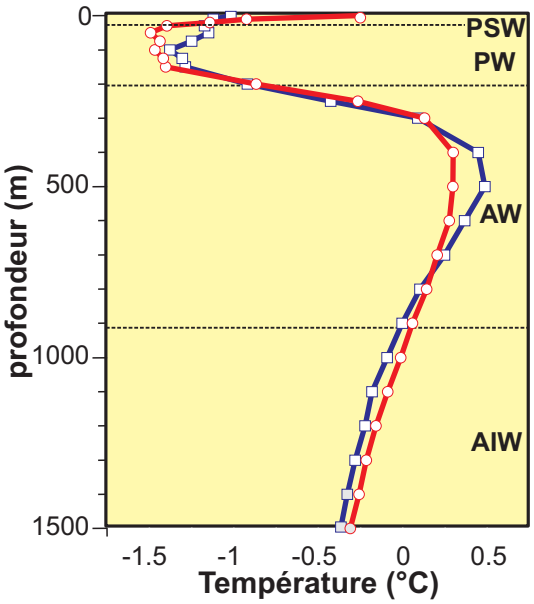

Figure 2: Profils des différentes masses d'eau circulant dans l'océan Arctique (adapté de Poirier et al., 2012).

Les PSW (0 à 50 m) sont principalement formées par la fonte des glaciers et les apports d'eau douce des fleuves. Ces eaux sont relativement froides (< 0°C) et peu salées (32 à 34 psu ; Rudels et al., 2004). Les entrées d'eau pacifique au sein de l'océan Arctique ce font à travers le détroit de Béring et constituent un apport de 0,8 Sv (1 Sv = 10^6 $m^3.s^{-1}$) ; avec des températures et des salinités allant respectivement de -2°C à 2°C et 32 à 33 psu (Woodgate, 2013). L'AW est formée par les eaux atlantiques entrant par le détroit de Fram et la mer de Barents. La profondeur des eaux atlantiques est comprise entre 200 et 1000 m ;

la température est supérieure à 0°C et la salinité est plus élevée que les eaux pacifiques (35 psu ; Rudels et al., 2004). La circulation AW est anti-horaire le long des marges de l'océan Arctique. Elle commence le long de la marge eurasienne, pour ensuite se séparer au niveau de la ride de Lomonosov. Une branche diverge vers la face est de la ride de Lomonosov et l'autre branche continue dans le bassin du Canada. Une fois dans le bassin du Canada, la AW peut éventuellement retourner vers la branche ouest ou rejoindre la branche Est de la ride de Lomonosov et finalement sortir de l'Arctique via le détroit de Fram (Poirier et al., 2012). L'AIW est en partie formée par l'AW et elle est située à des profondeurs comprises entre 1000 et 1500 m et suit la même circulation que la AW. Les températures varient de -0,5°C à 0° et les salinités de 34,6 à 34,8 psu pour les AW. Finalement, l'AODW occupe les bassins profonds de l'Arctique située sous l'AIW, à des profondeurs d'eau supérieures à 2000 m dans le bassin du Canada et supérieures à 1500 m dans le bassin eurasien. En général, ces AODW sont plus froides et plus salées (donc plus denses) que les AIW (Bassin du Canada : -0,5 à -0,3 °C et 34,95 psu ; Bassin Eurasien : -1,0 à -0,6 ° C et 34,93 psu ; Poirier et al., 2012).

Circulation océanique de surface et oscillations climatiques

Les deux principaux courants de surface dans l'océan Arctique sont la gyre de Beaufort (BG) et le courant transpolaire (TPD ; Fig. 3). La BG est un courant géostrophique anti-horaire dans l'Arctique de l'ouest (Darby et al., 2012). Le TPD est habituellement décrit comme la réunion de deux branches, la première venant de la mer de Laptev et la seconde de la bordure de la gyre de Beaufort et à la limite entre la mer de Sibérie orientale et la mer des Tchouktches (Dyke et al., 1997). Cette circulation océanique de surface est contrôlée par des oscillations climatiques couplées entre l'océan et l'atmosphère telle que l'oscillation arctique (AO). L'AO est le principal mode de variabilité des hautes latitudes et se caractérise par des changements de pression au-dessus du niveau marin et des régimes de vent (Thompson et Wallace, 1998). L'AO a également été identifiée comme un mécanisme responsable des changements dans la dérive des glaces à des échelles de temps décennales à millénaires (Darby,

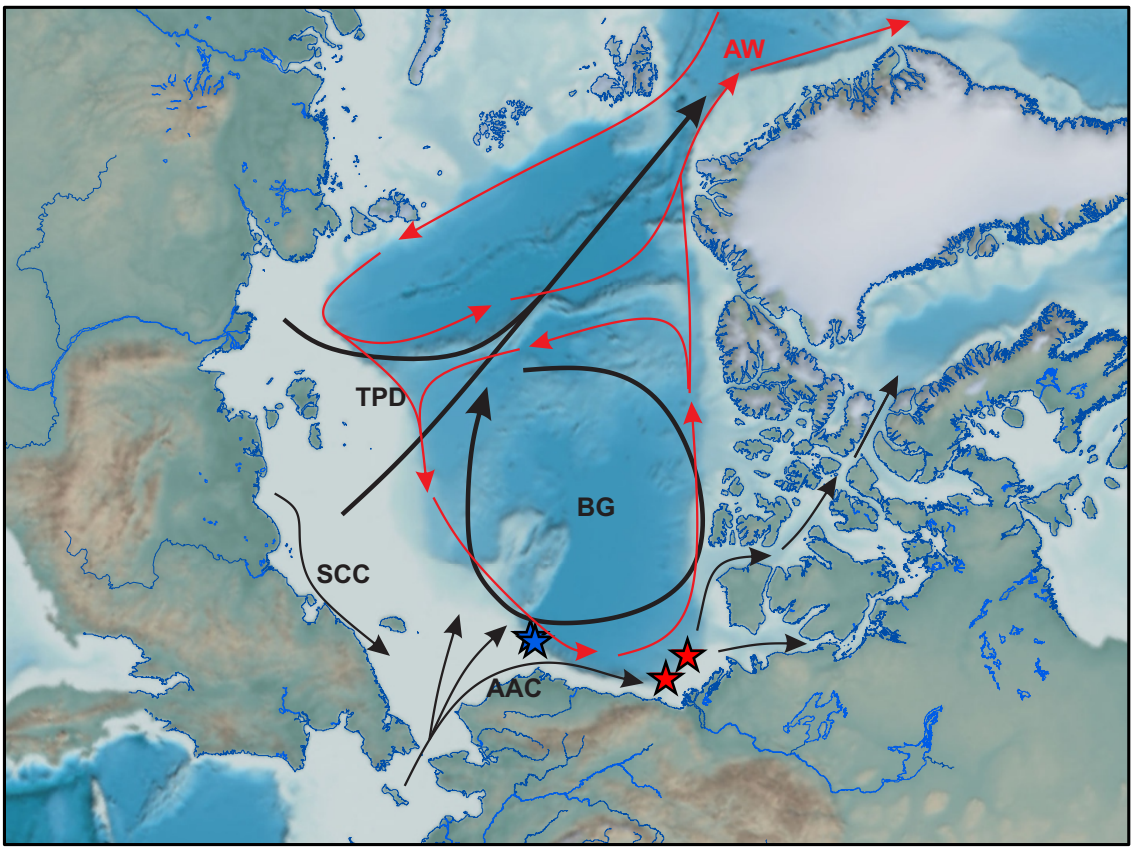

Figure 3: Carte de la circulation générale de surface (en noir) et profonde (en rouge) de l'océan Arctique. SCC : courant côtier sibérien ; AAC : courant côtier d'Alaska ; TPD : courant transpolaire ; BG : gyre de Beaufort ; AW : eau Atlantique. La localisation des carottes 02PC et 03PC (étoiles rouges) ainsi que les carottes 01JPC et 05JPC (étoiles bleues) est aussi montrée.

2002; Darby and Bischof, 2004). De ce fait, la BG et le TPD affectent la sédimentation dans l'Arctique. Pendant une phase négative de l'AO, le TPD se déplace vers l'est et la BG s'intensifie, alors que pendant une phase positive de l'AO, le TPD se déplace vers l'ouest et la BG se contracte (Fig. 4 ; Darby and Bischof, 2004). Darby and Bischof (2004) ainsi que Darby et al. (2012) ont mis en évidence les variations des conditions de circulation dominant entre les modes d'oscillations positives et négatives de l'AO depuis la dernière déglaciation. Leurs résultats montrent que le TPD est plus proche de la marge nord-américaine induisant des conditions similaires à une phase positive de l'AO depuis ~9-11 cal ka BP. Not et Hillaire-

Marcel (2012) ont montré que la gyre de Beaufort est plus active durant la déglaciation (~12 cal ka BP), ce qui correspond à des conditions similaires à une phase positive de l'AO.

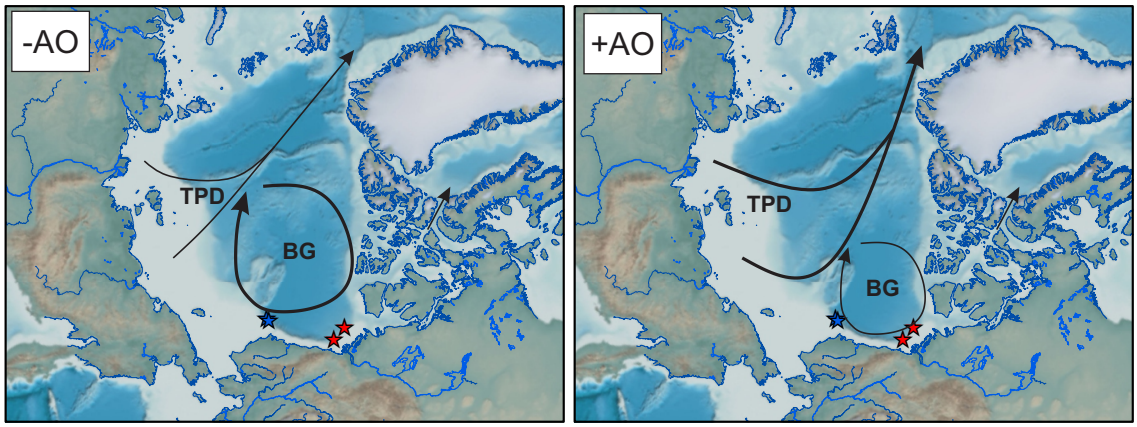

Figure 4: Schéma représentant les changements de la circulation océanique de surface (BG, TPD) en fonction des phases négatives (gauche) et positives (droite) de l'AO. La localisation des carottes 02PC et 03PC (étoiles rouges) ainsi que les carottes 01JPC et 05JPC (étoiles bleues) sont aussi montrées.

Cependant, l'AO explique seulement 20 % de la variabilité dans le champ de pression atmosphérique de l'hémisphère Nord (MacDonald et Case, 2005). L'oscillation pacifique décennale (PDO) est un mode majeur de variabilité climatique du Pacifique nord contrôlant la plupart des précipitations quotidiennes dans les bassins versant des fleuves Mackenzie et Yukon (Cassano et Cassano, 2010) et l'advection des eaux pacifiques dans l'océan Arctique (Danielson et al., 2011). Les apports d'eau pacifique représentent 1/3 des apports de chaleur vers l'océan Arctique et jouent un rôle important dans l'extension du couvert de glace en Arctique de l'ouest (Shimada et al., 2006; Woodgate et al., 2012). Le transport d'eau pacifique via le détroit de Béring se divise en trois branches dans la mer des Tchouktches (Fig. 3). La première branche tourne vers l'ouest autour du canyon d'Herald. La troisième branche se déverse dans le canyon de Barrow tandis que la seconde branche s'écoule entre la première et la troisième branche (Weingartner et al., 2005).

Depuis l'ouverture du détroit de Béring, qui a eu lieu vers 11 cal ka BP (Jakobsson et al., 2017), plusieurs études ont montré une augmentation des entrées d'eau pacifique entre

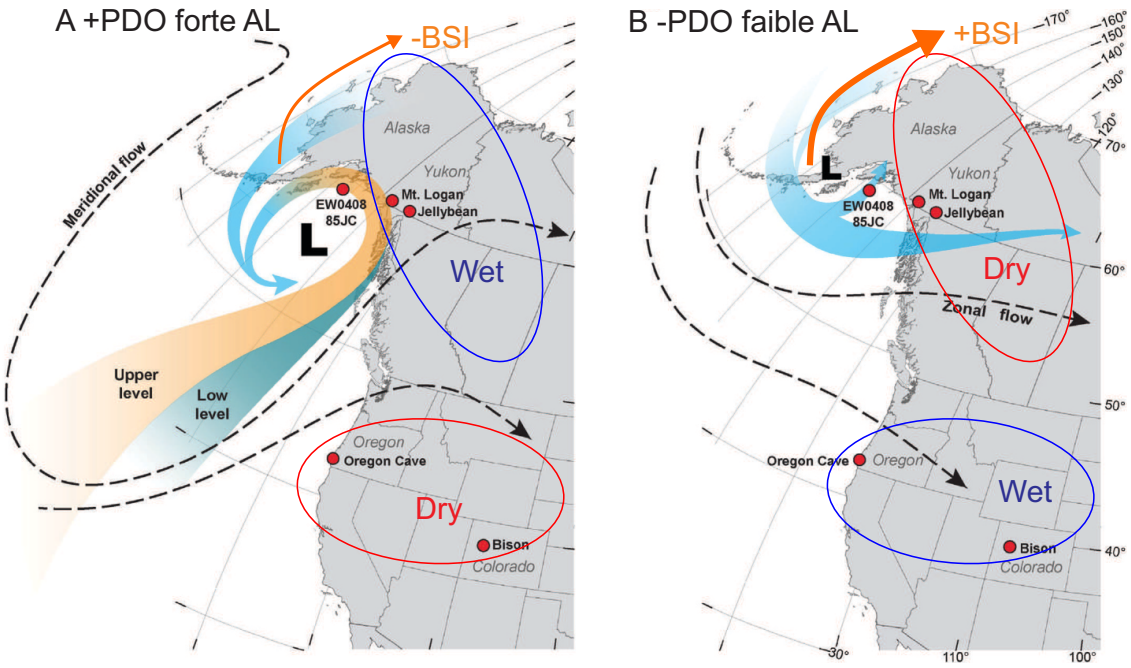

Figure 5: Schéma montrant la position de la dépression des Aléoutiennes, le régime des précipitations et l'intensité des apports d'eau pacifique lors des phases (A) positives et (B) négatives de la PDO (adapté de Anderson et al., 2016). BSI : entrée d'eau pacifique.

3.6 et 6 cal ka BP en réponse à un forte insolation d'été (Stein et al., 2017; Yamamoto et al., 2017). Les changements Holocène dans l'afflux du détroit de Béring ont été attribués à des changements dans le système dépressionnaire des Aléoutiennes situé dans le Pacifique nord (Yamamoto et al., 2017). Cette dépression des Aléoutiennes est sensible aux anomalies de température de surface de la mer du Pacifique tropical (Anderson et al., 2016; Trenberth et Hurrell, 1994). En général, l'augmentation des températures de surface du Pacifique oriental est caractérisée par une dépression Aléoutienne plus forte et décalée vers le sud-est, tandis qu'une anomalie négative des températures de surface dans l'est du Pacifique est associée à une dépression Aléoutienne plus faible et décalée vers le nord-ouest (Fig. 5). Durant une phase positive (ou négative) de la PDO, les températures de surface de l'eau pacifique advectée dans l'océan Arctique sont anormalement chaudes (ou froides) (MacDonald et Case, 2005; Pickart et al., 2009).

En plus des effets sur la circulation océanique de surface comme décrit précédemment, l'AO a une forte influence sur les précipitations dans l'Arctique. En effet, les données modernes ont montré une augmentation de 7 % des débits des fleuves eurasiens associée à une phase positive de l'AO (Peterson et al., 2002). De la même manière, la PDO et les changements de position de la dépression des Aléoutiennes contrôlent le régime des précipitations sur le continent nord-américain (Fig. 5). Pendant une phase positive de la PDO, les précipitations hivernales augmentent dans le sud-ouest des États-Unis et le long de la côte sud-est de l'Alaska, alors que les précipitations hivernales diminuent dans le nord-ouest des États-Unis et le sud-ouest du Canada (Barron et Anderson, 2011; MacDonald et Case, 2005). Déry et Wood (2005) ont observé une diminution de 9 % à 11 % sur les débits des fleuves nord canadiens (incluant le fleuve Mackenzie) entre 1964 et 2003. Or le débit de ces fleuves est principalement contrôlé par les précipitations sur les bassins de drainage. De plus, la variabilité et la tendance récente des rejets d'eau douce des fleuves nord canadiens sont principalement influencées par les téléconnexions à grande échelle telles que l'AO et la PDO. Les tendances récentes vers des phases positives plus intense de l'AO et négative de la PDO ont entraîné une diminution des précipitations et par conséquent une diminution du débit des rivières dans le nord du Canada (Déry et Wood, 2005).

Couvert de glace de mer dans l'océan Arctique

L'océan Arctique est influencé par une suite de rétroactions amplifiant les températures en réponse aux changements climatiques actuels (Serreze et al., 2007). Les plus fortes rétroactions sont associées aux changements du couvert de glace de mer, de la couverture de neige mais aussi des glaciers terrestres (Serreze et al., 2007). La rétroaction induite par la couverture de glace de mer est considérée comme rapide, avec une réponse saisonnière, contrairement aux glaciers terrestres qui ont un temps de réponse millénaire (Miller et al., 2010). La neige fraiche et le couvert de glace de mer possèdent les plus forts albédos et leurs changements de surface causés par la saisonnalité ont une très forte influence sur la

balance énergétique de la planète (Screen et Simmonds, 2010). L'augmentation moyenne des températures globales en raison du changement climatique provoque une diminution de l'extension de la glace de mer. En effet, depuis les années 70, l'imagerie satellite a permis de mettre en évidence une réduction de la couverture de glace de mer respectivement entre 1979 et 2006 avec une diminution comprise entre -3,1 % et -8,6 % pour les mois de janvier et septembre (Screen et Simmonds, 2010; Serreze et al., 2007). Ces changements induisent une diminution de l'albédo et une plus forte absorption des rayons solaires et finalement, par rétroaction, une augmentation plus rapide des températures dans l'Arctique (Screen et Francis, 2016; Screen et Simmonds, 2010; Serreze et al., 2000, 2007; Vihma, 2014).

Les variations de la circulation océanique dans le bassin Arctique jouent un rôle important dans les variations du couvert de glace (de Vernal et al., 2013). Entre 2001 et 2011, les apports d'eau du Pacifique entrant en Arctique ont augmenté de 50 % (Woodgate et al., 2012). Ces apports induisent un apport plus important de chaleur dans l'océan Arctique et agissent comme déclencheur du retrait de la glace de mer dans la mer des Tchouktches (Woodgate et al., 2012). Selon Shimada et al. (2006), une augmentation des apports d'eau chaude du Pacifique Nord retarde la formation de glace de mer durant l'hiver, et au final, accélère la diminution du couvert de glace. Plus récemment, Screen et Francis (2016) ont récemment conclu que le réchauffement suite à la diminution du couvert de glace de mer à long terme est plus (moins) important durant une phase négative (positive) de la PDO. En effet durant une phase négative de la PDO, l'advection d'air chaud provenant du Pacifique durant la période hivernale (reflétant un affaiblissement de la dépression des Aléoutiennes) est associé à une diminution du couvert de glace dans la mer de Béring (Screen et Francis, 2016). L'ensemble de ces études montrent bien nos difficultés à comprendre un système où interagissent couvert de glace, circulation océanique et circulation atmosphérique. En plus des eaux pacifiques, les eaux chaudes provenant de l'Atlantique Nord jouent aussi un rôle important sur le couvert de glace en Arctique (de Vernal et al., 2013). En effet, l'augmentation de l'advection d'eau chaude atlantique au cours des 2000 dernières années semble être le principal facteur de déclin de l'extension de la glace de mer (Kinnard et al., 2011; Spielhagen et al., 2011).

Cependant, les détails de la façon dont l'échange des masses d'eau entre le Pacifique, l'Arctique et l'Atlantique fonctionne sur des échelles de temps plus longues (> 1000 ans) ont été mal documentés en raison de la rareté des enregistrements sédimentaires à haute résolution (Haley et al., 2008; Spielhagen et al., 2011; Hoffmann et al., 2013).

Sources sédimentaires

Les apports détritiques en Arctique sont dérivés des masses continentales ayant des âges et des conditions tectoniques différentes (Fig. 6). Les zones géologiques peuvent être regroupées en quatre lithologies géologiques distinctes : (1) plate-forme, (2) volcanique, (3) orogénique et (4) le bouclier comme décrit par Fagel et al. (2014). (1) Les zones de la plate-forme sont reliées à la partie australe de l'archipel arctique canadien et la région du delta du Mackenzie. La plate-forme sibérienne est composée de calcaires précambriens et cambriens, de sédiments terrigènes jurassiques à crétacés et de matériaux alluviaux quaternaires (Phillips et Grantz, 2001; Rachold, 1999; Schoster et al., 2000). (2) La province volcanique est formée par la ceinture volcanique Okhotsk-Chukotka principalement constituée de roches acides à intermédiaire prédominant dans l'ouest et des roches intermédiaires à basiques à l'est (Viscosi-Shirley et al., 2003b). Les autres zones volcaniques sont formées par les épanchements basaltiques en Sibérie et l'arc volcanique des Aléoutiennes. (3) Les ceintures orogéniques sont principalement formées par le Bassin de Sverdrup dans l'archipel arctique canadien (Patchett et al., 2004), mais aussi par la cordillère nord-américaine et le nord du Groenland. (4) Les zone de bouclier sont le bouclier canadien et le craton du Groenland et consistent principalement en des roches plutoniques et métamorphiques.

Les apports détritiques en Arctique sont principalement dérivés des apports fluviatiles et de l'érosion côtière et sont caractérisés par des signatures élémentaires différentes (Asahara et al., 2012; Martinez et al., 2009). La proximité ou non des fleuves explique les hautes variations du taux de sédimentation dans l'ouest de l'arctique (40-1200 $cm.ka^{-1}$; Darby et al.,

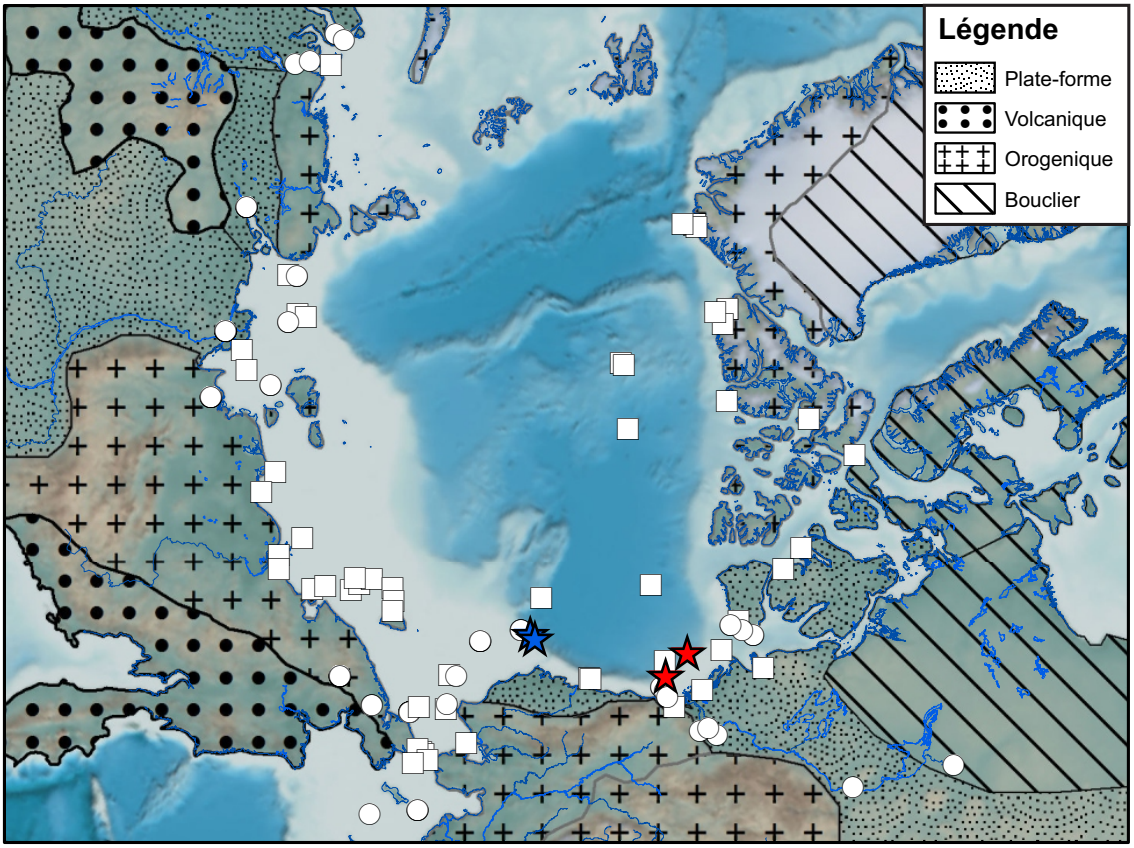

Figure 6: Carte géologique simplifiée des terrains bordant l'océan Arctique d'après Fagel et al. (2014). La base de données de chimie (cercles) et de minéralogie (carrés) est aussi montrée.

2009) contrairement au centre de l'Arctique où les taux de sédimentation sont quasi nuls (Not et Hillaire-Marcel, 2012). Sur le continent nord-américain, les deux principaux fleuves sont le Mackenzie et le Yukon. Le fleuve Mackenzie est la principale source de sédiments pour la mer de Beaufort (Gamboa et al., 2017). Le fleuve Mackenzie est le quatrième plus grand fleuve de l'Arctique (après les fleuves Ienisseï, Lena et Ob) en termes de débit d'eau douce ($\sim$ 420 $km^3.a^{-1}$; Wagner et al., 2011), mais le premier en terme de charge particulaire ($\sim$ 127 $Mt.a^{-1}$; Carson et al., 1998). Les roches sédimentaires représentent 70 % du bassin du Mackenzie (clast et carbonate), tandis que 22 % sont des roches du Bouclier canadien (Millot et al., 2003). Les apports sédimentaires modernes de la mer des Tchouktches sont un mélange de sédiments provenant du détroit de Béring (fleuve Yukon et arc aléoutien), de la

mer de Sibérie orientale et de la mer de Beaufort (Asahara et al., 2012; Kobayashi et al., 2016; Ortiz et al., 2009; Viscosi-Shirley et al., 2003b). Les sédiments du fleuve Yukon se déversant dans la mer de Béring représentent environ 55 $Mt.a^{-1}$ (Eberl, 2004). Les sédiments de la mer de Béring sont un mélange de roche mafique de l'arc des Aléoutiennes et de roche felsique provenant du bassin de drainage du fleuve Yukon (Gardner et al., 1980; Nagashima et al., 2012). Les sédiments transportés dans la mer de Sibérie orientale sont dérivés de la ceinture volcanique d'Okhotsk-Chukotka et de la province de Verkhoïansk-Chukotka (Viscosi-Shirley et al., 2003a).

De nombreuse études ont caractérisé et compilé la composition minéralogique et géochimique régionale des sédiments détritiques sur le plateau continental eurasien (Bazhenova, 2012; Schoster et al., 2000; Stein, 2008; Viscosi-Shirley et al., 2003a; Vogt, 1997), la mer des Tchouktches-détroit de Béring (Asahara et al., 2012; Bischof, 1997; Dong et al., 2014, 2017; Kobayashi et al., 2016; Stein et al., 2017), la marge d'Alaska (Darby et al., 2012; Naidu et al., 1982; Naidu et Mowatt, 1983; Ortiz et al., 2009) et la mer de Beaufort ainsi que le golfe d'Amundsen (Darby et al., 2011; Gamboa et al., 2017; Naidu et al., 1971). En général, les teneurs en quartz-dolomite-illite-kaolinite et Al-K-Ti-Fe-Cr-V-Zn-P sont dominantes le long de la marge nord-américaine où affleurent les terrains sédimentaires du paléozoïques-mésozoïques et glaciaires du Pléistocène (Harrison et al., 2011). La dolomite et Ca-Mg-Si-Zr sont particulièrement riches dans l'archipel Arctique canadien (iles de Banks et de Victoria) où les roches sédimentaires paléozoïques-mésozoïques du bassin de Sverdrup et les dépôts glaciaires du Tertiaire-Quaternaire sont riches en carbonate (Harrison et al., 2011). Les feldspaths-pyroxènes-amphiboles-smectites et Mg-Fe-Ti-K sont dominants dans les sédiments du plateau eurasien où les rivières drainent de grandes provinces basaltiques (Viscosi-Shirley et al., 2003a). Les sédiments de la mer des Tchouktches sont riches en quartz-feldspaths-chlorites-muscovites-smectites-vermiculites et proviennent probablement de la mer de Béring et des côtes d'Alaska (notamment du fleuve Yukon) ainsi que de l'arc volcanique des Aléoutiennes (Gardner et al., 1980; Naidu et Mowatt, 1983).

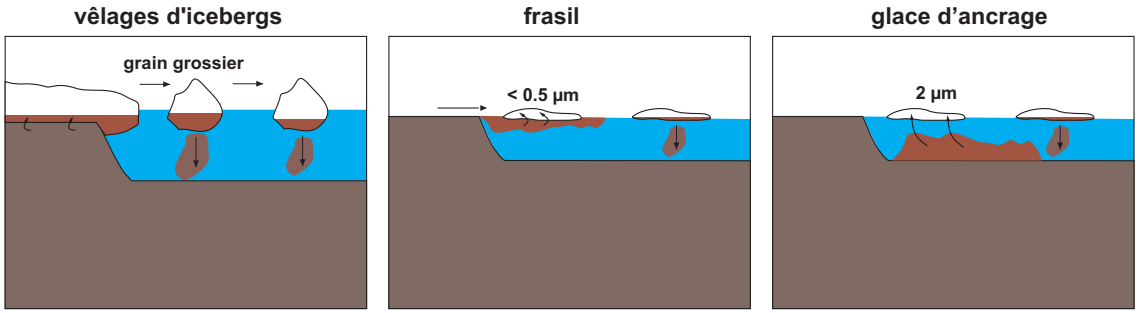

Figure 7: Représentation schématique des différents types de transport propre à la glace dans l'océan Arctique.

Ces études ont montré que la provenance des sédiments a varié depuis la dernière glaciation. En effet, la glace de mer, la glace continentale, mais aussi les courants de fond jouent un rôle important mais difficile à estimer dans le transport sédimentaire dans l'océan Arctique (Darby et al., 2009; Nürnberg et al., 1994; Reimnitz et al., 1987, 1994). Les vêlages d'icebergs (IRD) emprisonnent les sédiments lors de leur écoulement sur les masses continentales (Fig. 7). Cependant il existe différents types de transport propre à la glace de mer : le frasil (ou *suspension freezing*) et la glace d'ancrage (ou *anchor ice*). L'incorporation des sédiments par le frasil requiert des eaux libres associées à des conditions de polynie hivernale. Les sédiments des plateaux sont transportés par les cristaux de glace qui se forment près du fond ou sont remis en suspension par les courants de fond, les vagues ou les marées (Darby et al., 2011). La formation de glace d'ancrage se produit sans eau libre et nécessite seulement des conditions de remobilisation au fond (Reimnitz et al., 1987). Par exemple, les grains détritiques provenant de la marge eurasienne, notamment de la mer de Kara, sont transportés par la glace de mer via le courant transpolaire vers la mer des Tchouktches au cours de l'Holocène (Darby et al., 2012).

Objectifs de recherche

L'objectif général de cette thèse est de comprendre les variations des sources sédimentaires et les variations de la circulation océanique de surface et profonde depuis la dernière déglaciation dans l'ouest de l'Arctique. Pour ce faire, la thèse s'appuie sur trois objectifs spécifiques organisés de manière à produire quatre articles scientifiques formant les trois chapitres suivants de la thèse.

Objectif 1-Chronologie et propriétés magnétiques des sédiments des marges continentales de la mer de Beaufort et de la mer des Tchouktches depuis la dernière déglaciation.

Le prérequis pour une étude paléoclimatique basée sur des enregistrements sédimentaires est la réalisation d'un modèle d'âge dans le but de transformer l'échelle de profondeur d'une carotte sédimentaire en chronologie. En ce sens, Barletta et al. (2008) et Lisé-Pronovost et al. (2009) ont démontré le potentiel d'utiliser la variabilité millénaire à séculaire du champ magnétique terrestre en Arctique de l'ouest. L'identification de marqueurs chronostratigraphiques régionaux permettra d'établir une chronologie robuste des sédiments holocènes. **Ainsi, le premier objectif spécifique est de reconstruire les modèles d'âges de trois carottes sédimentaires situées en mer de Beaufort canadienne et en mer des Tchouktches en utilisant les variations du champ magnétique terrestre (inclinaison, déclinaison et paléointensité relative)**. Cependant, plusieurs questions pourront être soulevées : cette méthode peut-elle être utilisée sur des carottes sédimentaires de régions différentes avec des taux de sédimentation différents ? La compilation des données magnétiques de différentes carottes va-t-elle nous permettre d'étudier l'évolution des propriétés magnétiques depuis la déglaciation ? Comment les propriétés magnétiques des sédiments des mers de Beaufort et des Tchouktches ont évolué depuis la déglaciation ? Existe-t-il des différences inter- et intra-marges ou des différences entre la déglaciation et l'Holocène ? Ces différences proviennent-elles de différences entre des sources sédimentaires

ou de processus sédimentaires ? Les réponses à ces questions fourniront d'importants indices pour établir un cadre chronostratigraphique précis qui va permettre de mieux documenter l'évolution de la dynamique sédimentaire dans l'ouest de l'océan Arctique depuis la dernière déglaciation.

Objectifs 2–Variabilité à long terme de l'origine des sédiments et la dynamique sédimentaire dans l'Arctique de l'ouest depuis la dernière déglaciation

Dans un cadre chronostratigraphique précis, l'objectif 2 de cette thèse vise à utiliser la minéralogie (fraction totale et argileuse) et la géochimie (éléments majeurs, traces et terres rares) de deux carottes sédimentaires recueillies sur les marges continentales de la mer de Beaufort et de la mer des Tchouktches. **Ces données serviront à reconstituer la provenance, les mécanismes de transport et la dynamique sédimentaire résultant de la circulation océanique de surface dans l'ouest de l'océan Arctique depuis la dernière déglaciation**. Les minéraux tels que la chlorite et la muscovite transportés par les courants marins, permettent de tracer l'intensité des entrées d'eau pacifique dans l'Arctique. De plus, les traceurs des apports d'eau pacifique montrent une tendance générale à l'augmentation au cours de l'Holocène mais avec des périodes d'intensification différente selon la localisation des carottes (Kobayashi et al., 2016; Ortiz et al., 2009; Stein et al., 2017; Yamamoto et al., 2017). **Dans le cas de la marge des Tchouktches, de nouvelles données permettront non seulement de vérifier si les apports sédimentaires *via* le détroit de Béring ont augmenté ou non au cours de l'Holocène, de connaitre l'influence entre les apports des marges nord-américaine et eurasienne depuis la dernière déglaciation, mais aussi de les quantifier.**

Au cours de la dernière déglaciation, des sédiments issus du vêlage d'iceberg résultant de la fonte de la calotte laurentidienne sont retrouvés en mers de Beaufort et des Tchouktches (Darby and Bischof, 2004; Phillips et Grantz, 2001; Polyak et al., 2007). Au cours de la dernière déglaciation, les deux langues glaciaires actives durant la fonte de la calotte laurentidienne sont le détroit de M'Clure et le golfe d'Amundsen (Stokes et al., 2005, 2009).

Actuellement, il n'y a aucune étude sur la provenance et la dynamique sédimentaire depuis la dernière déglaciation en mer de Beaufort canadienne. Pourtant la mer de Beaufort canadienne est une zone clef pour comprendre avec précision la dynamique de la calotte laurentidienne au cours du temps.**Son étude permettra de comparer les données terrestres et de modélisation (Stokes et al., 2005, 2009; Stokes et Tarasov, 2010) avec les enregistrements sédimentaires marins.** Les données continentales (Murton et al., 2010) ainsi que les modèles numériques (Tarasov et Peltier, 2005) suggèrent une vidange du lac pro-glaciaire Agassiz *via* le fleuve Mackenzie. Cet apport d'eau douce important est ensuite exporté à travers le détroit de Fram vers l'océan Atlantique nord entrainant une diminution de la formation d'eau profonde et finalement la période froide du Drays récent (Condron et Winsor, 2012). Différentes études montrent bien un apport d'eau douce important provenant de la marge canadienne entre 12 et 13 ka cal BP (Hillaire-Marcel et al., 2013; Maccali et al., 2012, 2013). Cependant, au niveau de la marge canadienne de la mer de Beaufort, il n'existe à ce jour aucune évidence sédimentaire de la vidange du lac Agassiz. En effet, les données d'isotopes d'oxygène (δ^{18}O) de carottes sédimentaire de la mer de Beaufort canadienne ne montrent pas un apport important d'eau de fonte au cours de la dernière déglaciation (Schell et al., 2008; Scott et al., 2009). **Ainsi, l'étude des apports sédimentaires du fleuve Mackenzie permettra d'observer les variations sédimentologiques, géochimiques et minéralogiques de la vidange du lac Agassiz durant la dernière déglaciation (Murton et al., 2010).**

Finalement, de nombreuses incertitudes demeurent au sujet des variations de provenance sédimentaire et des changements de la circulation océanique. Une étude multi-traceur comprenant la géochimie, la minéralogie et les isotopes permettra de mieux quantifier les variations des sources sédimentaires mais aussi de comprendre les changements de la circulation océanique résultant de la variabilité climatique depuis la dernière déglaciation.

Á travers ce deuxième objectif, plusieurs questions seront abordées : comment les propriétés minéralogiques et géochimiques des sédiments ont-elles évolué au cours du temps ?

Quels sont les processus contrôlant les transports sédimentaires de l'Arctique de l'ouest (glace de mer, circulation océanique, glace continentale) ? Comment la fonte des langues glaciaires du détroit de M'Clure et le golfe d'Amundsen ont-ils influencé la dynamique sédimentaire de l'Arctique de l'ouest ? La proportion de sédiments provenant de la mer de Béring augmente-t-elle dans la mer des Tchouktches au cours de l'Holocène ? Dans l'ensemble cette approche multi-traceur permettra de mieux documenter l'impact de la débâcle de la calotte laurentidienne sur la dynamique sédimentaire dans l'ouest de l'océan Arctique depuis la dernière déglaciation.

Objectifs 3–Reconstitution des changements de provenance des masses d'eau profonde dans l'ouest de l'Arctique depuis la dernière déglaciation

Dans le domaine de la paléocéanographie, de nombreux traceurs géochimiques ont été utilisé pour reconstituer les variations de la répartition des masses d'eau océanique au cours des temps géologiques (Henderson, 2002). Les isotopes radiogéniques du neodyme (Nd) et du hafnium (Hf) constituent des traceurs émergents pour étudier les variations de la circulation océanique. **Dans ce contexte, l'objectif 3 de cette thèse vise à utiliser la composition isotopique en Nd et Hf extraites des oxyhydroxides ferromagnésien des sédiments de deux carottes sédimentaires recueillis sur les marges continentales de la mer de Beaufort et de la mer des Tchouktches pour reconstituer la dynamique de la circulation profonde dans l'ouest de l'Arctique depuis la dernière déglaciation**.

La variabilité du couvert de glace au cours de l'Holocène a été relativement bien étudié en utilisant des enregistrements sédimentaires (de Vernal et al., 2005; de Vernal et Rochon, 2011; de Vernal et al., 2013; Ledu et al., 2010; McKay et al., 2008; Polyak et al., 2010, 2016; Stein et al., 2017). Ces enregistrements montrent différentes variations de l'extension de la glace de mer entre l'Arctique de l'ouest et de l'est durant l'Holocène, ce qui suppose que les mécanismes contrôlant l'extension de la glace de mer ne sont pas les mêmes à travers l'Arctique (de Vernal et al., 2013). En effet, les conditions de glace de mer sont restées relativement stables au cours des derniers 4600 ans dans la mer de Beaufort (Bringué et Rochon,

2012). Au contraire, la couverture de glace de mer montre une grande variabilité dans la mer des Tchouktches au cours de l'Holocène et les résultats diffèrent selon la localisation des enregistrements sédimentaires. L'ensemble de ces résultats concorde pour une diminution de la couverture de glace de mer entre 8 et 6 cal ka BP, mais diffère pour une augmentation de la couverture de glace de mer qui commence vers 6 cal ka BP le long de la marge d'Alaska et vers 4.5 cal ka BP dans la partie centrale de la mer des Tchouktches (McKay et al., 2008; Polyak et al., 2016; Stein et al., 2017). L'une des raisons avancée pour expliquer ce décalage est une faible advection d'eau chaude provenant du Pacifique et un apport plus important de glace de mer via la gyre de Beaufort (Polyak et al., 2016; Stein et al., 2017). **Pour ces raisons, l'étude de la circulation océanique dans le bassin Arctique et de ces variations passées peuvent fournir d'importants indices pour améliorer nos connaissances sur les échanges à long terme des masses d'eau dans l'ouest de l'océan Arctique et ses possibles relations avec les variations du couvert de glace.** Or, Il existe actuellement peu d'études en Arctique sur les variations de la circulation profonde depuis la dernière déglaciation. Or les eaux atlantiques entrant en Arctique sont une composante importante de la circulation thermohaline. Chen et al. (2012) ont observé que les apports d'eau atlantique étaient réduits durant les périodes glaciaires au cours des 14 derniers millions d'années. Ces résultats coïncident avec une diminution de la ventilation des eaux arctiques durant les périodes glaciaires (März et al., 2011). Au cours de l'Holocène, la diminution du couvert de glace dans la mer des Tchouktches proviendrait des apports plus important d'eau atlantique entre 9 et 7 cal ka BP (Hillaire-Marcel et al., 2004; de Vernal et al., 2013). Ainsi, l'étude à haute résolution de la circulation depuis la dernière déglaciation permettrait une meilleure compréhension des variations climatiques au sein de l'Arctique.

Á travers ce troisième objectif, les questions suivantes seront abordées : quelles sont les facteurs climatiques et océanographiques influençant la signature isotopique en Nd et Hf des masses d'eau profonde dans l'ouest de l'Arctique depuis la dernière déglaciation ? La proportion des masses d'eau provenant du Pacifique Nord augmente-t-elle dans la mer des Tchouktches au cours de l'Holocène ?

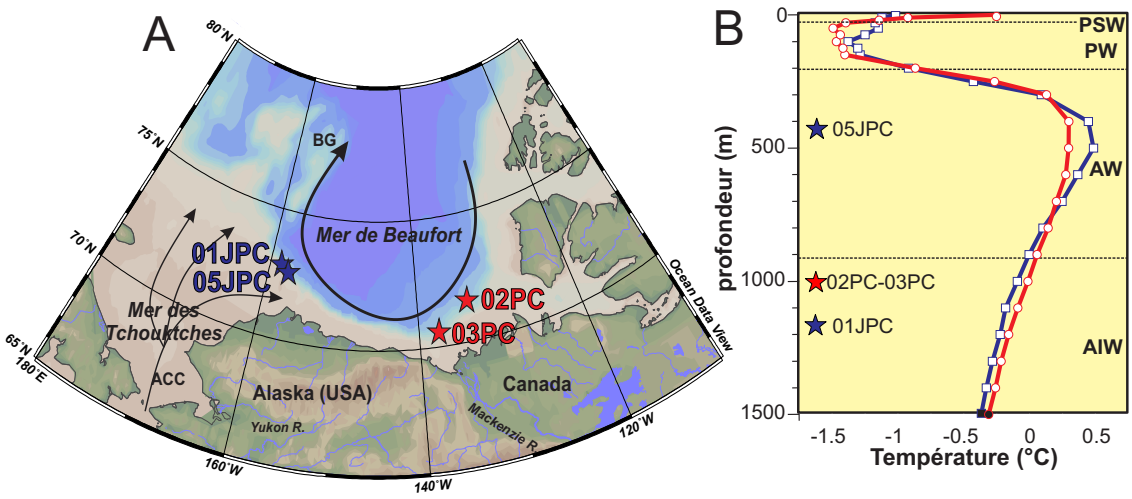

Figure 8: (A) Localisation et (B) profondeur des carottes sédimentaire 01JPC et 05JPC (étoiles bleues) en mer des Tchoutkches et des carottes 03PC et 02PC (étoiles rouge) situées en mer de Beaufort.

Matériels et méthodes

Les quatre carottes sédimentaires étudiées au cours de cette thèse ont été prélevées sur les marges continentales de la mer de Beaufort canadienne (AMD0214-02PC et AMD0214-03PC ; Fig. 8) et de la mer des Tchouktches (HLY0501-01JPC et HLY0501-05JPC ; Fig. 8). Les carottes sédimentaires ont été prélevées au cours des missions océanographiques qui se sont déroulées à bord du brise-glace canadien NGCC Amundsen en septembre 2014 (Montero-Serrano et al., 2014) et à bord du brise-glace américain USCGC Healy en juin 2005 (Darby et al., 2005), respectivement. Les carottes sédimentaires 02PC et 03PC ont été prélevées à l'aide d'un carottier à piston, permettant l'échantillonnage de carottes sédimentaires atteignant jusqu'à 9 m de longueur. Tandis que les carottes 01JPC et 05JPC ont été prélevées à l'aide d'un carottier de type "jumbo piston core" permettant l'échantillonnage de carottes sédimentaires atteignant jusqu'à 25 m de longueur. Des profils sismiques de haute résolution (Annexe 1) obtenus sur chacun des sites ont permis d'indiquer la location exacte du carottage, s'assurant ainsi que les dépôts sédimentaires ne sont pas perturbés par des

écoulements de masse (Darby et al., 2005; Montero-Serrano et al., 2014). La méthodologie détaillée se trouve dans les articles des chapitres de la thèse, mais aussi résumé dans la figure 9.

Chronostratigraphie et paléomagnétisme

La datation par radiocarbone est la méthode la plus utilisée pour déterminer l'âge des fossiles ou de la matière organique préservée dans les carottes sédimentaires marine et connaître l'âge des sédiments. La datation de séquences sédimentaires est souvent problématique en Arctique puisque la dissolution du matériel carbonaté raréfie la conservation de coquilles ou des tests dans les sédiments (Jutterström et Anderson, 2005). De plus, la datation par radiocarbone dans l'Arctique est souvent compliquée par un âge de réservoir local faiblement contraint (Hanslik et al., 2010). En conséquence, les reconstructions paléocéanographiques dans cette région climatique sensible sont entravées par un manque de chronologie robuste.

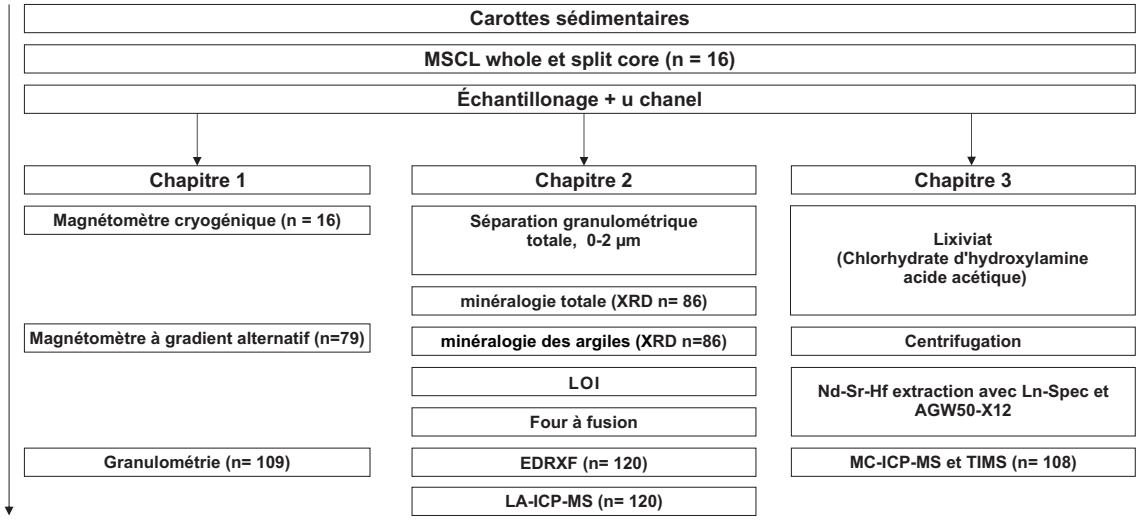

Figure 9: Schéma de la méthodologie pour les différents chapitres de la thèse.

Depuis une décennie, une nouvelle méthode utilisant la variabilité millénaire à séculaire

du champ magnétique terrestre a été mise au point pour pouvoir construire des modèles d'âge en Arctique de l'ouest (Barletta et al., 2008; Lisé-Pronovost et al., 2009). Le champ magnétique de la Terre résulte d'un mécanisme de dynamo auto-excité dans le noyau externe de la Terre produisant des courants électriques générés par les mouvements de convection d'un conducteur liquide en alliage de fer et de nickel (Stoner et St-Onge, 2007). Le paléomagnétisme est l'étude du champ magnétique terrestre tel qu'il est conservé dans des matériaux géologiques. En effet les sédiments ont la capacité de s'aligner en fonction de l'intensité et de la direction du champ magnétique terrestre au moment de leur déposition (Stoner et St-Onge, 2007; Tauxe et Yamazaki, 2007; Tauxe, 1993). La reconstruction des variations centennales/millénaires du champ magnétique de la Terre (PSV : Paleomagnetic Secular Variation) permet d'identifier des marqueurs chronostratigraphiques régionaux en observant des changements synchrones de l'inclinaison, la déclinaison et l'intensité du champ magnétique (Fig. 10). Ainsi, quelques études ont utilisé la magnétostratigraphie comme un outil de datation régionale pour les sédiments de l'Holocène sur les marges continentales de l'Arctique occidental en l'absence de matériel datable ou pour soutenir et améliorer de façon indépendante la chronostratigraphie basée sur la datation par radiocarbone (Barletta et al., 2008, 2010; Darby et al., 2012; Lisé-Pronovost et al., 2009; Lund et al., 2016). De plus, les hautes latitudes nord et l'hémisphère sud sont des zones manquant d'enregistrement des PSV. Le développement de la reconstruction des PSV dans ces régions permet l'amélioration des modèles géomatiques tels que cals10k (Korte et al., 2011) et d'améliorer la chronostratigraphie des carottes sédimentaires dans l'Arctique de l'ouest.

En plus de l'aspect chronostratigraphique, les propriétés magnétiques sont aussi un outil robuste pour reconstituer la variabilité environnementale et climatique (Liu et al., 2012). Les principaux paramètres des propriétés magnétiques sont la taille, la concentration et la minéralogie des grains magnétiques. Ces trois paramètres peuvent être interprétés de manières différentes puisqu'ils sont dépendants de la roche mère, du transport, du climat et du lieu de dépôt (Liu et al., 2012). Les propriétés magnétiques couplées avec d'autres traceurs utilisés en paléoocéanographie (microfossile, géochimie, minéralogie) permettent de nom-

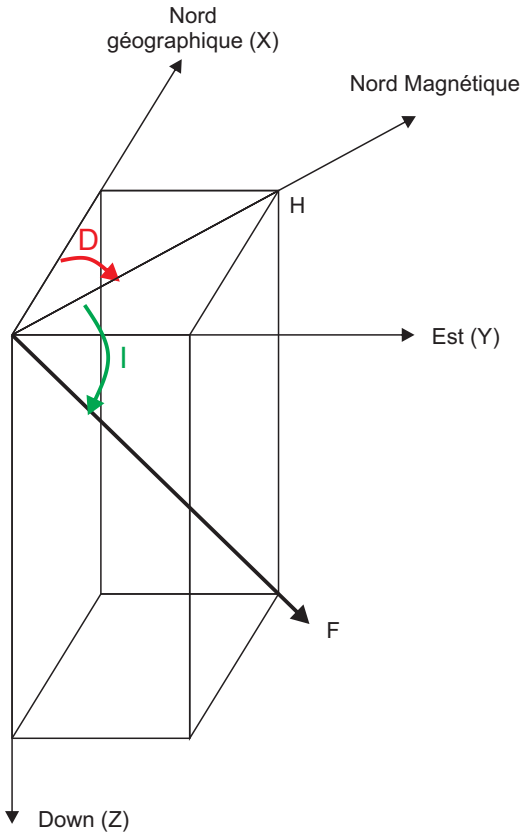

Figure 10: La direction du champ magnétique total est représentée par F. La déclinaison (D) représente la différence entre le pôle nord magnétique et géographique mesurée vers l'est et allant de 0 à 360°. L'inclinaison (I) est l'angle formé par le vecteur magnétique avec le plan horizontal (H).

breuses applications tels que tracer les sources sédimentaires (Hu et al., 2013; Venuti et al., 2011), la circulation océanique (Kissel et al., 2008; Mazaud et al., 2007), atmosphérique (Lisé-Pronovost et al., 2015; Peck et al., 2004) et la glace de mer (Brachfeld et al., 2009; Sagnotti et al., 2001). Grâce à un nombre croissant de données paléomagnétiques dans l'Arctique de l'ouest et à la compilation de l'ensemble des données, les propriétés magnétiques peuvent donner des indices sur les conditions environnementales depuis la dernière glaciation.

Géochimie et minéralogie

La taille des grains, les assemblages minéralogiques et la composition chimique constituent des attributs fondamentaux des sédiments détritiques. Ces attributs varient en fonction de la pétrologie et de la distance des zones sources. Dans ce contexte, selon leur taille, leur composition minéralogique et chimique (élémentaire et isotopique), et l'endroit où elles se sont déposées, les particules minérales détritiques des sédiments marins peuvent fournir de précieuses informations sur le contexte tectonique (Armstrong-Altrin et Verma, 2005; Verma et Armstrong-Altrin, 2013), sur les zones sources du matériel détritique (Andrews et Vogt, 2014; Martinez et al., 2009; Montero-Serrano et al., 2009, 2010; Riboulleau et al., 2014), sur le taux d'altération chimique des sédiments (Nesbitt et Young, 1982), sur la circulation atmosphérique (Bullard et al., 2016), l'intensité et la direction des courants océaniques (Bianchi et McCave, 1999; Fagel, 2007) et les débâcles d'icebergs et d'eau de fonte en provenance des calottes glaciaires (Andrews et MacLean, 2003; Montero-Serrano et al., 2009).

La composition chimique des sédiments détritiques est aussi contrôlée par plusieurs processus qui modifient les caractéristiques sédimentaires telles que l'altération chimique, la fragmentation mécanique et l'abrasion pendant le transport, le tri hydrodynamique et les conditions spécifiques de l'environnement de dépôt (Armstrong-Altrin et al., 2015; Von Eynatten et al., 2016). Ces processus conduisent à l'enrichissement préférentiel de matériaux spécifiques dans certaines fractions granulométriques et, par conséquent, la composition des sédiments tend à être fonction de la taille des grains. Par exemple, le rapport SiO_2/Al_2O_3 diminue généralement avec la taille des grains en raison de l'enrichissement relatif des phyllosilicates riches en Al au détriment des phases riches en Si dans la fraction des silts (Weltje et Von Eynatten, 2004).

Parmi l'ensemble des éléments chimiques, les terres-rares (REE) sont des éléments traces présent dans la plupart des contextes géologiques et ils sont d'une grande utilité pour comprendre une grande variété de processus géologiques, géochimiques et cosmochimiques

qui ont lieu sur les réservoirs internes et externes de la Terre. Les REE sont des éléments lithophiles, subdivisés en différents groupes : terres-rares légers (LREE : La-Ce-Pr-Nd), terres-rares moyens (MREE : Sm-Eu-Gd-Tb-Dy) et les terres-rares lourds (HREE : Ho-Er-Tm-Yb-Lu) (McLennan et Taylor, 2012). Les REE sont un groupe extrêmement cohérent d'éléments traces possédant les même propriétés géochimiques, ce qui les rend particulièrement précieux pour le suivi des processus magmatiques (McLennan et Taylor, 2012). De plus, leur courte durée de séjour dans l'eau de mer et leur faible mobilité lors des processus sédimentaires (altération, diagenèse) en font un outil très utile en géochimie sédimentaire. Au cours des dernières décennies, les REE ont été utilisés pour étudier l'évolution géochimique de la croûte continentale ainsi que l'altération chimique dans les bassins hydrographiques (Ali et al., 2014; McLennan, 1989; Taylor et al., 1981; Wu et al., 2013), les processus de déposition (Chen et al., 2003; Martins et al., 2013; Prego et al., 2012), la provenance des sédiments et les changements paléoenvironnementaux (Armstrong-Altrin et al., 2015; Asahara et al., 2012; Campodonico et al., 2016; Jung et al., 2012; Lim et al., 2014; Martinez et al., 2009; Verma et Armstrong-Altrin, 2013).

La composition minéralogique des sédiments est principalement contrôlée par la composition des roches sources (Fagel et al., 2014). Similairement à la composition géochimique des sédiments, la composition minéralogique totale des sédiments est soumise à différents processus tels que l'altération chimique, la fragmentation mécanique et le tri hydrodynamique. De ces processus, résulte un contrôle granulométrique sur l'assemblage minéralogique total (Von Eynatten et al., 2012). Ainsi, de la même manière que le rapport SiO_2/Al_2O_3, le rapport quartz/phylosillicates diminue généralement avec la taille des grains en raison de l'enrichissement relatif des phyllosilicates (Al_2O_3) dans la fraction fine au détriment des phases riches en quartz (SiO_2) dans la fraction des silts. Cependant, de par la lithologie très différente des terrains circum-arctique, la minéralogie totale des sédiments permet de reconstruire avec succès la provenance des sédiments marins (Darby et al., 2011; Dong et al., 2017; Kobayashi et al., 2016; Yamamoto et al., 2017).

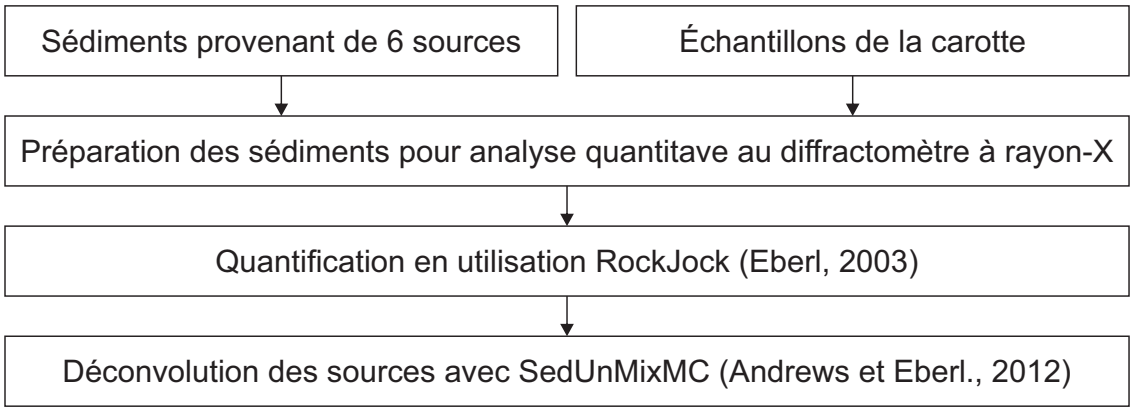

Figure 11: Diagramme montrant les étapes de la méthodologie depuis la préparation initiale de l'échantillon jusqu'à l'analyse quantitative par diffraction des rayon- X en utilisant RockJock (Eberl, 2003).

Finalement un échantillon de sédiments peut être composé d'un mélange de sédiments provenant de diverses sources. Le programme SedUnMixMC permet de calculer la contribution de chaque source (Andrews et Eberl, 2012). La première étape consiste à mesurer avec précision la minéralogie de chaque source et des échantillons par diffraction quantitative aux rayons-X en utilisant RockJock v.11 (Eberl, 2003 ; Fig. 11). La provenance des sédiments est définie par les mélanges de sédiments connus (ou sources), alors que la composition observée (échantillons) est celle calculée par SedUnMixMC. Cette méthode a été utiliser régulièrement pour déterminer la provenance des sédiments le long des marges est et ouest du Groenland (Andrews et Vogt, 2014; Andrews et al., 2015, 2016). Dans cette étude, il s'agit de la première utilisation de cette méthode dans l'océan Arctique. L'utilisation de SedUnMixMC va nous permettre d'acquérir une évaluation quantitative sur la provenance des sédiments.

En général, les minéraux argileux sont constitués de feuilles tétraédriques et octaédriques comprenant des cations interstratifiés. Un cation de silicium est situé au centre de chaque tétraèdre et un cation d'alumimium se trouve sur la position centrale des octaèdres (Fagel, 2007). Les coins de ces structures sont occupés par des anions d'oxygène. Les minéraux argileux couramment utilisés dans les études sédimentologiques sont la kaolinite, l'illite, la smectite et la chlorite. La kaolinite est le minéral argileux 1 :1 le plus abondant

(c'est-à-dire une feuille tétraédrique, une feuille octaédrique), alors que l'illite et la smectite constituent les principaux minéraux argileux de type 2 :1. La chlorite est considérée comme ayant une structure de couche 2 :1 :1 comportant un feuillet d'hydroxyde d'aluminium ajoutée au type argileux général 2 :1 (Fagel, 2007). Les minéraux argileux sont formés par pédogenèse des surfaces rocheuse par des processus d'altération physique et chimique. L'altération chimique dominant le processus est l'hydrolyse (5<pH<9,6), qui dépend largement des précipitations, de l'insolation et de la température. L'altération des différentes lithologies fournit des assemblages de minéraux argileux pouvant être caractéristique des sources locales. Les minéraux argileux dans les sédiments (fraction des argiles < 2 μm) sont transportés vers les océans *via* le ruissèlement de surface, les décharges particulaires des fleuves et la circulation atmosphérique. Dans ce contexte, l'assemblage de minéraux argileux est largement utilisé comme outil pour déterminer l'origine des sédiments marins (Kalinenko, 2001; Krylov et al., 2014; Naidu et al., 1971, 1982; Naidu et Mowatt, 1983; Stein et al., 2017 ; Fig. 12).

Granulométrie

Pour décrire les propriétés sédimentaires, la granulométrie fait partie des analyses principales en géologie marine. La granulométrie est dépendante des processus hydrodynamiques et du type de transport des grains détritiques. Par exemple, le transport des sédiments est influencé par les gammes granulométriques de la zone source, l'apport sédimentaires et le ruissellement, tandis que la taille des grains plus grossiers dans un lac peut également être liée à une baisse du niveau du lac (Dietze et al., 2012). D'une manière générale, il est admis que la fraction argileuse (< 2 μm) est transportée plus loin au large par les courants océaniques et cette fraction est moins sensible à la remobilisation après dépôt en raison de son comportement cohésif (Gingele et al., 2004; Stumpf, 2011).

Dans le contexte de l'océan Arctique, la granulométrie est fortement influencée par le

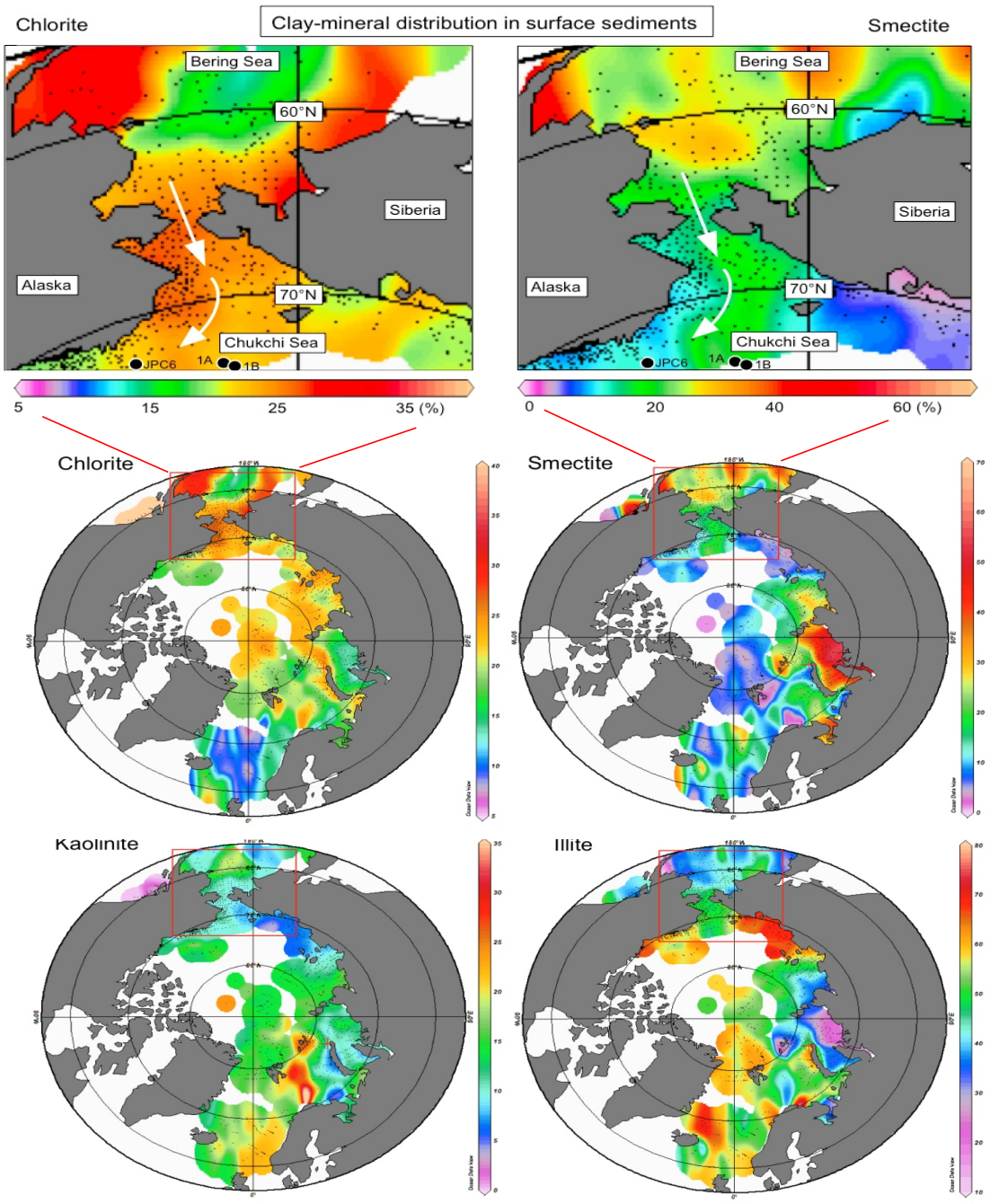

Figure 12: Assemblage de la minéralogie des argiles des sédiments de surface de l'océan Arctique. Un zoom sur le détroit de Béring permet de voir la dispersion de la chlorite et la smectite avec l'advection des eaux pacifiques (Stein et al., 2017).

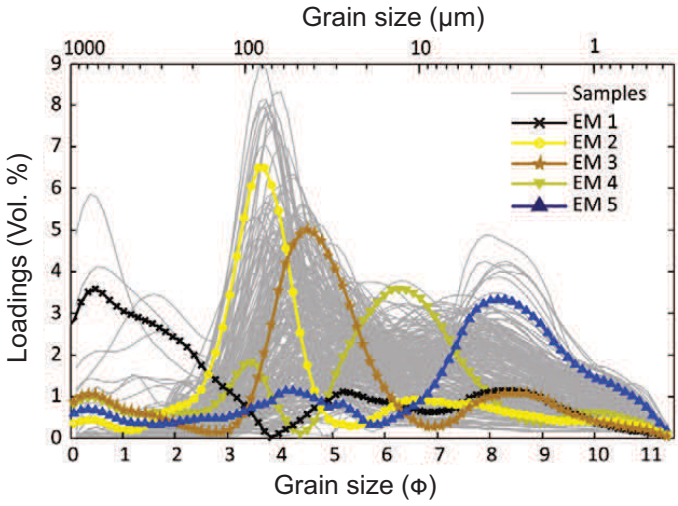

Figure 13: Exemple de distribution granulométrique d'échantillons (en gris) et les "end-members" calculés en utilisant l'algorithme de modélisation par mélange de pôles "EMMA" (Dietze et al., 2013).

type de transport sédimentaire (glace de mer, courant de fond et IRD) car chaque type de transport correspond à une gamme granulométrique précise (Darby et al., 2009). Cependant, lorsque des sédiments de différentes sources et processus de transport sont déposés dans un même endroit, ils se mélangent (Dietze et al., 2012). L'algorithme de modélisation par mélange de pôles (EMMA) développé par Weltje (1997) et adapté par Dietze et al. (2012) permet d'extraire de distributions granulométriques significatives (qu'on appellera les end-members, EM) et d'estimer leur contribution proportionnelle aux sédiments (Fig. 13). De plus, l'analyse de la composition géochimique des carottes 02PC et 05JPC a été réalisée sur la fraction totale et des argiles ($< 2\ \mu$m). Cette approche nous permet de mettre en relation la différence de composition chimique entre les fractions avec les différents types de transports sédimentaires (Fig. 5). Dans l'ensemble, la distribution de la taille des grains et la modélisation des EM ont été utilisées pour étudier la dynamique sédimentaire, car la distribution granulométrique des sédiments reflète les conditions de transport (Dietze et al., 2012; Montero-Serrano et al., 2009; Simon et al., 2012).

Isotopes radiogéniques (hafnium, néodyme et strontium)

Le Hf (hafniun) et le Nd (néodyme) peuvent être utilisés comme traceurs pour les processus ignés ou les régimes d'altération, ainsi que sur la provenance des roches et leurs produits d'altération (Frank, 2002). Les décroissances radioactives du ^{176}Lu ($t_{1/2}$=3,71x10^{10} ans) et ^{147}Sm ($t_{1/2}$=1,06x10^{11} ans) produisent respectivement du ^{176}Hf et ^{143}Nd. La désintégration radioactive conduit ainsi à l'augmentation de l'abondance des isotopes fils respectif dans les rapports isotopiques (^{176}Hf/^{177}Hf, ^{143}Nd /^{144}Nd) au fil du temps. La composition isotopique de tout échantillon géologique est par conséquent régie par l'abondance des rapports isotopiques parents/fils, qui varie en fonction des processus minéralogiques tels que la cristallisation ou l'altération (Frank, 2002). Par exemple, les minéraux ayant un faible rapport Lu/Hf auront par conséquent un faible ^{176}Hf/^{177}Hf au fil du temps. Au cours des processus ignés, le fractionnement élémentaire, en particulier entre les éléments tels que les terres-rares (Lu, Sm et Nd) ou les éléments à forte intensité de champs (Hf), se produisent fréquemment. Ces processus de fractionnement entraînent une incorporation différente de ces éléments dans les minéraux au cours de la formation des roches. Par exemple, le Nd est légèrement moins compatible que le Sm, ce qui entraîne un enrichissement relatif en Nd dans la croûte continentale. Les compositions isotopiques Nd et Hf sont généralement exprimées en unité epsilon (ε), ce qui correspond à l'écart relatif du ^{143}Nd/^{144}Nd et du ^{176}Hf/^{177}Hf d'un échantillon à celui du Réservoir Uniforme Chondritique (CHUR) avec ^{143}Nd/^{144}Nd = 0,512638 (Jacobsen et Wasserburg, 1980), et ^{176}Hf/^{177}Hf = 0,282769 (Nowell et al., 1998)) fois 10 000. La composition isotopique des Hf et Nd dépend en grande partie de la lithologie et de l'âge de la croûte, un faible ratio ^{143}Nd/^{144}Nd (εNd de -40) reflétant une ancienne croûte continentale et un ratio ^{143}Nd/^{144}Ndd (εNd de +20) élevé reflétant les roches dérivées du manteau (Frank, 2002). La variabilité de la composition isotopique du Hf dans les roches terrestres est deux fois plus grande que celle du Nd, allant des valeurs faiblement radiogéniques en εHf de -50 dans les roches archéennes jusqu'à des valeurs allant jusqu'à +25 dans les basaltes océaniques (Zimmermann et al., 2009b).

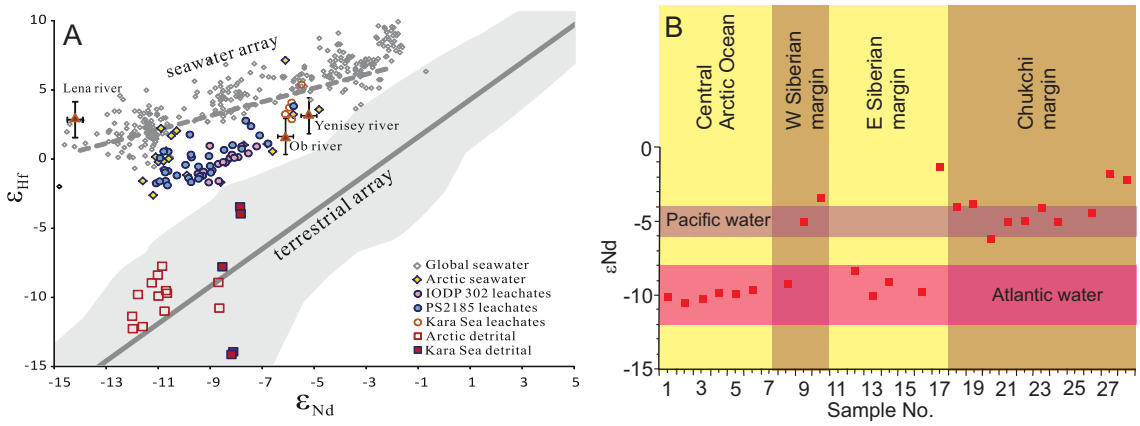

Figure 14: (A) Compositions isotopiques en Nf-Hf de l'eau de mer, lixiviats et de sédiment détritique dans l'océan Arctique (Chen et al., 2012) et (B) signatures isotopiques en Nd des eaux atlantiques et pacifiques (Haley et Polyak, 2013).

La composition en Nd et Hf de l'eau de mer reflète la différence dans la composition isotopique des roches continentales environnantes transportées à l'océan *via* les fleuves (Goldstein et Jacobsen, 1987). Le Nd et le Hf ont des temps de résidence dans l'océan (Nd : 500 à 2000 ans ; Hf : 250 à 7500 ans) permettant de les utiliser comme traceur pour la signature des masses d'eau (Zimmermann et al., 2009a,b), pour les changements de provenance et le mélange de la masse d'eau (Chen et al., 2012; Rickli et al., 2009; Stichel et al., 2012) et comme traceurs pour l'altération continentale passée (Gutjahr et al., 2014; Rickli et al., 2010). En effet, les différentes masses d'eau océanique se caractérisent alors par des compositions isotopiques en Nd et Hf contrastées, qui dépendent de la distribution hétérogène des compositions isotopiques en Nd et Hf des formations géologiques contribuant aux sources de Nd et Hf dissoutes dans l'océan. A priori indépendant de tout processus de fractionnement biologique dans la colonne d'eau, les isotopes du Nd et du Hf font partie des traceurs émergents dans la communauté paléocéanographique afin d'effectuer des reconstructions de circulation océanique du passée. D'ailleurs, il est possible d'estimer la composition isotopique du Nd et du Hf de l'eau de mer dans le passé, en analysant les fossiles carbonatés (Colin et al., 2010; van de Flierdt et al., 2010) ainsi que la fraction authigène des hydroxydes ferromagnésien des sédiments marins (Gutjahr et al., 2007). Ces derniers reflètent directement la composi-

tion en eau de mer lors de leur formation car les éléments traces (tels que le Sr, Nd et Hf) y sont incorporés par des processus de co-précipitation (Bayon et al., 2004; Frank, 2002). La composition isotopique entre la fraction authigène et détritique est très différente avec un enrichissement en Hf radiogénique pour une valeur en Nd donnée. Cette différence permet la séparation entre la composition isotopique terrestre ("terrestrial array ") et la combinaison des compositions de l'eau de mer et des encroutements ferromagnésiens ("seawater array ") comme le montre la figure 14A.

La composition isotopique en Nd des eaux profondes de l'océan Arctique est principalement dominée par les masses d'eau d'origine Atlantique, bien que les décharges des rivières et les masses d'eau de source Pacifique aient aussi des impacts perceptibles (Haley et Polyak, 2013; Porcelli et al., 2009). L'eau atlantique se caractérise par des signatures en εNd plus radiogénique (-9 à -11 ; Haley et Polyak, 2013; Porcelli et al., 2009) et en εHf moins radiogénique (1,6 ; Zimmermann et al., 2009a). Les eaux du Pacifique Nord, entrant dans l'Arctique par le détroit de Béring, sont caractérisées par de faibles valeurs en εNd (-4 à -6 ; Haley et Polyak, 2013; Porcelli et al., 2009) et des valeurs en εHf plus radiogénique (5,8 ; Porcelli et al., 2009). Grace à cette différence, les isotopes du Nd et du Hf peuvent fournir des renseignements sur les échanges des masses d'eau dans l'ouest de l'océan Arctique au cours de l'Holocène (Fig. 14B).

Finalement, le strontium (Sr) est un élément conservateur dans l'eau de mer, il a un long temps de résidence dans la colonne d'eau, de l'ordre de plusieurs millions d'années (2,5 Ma ; Hodell et al., 1990) par rapport au taux de mélange des océans (500-1000 years ; Tachikawa, 2003). La composition isotopique du Sr ($^{87}Sr/^{86}Sr$) extraite des Fe-Mn oxyhydroxides dans les sédiments pélagiques récents devrait donc reproduire la valeur isotopique de l'eau de mer actuelle de 0,70918 (Gutjahr et al., 2007; Palmer et Elderfield, 1985).

Organisation de la thèse

Cette thèse est structurée en quatres articles formant les trois chapitres qui répondent à chacun des objectifs du projet de recherche. Le premier article correspondant au premier chapitre. Le second est troisième article forment le second chapitre deux de cette thèse et finalement le quatrième article correspond au chapitre trois À noter que les références bibliographiques de l'introduction générale, de la conclusion générale ainsi que les références utilisées dans les articles qui constituent les trois chapitres suivants sont présentées à la fin de la thèse

Le premier chapitre (Article 1) présente les modèles d'âge de trois carottes sédimentaires (01JPC, 02PC et 03PC) ainsi que l'étude des propriétés magnétiques de sédiments des marges de la mer de Beaufort et de la mer des Tchouktches. La chronologie des carottes ainsi que les principales conclusions obtenues en réponse au premier objectif ont été publiées en décembre 2017 dans la revue *Boreas*.

Deschamps C.-E., St-Onge G., Montero-Serrano J.-C., Polyak L. 2018. *Chronostratigraphy and spatial distribution of magnetic sediments in the Chukchi and Beaufort seas since the last deglaciation. Boreas 47(2), 544-564. https ://doi.org/10.1111*

Le deuxième chapitre (Articles 2 et 3) caractérise la composition minéralogique et chimique des deux carottes sédimentaires récoltées sur la marge continentale des mers de Beaufort (02PC) et des Tchouktches (05JPC). C'est la première étude en Arctique de l'ouest combinant à la fois la minéralogie (fraction totale et argileuse), les éléments majeurs, traces et REE sur un jeu de longues carottes sédimentaires. Ce chapitre se découpe en deux articles : le premier est centré sur la minéralogie et les éléments majeurs et le second article porte sur les REE. Ce dernier article synthétise les principaux résultats présentés dans le première article tout en intégrant de nouvelles données sur la concentration en éléments traces et terres-rares. Dans l'ensemble, les résultats obtenus permettent de donner un portrait plus robuste sur la dynamique sédimentaire dans l'Arctique de l'ouest en lien avec les variations climatiques et

océanographiques depuis la dernière déglaciation.

Deschamps C.E., Montero-Serrano J.C., St-Onge G. 2018. *Sediment provenance changes in the western Arctic Ocean in response to ice-rafting, sea-level and oceanic circulation variations since the last deglaciation. Geochemistry, Geophysics, Geosystem*, https ://doi.org/10.1029/2017GC007411.

Deschamps C.-E., Montero-Serrano J.-C., St-Onge G. *Provenance of postglacial sediments from the Canadian Beaufort and Chukchi-Alaskan margins (western Arctic Ocean) : a geochemical perspective.* L'article sera soumis prochainement à la revue *Journal of Quaternary Science*.

Le troisième chapitre (Article 4) présente des données sur la composition isotopique en Nd et Hf extraites des oxyhydroxides de Fe et de Mn de sédiments issus de deux carottes sédimentaires prélevées sur la marge continentale des mers de Beaufort (02PC) et des Tchouktches (01JPC) à 1000 m de profondeur. Les résultats obtenus permettent de reconstituer la dynamique de la circulation profonde dans l'ouest de l'Arctique depuis la dernière déglaciation.

Deschamps C.-E., Montero-Serrano J.-C., St-Onge G.Poirier A. *Deep water changes in the Beaufort and Chukchi Seas since the deglacial inferred to Nd-Hf isotopes.* L'article est en préparation avancée et sera soumis à la revue *Paleoceanography and Paleoclimatology*.

Enfin, les principales conclusions sont présentées à la toute fin de ces quatres articles qui composent le cœur de la thèse. Ces conclusions générales sont exposées sous forme d'une discussion générale montrant l'ensemble des problématiques abordées au cours de ce projet, les principaux résultats obtenus ainsi que quelques perspectives possibles pour de futures recherches associées aux problématiques soulevées dans ce projet.

Autres réalisations

Au cours de mon doctorat, j'ai eu l'occasion de participer à des activités directement reliées à mon projet de thèse. J'ai participé à trois congrès internationaux (Arctic Change, International conference on paleoceanography) ainsi qu'à cinq congrès scientifiques nationaux (GEOTOP, Québec-Océan et l'Acfas) pour présenter les principaux résultats de mon projet de recherche. De plus, j'ai aussi participé à un colloque de vulgarisation scientifique à l'UQAR (la nature dans tous ses états) pour vulgariser mon projet de recherche sur les études paléoclimatologiques dans l'Arctique. En plus de l'expédition 2014 à bord du brise-glace canadien NGCC Amundsen pour récupérer les carottes sédimentaires utilisées au cours de ce doctorat, j'ai eu la chance de participer à d'autres missions océanographiques. La seconde mission fut le projet CASEIS en collaboration avec l'*Institut de physique du globe de Paris* (IPGP) sur le N/O Pourquoi pas ? en 2016. La troisième mission océanographique fut à bord du NCGS Amundsen pour récupérer des échantillons dans l'archipel Arctique canadien en 2016. En plus d'offrir mon aide sur le terrain, j'ai pu contribuer à la réalisation des rapports de mission pour les expéditions 2014 et 2016 sur l'Amundsen (ouvrages collectifs).

Communications

Deschamps C.-E., Montero-Serrano J.-C., St-Onge G. 2014. *Holocene paleoceanography and clinate variability in the Western Arctic Ocean*. Congrès annuel des étudiants du Geotop, Pohénégamook (Québec,Canada). Affiche.

Deschamps C.-E., St-Onge G., Montero-Serrano J.-C. 2014. *Chronostratygraphy challenges and climate variability in the Western Arctic Ocean*. Congrès Arctic Change, Ottawa (Ontario, Canada). Affiche.

Deschamps C.-E., Montero-Serrano J.-C., St-Onge G. 2015. *Tracking sediment provenance in the Western Arctic Ocean throught the last 14,000 years : preliminary results*. Congrès annuel des étudiants du Geotop, Jouvence (Québec,Canada). Affiche.

Deschamps C.-E. 2015. *Paléoclimatologie : les contes du passé*. Colloque la nature dans tous ses états. Rimouski (Québec, Canada). Présentation orale, vulgarisation scientifique.

Deschamps C.-E., Montero-Serrano J.-C., St-Onge G. 2015. *Géochimie et minéralogie des sédiments des mers de Beaufort et des Tchouktches au cours des 15000 dernières années*. 83 ème congrès de l'Acfas, Rimouski (Québec, Canada)). Présentation orale.

Deschamps C.-E., St-Onge G., Montero-Serrano J.-C. 2016. *New high-resolution paleomagnetic records and magnetic properties of sediments from the Chukchi and Beaufort Seas*. Congrès annuel des étudiants du Geotop, Montréal (Québec, Canada). Présentation orale.

Deschamps C.-E., Montero-Serrano J.-C., St-Onge G. 2016. *Sediment provenance in the western Arctic Ocean since the last deglaciation : paleoceanographic implications*. International conference on paleoceanography, Utrecht (Pays-Bas). Affiche.

Deschamps C.-E., Montero-Serrano J.-C., St-Onge G. 2016. *Étude de la provenance des sédiments à partir de la géochimie et de la minéralogie depuis la déglaciation en Arctique de l'ouest*. Congrès annuel de Québec-Océan, Rimouski (Québec, Canada). Affiche.

Deschamps C.-E., Montero-Serrano J.-C., St-Onge G. 2017. *Discrimination of sediment provenance in the continental margin of the Beaufort Sea and Chukchi Seas (Arctic Ocean) since the deglaciation : insight from trace and rare earth elements*. Congrès annuel des étudiants du Geotop, Montmenrency (Québec, Canada). Présentation orale.

Deschamps C.-E., Montero-Serrano J.-C., St-Onge G. 2017. *Mineralogy and rare earth elements geochemistry of sediments from the western Arctic Ocean : implications for sediment provenance and paleoclimate*. Congrès Arctic Change, Québec (Québec, Canada). Présentation orale.

Ouvrage collectifs

Montero-Serrano, J.-C, **Deschamps, C.-E.**, Jaegle, M., 2014. *Amundsen Expedition Report : Geology and paleoceanography leg 2a. ArctiNet*, Université Laval. Disponible en ligne :

http ://www.arcticnet.ulaval.ca/pdf/media/2014_Amundsen_Expedition_Report.pdf.

Montero-Serrano J.-C., **Deschamps C.-E.** 2016. *Amundsen Expedition Report : Geology and paleoceanography leg 3a-b*. ArctiNet, Université Laval.

ARTICLE 1

CHRONOSTRATIGRAPHIE ET DISTRIBUTION SPATIALE DES SÉDIMENTS MAGNÉTIQUES DES MERS DE BEAUFORT ET DES TCHOUKTCHES DEUIS LA DERNIÈRE DÉGLACIATION

1.1 Résumé en français du premier article

L'étude paléomagnétique de trois carottes sédimentaires recueillies sur les marges continentales de la mer de Tchouktches (01JPC) et de la mer Beaufort (02PC et 03PC) a été réalisée afin d'établir une chronologie de référence et d'étudier les propriétés magnétiques des sédiments depuis la dernière déglaciation. Les analyses paléomagnétiques révèlent que les sédiments étudiés sont caractérisés par des minéraux ferrimagnétiques à basse coercivité (tel que la magnétite), principalement dans la gamme granulométrique pseudo-mono-domaine, et par une aimantation rémanente forte, stable et bien définie (MAD < 5°). La chronologie pour ces carottes sédimentaires a été déterminée en comparant les PSV (inclinaison, déclinaison et paléointensité relative) avec des enregistrements publiés antérieurement et indépendamment datés dans la même zone d'étude. Les modèles d'âge ont été vérifiés par datation radiocarbone dans les carottes 02PC et 03PC, et par tephrochronologie et estimation de vitesse de sédimentation basée sur le ^{210}Pb pour la carotte 01JPC. Les résultats indiquent que les carottes sédimentaires 01JPC, 03PC et 02PC couvrent respectivement les derniers 6, 10,5 et 13,5 cal ka BP. La chronologie des carottes 01JPC et 03PC indiquent des taux de sédimentation stables depuis la déglaciation (60 cm.ka^{-1} et 40-70 cm.ka^{-1}). Tandis que dans la carotte 02PC, le taux de sédimentation montrent une diminution considérable entre la déglaciation et l'Holocène allant de ~ 60 cm.ka^{-1} à 10-20 cm.ka^{-1}). Dans l'ensemble, cette étude illustre l'utilité du paléomagnétisme pour améliorer la datation des enregistrements sédimentaires de l'Holocène dans l'océan Arctique.

L'article intitulé "*Chronostratigraphy and spatial distribution of magnetic sediments in the Chukchi and Beaufort Seas since the last deglaciation*" fut rédigé par moi-même sous la supervision de mon directeur Jean-Carlos Montero-Serrano (UQAR-ISMER) et de mon co-directeur Guillaume St-Onge (UQAR-ISMER). Leonid Polyak, chercheur du Byrd Polar and Climate Research Center (Ohio, USA) a aussi contribué à la rédaction de cet article. Quentin Beauvais (UQAR-ISMER) et Marie-Pier St-Onge (UQA-ISMER) ont également apporté leur aide pour les analyses en laboratoire. L'article a grandement bénéficié des commentaires et des suggestions constructifs faits par Dennis A. Darby, Daniel Rey et de Jan A. Piotrowski. L'article a été accepté par l'éditeur pour publication dans sa version finale le 18 octobre 2017 dans la revue *Boreas*.

Une version abrégée de ces travaux de recherche ont été présentés sous forme d'affiches au congrès Arctic Change qui s'est déroulé à Ottawa en 2014. De plus, une version préliminaire de l'article a été présentée sous la forme de présentation orale au congrès annuel des étudiants du GEOTOP qui a eu lieu à Montréal en 2016.

1.2 Chronostratigraphy and spatial distribution of magnetic sediments in the Chukchi and Beaufort seas since the last deglaciation

Paleomagnetic investigation of three sediment cores from the Chukchi and Beaufort margins was performed for better constrain the regional chronostratigraphy and to gain insights into sediment magnetic properties at the North American Arctic margin during the Holocene and the preceding deglaciation. Paleomagnetic analyses reveal that sediments under study are characterized by low-coercivity ferrimagnetic minerals (magnetite), mostly in the pseudo-single domain grain-size range, and by a strong, stable, well-defined remanent magnetization (MAD < 5°). Age models for these sediment cores were constrained by comparing their paleomagnetic secular variations (inclination, declination, and relative paleointensity) with previously published and independently dated sedimentary marine records from the study area. The magnetostratigraphic age models were verified by AMS radiocarbon dating tie points in the AMD cores, and by tephrochronology and ^{210}Pb-based sedimentation rate estimate for 01JPC1. The analyzed cores 01JPC, 03PC and 02PC span the last ~6, 10.5 and 13.5 cal ka BP, respectively. The estimated sedimentation rates were stable since the deglaciation in cores 01JPC (60 cm.ka^{-1}) and 03PC (40-70 cm.ka^{-1}). Core 02PC show much lower Holocene sedimentation rates with a strong decrease after the deglaciation from ~60 cm.ka^{-1} to 10-20 cm.ka^{-1}). Overall, this study illustrates the usefulness of palaeomagnetism to improve the dating of Late Quaternary sedimentary records in the Arctic Ocean.

1.3 Introduction

Radiocarbon dating is the most widespread method used to determine the age of fossils or organic matter deposited in marine sediment cores during the last ~40-50 ka. However, the scarcity and poor preservation of calcareous tests and a high content of redeposited terrestrial organic matter in the Arctic Ocean complicates the dating of sediments (Barletta et al., 2010; Ledu et al., 2008; McKay et al., 2008). Moreover, radiocarbon dating in the Arctic is compli-

cated by an often poorly constrained radiocarbon reservoir age (Hanslik et al., 2010). Consequently, paleoceanographic reconstructions in this climatically sensitive region are hampered by a lack of robust chronologies. One tool that has a potential to circumvent these difficulties is paleomagnetism, which can be used to reconstruct centennial/millennial-scale variations in the Earth's magnetic field and to identify regional chronostratigraphic markers by observing synchronous changes such as inclination, declination, or intensity of the magnetic field (Barletta et al., 2008, 2010; Darby et al., 2012; Lisé-Pronovost et al., 2009; Lund et al., 2016). As a result, paleomagnetism helps to establish the age control in chronostratigraphycally challenging environments (St-Onge et al., 2007; St-Onge and Stoner, 2011).

A few studies have used magnetostratigraphy as a regional dating tool for Holocene sediments on the western Arctic continental margins in the absence of datable material or to independently support and improve chronostratigraphy based on radiocarbon dating (Barletta et al., 2008, 2010; Darby et al., 2012; Lisé-Pronovost et al., 2009). These studies have compared the identified chronostratigraphic markers with Holocene paleomagnetic curves, such as for western North American volcanic rocks (PSVL; Hagstrum and Champion, 2002) or Grandfather Lake sediments in Alaska (GFL; Geiss and Banerjee, 2003), and also with global geomagnetic field models (CALS7k.2) based on spherical harmonic analysis (Korte and Constable, 2005). However, most of the paleomagnetic records generated in the Beaufort Sea fall short of recovering the entire Holocene and the deglacial sediments (Barletta et al., 2008, 2010; Lisé-Pronovost et al., 2009). This lack of data on paleomagnetic secular variation in the early Holocene and deglaciation is mainly due to the use of cores recovered by relatively short piston coring at sites with high sedimentation rates (>100 cm.ka^{-1}; Barletta et al., 2008; Darby et al., 2009). In stratigraphically longer records studied at the Chukchi margin, the deglacial sediments contained large amounts ice-rafted debris (IRD), which makes them unsuitable for paleomagnetic reconstructions (Barletta et al., 2008; Lisé-Pronovost et al., 2009).

In this paper, we present the full-vector paleomagnetic records (inclination, declination,

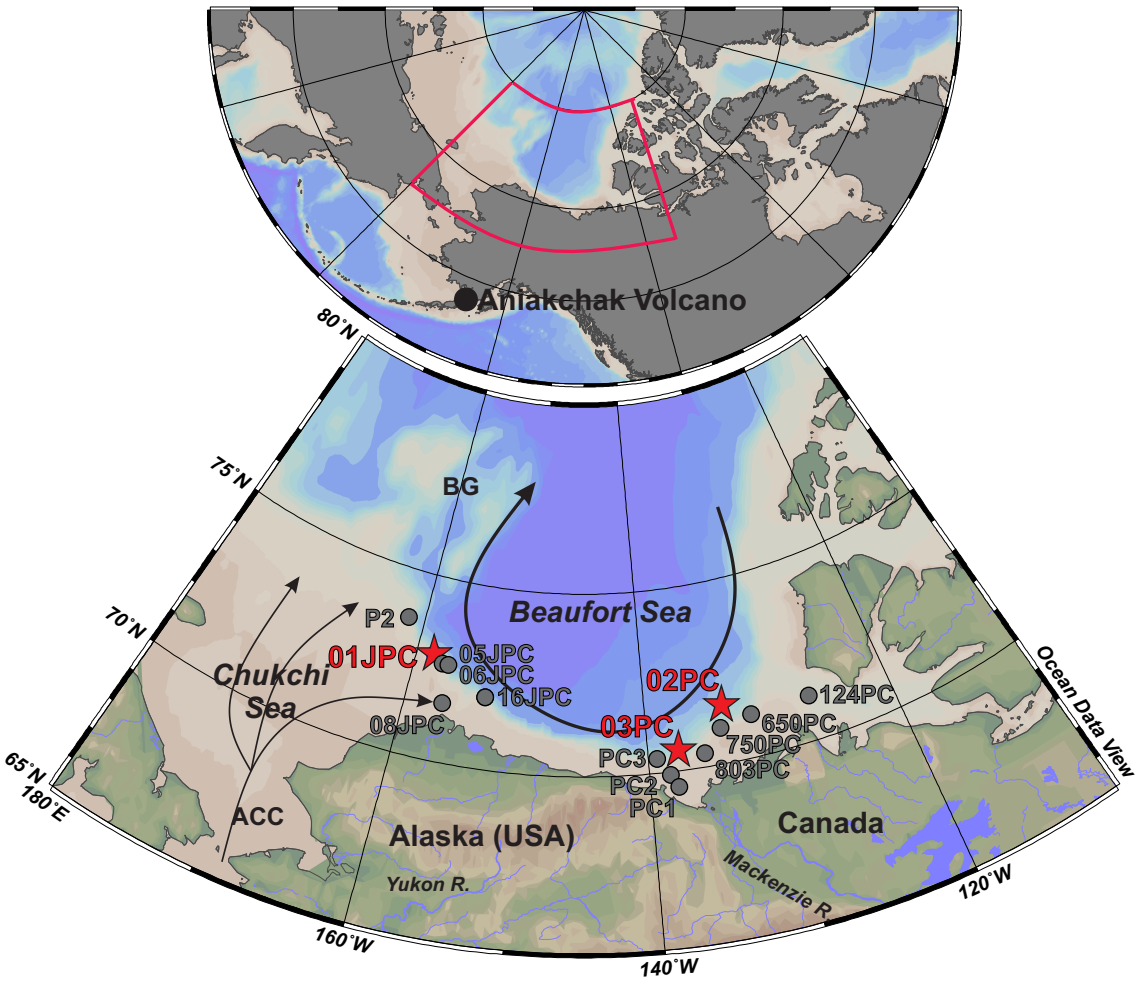

Figure 15: Index map of the Beaufort and Chukchi margins and adjacent western Arctic Ocean showing location of cores 01JPC, 02PC and 03PC (red stars). Also shown is location of earlier investigated cores (grey circles) used for comparison (Barletta et al., 2008, 2010; Darby et al., 2012; Lisé-Pronovost et al., 2009; Polyak et al., 2007; Schell et al., 2008; Scott et al., 2009). The location of the Aniakchak Volcano is illustrated in the insert. ACC = Alaskan Coastal Current; BG = Beaufort Gyre.

and relative paleointensity) of three piston cores from the Alaska-Chukchi and Beaufort margins, as well as the magnetic properties of several sediment cores along the North American margin (Fig. 15) in order to: improve chronostratigraphy of the Holocene to deglacial sediments in the western Arctic Ocean, and characterize and understand the spatial and temporal distribution patterns of magnetic parameters along the Beaufort and Chukchi shelves.

1.4 Regional Settings

The shallow Chukchi and Beaufort sea margins were last flooded during the glacial/Holocene transition (Keigwin et al., 2006). The Chukchi shelf circulation is controlled by an inflow of Pacific waters via the Bering Strait, the Siberian coastal current, and the Atlantic Intermediate Water affecting the northern margin (Pickart, 2004; Weingartner et al., 2005). Modern sediment in the Chukchi Sea is believed to be mainly derived from northeastern Siberia and Bering Strait inflow (especially from the Yukon River), whereas, the Beaufort margin sediment originates primarily from the Mackenzie River basin (Asahara et al., 2012; Ortiz et al., 2009; Viscosi-Shirley et al., 2003b). Smaller Alaskan rivers have a more local impact but may have been a more important sediment source at the early stages of the last transgression (Hill and Driscoll, 2008). The ice-rafted debris (IRD) is also an important sediment component in the Chukchi and Beaufort seas (Darby, 2003; Ortiz et al., 2009). In modern and Holocene sediments the IRD may originate from multiple sources including local and distant provenance, depending on circulation that controls the ice drift (Darby and Bischof, 2004; Darby et al., 2012; Polyak et al., 2016).

The Canadian Beaufort Shelf occupies a broad, rectangular area (about 120 km width and 530 km of length) bordered by the Amundsen Gulf to the east, Mackenzie Canyon to the west, the Mackenzie River delta to the south, and the deep basin of the Beaufort Sea to the north. Sedimentation on the Canadian Beaufort Shelf is mostly influenced by the Mackenzie River plume (Richerol et al. 2008). Although the Mackenzie River discharges less water (~420 $km^3.a^{-1}$; Wagner et al., 2011) than the Siberian rivers, the suspended sediment load from the Mackenzie River is three to four times higher than from the Siberian rivers (Matthiessen et al., 2000). The total sediment load delivered to the head of the delta reaches up to 128 $Mt.a^{-1}$ (Carson et al., 1998; O'Brien et al., 2006), which explains very high sedimentation rates in this area (about 30 to 320 $cm.ka^{-1}$; Barletta et al., 2008, 2010; Bringué and Rochon, 2012; Durantou et al., 2012).

During deglaciation and the early Holocene, sediment inputs to the Chukchi and Beaufort margins were presumably higher than at later times due to the rising sea level associated with meltwater and iceberg discharge from the retreating Laurentide Ice Sheet, although the age control for these sediments is not well constrained (Hill et al., 2007; Hill and Driscoll, 2008; Scott et al., 2009). The deglacial/glacial IRD was derived primarily from the Laurentide Ice Sheet area, such as the Canadian Arctic Archipelago, that has characteristically high content of dolomites (Phillips and Grantz, 2001; Polyak et al., 2007; Schell et al., 2008; Stokes et al., 2005).

1.5 Material and Methods

1.5.1 Coring sites

Cores HLY0501-01JPC/TWC (jumbo piston core and companion trigger weight core) and HLY0501-01MC (multicore), hereinafter referred to as 01JPC, were collected from the Chukchi-Alaskan margin on board the USCGC Healy as part of the 2005 Healy-Oden Trans-Arctic Expedition (HOTRAX) (Darby et al., 2005). Cores 1JPC/TWC were recovered in the slope of a canyon about 100 km north of Barrow at 1 163 m water depth (Table 1; Fig. 15). The 01MC was recovered nearby, but the exact water depth was not recorded.

Table 1: Location, water depth and length of sediment cores used in this study.

Core	Latitude (°N)	Longitude (°W)	Water depth (m)	Length (m)
01JPC/TWC	72.90	-158.42	1163	13.72/2
01MC	72.90	-158.42	Unknown	0.5
02PC/TWC	71.61	-133.57	998	5.48/1.32
03PC/TWC	70.55	-137.54	1051	5.85/1.74

Cores AMD0214-02PC/02TWC and AMD0214-03PC/03TWC (hereinafter referred to as cores 02PC and 03PC) were collected on board the CCGS Amundsen during the 2014 Arc-

ticNet expedition (Montero-Serrano et al., 2014). These cores were recovered at the Canadian Beaufort margin, with core 03PC located in front of the Mackenzie River delta (Table 1, Fig. 15).

Magnetic properties of several cores investigated in earlier studies have been used for comparison with the data presented in this paper. These cores included HLY0501-05JPC (Barletta et al., 2008), HLY0501-06JPC and HLY0501-08JPC (Lisé-Pronovost et al., 2009) and also HLY0203-16JPC (Darby et al., 2012) from the Chukchi Sea, as well as cores 2004-804-650PC and 2004-804-803PC (Barletta et al., 2010) from the Beaufort Shelf. Cores PC1, PC2, PC3 (Schell et al., 2008) and 2004-804-750PC (Scott et al., 2009) from the Canadian Beaufort margin were used for the age model comparison. The Chukchi-Alaskan cores were hereinafter referred to 05JPC, 06JPC, 08JPC and 16JPC.

1.5.2 Multi Sensor Core Logger analysis and core sampling

The bulk density (obtained by gamma ray attenuation) and volumetric magnetic susceptibility (k_{LF}) of all the sediment cores were measured using a GEOTEK Multi Sensor Core Logger (MSCL) at 1-cm intervals. Diffuse spectral reflectance data (sediment colour) were also acquired at 1-cm resolution immediately after splitting the cores using a Minolta CM-2600d handheld spectrophotometer and then converted into the L*, a*, b* colour space of the International Commission on Illumination (CIE). L* is a black-to-white scale (0 to 100), a* is a green-to-red scale (-60 to +60), and b* is a blue-to-yellow scale (-60 to +60) (Debret et al., 2011; St-Onge et al., 2007). The MSCL and diffuse spectral reflectance analyses were performed on board for core 01JPC and at the Institut des sciences de la mer de Rimouski (ISMER, Canada) for cores 03PC and 02PC (Annexe 2).

All cores were sampled with u-channels (u-shaped plastic liners 2×2 cm in cross-section and up to 1.5 m in length) for paleomagnetic analyses. Cores 02PC and 03PC were also ran through a CT scanner at the Institut national de recherche scientifique – Centre eau,

terre et environnement (INRS-ETE, Québec, Canada). The resulting digital X-ray images were displayed in grey scale and expressed as CT numbers, which primarily reflect changes in bulk density (St-Onge et al., 2007; St-Onge and Long, 2009). Cores 01JPC, 02PC, and 03PC were systematically sampled at every 20 cm (except for core 02PC, where IRD intervals were additionally sub-sampled) and correspond to a total of 21, 31, and 27 samples, respectively, used for grain-size and rock magnetism analyses.

1.5.3 Grain-size analyses

Sediment grain-size analyses were performed on the sediment bulk fraction using a Beckman Coulter LS13320 laser diffraction grain-size analyzer, which has a detection range of 0.04–2000 μm. Samples were deflocculated by mixing about 0.5 g of wet sediment with Calgon electrolytic solution (sodium hexametaphosphate, 20 g.L^{-1}) and subsequently shaking for at least 3 h using an in-house rotator. The grain-size distribution and statistical parameters (e.g. mean, sorting) were calculated using the moment methods from the GRADISTAT software (Blott and Pye, 2001).

1.5.4 Carbon analyses

Total carbon (C_{total}) and organic carbon (C_{org}) contents for core HLY01-1MC were determined on the bulk and carbonate-free fraction using a CHN Elemental Analyser (COSTECH 4010). The carbonate-free fraction was obtained by double 10 % HCl treatment. Precision was better than 1 % based on an internal standard (acetanilide) and replicate samples. A blank capsule was also analysed in every run to confirm the absence of contamination.

1.5.5 Paleomagnetic analysis

Paleomagnetic data were acquired at 1-cm intervals on u-channel samples using a high-resolution 2G Enterprises™ cryogenic magnetometer model 755 SRM and pulse magnetizer module (for isothermal remanent magnetization, IRM) at the Institut des sciences de la mer de Rimouski (ISMER, Canada). The natural remanent magnetization (NRM) was stepwise demagnetized and measured with 15 steps (0, 5, 10, 15, 20, 25, 30, 35, 40, 45, 50, 55, 60, 70, and 80 mT). The anhysteretic remanent magnetization (ARM) was induced in a peak alternative field of 100 mT in the presence of a weak direct current (DC) biasing field of 0.05 mT. The isothermal remanent magnetization (IRM) and saturated isothermal remanent magnetization (SIRM) were induced using the pulse magnetizer in a DC field of 0.3 and 0.95 T respectively. ARM, IRM, and SIRM were demagnetized with the same step as the NRM. The ARM was also expressed as anhysteretic susceptibility (kARM) by normalizing the ARM with the DC bias field. The median destructive field (MDF) of the NRM (labelled as MDF_{NRM}) expresses the value of the peak AF necessary to reduce the NRM intensity to half of its initial value and was calculated using the software developed by Mazaud (2005).

In order to determine the characteristic remanent magnetization (ChRM), the magnetic declination and inclination of the ChRM (labelled ChRM D and ChRM I, respectively) was computed with nine demagnetization steps between 15 and 55 mT for cores 02PC and 03PC at 1-cm intervals using standard principal component analysis (Kirschvink, 1980) which also provides the maximum angular deviation (MAD) values. The same procedure has been carried out for core 01JPC, but using 11 demagnetization steps between 10 and 60 mT. Furthermore, the ChRM declinations were corrected for rotation at section breaks and corrected for similar circular values (e.g. 0 and 360°) to derive a continuous record. MAD values lower than 5° are indicative of high-quality directional data (Stoner and St-Onge, 2007). In the absence of azimuthal orientation during coring and for better comparison with previsouly published results, the declination were corrected to provide an arbitrary mean declination of 0° over the time interval. Estimation of the relative paleointensity (RPI) from sediments is

obtained by normalizing the measured NRM by an appropriate magnetic parameter in order to compensate for the variable concentration of ferrimagnetic minerals (Tauxe, 1993).The RPI calculated for the different cores were standardized according to their mean and standard deviation (Barletta et al., 2010). Changes in inclination, declination and RPI are used in this study to establish a relative stratigraphy by comparing our new records with other independently dated paleomagnetic records from the Western Arctic.

1.5.6 Bulk magnetic properties

The magnetic assemblages were determined by measuring the hysteresis properties and the back-field remanence using a MicroMag 2900 alternating gradient force magnetometer (AGM) from Princeton Measurements Corporation. Both measurements were used to determine magnetic parameters such as Ms (saturation magnetization), Mrs (saturation remanence), Hc (bulk coercive force), and Hcr (remanent coercive force). The Mrs/Ms and Hcr/Hc ratios can be used as grain-size proxies (the so-called Day plot), as well as to identify the magnetic domain state when the main remanence-carrier mineral is magnetite (Day et al., 1977; Dunlop, 2002a,b).

1.5.7 ^{210}Pb and radiocarbon analysis

In order to support the chronostratigraphic framework derived from the paleomagnetic data, we used three radiocarbon (^{14}C) ages from foraminiferal tests in cores 02PC and 03PC, a cryptotephra study in 01-JPC/TWC (Ponomareva et al., 2017), and excess ^{210}Pb age measurements in the top 15 cm sediment in 01JPC-MC. Excess ^{210}Pb measurements were made by counting the activity of the daughter isotope ^{210}Po, ^{210}Po ($t_{1/2}$ = 138.4 days, a = 5.30 MeV) at the GEOTOP research centre (Montréal, Canada). No foraminifera were recovered in core 01JPC. Considerably high numbers of foraminifera were found at 200 and 370 cm in core 03PC and 132 cm in cores 02PC. In order to collect sufficient amounts of foraminifera for ac-

celerator mass spectrometry (AMS) analysis, intervals of 3 to 4 cm were sampled and sieved from cores 03PC (204-206 cm, 368-372 cm) and 02PC (131-133 cm) in both the working and archive halves (Table 2). AMS ^{14}C measurements were performed on mixed planktonic and benthic foraminifera at Beta Analytic Inc. (Miami, Florida) and LSCE (Laboratoire des Sciences du Climat et de l'Environnement, Paris, France). Radiocarbon ages were calibrated using the CALIB version 7.1 software (Stuiver and Reimer 1986–2017; http://calib.org/calib/) and the Marine13 calibration curve (Reimer et al., 2013). A standard oceanic reservoir age of 400 years and a regional reservoir correction (ΔR) of 400 years was applied (total: 800 years) based on the average ΔR values derived from the dates measured on five mollusc shells collected in Amundsen Gulf prior to nuclear testing (Andrews and Dunhill, 2004; McNeely et al., 2006; Scott et al., 2009). The use of this ΔR value is also supported by a comparison of paleomagnetic data for cores 2004-804-803PC and 2004-804-650PC with other well-dated Northern Hemisphere paleomagnetic records (Barletta et al., 2010).

Table 2: Ages from radiocarbon analyses (cores 02PC and 03PC) and cryptotephra identification (Ponomareva et al., 2017). Radiocarbon ages were calibrated ages using the CALIB version 7.1 software (Stuiver and Reimer 1986–2017; http://calib.org) and the Marine13 calibration curve (Reimer et al., 2013).

Core	Depth (cm)	Cor. Depth (cm)	Material	Conv. Age	Cal. Age	Lab number
01JPC	157	-	Cryptotephra	-	3600	-
03PC	200	205	Forams (mixed)	5831±70	5631(5800)5946	ECho1870
03PC	365	370	Forams (mixed)	7590±30	7555(7645)7755	Beta-429147
02PC	122	132	Forams (mixed)	6160±30	6395(6520)6655	Beta-430871

1.5.8 Age modelling

The non-linear relation between radiocarbon and calendar time-scales often causes single-calibrated ^{14}C ages to have very large and sometimes disparate ranges of possible calendar ages (Yeloff et al., 2006). Moreover, the age–depth model constructed using a linear interpolation between the dated levels assumes that abrupt changes in accumulation rates took

place exactly at the dated depths. Although this assumption is often likely to be wrong, linear interpolation frequently produces seemingly plausible age–depth models (Blaauw, 2010). In this paper, the R software package BACON was used to produce the "best fit" linearly interpolated age models (Blaauw and Christen, 2011). BACON uses a Bayesian approach to estimate the best fit or weighted mean age for each depth with a 95 % confidence interval that allows us to calibrate single radiocarbon ages and take into account other chronostratigraphic markers (such as cryptotephra and paleomagnetic tie points).

1.6 Results

1.6.1 Stratigraphy

The correlation of the physical and magnetic parameters measured on the piston cores (PC) and their companion trigger weight cores (TWC) suggests that about 110 cm, 10 cm, and 5 cm of sediments were lost during piston coring at the top of cores 01JPC, 02PC, and 03PC, respectively. Therefore, a composite succession has been constructed for core 01JPC using the TWC and JPC data in order to obtain a full reconstruction of paleomagnetic vectors (Fig. 16). Note that 1.5 m of sediment was lost between section 3 and 4 of HLY0501-01JPC during coring operation (Darby et al., 2005). However this study only focuses on the two first section of the 01JPC. Similarly, the missing sediment at the top of cores 03PC and 02PC was taken into account and all depths are hereafter expressed as corrected depths. We note that matching of piston and trigger cores is inevitably approximate due to potentially different compression/extension of sediment in individual cores.

According to the visual description, core 01JPC can be subdivided into two main lithological units (Fig. 17). Unit II (400–320 cm) consists of laminated brown to grey (Munsell colour 5Y 4/1) silty muds with dropstones typical of postglacial sediments on the Chukchi-Alaskan margin (Barletta et al., 2008, 2010; Brachfeld et al., 2009; Darby et al., 2006; Lisé-Pronovost et al., 2009). In addition, the sediment contains numerous black speckles through-

out that are probably iron sulphides (Brachfeld et al., 2009; Lisé-Pronovost et al., 2009).

A significant change in all the physical and magnetic parameters occurs at 320 cm, corresponding to the boundary with Unit I. We also observed a small decrease for the mean grain size from 6 to 4 μm (Fig. 17). Lithological units Ia and Ib mainly comprise homogenous silty mud and the only difference is related to a slight change in sediment colour: Unit Ia is grey (5Y 5/1) and Unit Ib is olive grey (5Y 5/2) (Fig. 17). This lithostratigraphic unit has been identified in the study area as Holocene marine deposit resulting from a combination of sediment drift and ice-rafted material (Darby, 2003; Darby et al., 2009; Polyak et al., 2007, 2016).

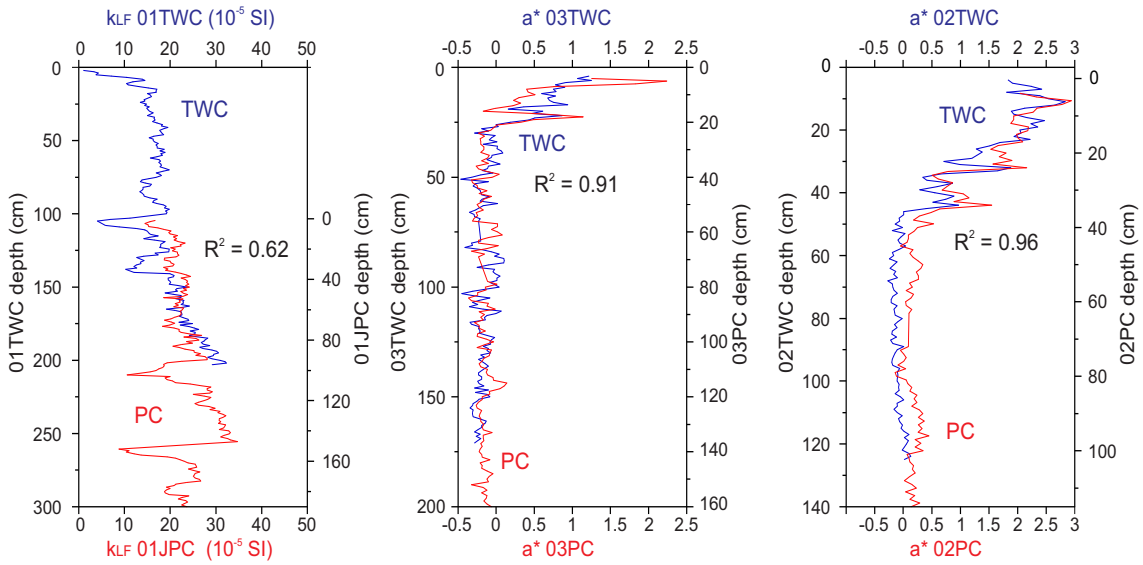

Figure 16: Correlation between piston and trigger weight cores (PC and TWC respectively) using k_{LF} for core 05JPC and a* for cores 02PC and 03PC. The correlation indicates that the top 110, 10, and 5 cm are missing from cores 01JPC, 02PC, and 03PC, respectively. Properties for the TWC and PC are shown in blue and red, respectively.

Abundant cryptotephra were counted in the upper part of core 01JPC with the main peak identified at 157 cm in the composite sequence (Fig. 17). Based on geochemical composition (including major, trace and rare earth elements), both dacitic and andesitic populations of glasses have similar patterns to bulk analyses of dacitic and andesitic tephras of the Aniakchak II eruption in southern Alaska (Ponomareva et al., 2017). Tephra layers with a

similar geochemical composition have been reported from lake cores in Alaska (Kaufman et al., 2012), eastern Canada (Pyne-O'Donnell, 2011), Greenland GRIP and NGRIP ice cores (Coulter et al., 2012; Pearce et al., 2004) and western Chukchi Sea (Pearce et al., 2017) and were dated to ~3.6 cal ka BP.

Based on CT-scan imaging of core 03PC, density gradually decreases throughout the core, along with the transition from laminated sediment at the base to homogenous sediment at the top, which allows us to subdivide it into three main lithological units (Fig.17). Despite the lithological changes, the mean grain size is quite constant along core 03PC (~3 μm; Fig. 17). In Unit III (from the base to 280 cm), the sediments are characterized by laminated olive-grey (5Y 5/2) fine muds. Likewise, numerous darker (5Y 3/2) laminations occur in this unit between 380 and 520 cm.The middle part of Unit III has been dated to 7590 cal a BP (Table 2, Fig. 17). Similar laminations have also been observed in sediment cores from the Alaskan shelf (Andrews and Dunhill, 2004) and Mackenzie Trough (Schell et al., 2008) and interpreted as the result of increased water column stratification related to deglacial environments dated to around 11 500 cal a BP in Schell et al. (2008). Between 180 and 280 cm (Unit II), the sediments are represented by a gradual lithological transition of olive-grey (5Y 4/2) laminated mud to dark-grey (5Y 4/1) faintly laminated mud. The upper part of Unit II has been dated to 5831 cal a BP (Table 2, Fig. 17). From 0 to 180 cm (Unit I), sediments consist of homogeneous dark grey (5Y 4/1) mud to olive brown (2.5Y 4/3) mud.

Core 02PC CT-scan image is quite similar to core 03PC, with a decrease in density associated with laminated sediments grading into homogeneous sediments from the base to the top of the core (Fig. 17). However, two additional major high-density intervals associated with a grain size increase (from 3 to 6 μm) can be observed between 140 and 170 cm (IRD1) and between 330 and 355 cm (IRD2, Fig. 17). For sediment core 02PC, the sediments consist of dark-grey (5Y 4/1) mud with laminations on the CT-scan image between 170 to 320 cm, as well as from 355 cm to the base of the core (Unit II) (Fig. 17). From 0 to 130 cm (Unit I), it consists of homogeneous olive-brown (2.5Y 4/3) to dark-grey (5Y 4/1) silt with a mean

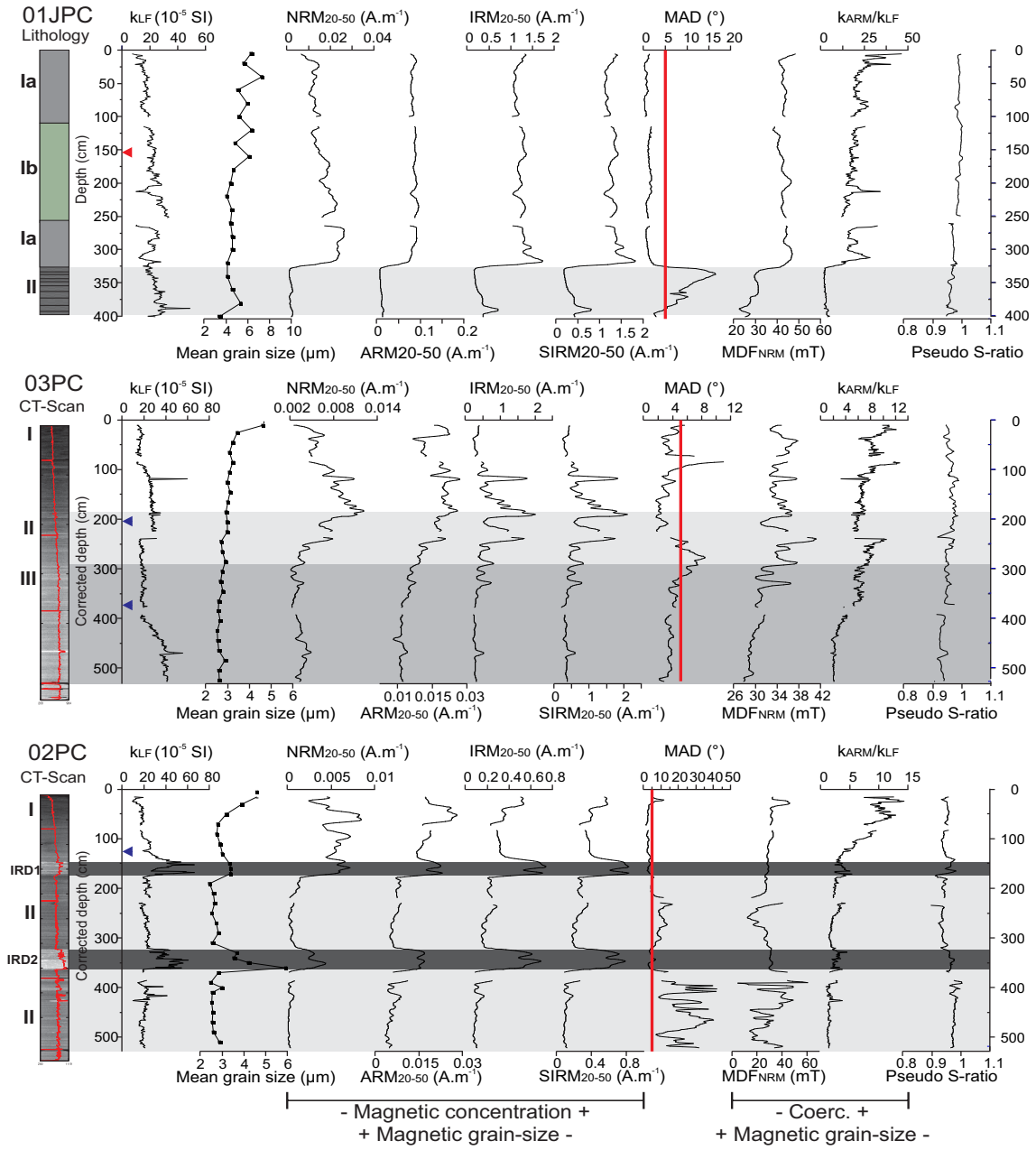

Figure 17: High-resolution magnetic properties of cores 01JPC, 03PC, and 02PC. Distinct lithological facies are numbered and highlighted in grey scale. The vertical red line delineates MAD value of 5°. CT-scan images are shown for cores 03PC and 02PC. The lithology of core 01JPC is shown schematically: units Ia and Ib are characterized by homogenous light grey and olive grey sediments, respectively, and unit II consists of laminated brown to grey sediments. Arrowheads show the position of tephra (red) in core 01JPC and ^{14}C (blue) in cores 03PC and 02PC.

grain size ranging from 3 to 4 μm (Fig. 17). The base of Unit I have been dated 6160 cal. a BP (Table 2, Fig. 17). IRD layers 1 and 2 have also been identified in the nearby core 2004-804-750PC (Scott et al. 2009) and dated to 11 580 and 13 500 cal a BP, respectively (Fig. 25). Furthermore, the white clasts in deglacial sediments from this region were previously recognised to be detrital carbonate (dolomite) transported as IRD from the Canadian Arctic Archipelago during the disintegration of the Laurentide Ice Sheet (Polyak et al., 2007; Scott et al., 2009). Similar dolomitic clasts were found in glacial/deglacial intervals in sediment cores across the entire western Arctic Ocean (Hillaire-Marcel et al., 2013; Phillips and Grantz, 2001; Polyak et al., 2009; Scott et al., 2009).

1.6.2 ^{210}Pb and Carbon data (core 01MC)

No evidence of correlation can be identified between cores 01MC and 01TWC by means of optical properties, which could indicate missing sediment from the top of core 01TWC (Fig. 26). The ^{210}Pb profile for 01MC illustrates a clear exponential decrease in the top 10 cm followed by a downcore increase started at 11 cm (Fig. 27). The increase in unsupported ^{210}Pb at 10.5 cm can be explained by an accumulation of organic matter at this depth (shown by the Corg profile in Fig. 27). The minimum value in the observed supported Pb is 5.1 dpm.g^{-1} (Fig. 27), consistent with the ~4–5 dpm.g^{-1} values reported for the Beaufort Sea (Bringué and Rochon, 2012; Scott et al., 2009). The neperian logarithm of the excess ^{210}Pb plotted against depth in core 01MC indicates an average sedimentation rate of 65 cm.ka^{-1} (Fig.27).

1.6.3 Magnetic mineralogy

The pseudo S-ratio (St-Onge et al., 2003) in core 01JPC is close to 1, with a mean value of 0.99 for Unit I and 0.95 for Unit II sediment. The pseudo S-ratio is similar for the different lithological units for cores 03PC and 02PC, with mean values of 0.94 and 0.96 respectively.

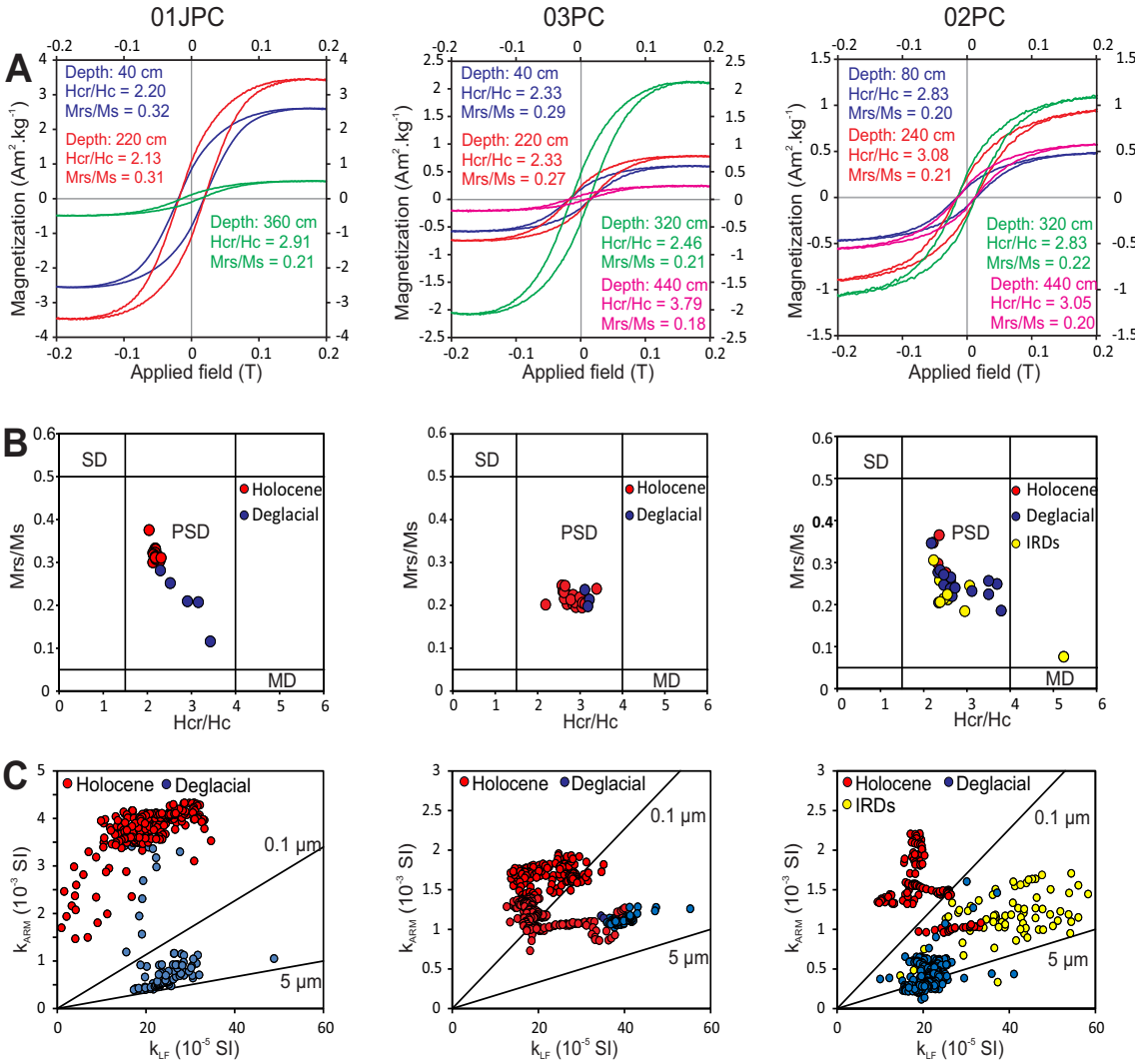

Figure 18: (A) Typical hysteresis curves and derived parameters. (B) Day plot (Day et al. 1977). (C) k_{ARM} vs k_{LF} plot representing estimated magnetic grain size for magnetite (King 1983) for cores 01JPC, 03PC and 02PC.

These values close to 1 indicate that saturation of the magnetic assemblage is achieved in a 0.3 T field, which is typical of low-coercivity minerals such as magnetite and/or titanomagnetite (Stoner and St-Onge, 2007) (Fig. 17). Furthermore, the shape of the hysteresis curves from the three sediment cores (Fig. 18A) is also characteristic of low-coercivity ferrimagnetic minerals like magnetite (Tauxe et al., 1996).

The MDF_{NRM} values are constant for lithological Unit II (mean value of 27.60 mT) and

increase in Unit I, with a mean value of 38.72 mT in core 01JPC (Fig. 17). In core 03PC, the MDF_{NRM} varies throughout the core, but increases from Unit III to Unit II (around 30 mT to 34 mT) (Fig. 17). In core 02PC, the MDF_{NRM} ranges widely from 25 mT to 49 mT between the base and 350 cm (Unit II) and is then stable from 350 cm to the top of the core (Units II and I). However, the mean values of those two distinct patterns are similar (30.84 mT and 29.24 mT, respectively; Fig. 17). MDF_{NRM} values ranging from 25–30 mT suggest the presence of low-coercivity minerals such as magnetite and/or titanomagnetite (Dankers, 1981). As the mean pseudo S ratio value in unit II of core 02PC from the base to 350 cm is very stable at 0.94, the higher frequency variations in this interval are probably related to grain size variations of the magnetic grains. In summary, the results indicate that magnetite and/or titanomagnetite is the dominant magnetic mineral throughout the cores under study.

1.6.4 Magnetic grain size and concentration

The NRM_{25-50}, ARM_{25-50}, IRM_{20-50}, and $SIRM_{25-50}$ are significantly higher in Unit I then in Unit II in core 01JPC, suggesting an increase in the concentration of ferrimagnetic minerals (Fig. 17). Unit II is characterized by a weaker k_{ARM}/k_{LF} ratio corresponding to coarser magnetic grains (Fig. 17). The presence of coarser magnetic grains is confirmed by the k_{ARM} vs k_{LF} diagram with the presence of magnetite at < 0.1 μm for Unit I and at 0.1 μm to 5 μm for Unit II (Fig. 18C). Even though these reference lines were obtained for synthetic magnetite grains, they are useful for identifying different sedimentary units. Furthermore, the Mrs/Ms and Hcr/Hc values between 0.1–0.3 and 2–5, respectively, match the pseudo-single domain (PSD) magnetite (Day et al., 1977; Dunlop, 2002a,b) (Fig. 18B).

NRM_{25-50}, ARM_{25-50}, IRM_{20-50}, and $SIRM_{25-50}$ in core 03PC are quite constant in Unit III and show several peaks in Units II and I associated with higher k_{LF} values corresponding to higher concentrations of ferrimagnetic minerals (Fig. 17). The k_{ARM}/k_{LF} ratio increases up-core, suggesting finer magnetic grains (Fig. 17). Although concentrations of ferrimagnetic minerals vary throughout the core, the k_{ARM} vs k_{LF} diagram indicates the presence of

magnetite < 0.1 μm for Units I and II and between 0.1 μm to 5 μm for Unit III (Fig. 18C). The Mrs/Ms and Hcr/Hc ratios for core 03PC are related to a finer magnetic grain size (PSD range) (Fig. 18B).

The k_{ARM}/k_{LF} ratio for core 02PC is higher in Unit I compared to Unit II and is quite constant in Unit II, corresponding to coarser magnetic grains. The magnetic concentration parameters increase during IRD intervals 1 and 2, associated with a slight decrease in the k_{ARM}/k_{LF} ratio (Fig. 17). These results imply higher magnetic concentrations associated with finer magnetic grain size than in the remainder of Unit I. According to the k_{ARM} vs k_{LF} diagram, Unit I sediments are related to magnetite grains smaller than 0.1 μm, whereas sediments from Unit I are related to magnetic grains larger than 5 μm. Sediments from IRD intervals 1 and 2 show a wide scattering in the 0.1 μm to 5 μm range (Fig. 18C). The hysteresis curves and the Day plot indicate that the magnetic mineralogy of Units I and II is mostly dominated by PSD magnetite. One sample in IRD interval 1 is related to a mixture of single-domain/multi-domain (SD-MD) grains (Fig. 18B).

1.6.5 Natural remanent magnetization

The vector end-point diagrams (Zijderveld, 1967) reveal two magnetic components: a viscous remanent magnetization component, easily removed after demagnetization at 10 mT for cores 02PC and 03PC and 5 mT for core 01JPC, and a strong, stable characteristic remanent magnetization (ChRM) (Fig. 28).

The MAD values are lower than 5° in Unit I in all cores and increase to around 15° in Unit II in core 01JPC1. In core 02PC, the MAD values reach a maximum around 40° in Unit II, but are lower than 5° from the end of IRD interval 2 (around 350 cm) to the top of the core (Fig. 17). In core AMD03, the MAD values are lower than 5° for most of the core and increase to around 8° at around 380 cm, which is still indicative of good-quality data (Stoner and St-Onge, 2007). Furthermore, the ChRM is expected to fluctuate around

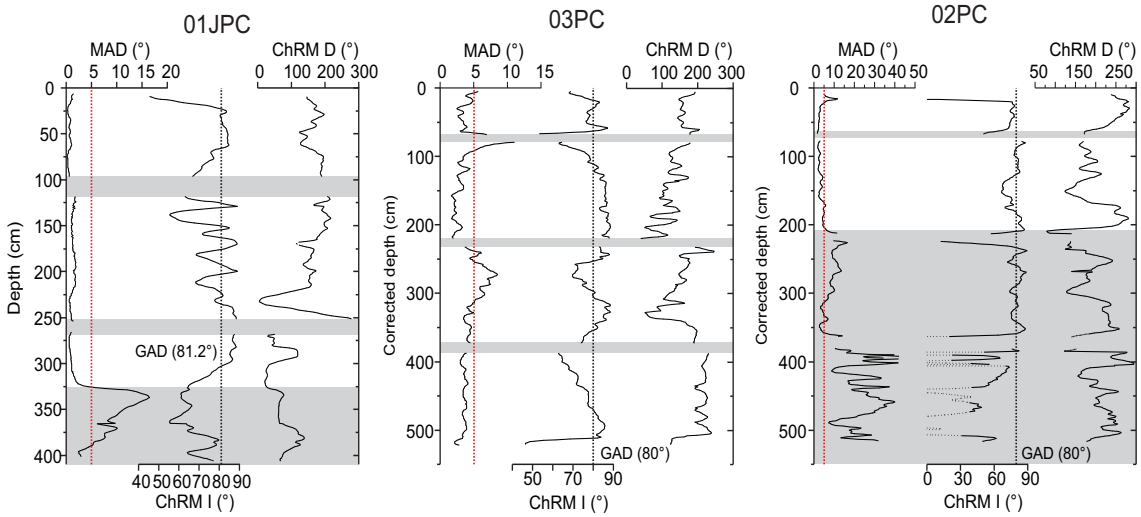

Figure 19: Characteristic remanent magnetization (ChRM) and MAD values of cores 01PC, 03PC and 02PC. The red vertical line delineates MAD value of 5°. Black vertical line in the ChRM I panel represents the expected inclination for a GAD model. Grey highlighted areas indicate section breaks and intervals problematic for palaeomagnetic reconstruction.

the inclination based on a geocentric axial dipole (GAD) model for the coring site latitude, which is 80° for cores 03PC and 02PC and 81.2° for core 01JPC (Fig. 19). To summarize, the three sediment cores are characterized by a strong, well-defined ChRM carried by low-coercivity PSD magnetite, except in the coarser intervals of unit II in cores01JPC and 02PC and at section breaks for all cores (highlighted areas in Fig. 19). The IRD intervals in core 02PC are strongly affected by the higher magnetic concentration (shown by k_{LF}; Fig. 17) and the coarser magnetic grain size (shown by k_{ARM} vs k_{LF} diagram; Fig. 18C). These coarser intervals were not used in our PSV and RPI reconstructions.

1.6.6 Relative paleointensity (RPI) determination

According to multiple studies (Levi and Banerjee, 1976; St-Onge and Stoner, 2011; Tauxe, 1993; Tauxe and Yamazaki, 2007), several criteria must be satisfied to validate the reliability of the RPI proxies. The NRM must be characterized by a strong, stable SD-PSD component magnetization carried by magnetite in the 1–15 μm grain-size range. In order to

determine the RPI, the NRM should be normalized by an appropriate magnetic parameter to compensate for the variation in ferrimagnetic mineral concentrations. The RPI cannot be correlated with its normalizer or with any of the lithological proxies. Based on the results in the sections above, the required criteria for RPI reconstruction have been fulfilled for cores under study.

The averages of the demagnetization steps of 25 to 50 mT (six steps) for core 01JPC and 20 to 50 mT (seven steps) for cores 03PC and 02PC were used for ARM and IRM as normalizers (Fig. 20B). k_{LF} was not used here because it is not only influenced by concentration and grain-size changes, but also by coarse MD grains, and by both diamagnetic and paramagnetic material. In order to identify the correct normalizer, two different normalization methods were compared for each paleointensity estimate. The average ratio method is widely used (Channell et al., 1997, 2000; Stoner et al., 2000; St-Onge et al., 2003), and is calculated by averaging the normalized NRM at different demagnetization steps. The pseudo-Thellier method also known as the slope method (Tauxe et al., 1995; Channell, 2002; Snowball and Sandgren, 2004; Xuan and Channell, 2010) uses the slope of the NRM versus the normalizer at different demagnetization steps. The two methods give similar results for NRM/ARM (Fig. 20A), and the NRM/IRM (not shown). The correlation coefficients (r) calculated from the slope method are high, except for Unit II in core 02PC.

For core 01JPC, the ARM and IRM as normalizers show the same variations for both methods, suggesting that the ARM and the IRM activate the same magnetic assemblages (Fig. 20A and 20B). The difference between ARM and IRM as normalizers is highlighted in Fig. 20A. These differences occur between 100 and 300 cm in core 03PC and in the IRD intervals in core 02PC, and thus indicate that the grains acquiring the ARM more closely match the coercivity of the grains carrying the NRM. This is also illustrated by looking at the demagnetization behaviour of NRM, ARM, and IRM for the sedimentary record, where ARM better matches the coercivity spectra of the NRM than IRM (Fig. 20B).

The NRM/ARM_{25-50} mT are not correlated with the ARM (r^2 = 0.01) for core 01JPC

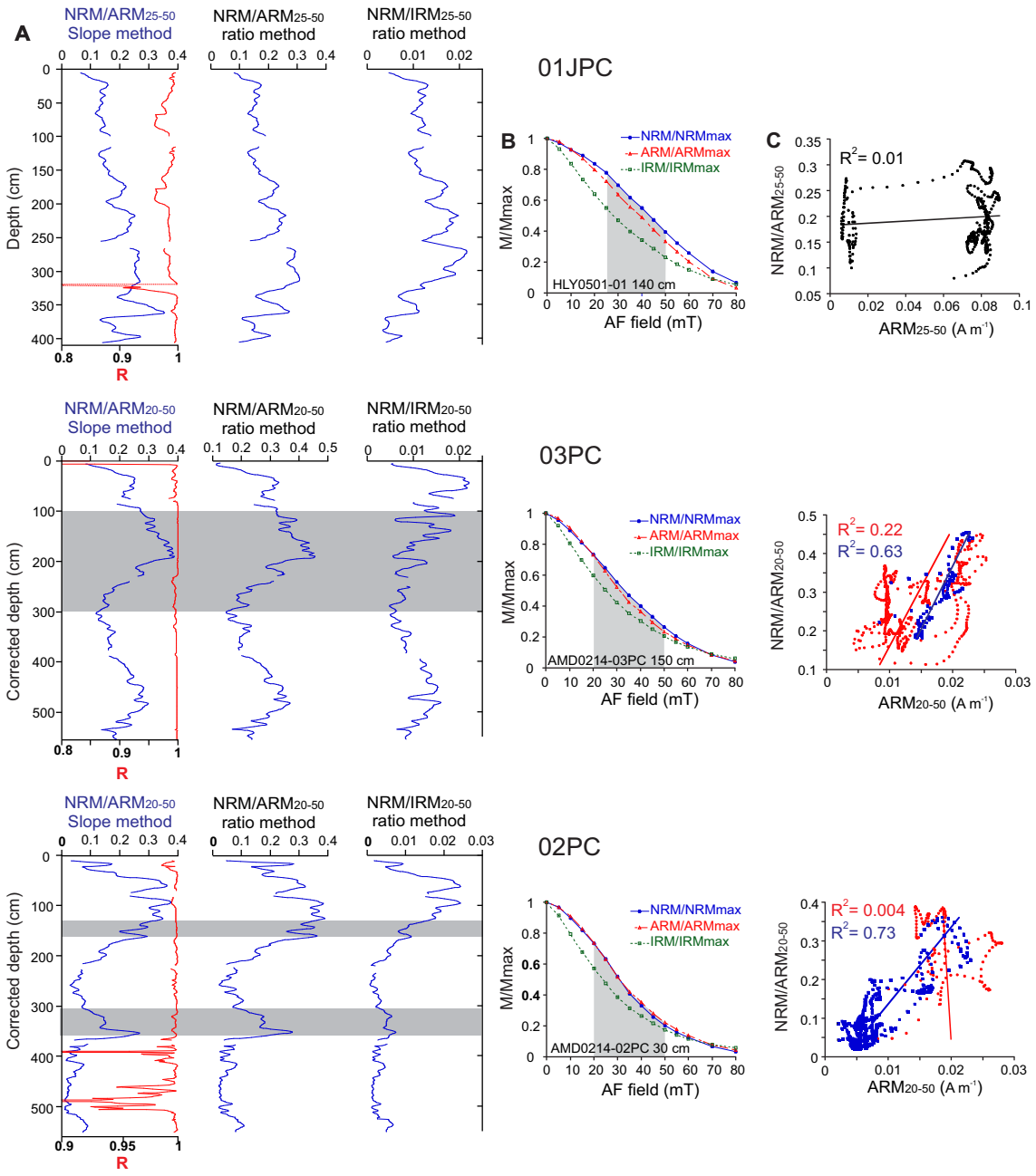

Figure 20: (A) Comparison of the relative palaeointensity estimates based on the average ratios and the slope methods with the average ratios of NRM/ARM and NRM/IRM at 25-50 mT (core 01JPC) and 20-50 mT (cores 03PC and 02PC). (B) Demagnetization curves for NRM, ARM, and IRM. (C) RPI proxy vs its normalizer for cores 01JPC, 03PC (blue points: 100-300 cm, red points: remaining sediments), and 02PC (blue points: IRDs intervals, red points are the remaining sediments).

(Fig. 20C). Comparatively, the NRM/ARM_{20-50} mT in core 03PC shows a correlation in Unit III (r^2 = 0.63) but not in the remaining sediment (r^2 = 0.22) (Fig. 20C). For 02PC, the ratio NRM/ARM_{20-50} mT did not show any correlation with the normalizer in Unit I (r^2 < 0.004) but does show a correlation in Unit II (r^2 < 0.73) (Fig. 20C). The RPI calculated between 300 and 100 cm in core 03PC and during the IRD intervals in cores 02PC are correlated with the normalized parameter (ARM), indicating the RPI cannot be used to determine chronostratigraphic markers at these intervals.

Finally, ARM was chosen as the preferred normalizer for cores 03PC and 02PC for reasons described above, and for core 01JPC based on its potential to activate only SD and PSD grains (Levi and Banerjee, 1976).

1.6.7 Magnetic properties of sediment in the Chukchi and Beaufort seas

To illustrate the variability of the magnetic properties along a west-east transect from the Chukchi Sea to the Beaufort Sea, they are plotted as a box plot (Fig. 29). Among the most visible patterns, the pseudo S-ratio (hematite-magnetite proportion) is close to 1 along the North American margin for both the Holocene and deglacial intervals. The second pattern is linked to the grain size. The NRM_{25-50}, ARM_{25-50} and k_{ARM}/k_{LF} (magnetic grain size and concentration) mean values are quite similar between the Chukchi and Beaufort seas for the deglacial sediments (NRM: 2.2 10^{-2} *vs* 1.9 10^{-2} A.m^{-1}, ARM: 0.9 10^{-2} vs 1.1 10^{-2} A.m^{-1}, k_{ARM}/k_{LF}: 4 vs 3.5 respectively), whereas, mean Holocene values are higher for the Chukchi Sea than the Beaufort Sea (Fig. 29).

The box plot shows that magnetic grain size displayed strong variation since the last deglaciation. The magnetic grain size (k_{ARM}/k_{LF} ratio) decreases generally from the deglacial to the Holocene unit in cores located both at the Beaufort and Chukchi margins (Fig. 21). However, some differences are discernible between the cores. The k_{ARM}/k_{LF} ratio increases respectively from 4 to 15 and from 4 to 50 in cores from the shallowest (05JPC and 08JPC)

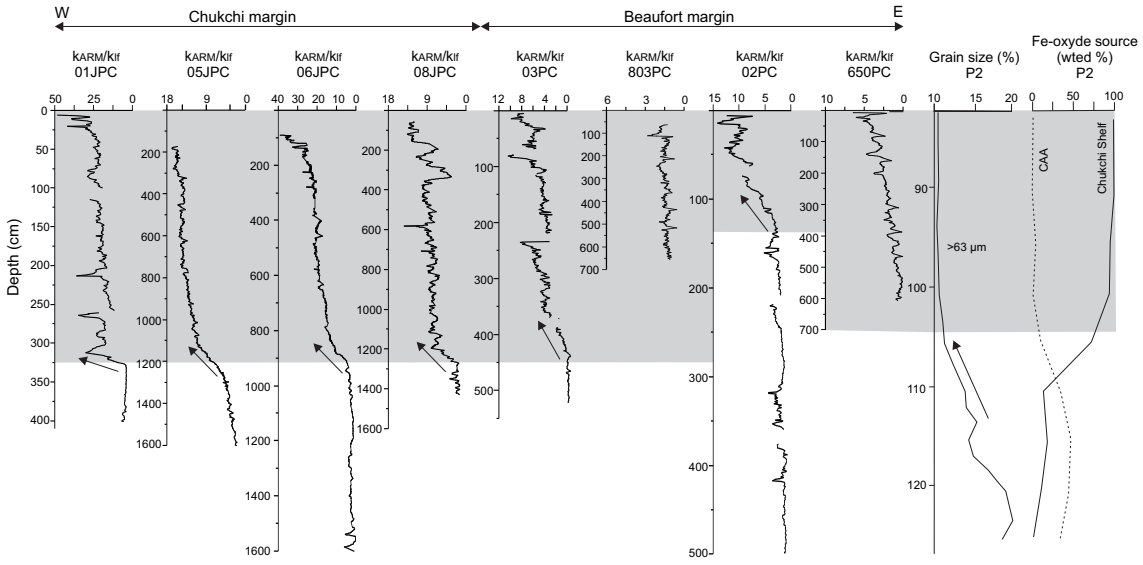

Figure 21: k_{ARM}/k_{LF} ratio for cores 01JPC (this study), 06JPC, 08JPC, 05JPC from the Chukchi margin and cores 03PC (this study), 803PC, 02PC (this study) and 650PC from the Beaufort Sea. Also shown are coarse grain (> 63 μm) and Fe-oxide provenance data from the Chukchi margin core P2 (Polyak et al., 2007). The arrows indicate a decreasing grain size trend from the last deglaciation to the Holocene.

and deepest (06JPC and 01JPC) Chukchi Sea sites. Comparatively, the k_{ARM}/k_{LF} ratio increases from 4 to 10 in all cores from the Beaufort margin. These observations imply (i) similar magnetic grain size during the deglaciation at both margins, (ii) coarser magnetic grains for the deeper coring sites and finer magnetic grains for the shallower sites at the Chukchi margin during the Holocene, and (iii) generally coarser magnetic grains at the Beaufort margin during the Holocene.

1.7 Discussion

1.7.1 Palaeomagnetic dating

Establishing chronostratigraphy in the Arctic is challenging, but the combined use of radiocarbon dating with PSV, relative palaeointensity and geomagnetic field model outputs offers a step forward (Barletta et al., 2010; St-Onge and Stoner, 2011). The PSV and rela-

tive palaeointensity records of cores 01JPC, 03PC, and 02PC were compared with the prior palaeomagnetic records from the Chukchi (05JPC, 06JPC, 08JPC, 16JPC; Barletta et al., 2008; Darby et al., 2012; Lisé-Pronovost et al., 2009; Lund et al., 2016) and Beaufort seas (803PC, 650PC; Barletta et al., 2008, 2010) (Fig. 23). The chronology of these cores was determined using a combination of radiocarbon ages with palaeomagnetic tie points and corroborated by geomagnetic model outputs (Table 4). All these cores show similar directional and relative palaeointensity features that can be correlated on a regional scale. Cores 803PC and 05JPC were also used to add tie points for the age model of core 16JPC (Darby et al., 2012).

Table 3: Palaeomagnetic tie points used in this study. Tie points marked with I, D, and P correspond to inclination, declination, and palaeointensity peaks, respectively and are shown in Fig. 23. Depth in cores has been corrected for missing sediments; age is expressed as cal BP.

Tie point	Depth 03PC	Depth 02PC	Depth 01JPC	Age Cals10k	Age 650PC	Age 803PC	Age 05JPC	Age 06JPC	Age 08JPC	Age 16JPC	Mean age	SD Age (1σ)
I1	31	-	-	600	340	445	-	-	-	-	462	107
I2	69	-	51	2010	2110	1920	1920	2068	2010	1975	2002	66
I3	-	-	96	2885	-	2450	2585	2490	2570	2313	2548	175
I4	-	85	170	4010	-	4140	4145	-	-	3793	4022	143
I5	254	127	295	6100	-	-	6040	5830	5815	5823	5921	122
I6	284	-	-	6525	-	-	-	6520	6280	-	6442	114
I7	335	127	-	7460	-	-	-	8155	-	7524	7713	313
I8	397	141	-	8630	-	-	-	8515	-	8159	8434	200
I9	427	-	-	9310	-	-	-	-	-	8952	9131	179
D1	-	-	-	225	200	-	-	-	-	-	212	12
D2	70	-	-	2240	2200	1865	-	-	-	2074	2095	146
D3	135	-	-	3730	3390	-	-	-	-	3870	3663	201
D4	-	99	232	4990	-	-	-	4900	4930	5068	4972	64
D5A	254	129	255	5700	-	-	5954	5630	5640	5193	5731	131
D5B	254	129	289	5700	-	-	5954	5630	5640	5193	5731	131
D6	360	139	-	7430	-	-	7580	-	-	6871	7293	305
P1	46	17	-	660	340	-	-	-	-	-	500	160
P2	-	32	-	2160	2180	2015	1940	-	-	1939	2047	105
P3	-	73	174	4050	4000	4035	4025	4050	x	4300	4076	101
P4	-	-	290	6250	-	-	5855	5685	5950	6174	5982	207
P5	366	138	-	8300	-	-	8130	-	-	-	8215	85
P6	434	144	-	9190	-	-	9300	-	x-	-	9245	55

Our records show similarities with other marine records from the Chukchi and Beaufort seas and also with the CALS10k model output for the latitude of the site (Korte and Constable, 2011), and allow for an identification of 22 tie-points in total (Fig. 23, Table 3).Nine common features for inclination, six common features for declination, and seven RPI common features have been identified in this study. Four of the inclination tie-points, I2 to I5, have been used in earlier studies for the inclination records between 2000 and 5800 cal a BP (Barletta et al., 2010; Lisé-Pronovost et al., 2009). Two of the declination features have also been observed in the Chukchi cores, one minimum (D4: 4900 cal a BP) and a maximum (D5: 5950 cal a BP) in Barletta et al., 2010 and Lisé-Pronovost et al., 2009. Furthermore, RPI tie point P6 was used in Lisé-Pronovost et al., 2009 for cores from the Chukchi margin. All tie points are presented in Table 3, and the mean and standard deviation ages (1σ) were calculated using the age of the identified tie points for the comparative cores.

1.7.2 Age modelling

Age models were first generated using the non-palaeomagnetic data: ^{14}C ages in cores 02JPC and 03JPC from the Beaufort Sea and the tephra peak in core 01JPC from the Chukchi Sea (Fig. 22A), and then improved by adding palaeomagnetic tie points (Fig. 22B). A constant linear sedimentation rate of 65 cm.ka^{-1} was assumed for the lithologically homogenous, ~300-cm long upper unit of 01JPC based on the ^{210}Pb data from 01MC (Fig. 22A). This initial age model was then improved using a stratigraphy-based Bayesian approach with Bacon (Blaauw and Christen, 2011) and the palaeomagnetic tie points (Fig. 22B). The D5-A tie point was excluded as an outlier based on the comparison of tie-point positions with the linear age model (Fig. 22A). The resulting composite age-depth model for core 01JPC shows that the Holocene (Unit I) sediment record spans the last 6000 years, with sedimentation rates averaging 60 cm.ka^{-1} (Fig. 22B). This value is very close to the sedimentation rate of 65 cm.ka^{-1} estimated from the ^{210}Pb data in 01MC that shows a clear exponential decrease (Fig. 27). Based on age model (Fig. 8B), the top age of core 01TWC is estimated around

1000 cal a BP, implying missing sediment at the top. This conclusion is consistent with the diffuse spectral reflectance data (L*, a* and b*) that do not show any visible correlations in either the absolute values or the relative variations between 01TWC and the 45-cm-long 01MC (Fig. 26). Assuming a top age of 1000 cal a BP for core 01TWC and sedimentation rates between 60 and 65 cm.ka^{-1}, the thickness of missing sediment is 60-65 cm.

Another implication of the age model above is that the base of the marine Unit I in core 01JPC has an age of around 6000 cal a BP, considerably younger than previously investigated cores from the study area (Darby et al., 2009, 2012; Lisé-Pronovost et al., 2009; Polyak et al., 2016), which suggests a hiatus in the bottom part of the Holocene. The absence of tephra related to the ~7000 cal a BP prominent Kamchatka KS2 eruption in 01JPC is consistent with an early Holocene hiatus in this core (Ponomareva et al., 2017). Furthermore, a similar hiatus of several ka duration has been identified in a well-dated sediment record from the Herald Canyon at the western (Siberian) part of the Chukchi margin (Pearce et al., 2017). Considering the absence of the 01JPC hiatus in nearby cores, this hiatus has to be associated with local bottom processes rather than with a regional halt in sedimentation. As this core is located in or close to a canyon in the lower part of the slope (Fig. 15), a disruption of normal sedimentation is not unlikely, and could be related to either downslope sediment movement (slump, debris flow or turbidite) or a winnowing/nondeposition by downwelling waters. The latter explanation is more plausible since no apparent erosional surface is visible at the level of the inferred hiatus. According to modern hydrographic observations, dense waters (brines) generated at the Chukchi-Alaskan margin during the fall/winter sea-ice formation can descend to the pycnocline depth of up to 200 m (Pickart et al., 2005; Woodgate et al., 2005). However, geochemical data from bottom sediments from the adjacent slope and deep-sea basin indicate the possibility of a much deeper convection in the recent past (Haley and Polyak, 2013). While this issue requires further investigation, the occurrence of a lower Holocene hiatus in cores from the Chukchi slope may indicate more intense sea-ice and brine formation during that time, possibly related to the flooding of Siberian shelves by rising postglacial sea level as predicted by numeric modelling experiments (Blaschek and Renssen, 2013).

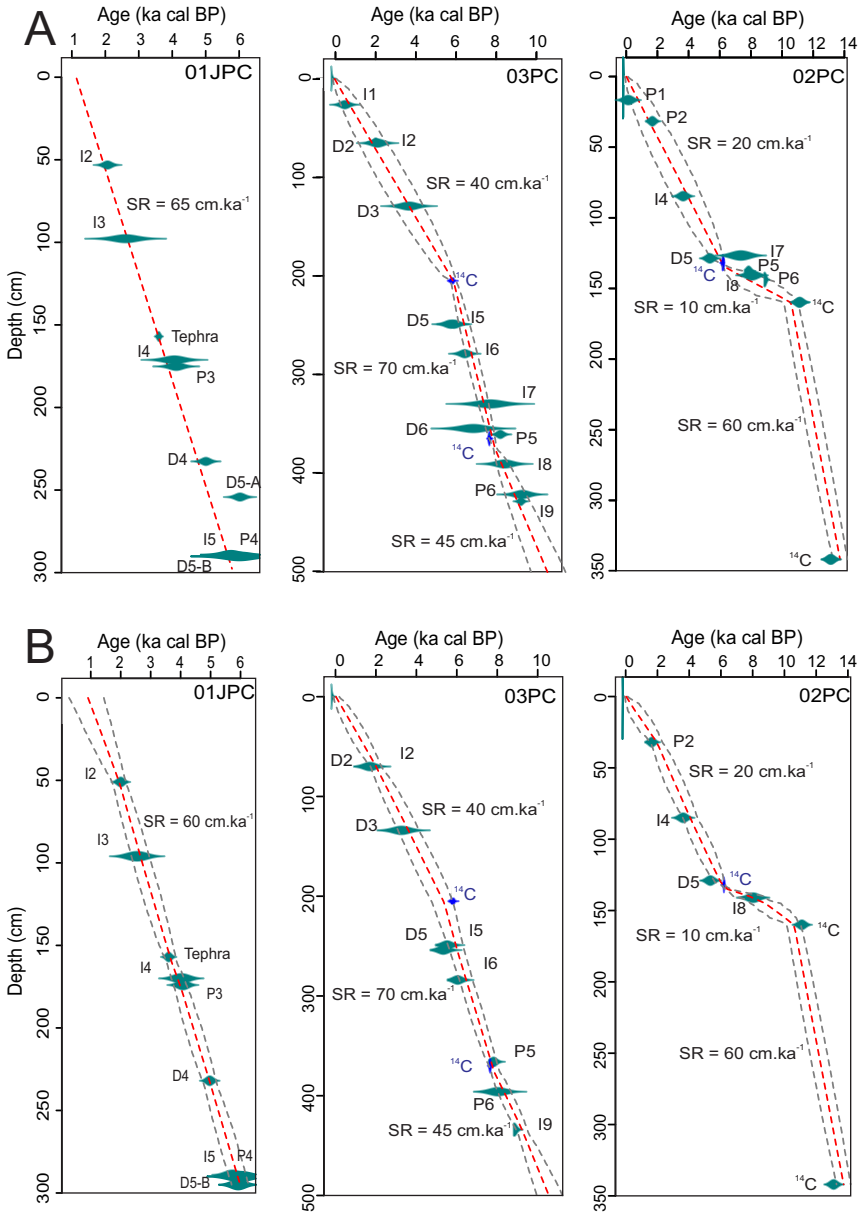

Figure 22: (A) Age modelling using the independent ages only (^{210}Pb, ^{14}C and tephra), with palaeomagnetic tie points shown but not used in the age models. (B) Composite age modelling using both the independent ages and palaeomagnetic tie points (Table 2). Age models, except for the linear model for 01JPC in Fig. 22A, are constructed using the R-package Bacon (Blaauw and Christen, 2011).

The preliminary age models for the Beaufort Sea cores 03PC and 02PC (Fig. 22A) were constructed using radiocarbon ages including the new radiocarbon dates and ages from nearby core 750PC correlated to the cores under study using the IRD layers as described

above. Apparently outlying (by ~300 years: Fig. 22A) palaeomagnetic tie points D6 and I7 were excluded from the construction of a more comprehensive age model for both cores. Tie point I1 was also excluded from the age model for core 03PC, as well as tie points P1, P5 and P6 for core 02PC for being a bit outside or on the 95 % confidence limit (Fig. 22A). A composite age model was then constructed for both cores based on the palaeomagnetic tie points and radiocarbon ages (Fig. 22B). The resulting age model for 02JPC spans the last 13 500 years and displays a considerable variation in sedimentation rates with a rapid decrease from 60 to 10-20 cm.ka^{-1} at the deglacial/Holocene transition. These results are similar to sedimentation patterns in core 750PC, with sedimentation rates of 15 cm.ka^{-1} estimated for the Holocene (Scott et al., 2009). The composite age model for 03JPC indicates that this core spans the last 10 500 years and is associated with sedimentation rates averaging ~70 cm.ka^{-1} between 6000 and 8000 cal a BP and ~40-45 cm.ka^{-1} above and below this interval (Fig. 22B). Core 03PC is the first complete marine succesion recording palaeomagnetic secular variations for the entire Holocene from the Beaufort Sea.

1.7.3 Limits of the palaeomagnetic reconstructions

Sedimentation rates play an important role in the temporal resolution of palaeomagnetic records. The Chukchi Sea cores used for a comparison with cores under study have sedimentation rates as high as > 100 cm ka^{-1}, probably as a resultof their proximity to the Barrow Canyon, a major conduit of sediment for the eastern Chukchi margin. The temporal resolution of cores studied in this paper is lower due to a more distal location from sediment sources (Barrow Canyon and Mackenzie delta; Fig. 15). Furthermore, the 7 cm smoothing effect of the cryogenic magnetometer combined with lower sedimentation rates may have impaired the identification of common features between the cores, as shown in Fig. 23. Indeed, based on the Holocene sedimentation rates derived from cores 01JPC, 03PC and 02PC, the 7 cm smoothing effect of the response function of the magnetometer creates a smoothing of respectively 115, 100-175 and 350-700 years. This is especially evident in core 02PC, where

the temporal resolution of the PSV profile is lower than in other cores, allowing us to identify only 3 common features in the inclination and declination profiles (Fig. 23). Nevertheless, the surface sediment of this core represents modern sediments, and the uppermost IRD layer can be identified and dated to 11 580 a cal BP (Scott et al., 2009), which enables a reliable age framework for this core. In addition, most of the tie points identified are within the 95 % confidence limit (< 300 years off the center line) of the age model based on ^{14}C ages (Fig. 22A). Only tie points D6 and I7 showed a higher offset in both cores 03PC and 02PC (Table 3).

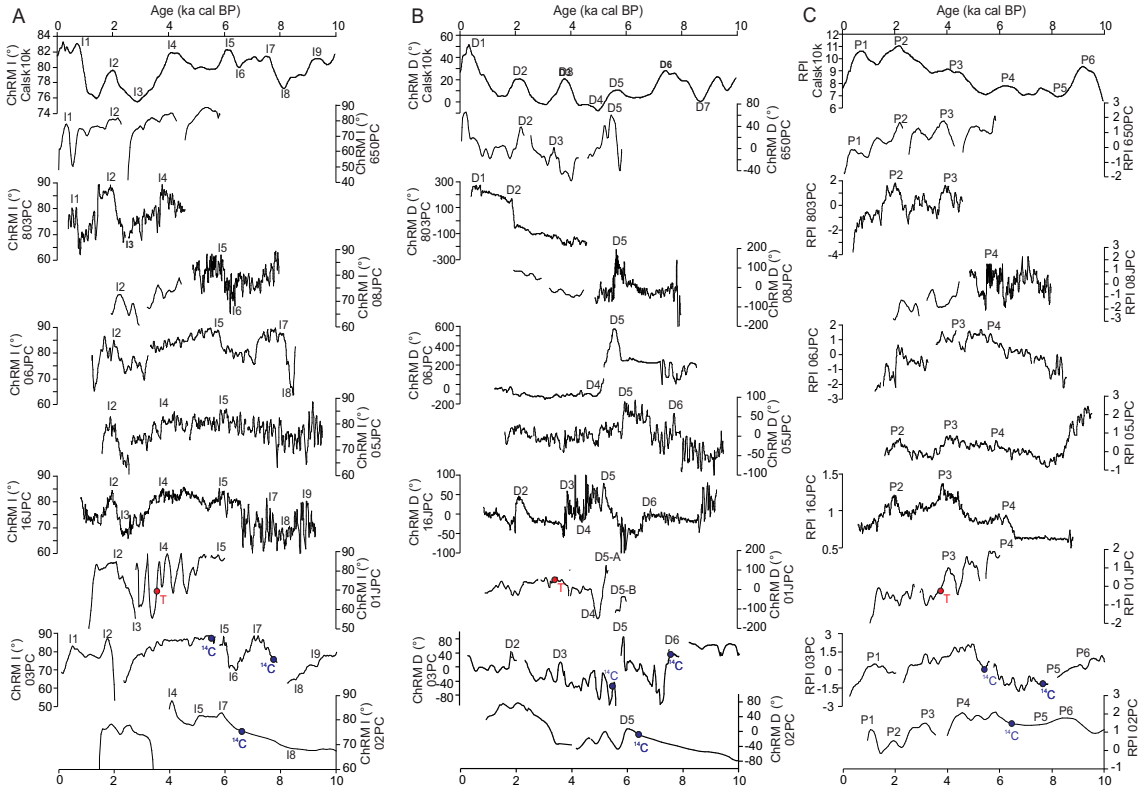

Figure 23: Full vector palaeomagnetic comparison of cores 01JPC, 03PC and 02PC with earlier developed regional records of (A) inclination, (B) declination, and (C) relative palaeointensity. Data on cores 650PC, 803PC and 05JPC are from Barletta et al., 2008, 2010, core 16JPC from Darby et al., 2012, and cores 06JPC and 08JPC from Lisé-Pronovost et al., 2009. Also shown are the CALS10k spherical harmonic model outputs for the Beaufort margin (71.61° N, 137.54° W; derived from Korte and Constable, 2011.

Palaeomagnetic records with greigite as the main magnetic mineral need to be interpreted with caution, as their PSV and relative palaeointensity variations can be biased and

reflects rock magnetic properties rather than geomagnetic variations (Ron et al., 2007). In the cores used in this study and for the comparison, greigite was found only in core 05JPC at restricted intervals (Brachfeld et al., 2009). Furthermore, the small amount of greigite in this core is not likely to compromise the palaeomagnetic data as the remanence is still carried by the low coercivity minerals such as magnetite (Barletta et al., 2008; Brachfeld et al., 2009; Lisé-Pronovost et al., 2009). The pseudo S-ratio, hysteresis curves and the Day plots for cores 06JPC, 08JPC and 650PC indicate a magnetic assemblage dominated by magnetite but not iron sulphides, such as greigite (Barletta et al., 2010; Lisé-Pronovost et al., 2009). In addition, the presence of greigite was not detected in cores under study using XRD (Fig. 31). Additionally, magnetite was found to be the dominant magnetic mineral and none greigite was found in surface sediments from the Beaufort Sea (Gamboa et al., 2017). As described in the magnetic mineralogy section, the hysteresis curves, pseudo-S ratio, and MDF_{NRM}, as well as the low MAD values are characteristic of low-coercivity ferrimagnetic minerals, such as magnetite, yielding reliable PSV data reconstruction (Tauxe et al., 1996). The magnetic results presented in this study are similar to those published in Barletta et al. (2010), Darby et al. (2012) and Lisé-Pronovost et al. (2009). In addition, the influence of reductive diagenesis can be measured by the ratio Fe/k_{LF} (Funk, 2004; Hofmann et al., 2005; Hoffmann and McManus, 2007; Hofmann and Fabian, 2009). For the studied cores, the mean Fe/k_{LF} ratio varies around 18-20 (Fig. 30). According to Funk (2004) and Hofmann et al. (2005), a Fe/k_{LF} ratio under 40 is indicative of weak reductive diagenesis. Based on the Fe/k_LF ratio and the magnetic properties, the data, thus, clearly indicate that the remanence is principally carried by low coercivity minerals, such as magnetite.

1.7.4 Sedimentation rates in the Canadian Beaufort Sea

As shown in Fig. 23, sedimentation rates in cores from the Beaufort Sea are heavily dependent on their location, with the largest difference in sedimentation patterns observed between the eastern Beaufort Sea and the Mackenzie delta. Before 11 500 cal a BP, sedimen-

tation rates were higher than 60 cm.ka^{-1} in both areas, probably due to higher input of the Mackenzie River and also meltwater discharge from the Laurentide Ice Sheet (Schell et al., 2008). After 11 500 cal a BP, sedimentation rates were still high in the Mackenzie area (> 40 cm.ka^{-1}), but lower in the eastern Beaufort sea (10-20 cm.ka^{-1}). Indeed, the age-model curve of core 02PC is very similar to the relative sea-level curves from the Mackenzie delta area (Hill et al., 1993; Héquette et al., 1995; Fig. 24). The rate of sea-level rise between 9000 and 3000 cal a BP was 700–1400 cm.ka^{-1}, followed by a decrease to 200 cm.ka^{-1} since 3000 cal a BP, resulting in high rates of coastal retreat that had a strong effect on the Mackenzie delta (Héquette et al., 1995). Sediment inputs from the Mackenzie delta are still very high in the Mackenzie Trough whereas they seems to be influenced by sea-level variation in the eastern Beaufort Sea (as shown by core 02PC) during the Holocene.

1.7.5 Magnetic properties of the sediments on the Arctic North American margin

The three new sediment cores considerably expand the data on magnetic properties from prior studies performed on sediment cores from the Chukchi and Beaufort seas (Barletta et al., 2008, 2010; Lisé-Pronovost et al., 2009). As shown in Fig. 29 for cores under study, the pseudo S-ratio close to 1 and the Mrs/Ms and Hcr/Hc ratios typical for low-coercivity ferrimagnetic grains indicate that magnetite in the PSD grain range is the dominant magnetic mineral on the North American margin.

As described previously, (i) the magnetic grain size was similarly high during deglaciation at both the Chukchi and Beaufort Sea margins, (ii) the Holocene magnetic grains at the Chukchi margin are coarser at shallower water depths, and (iii) during the Holocene magnetic grains are generally coarser at the Beaufort margin (Fig. 21). The magnetic grain size in the Chukchi Sea cores ranged between 4 to 16 μm (Barletta et al., 2008; Lisé-Pronovost et al., 2009; this study). This range of magnetic grain size matched the granulometry mode centered at 7 μm found in (Dong et al., 2017) and characteristic from glacial environment. Furthermore, coarse magnetic grain size during the deglaciation co-occurs with the high con-

tents of IRD at the Chukchi and Beaufort margins reflecting predominant sedimentation from icebergs (Polyak et al., 2007; Scott et al., 2009). For example, the coarse magnetic grain size presented in this study correlates with high IRD contents and Fe-oxide grains from the Canadian Arctic Archipelago source in the core P2 from the Chukchi margin (Polyak et al., 2007). The Canadian Arctic Archipelago is characterized by high content of magnetite and titanomagnetite. These magnetic minerals were entrained by icebergs from the Laurentide and Innuitian ice sheets during the deglacial (Bischof and Darby, 1999). These IRD pulses from the Canadian Arctic Archipelago have been linked to the deglacial discharge from the Laurentide ice sheet, primarily via the Amundsen Gulf and M'Clure Strait (Stokes et al., 2005, 2006). We suggest that glacial erosion and meltwater from the Laurentide Ice Sheet induced higher mechanical weathering and enhanced the transport of coarser magnetic and titomagnetique grains by IRD to the Beaufort and Chukchi seas. With the cessation of Laurentide Ice Sheet meltwater and iceberg inputs, the amount of IRD strongly decreased in the Holocene sediments at both margins.

During the Holocene, the eastern Beaufort Sea cores (02PC and 03PC) was under a strong, direct influence of the detrital material from the Mackenzie River (Darby et al., 2009; Schell et al., 2008; Scott et al., 2009). The Chukchi margin sedimentation in the Holocene was presumably predominated by transport by currents from the adjacent shelf and deposition from sea ice (Darby et al., 2009). The magnetic grain size in the Chukchi Sea cores ranges between 0.1 and 4 μm (Barletta et al., 2008; Lisé-Pronovost et al., 2009; this study). This range of magnetic grain size matches the granulometry mode centered at ~4 μm in interglacial sediments in the Arctic Ocean interpreted as a combination of deposition from sea ice and from suspension, possibly resulting from winnowing of the fine particles (Dong et al., 2017). Deposition from sea ice alone implies a generally uniform grain size distribution across the study area, which does not seem to be the case for the studied cores, where magnetic grains are finer and coarser at deeper and shallower sites, respectively. We, therefore, infer that cross-shelf and/or downslope currents had a major control on the Holocene sedimentation in the cores located close to the head of the Barrow Canyon, where currents

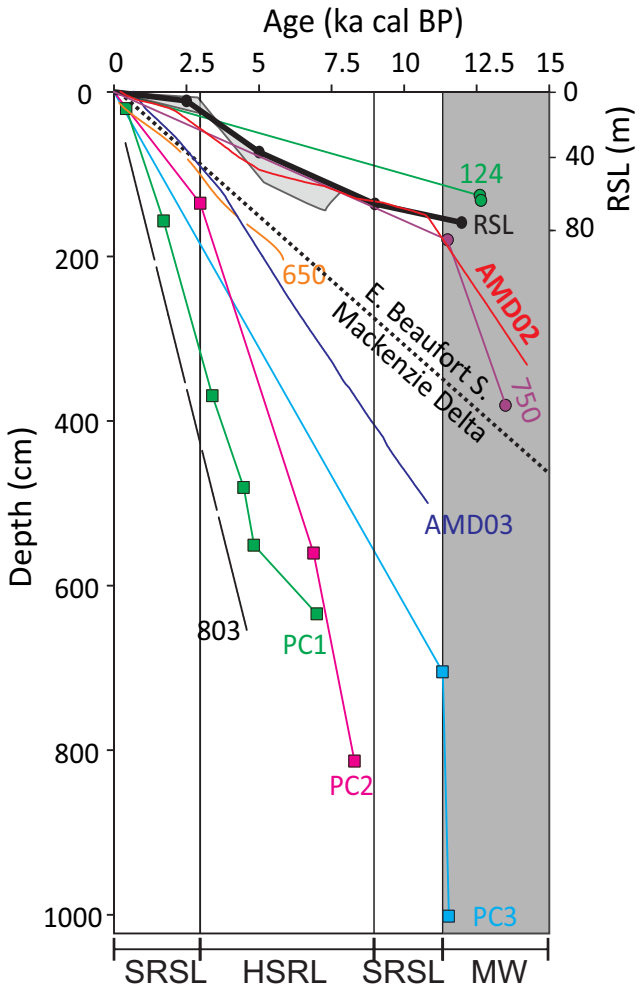

Figure 24: Age model for cores from the Beaufort Sea. Cores 124PC and 750PC are from Scott et al. (2009), cores 650PC and 803PC from Barletta et al. (2008, 2010), and cores PC1, PC2 and PC3 from Schell et al. (2008). Also shown is reconstruction of the relative sea level from Hill et al. (1993) and Héquette et al. (1995). SRSL = slow rising sea level; HSRL = high rising sea level; MW = meltwater.

average about 14 cm.s^{-1} and can reach nearly 100 cm.s^{-1} (Darby et al., 2009). The upwelling currents along the slope might mix with the down-canyon flows to create eddies or decrease net currents thus promoting deposition (Darby et al., 2009). In this setting, the current impact decreased downslope, consistent with the observed preferential redeposition of fine grains at deeper sites. Bottom currents may therefore account for the magnetic grain size differences between cores from the shelf (08JPC) and from deeper sites on the adjacent slope (01JPC, 06JPC). However, we cannot exclude sea ice as an additional mechanism for transporting

finer magnetic grains to the deeper sites, especially considering their geographic proximity to the position of sea-ice margin suggested for a considerable part of the Holocene (Polyak et al., 2016).

1.8 Conclusions

The natural remanent magnetization of sediments from the Chukchi and Beaufort Sea margins is characterized by a strong, well-defined, stable single component magnetization carried by single to pseudo-single domain magnetite, thus highlighting the quality of palaeomagnetic data for sediment cores from this area. This paper presents three new records of the Holocene palaeomagnetic secular variations and relative palaeointensity in sediment cores from the Chukchi and Beaufort margins, including the first full vector data for the entire Holocene in the Beaufort Sea (cores 02PC and 03PC). These data enabled us to construct age models for both areas, where obtaining radiocarbon ages are complicated by a scarcity of biogenic calcareous material suitable for dating. Previously reported regional palaeomagnetic records helped to constrain the chronology of cores under this study. The age model derived from magnetostratigraphy was verified by independent dating techniques such as radiocarbon in cores 02PC and 03PC, and ^{210}Pb and tephrochronology in 01JPC. Our results for the Beaufort margin cores illustrate a large difference in resolution for the Holocene records related to a decrease in sedimentation rates away from the Mackenzie River delta, which is an important factor that needs to be considered in regional palaeoceanographic investigations.

The presented data also suggest that deposition of coarse magnetic grains in the lower part of the stratigraphy was controlled by high IRD inputs from the Laurentide Ice Sheet during deglaciation throughout both the Beaufort and Chukchi margins. In the Holocene deposits, greater variability in magnetic parameters is observed in cores from the Chukchi margin, where finer magnetic grains characterize larger water depths, presumably in relation to a bottom current control.

Overall, this study illustrates the usefulness of palaeomagnetism for improving the dating of Arctic geological material.

1.9 Acknowledgments

We sincerely thank the captains, officers, crew and scientists on board the USCGC Healy and the CCGS Amundsen for the recovery the cores used in this study. These cores were collected as part of the HOTRAX expedition (USCGC Healy), as well as the CASES and ArcticNet (CCGS Amundsen) programs. We also thank Quentin Beauvais (ISMER), Mathieu Babin (ISMER), and Bassam Ghaleb (UQAM-GEOTOP) for their technical support and advice in the laboratory. We would also like to thank Steve Lund (University of South California, Los Angeles, USA) for sharing the PSV data of the core 16JPC. This research was funded by the Natural Sciences and Engineering Research Council of Canada (NSERC) through Discovery Grants to G. St-Onge and J-C Montero-Serrano, as well as through ship time support for several expeditions (J.-C. Montero-Serrano, G. St-Onge). L. Polyak's contribution was supported by the US National Science Foundation award ARC-0612493. Finally, we thank Christine Laurin for reviewing the grammar as well as the editor Jan A. Piotrowski and the reviewers Dennis A. Darby and Daniel Rey for their constructive comments that helped improved the manuscript.

1.10 Supporting information

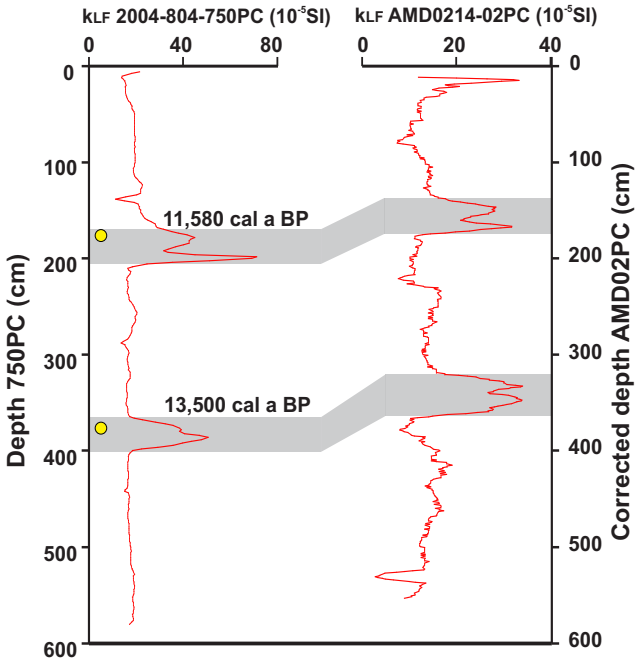

Figure 25: Magnetic susceptibility comparison of cores 2004-804-750PC (Scott et al., 2009) and 02PC. Yellow circles represent depths of radiocarbon dating.

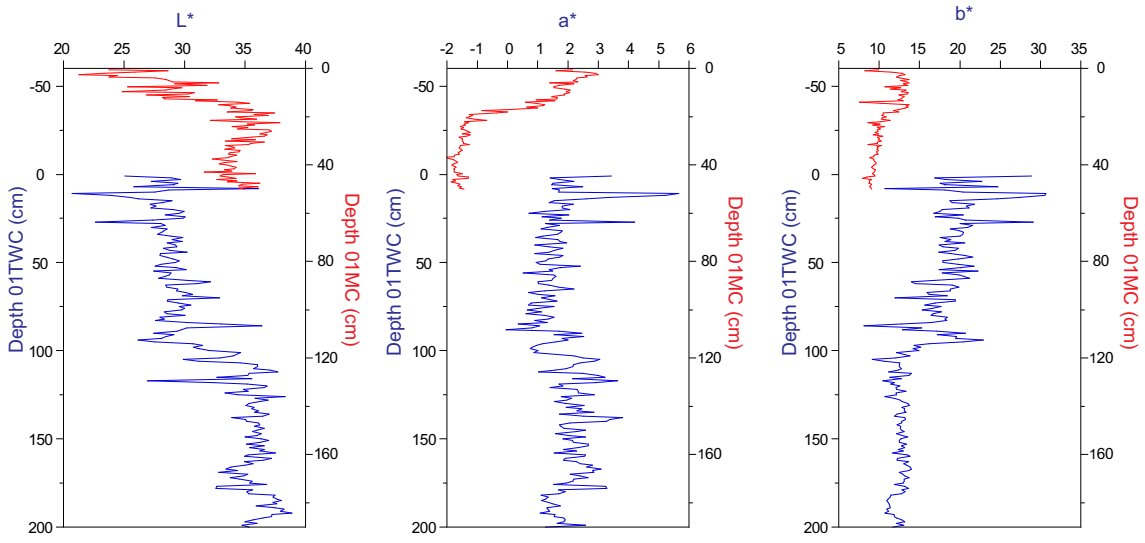

Figure 26: Core-top correlation using the optical properties (L*, a* and b*) between the 01MC and 01TWC. The results indicate there is no correlation between 01MC and 01TWC and suggesting that the first 45 cm are missing at the top of the TWC.

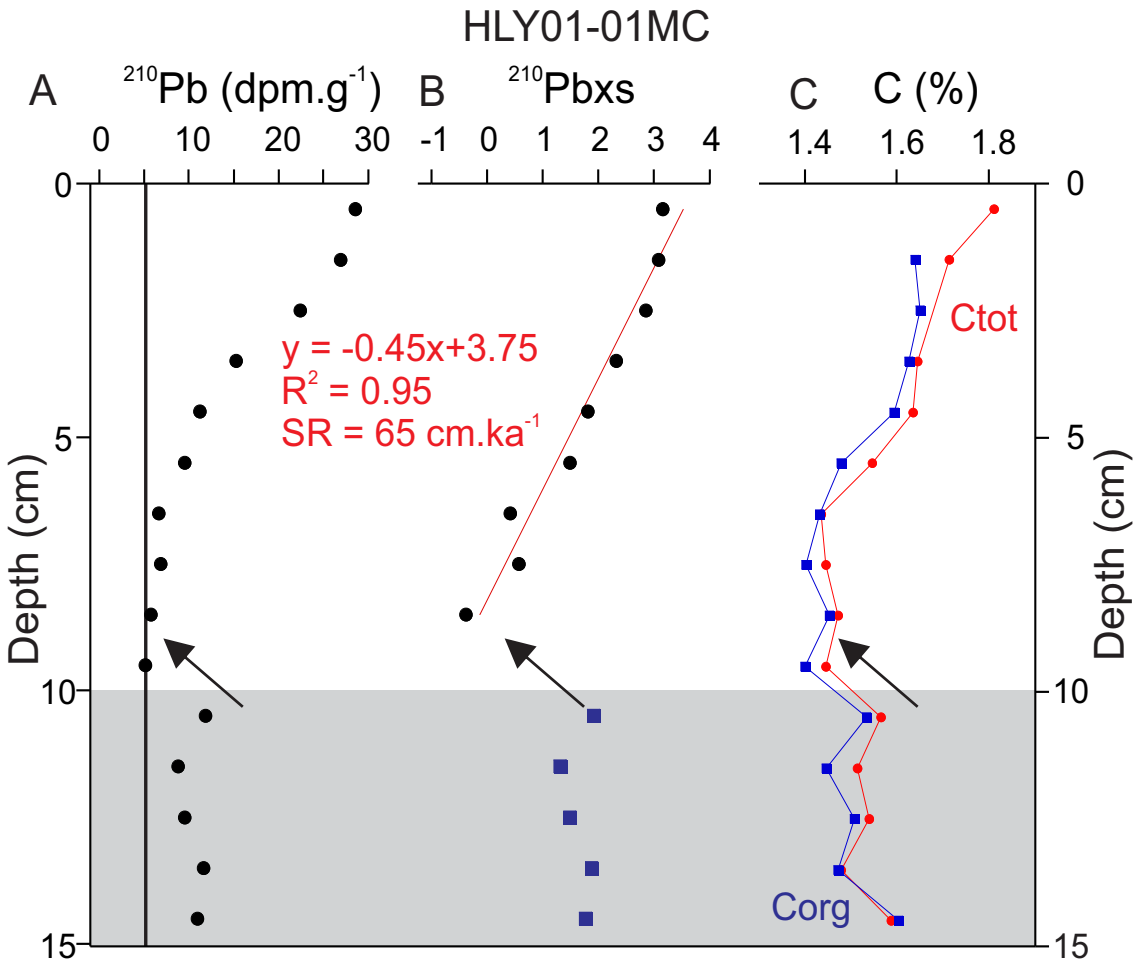

Figure 27: ^{210}Pb and carbon content measurements for box core HLY01-01MC. (A) ^{210}Pb total activity (dpm: disintegration per minute) in the top 15 cm. The supported ^{210}Pb activity is illustrated by the vertical black line. (B) Napierian logarithm of the ^{210}Pb excess activity used for the estimation of the sedimentation rate. (C) Total (red) and organic (blue) carbon contents.

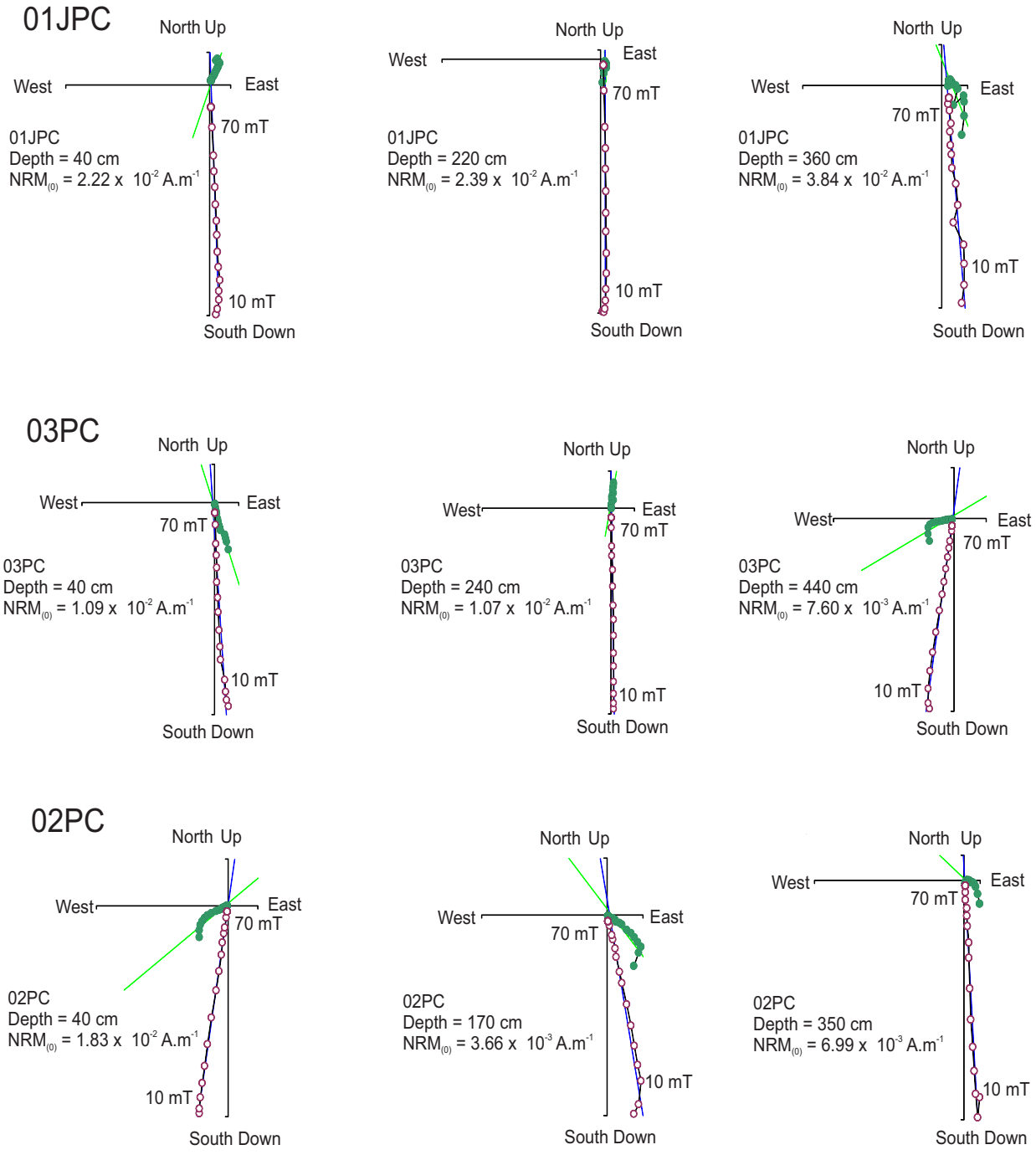

Figure 28: Orthogonal projection diagrams (Zijderveld, 1967) at three selected depths for cores 01JPC, 03PC, and 02PC. Open (closed) symbols represent vector end points projected on the vertical (horizontal) plane, respectively.

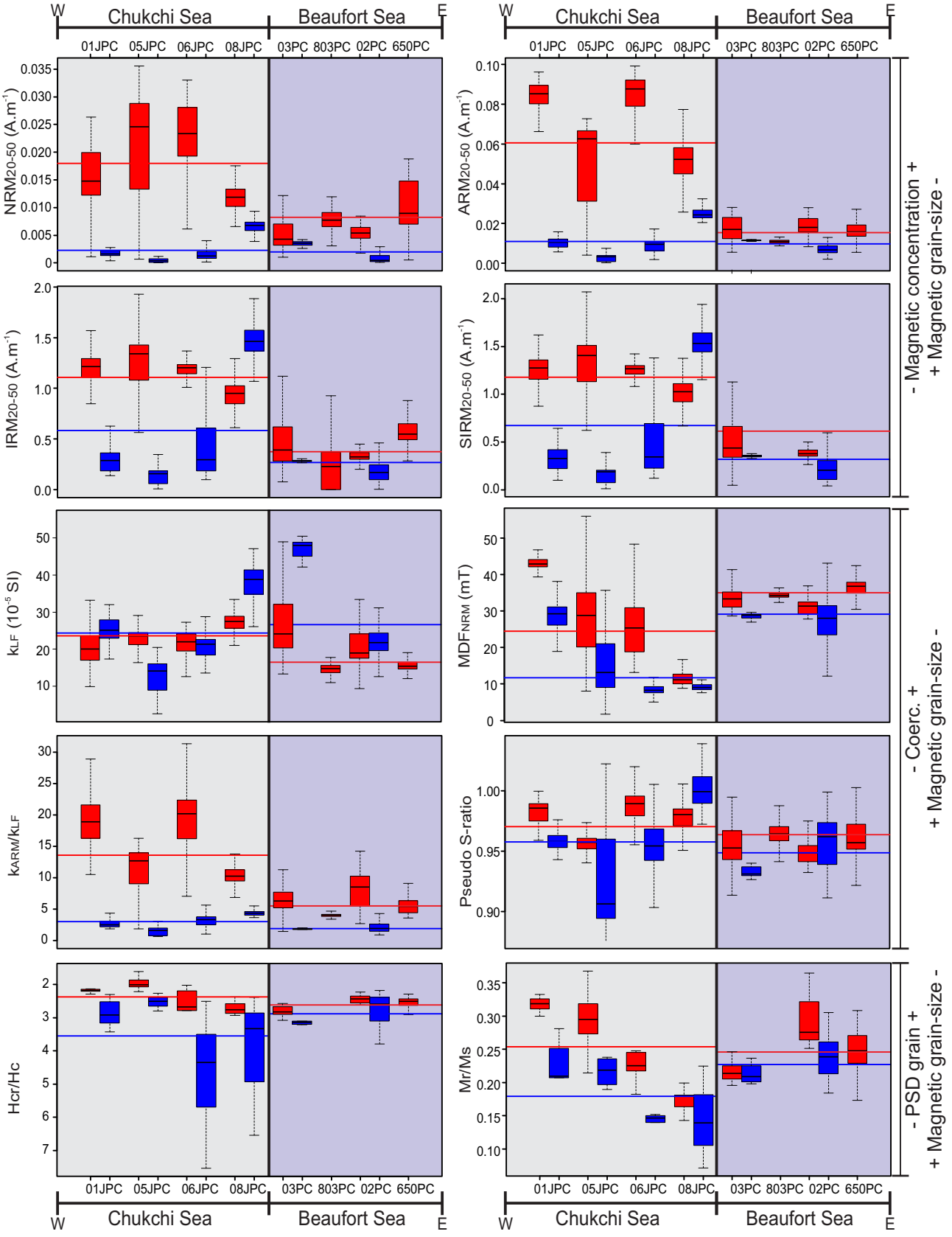

Figure 29: Box-plot of several magnetic properties of marine cores on the North American margin along a west-east transect for the Holocene (red) and the deglaciation (blue). The mean values for both areas and periods are given by the horizontal lines. The box plots showed the median (horizontal line) and the box includes 50% of the distribution. Data from cores 06JPCand 08JPC are from Lisé-Pronovost et al. (2009) and cores 05JPC, 650PC, and 803PC are from Barletta et al. (2008, 2010).

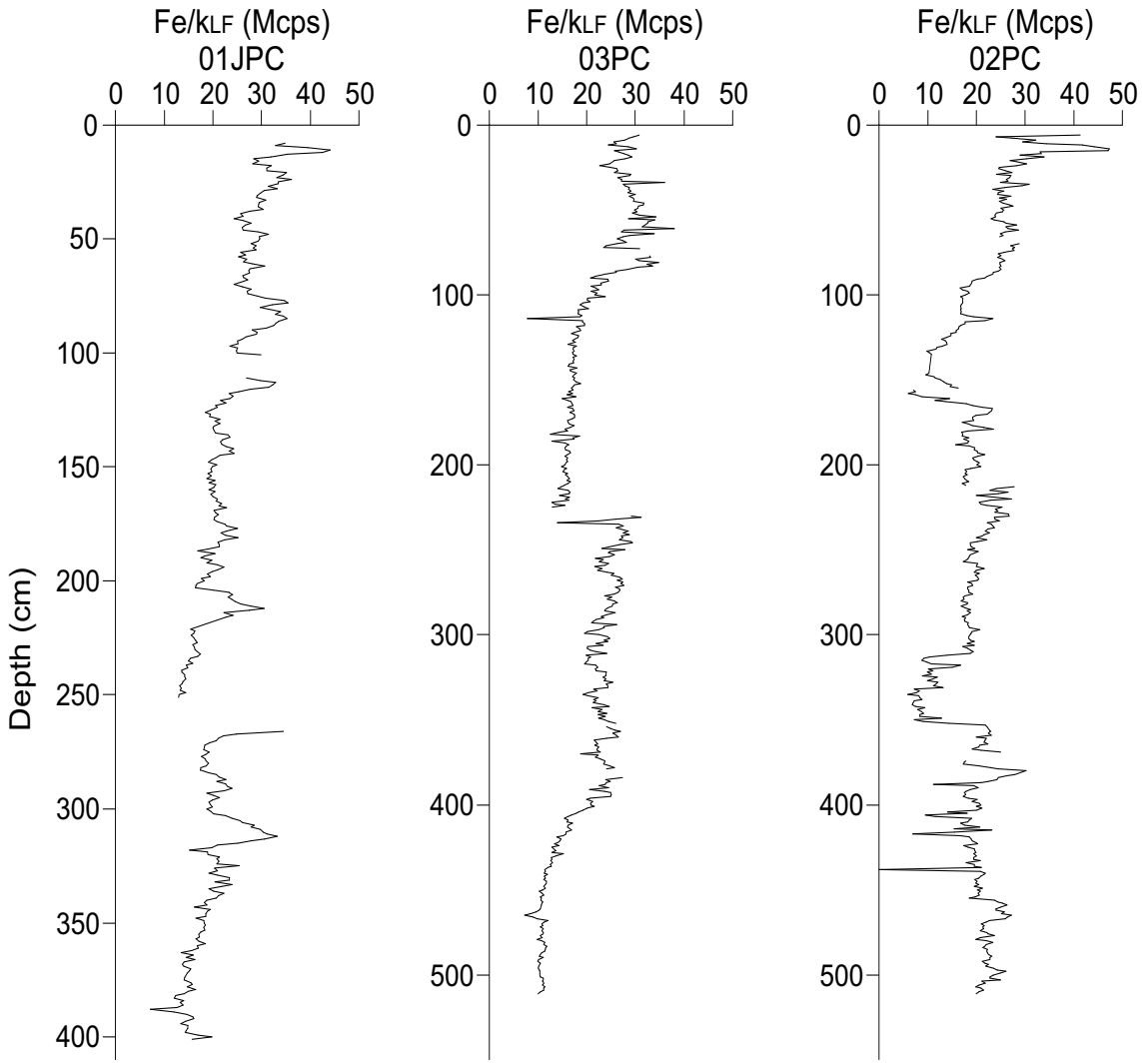

Figure 30: Ratio Fe/k_{LF} for cores 01JPC, 03PC and 02PC indicative reductive diagenesis when Fe/k_{LF} >40 Mcps (Funk, 2004; Hofmann et al., 2005).

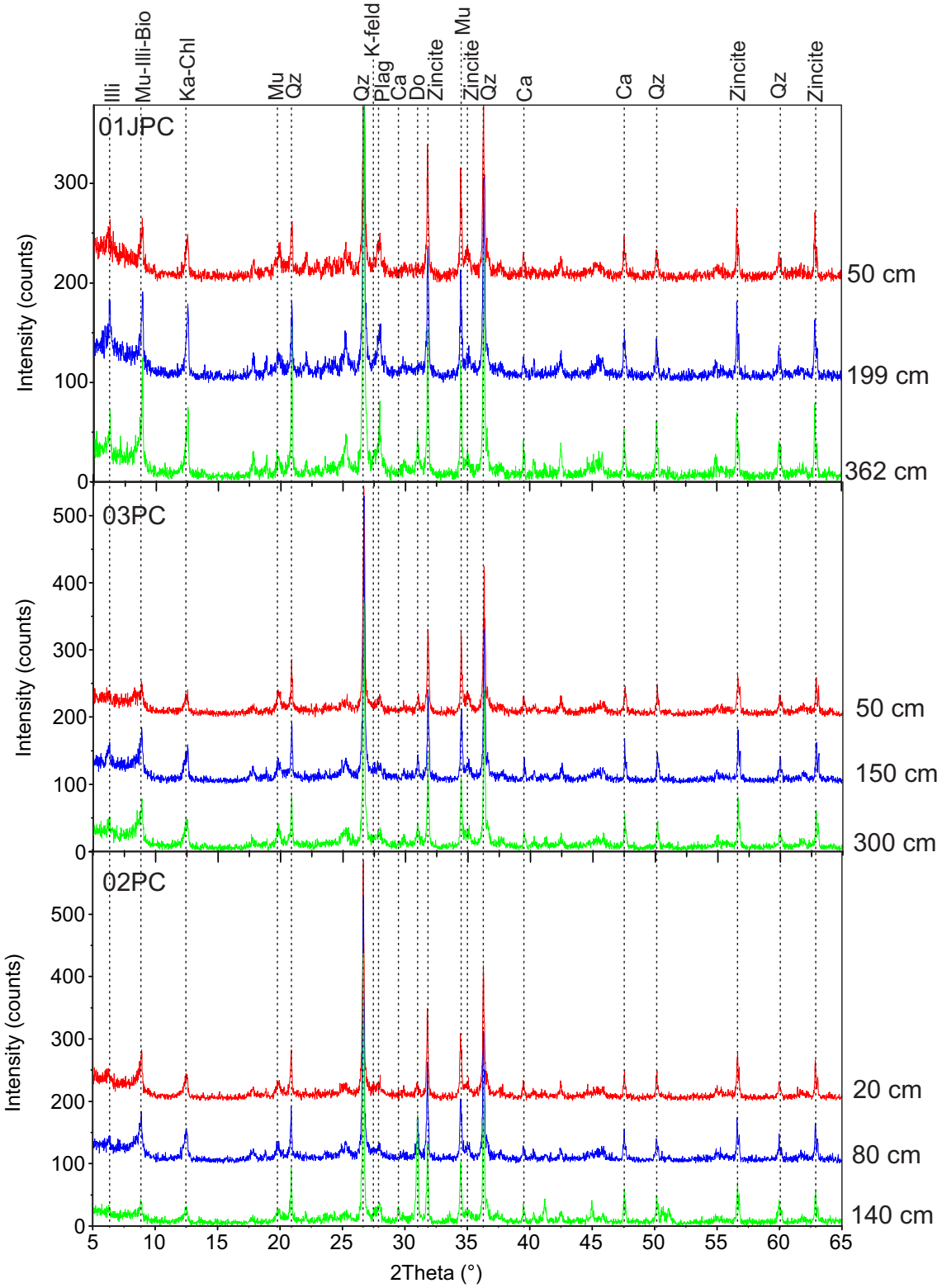

Figure 31: Diffractogram of the cores 01JPC, 03PC and 02PC with the addition 0.111 g of zincite to 1 g of bulk sediment following the protocole of Eberl (2003). Briefly, 0.111 g of zincite was added to 1 g of bulk sediment. Samples were X-rayed from 5 to 65 degrees two theta with Cu K-alpha radiation (45 kV, 40 mA) using a PANalytical X'Pert Powder diffractometer. The XRD data were converted into weight percent minerals using the RockJock computer program (Andrews and Eberl, 2012; Andrews et al., 2013; Eberl, 2003; Ortiz et al., 2009).

Table 4: Number of ^{14}C datation, chronostratigraphic tie points and if model comparison were applied on the core 16JPC, 05JPC, 06JPC, 08JPC, 803PC and 650PC used in this study for comparison (Barletta et al., 2008, 2010; Darby et al., 2012; Lisé-Pronovost et al., 2009).

Cores	Nb. ^{14}C	Nb. tie points	Model comparison
16JPC	4	39	yes
05JPC	6	6	yes
06JPC	1	10	yes
08JPC	9	10	yes
803PC	4	6	yes
650PC	1	17	yes

ARTICLE 2

CHANGEMENT DE PROVENANCE DES SÉDIMENTS DE L'ARCTIQUE DE L'OUEST EN RÉPONSE AUX VELÂGE D'ICEBERGS, VARIATIONS DU NIVEAU MARIN ET DE LA CIRCULATION OCÉANIQUE DEPUIS LA DERNIÈRE DÉGLACIATION

2.1 Résumé en français du deuxième article

Deux carottes sédimentaire ont été récupérées sur les marges continentales d'Alaska (05JPC) et canadienne de la mer de Beaufort (02PC) afin d'étudier les signatures granulométriques, chimiques et minéralogiques des sédiments. Ces données ont permis de reconstituer les changements de provenance et de transport des sédiments liés à la variabilité climatique depuis la dernière déglaciation. Les analyses de modélisation de la taille des grains indiquent que le transport sédimentaire par la glace de mer et par les courants de fonds (néphéloïdes) ainsi que le panache de sédiments du fleuve Mackenzie sont des facteurs importants influençant la sédimentation le long des marges continentales de la mer des Tchouktches et de la mer Beaufort. Les signatures chimiques et minéralogiques en conjonction avec le programme SedUnMixMC indiquent que les sédiments détritiques de la carotte 02PC proviennent principalement du fleuve Mackenzie. Tandis que les sédiments de la carotte 05JPC proviennent du fleuve Mackenzie pendant la déglaciation et sont un mélange de sédiments provenant du détroit de Béring, du fleuve Mackenzie et de la marge eurasienne durant l'Holocène. Les IRD riches en dolomite sont reliés aux différentes phases des décharges d'icebergs provenant du golfe d'Amundsen. Cependant, les IRD riches en quartz et en feldspath résultent des événements de fonte des eaux provenant de la calotte Laurentidienne (13 cal ka BP) pour la carotte 02PC et de la chaîne de Brooks (10.6 cal ka BP) pour la carotte 05JPC. Nous concluons que l'apport d'eau de fonte provenant du lac Agassiz et la

débacle d'icebergs provenant de la langue glaciaire du golfe d'Amundsen sont responsable de la période froide du Drays récent. Finalement, les similitudes observées entre les courbes du niveau marin et nos données suggèrent que les changements du niveau marin influencent la dynamique sédimentaire au début et au milieu de l'Holocène dans l'océan Arctique de l'ouest.

Le second article de cette thèse intitulé "*Sediment provenance changes in the western Arctic Ocean in response to ice-rafting, sea-level and oceanic circulation variations since the last deglaciation*" a été rédigé par moi-même sous la supervision de mon directeur et mon co-directeur soit Jean-Carlos Montero-Serrano (UQAR-ISMER) et Guillaume St-Onge (UQAR-ISMER). L'article a été soumis pour publication dans l'édition spéciale *The Arctic: An AGU Joint Special Collection* de la revue *Geochemistry, Geophysics, Geosystem* le 22 décembre 2017.

2.2 Sediment provenance changes in the western Arctic Ocean in response to ice-rafting, sea-level and oceanic circulation variations since the last deglaciation

Two sediment piston cores were recovered from the Chukchi-Alaskan (05JPC) and Canadian Beaufort (02PC) margins to investigate grain-size, elemental geochemical and mineralogical compositions. This allowed the reconstruction of changes in detrital sediment provenance and transport related to climate variability since the last deglaciation. The end-member modelling analyses of grain-size indicate that sea ice and nepheloid transport as well as the Mackenzie River sediment plume are major factors influencing sedimentation in the Chukchi-Alaskan and Canadian Beaufort margins, respectively. Unmixing of the sediment composition indicates that detrital sediments in core 02PC are derived mainly from the Mackenzie River, whereas sediments from core 05JPC are derived mainly from the Mackenzie River during the deglaciation and include a mixture of Holocene sediments from the Bering Strait inflow, Mackenzie River, and Eurasian margin. The dolomite-rich IRD recorded in both cores could be related to the different phases of iceberg discharges from the Amundsen Gulf Ice Stream. Quartz and feldspar-rich IRD dated at 13 and 10.6 cal ka BP are related to the Lake Agassiz outburst in core 02PC and meltwater discharge from the Brooks Range glaciers in core 05JPC. Our detrital proxies in core 02PC support the hypothesis that large meltwater and iceberg discharges from the Lake Agassiz outburst and Amundsen Gulf ice stream to the Arctic Ocean may have triggered the Younger Dryas. Finally, similar trends observed between the regional sea-level curves and our detrital proxy data suggest that the sea-level changes in the western Arctic Ocean have an important influence on the sediment dynamic during the early- to mid-Holocene.

2.3 Introduction

Sedimentation in the Arctic Ocean and marginal seas has many peculiar characteristics related to the dominance of terrigenous input, which is derived mainly from the surround-

ing continents with different mineral assemblages and geochemical signatures (Darby et al., 2011; Fagel et al., 2014; Maccali et al., 2013; Vogt, 1997). This land-derived terrigenous material originated from a cold climate under conditions of minimal chemical weathering, and therefore consists of weakly altered detrital particles from the original source rocks. This allows correlation between the mineralogical and geochemical signatures preserved in the Arctic shelf sediments and the petrographic composition of the surrounding continents (Gamboa et al., 2017). Detrital sediments are delivered into the Arctic Ocean mainly as suspended particulate matter and bed loads from several large river systems including the Mackenzie, Yukon, Kolyma, Lena, Ob, and Yenisei Rivers (Wagner et al., 2011), as well as from coastal erosion (Gamboa et al., 2017). In shallow continental margins, suspended terrigenous particles are further dispersed by ocean currents and/or incorporated into the sea ice during formation and are then transported over long distances by the surface currents throughout the Arctic Ocean, finally settling far from their source of origin (Darby et al., 2012).

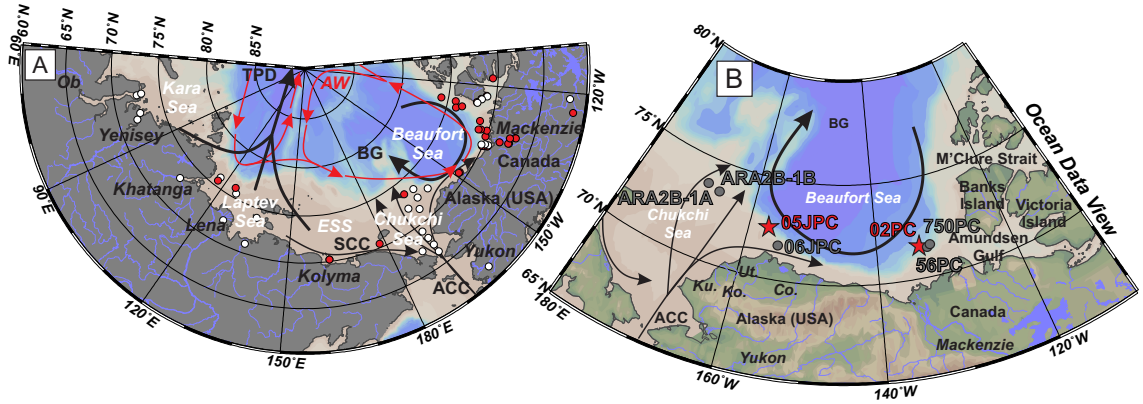

Figure 32: (A) Schematic map of Arctic oceanic circulation and localization of the mineralogical (red circles) and geochemical (white circles) data used in this study. (B) Localization of cores 05JPC and 02PC (this study) as well as cores 56PC (Lakeman et al., 2018), 750PC (Scott et al., 2009), ARA2B-1A (Yamamoto et al., 2017), ARA2B-1B (Stein et al., 2017) and core 06JPC (Ortiz et al., 2009). References used for the geochemical and mineralogical database are listed in Table 6.

Under this framework, a number of studies have characterized and compiled the regional mineralogical and geochemical composition of the detrital sediments over the continental shelf from the Eurasian Basin (Schoster et al., 2000; Viscosi-Shirley et al., 2003a; Vogt, 1997), Chukchi Sea-Bering Strait (Kobayashi et al., 2016; Stein et al., 2017), Chukchi-

Alaskan margin (Darby et al., 2012; Naidu et al., 1982; Naidu and Mowatt, 1983; Ortiz et al., 2009; Yamamoto et al., 2017), Canadian Beaufort Shelf and Amundsen Gulf (Gamboa et al., 2017; Naidu et al., 1971). These datasets allow characterizing the regional surface sediment patterns of the mineralogical and geochemical composition related to the main sediment sources in the circum-Artic region. Once this first crucial step has been achieved, it is possible to use the mineralogical and geochemical signatures preserved in the Arctic Ocean sedimentary records to reconstruct and better interpret the past variations in sediment inputs, as well as the transport pathways related to late Quaternary climate and oceanographic changes. However, most of the bulk mineralogical records that have been generated do not quantify the contribution of possible sediment sources in the western Arctic Ocean, nor their long-term variability. On the other hand, the high sedimentation rates observed in the post-glacial sedimentary sequences from the continental margins of the Canadian Beaufort (10-60 $cm.ka^{-1}$; Deschamps et al. 2018b) and Chukchi (30-300 $cm.ka^{-1}$; Barletta et al. 2008; Lisé-Pronovost et al. 2009) seas in Arctic Ocean offer unique records for reconstructing sediment dynamics and past climate conditions at the centennial to millennial time scales.

In this regard, in the present study, grain-size, mineralogical and elemental geochemical analysis of the bulk (< 2 mm) and clay (< 2 μm) fractions were carried out on two sediment piston cores recovered from the Chukchi-Alaskan (core HLY01-05JPC) and Canadian Beaufort (core AMD0214-02PC) margins in order to (1) assess the contributions from specific sediment sources (e.g., East Siberian Sea, Kara Sea, Northwest Alaska, Mackenzie River, Bering Strait inflow, and Canadian Arctic Archipelago) and (2) provide new insights on potential relations between ice-rafting, sea-level and oceanic circulation variations and sediment dynamics in the western Arctic Ocean since the last deglaciation. Thus, our study differs from these earlier publications in terms of methodological approach (quantitative mineralogy and multiproxy study), inter-margin comparison (Chukchi-Alaskan *vs*. Canadian Beaufort margins), and enhanced discrimination of circum-Arctic sediment sources. Therefore, this multiproxy record provides a unique opportunity to reconstruct sediment dynamics within the western Arctic Ocean since the deglaciation.

2.4 Regional Setting

2.4.1 Oceanic circulations

The Arctic surface oceanic circulation is related to two main, wind-driven circulation systems, which are the anticyclonic Beaufort Gyre (BG) in the western Arctic and the Transpolar Drift (TPD; Darby and Bischof, 2004; Tremblay et al., 1997). At a regional level, these surface circulation regimes are controlled mainly by changes in the phase of large-scale atmospheric patterns, such as the Arctic Oscillation (AO; Darby and Bischof, 2004; Darby et al., 2012) and the Pacific Decadal Oscillation (PDO; Overland et al., 1999), which are both significant natural patterns in global climate variability. On the other hand, the Chukchi shelf circulation is controlled by an inflow of Pacific waters via the Bering Strait (referred to as the Bering Strait inflow), the Siberian coastal current, and the Atlantic Intermediate Water affecting the northern margin (Pickart, 2004; Weingartner et al., 2005). The Pacific inflow can be divided into 3 major branches (Fig. 32). The first branch turns westward around Herald Canyon. The third branch flows into Barrow Canyon, whereas the second branch flows between the first and the third branches (Weingartner et al., 2005). The Bering Strait inflows are controlled mainly by the Aleutian Low strength and position at the interannual time scales (Yamamoto et al., 2017). Indeed, periods of strengthening of the Aleutian Low pressure center, located over the eastern North Pacific, induce an increase of the Bering Strait inflow into the Arctic Ocean (Danielson et al., 2014). On the Canadian Beaufort shelf, the anticyclonic BG pushes both surface currents and sea ice westward at the shelf break. Conversely, closer to shore around the 50-m isobath, the Beaufort Undercurrent transports both Pacific and Atlantic waters eastward along the continental margin and into the Amundsen Gulf (Forest et al., 2011).

2.4.2 Surrounding geology

Because the Arctic Ocean is a semi-enclosed basin, detrital sediment source regions for the Arctic are limited to the surrounding terrains: the Canadian Arctic Archipelago, the Mackenzie delta region, Northern Alaska, the Chukchi Sea with Pacific influences, the East Siberian Sea, the Laptev Sea, the Kara Sea, the Barents Sea, and the Pan-African terrains of Northern Greenland (Fagel et al., 2014). These circum-Arctic sources areas have variable geological ages and tectonic settings, and are therefore characterized by different petrographic signatures. The Canadian Arctic Archipelago and the Mackenzie Delta region are comprise shales and sandstones from marine and non-marine sedimentary rocks (Harrison et al., 2011). In addition, Banks and Victoria Islands are composed of shale and sandstones rich in dolomite clasts, as well as quartz and feldspar grains (Bischof and Darby, 1999). As part of the North American margin, the Canadian Shield is made of Archean plutonic and metamorphic rocks (Padgham and Fyson, 1992). Alaskan terrains include Canadian–Alaskan Cordillera, Brooks Range, and part of the North American platform containing mostly metamorphic, and clastic rocks (Hamilton, 1986). The Siberian platform is composed by Precambrian and Cambrian limestones, Jurassic to Cretaceous terrigenous sediments and Quaternary alluvial material (Harrison et al., 2011). The volcanic areas can be separate in different zones: the intraplate Okhtosk-Chukotka composed by acidic to intermediate rocks predominating in the west and intermediate to basic rocks in the east (Viscosi-Shirley et al., 2003b), as well as Bering Sea Basalt Province, and the Permian and Triassic volcanic rocks of Siberian traps, and the convergent margins of the Pacific Aleutian (Harrison et al., 2011).

2.4.3 Sedimentation

On the Canadian Beaufort shelf, most of the surficial seabed sediments are predominantly composed of Holocene marine olive-grey silts and clays (Gamboa et al., 2017). Surface sediments from the Chukchi Sea are composed of bioturbated grey to clayey silts (Kobayashi

et al., 2016). Modern sedimentation in the Chukchi Sea is believed to be mainly derived from northeastern Siberia, Bering Strait inflow (especially from the Yukon River) and Mackenzie River, whereas, the Canadian Beaufort margin sediment originates primarily from the Mackenzie River basin (Darby et al., 2011; Gamboa et al., 2017; Kobayashi et al., 2016). Smaller Alaskan rivers have a more local impact, but may have been a more important sediment source at the early stages of the last transgression (Hill and Driscoll, 2008). During deglaciation and the early Holocene, sediment inputs to the Chukchi and Beaufort margins were presumably higher due to the rising sea level associated with meltwater and iceberg discharge from the retreating of large ice sheets (Deschamps et al., 2018b). During the Holocene or interglacial, sediment redistribution is strongly controlled by bottom current while during deglacial/glacial period sea ice and ice rafted debris (IRD) strongly affected sediment dispersal and deposition (Darby et al., 2009). Several IRD have been recorded in the sedimentation along the North American margin associated with the calving of the Laurentide and Innuitian Ice Sheets (Darby and Zimmerman, 2008).

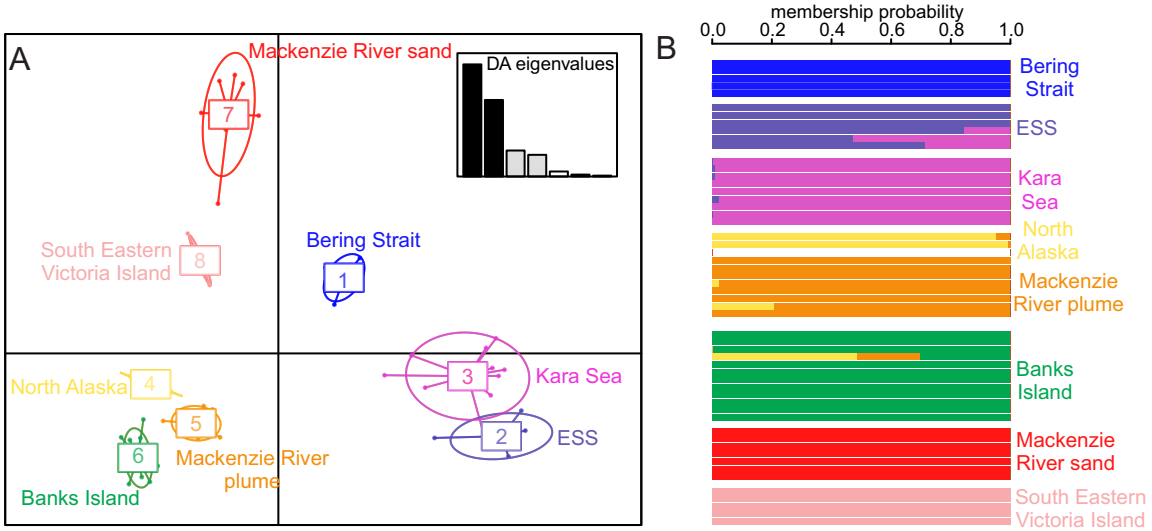

Figure 33: (A) Discriminant function analyses (DFA) and (B) membership probability of the circum-Arctic sources based on log ratio mineral data.

2.5 Materials and methods

2.5.1 Samples, sediment characteristics and chronology

The sediment core HLY0501-05JPC (hereafter referred to as core 05JPC; location: 72°51.618'N, 158°25.26'W) was recovered from the Chukchi-Alaskan margin on board the USCGC Healy as part of the 2005 Healy-Oden Trans-Arctic Expedition (Darby et al., 2005; Fig. 32b).Physical properties of the sediment core 05JPC have been previously published in Barletta et al. (2008). Core AMD0214-02PC (hereafter referred to as core 02PC; location: 71°22.910'N, 133°34.040'W) was collected on the Canadian Beaufort margin on board the CCGS Amundsen during the 2014 ArcticNet expedition (Montero-Serrano et al., 2014; Fig. 32b). The age model and physical properties of the sediment core 02PC have been described in Deschamps et al. (2018b). Note that cores 05JPC and 02PC were raised from the continental slope at 415 m and 998 m depth, respectively, where sediment deposition was not interrupted by sea-level changes. The sediment core 02PC was sampled evenly every 10 cm in the Holocene and IRD intervals, as well as every 20 cm in the deglacial interval for a total of 42 samples. The sediment core 05JPC was sampled every 60 cm in the Holocene interval and every 30 cm for the remaining sections (corresponding to the deglacial interval) for a total of 30 samples.

The sediment cores 05JPC and 02PC present two distinct sedimentary units. According to Barletta et al. (2008), the upper unit in core 05JPC is composed of olive-gray mud, and the second unit is characterized by dark-gray mud with sandy layers and IRD. Core 02PC consists of homogeneous olive-brown to dark-gray for the upper unit, while the second unit consists of dark-gray with the presence of white clasts and was interpreted as IRD (Deschamps et al., 2018b). The sedimentation rate for core 02PC was lower in the postglacial parts (2-20 $cm.ka^{-1}$) and higher in the glacial parts (50-380 $cm.ka^{-1}$). Based on the physical properties and grain-size analyses, the IRD layers were found in the glacial unit in both cores. The IRD were identified between 1350 (IRD1A) and 1600 (IRD1B) cm in core 05JPC

(Barletta et al., 2008). Likewise, the IRD in core 02PC consists of white clasts found between 140 and 160 cm (IRD1A), 320 and 350 cm (IRD2A) as well as 350 and 360 cm (IRD2B). These fine-grained IRD are generally < 63 μm, poorly sorted, have sharp contacts, and consist mainly of rock flour (dolomite- and quartz-rich). These IRD are interpreted to reflect enhanced meltwater discharge and iceberg rafting from the Laurentide Ice Sheet (Andrews, 2000; Deschamps et al., 2018b; Polyak et al., 2007; Lakeman et al., 2018).

The age model of core 05JPC was constructed using a linear interpolation between the ^{14}C ages for the Holocene and deglacial sections (Barletta et al., 2008) and assuming a ΔR=460 as suggested in Darby et al. (2009). The best ^{14}C-based age control covers the interval of 2–6.9 cal ka BP in 05JPC. Ages below this dated interval were extrapolated and our interpretations thus remain hypothetic. However, the identical paleomagnetic secular variations between core 05JPC and other Arctic records (Barletta et al., 2008) suggest a valid age model around 8.5-9 cal ka BP. Based on this age model, core 05JPC spans the last 11 cal ka BP and IRD1A-B were dated at 9.5 and 10.6 cal ka BP, respectively. In the same way, the age model of core 02PC published in Deschamps et al. (2018b) was improved using the new ages from the nearby core 56PC presented in Lakeman et al. (2018) and assuming a ΔR= 335±85 for the Holocene interval and a ΔR= 1000 for the deglacial interval (Coulthard et al., 2010; Hanslik et al., 2010). Contemporaneous IRD peaks have been identified in magnetic susceptibility curves and used in order to transfer the age model of core 56PC to core 02PC (see Supplementary Material). Finally, core 02PC spans the last 13.2 cal ka BP and the IRD1A and IRD2A-2B are dated to ~11, 12.8 and 13 cal ka BP, respectively (Fig. 42).

2.5.2 Grain-size distribution and end-member modelling analysis

Sediment grain-size analyses were performed on the detrital bulk sediment samples using a Beckman Coulter LS13320 laser diffraction grain-size analyzer following the protocol in Deschamps et al. (2018b). The grain-size distribution and statistical parameters (e.g. mean and sorting) were calculated using the moment methods from the GRADISTAT software

(Blott and Pye, 2001). The end-member modelling algorithm (EMMA), developed by Weltje (1997) and adapted by Dietze et al. (2012), was applied to the grain-size data in order to extract meaningful end-member (EM) grain-size distributions and estimate their proportional contribution to the sediments. A more detailed description of the EMMA method that we applied can be found in Dietze et al. (2012). Overall, the grain-size distribution and end-member modelling analyses were used to investigate the sedimentary transfer regime because the sediment grain-size distribution (primarily driven by sedimentary processes) reflects transport conditions (Dietze et al., 2012; Gamboa et al., 2017).

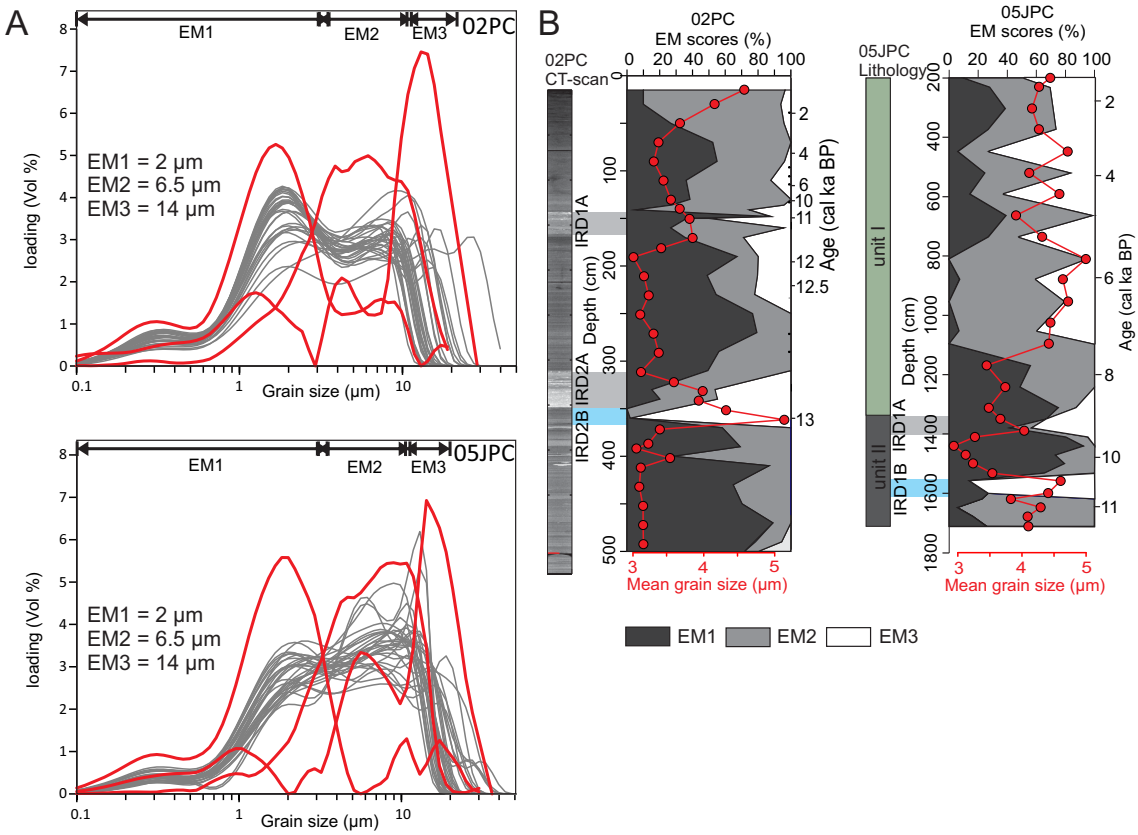

Figure 34: End-member modelling analyses (EMMA) performed on the grain-size distribution of the detrital fraction from cores 01JPC, 05JPC, 03PC and 02PC. (A) Three representatives, unmixed grain-size distributions, as well as (B) end-member scores (%) derived from EMMA are shown.

2.5.3 Geochemical and mineralogical analysis

Before geochemical and mineralogical analysis, the sediment samples were rinsed five times with distilled water after the removal of the organic matter fraction with 10 mL of hydrogen peroxide (30 % H_2O_2). Next, an aliquot of this sediment sample was used as the bulk fraction (< 2 mm), whereas another aliquot was used to separate the clay-sized fraction (< 2 μm). A centrifuge-based Atterberg method was used according to Stoke's Law to separate the clay-sized fraction. The required settling times were calculated using the software SediCalc (Krumm, 2006). Subsequently, aliquots of the separated bulk and clay-sized samples were oven dried overnight at approximately 60°C and then slightly homogenized with an agate mortar. These homogenized sediment fractions were used for geochemical and mineralogical analysis.

2.5.4 Bulk elemental concentrations

A total of 14 elements (Al, Si, K, Mg, Ca, Ti, Mn, Fe, P, Sr, V, Cr, Zn, and Zr) were analyzed on both bulk and clay-sized fractions by energy dispersive X-ray fluorescence (EDXRF) spectrometry using a PANalytical Epsilon 3-XL. Before EDXRF analysis, samples were treated by borate fusion in an automated fusion furnace (CLAISSE®M4 Fluxer). The analytical procedures were similar to (Gamboa et al., 2017). Analytical accuracy and precision were found to be better than 1–5 % for major elements and 5–10 % for the other elements, as checked against an international standard (USGS SDC-1) and analysis of replicate samples.

2.5.5 Quantitative bulk mineralogy

Bulk mineral associations (< 2 mm) were studied by quantitative X-ray diffraction (qXRD) following the method developed by Eberl (2003) and used in other Quaternary

glacial marine studies that address sediment mineralogy (Andrews et al., 2015, 2016; Darby et al., 2011; Stein et al., 2017). For this, ~1 g of each sample was spiked with 0.25 g of corundum and then ground in a McCrone micronizing mill using 5 mL of ethanol to obtain a homogenous powder. The slurry was oven dried overnight at approximately 60°C and then slightly homogenized with an agate mortar. Next, 0.5 mL of vertrel was added to the mixture to prevent the possible agglomeration of finer particles. The powder sample is then sieved (< 300 μm), back-loaded into the holders and analyzed on a PANalytical X'Pert Powder diffractometer. Samples were scanned from 5° to 65° two-theta in steps of 0.02° two-theta, with a counting time of 4 seconds per step. For the quantification of the major mineralogical components, sediment XRD scans obtained were converted into mineral weight percent (wt. %) using the Excel macro program ROCKJOCK v11 (Eberl, 2003). This program uses a full-pattern fitting method that permits the quantification of whole-sediment mineralogy with a precision of ±3 wt. % (Eberl, 2003). The calculated total mineral wt. % was normalized to a sum of 100%. We focused on 15 key minerals (quartz, K-feldspar, plagioclase, calcite, dolomite, amphibole, Fe-bearing, amorphous silica, kaolinite, chlorite, illite, biotite, muscovite, smectite and vermiculite) that represented more than 96 % of the overall mineral concentration in the bulk sediment sample.

2.5.6 Clay mineralogy

In this paper, clay minerals were quantified in the bulk sediment fraction (< 2 mm) using the Excel macro program RockJock. However, nearly all previous clay-mineral provenance studies in the Arctic Ocean used oriented mounts of the < 2 μm sediment fraction to identify and semi-quantify the clay-mineral abundance, notably illite, kaolinite, chlorite, and smectite (Naidu et al., 1971, 1982; Naidu and Mowatt, 1983). Therefore, in this study, the clay-size fraction of all sediment samples was isolated and analyzed in this manner for comparison. Clay mineral were thus studied using XRD following established protocols (Bout-Roumazeilles et al., 1999; El Ouahabi et al., 2017). The separated clay-sized frac-

tion was concentrated by centrifugation and oriented by wet smearing on glass slides. The analyses were run from 2.49° to 32.49° 2θ on a PANalytical X'Pert Powder diffractometer. Three X-ray diagrams were performed, after the sample was air-dried, ethylene glycol vapor saturation was completed for 12 h, followed by heating at 490°C for 2 h. Semi-quantitative estimation of clay mineral abundances (smectite, illite, chlorite, kaolinite, vermiculite and a chlorite/smectite mixed layer) based on peak areas was performed using the MacDiff®4.2.5 software (Petschick, 2000). Similar to others Arctic clay mineral studies (Schoster et al., 2000; Wahsner et al., 1999), clay mineral contents were calculated by using the weighting factors introduced by Biscaye (1965) and calculated to a sum of 100 %. The error on the reproducibility of measurements is estimated to be 5 % for each clay mineral, as checked during the analysis of replicate samples. Overall, the combinations of both RockJock and oriented mounted methods are supporting each other and give independent information (Darby et al., 2011).

2.5.7 Sediment unmixing model

We used the non-linear unmixing Excel macro program SedUnMixMC (Andrews and Eberl, 2012; Andrews et al., 2015, 2016) to gain a quantitative understanding of the downcore changes in bulk sediment provenance. To avoid misinterpretation of bulk mineralogical results caused by the methodological differences between sources and downcore sediment samples, all sediment source samples used here were processed for qXRD (Andrews et al., 2016; Belt et al., 2010; Darby et al., 2011; Gamboa et al., 2017; Lakeman et al., 2018; Stein et al., 2017; Table 6).

2.5.8 Statistical approach

The mineralogical and geochemical data are of a compositional nature, that is, they are vectors of non-negative values subjected to a constant-sum constraint (usually 100%). This

implies that relevant information is contained in the relative magnitudes, so statistical analyses must focus on the ratios between components (Aitchison, 1990). Under this framework, the vertical distributions of the sediment provenance proxies, as well as the discriminant scatter plots based on mineralogical and geochemical data were represented here as log-ratios. Note that a log-transformation will reduce the very high values and spread out the small data values and is thus well suited for right-skewed distributions (Boogaart and Tolosana-Delgado, 2013). Thus, compared to the raw data, the log-ratio scatter plots exhibit better sediment discrimination. In addition, discriminant and membership's probability analyses were performed using the mineralogical dataset with the goal of ascertaining whether the differences observed between each sediment source area are statistically valid (Andrews and Vogt, 2014; Fig. 34). Prior to discriminant and membership's probability, a log-centered (clr) transform was applied to the dataset (Aitchison, 1990). The discriminant analysis were conducted with "R" software using the packages "adegenet" (Jombart, 2008) and "compositions" (Van Den Boogaart and Tolosana-Delgado, 2008). All analytical data presented are available electronically in the PANGAEA database (https://www.pangaea.de/).

2.6 Results and interpretations

2.6.1 Grain-size distribution and end-member modeling

The algorithm of the end-member modelling analysis EMMA showed a polymodal distribution and revealed a three-EM model in cores 05JPC and 02PC (Fig. 34A). This explains more than 95 % of the total variance (Fig. 49). The end-member EM3 is associated with medium to coarse silts (10 to 30 μm), end-members EM2 correspond to fine to medium silts (2 to 10 μm), and end-member EM1 is associated with clays (< 2 μm) and fine silts (2 to 4 μm). Finding the same grain-size end-members in both margins highlights the robustness of the results, and suggests that both margins are probably influenced by similar sedimentary processes. The relative contributions of these end-members are plotted against depth in

Fig. 34B. Darby et al. (2009) have shown the detailed grain-size distribution for sediment transport processes in the western Arctic Ocean using varimax-rotated principal component analysis on several Holocene sediment cores in the Chukchi Sea and including core 05JPC. In their study, they found four main end-members: (i) EM < 0.5 μm relates to suspension freezing and sediment wash load; (ii) EM centered on 2 μm relates to anchor sea ice; (ii) EM centered on 5 μm is associated with the non-cohesive (sortable) fine silt that is commonly transported in suspension by weak currents along the bottom or in nepheloid layers above the bottom, and (iv) specific to the Chukchi margin, EM of 43-64 μm is associated with intermittent suspended load. Overall, these grain size end member obtained by Darby et al. (2009) are similar to then obtain in this study, and therefore, we infer that our grain-size pattern reflects the same sedimentary processes. However, surface sediments derived from the Mackenzie River are also characterized by a fine to medium grain-size (4-5 μm; Gamboa et al., 2017), which is similar to the EM centered on 5 μm that is related to nepheloid transport (Darby et al., 2009). Thus, this end-member could be interpreted differently between the Chukchi (nepheloid transport) and Canadian Beaufort margins (Mackenzie River sediment plume). Based on these results, the log(EM1/EM2) ratio is used to elucidate downcore variations in the proportion of grains transported by sea ice or nepheloid flow for core 05JPC and by sea ice and/or Mackenzie River discharges for core 02PC.

2.6.2 Elemental geochemistry

Stratigraphic distributions of the elemental geochemical data from the two sedimentary cores studied here are shown in Fig. 43. Looking at the variation of the proportion between the different fractions (bulk and clay), we can observe 2 groups with a different behavior. The first group was related to elements with a higher concentration in the bulk fraction, which included Si, Ti, and Zr, as well as Ca, Mg, and Mn in the IRD intervals. However, note that Ca and Mg in the IRD layers are more enriched in core 02PC than in core 05JPC (maximum values of ~15 wt. % and ~3.5 wt. %, respectively). The second group was linked to elements

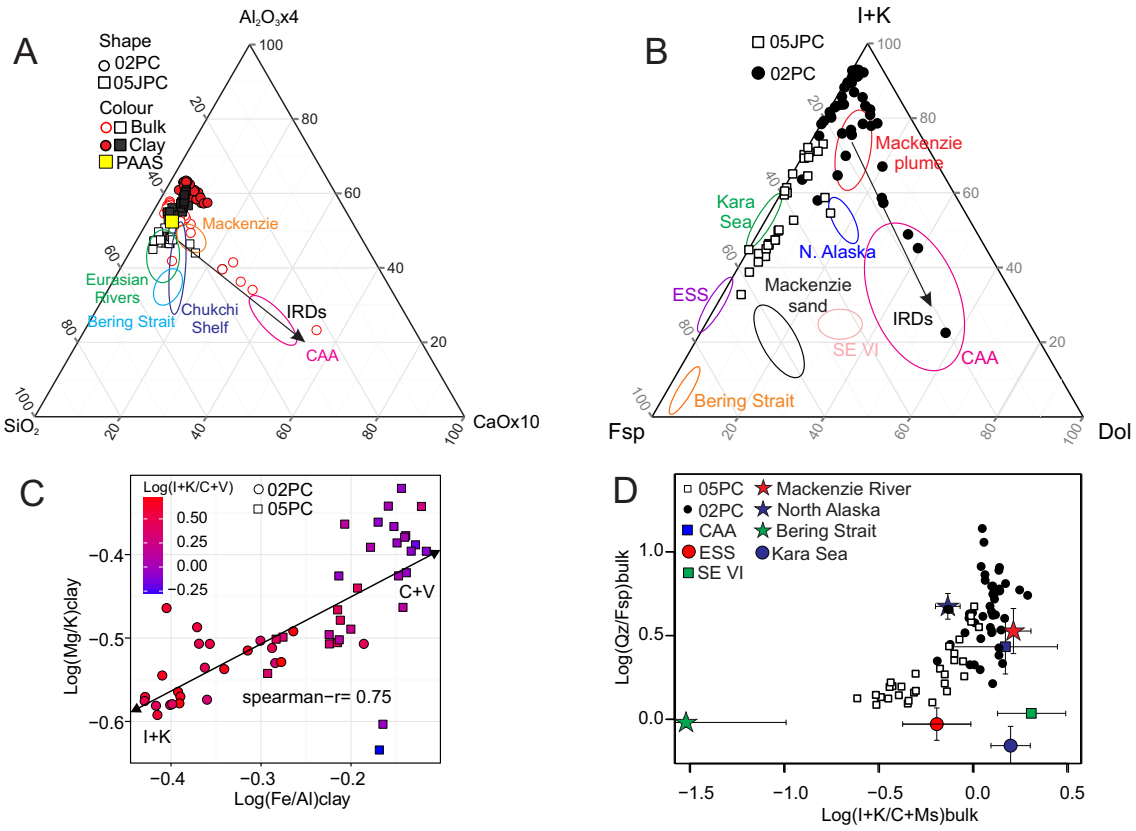

Figure 35: (A) Al_2O_3-SiO_2-CaO ternary plot showing the overall composition (bulk and clay fractions) of the sediment from cores 05JPC and 02PC in comparison to the average shale and circum-Arctic source areas. (B) Kaolinite+Illite (K+I) – total feldspars (Fsp) – dolomite (Dol) ternary plot for cores 05JPC and 02PC based on bulk mineralogy. (C) Relationship between Log(Mg/K) and Log(Fe/Al) ratios derived from the clay fraction of sediment cores 05JPC (square) and 02PC (circle). The log ratio I+K/C is represented by a gradient color from high (red) to low (blue) values. (D) Log(Qz/Fsd) versus Log(I+K/Ch+Ms) diagram illustrating the bulk mineralogical difference between cores 02PC and 05JPC and some circum-Arctic regions. Geochemical and mineralogical data of the circum-Arctic regions are shown in Table 6.

with a higher concentration in the clay fraction, which included Al, K, Fe, V, and Zn for both cores. The downcore variations are quite similar between the bulk and clay fractions in core 02PC. However, some differences in the long-term variations between the bulk and clay fractions are observed in core 05JPC with an increase of Ca, Mg and Fe in the clay fraction during the early to late Holocene (Fig. 44).

Because Al and Si are associated to clay minerals, aluminosilicates and quartz, and Ca is associated to carbonates, the ternary plot Al, Si, and Ca (expressed as oxides; Fig. 35A) was

used in order to obtain a general geochemical classification of the sediments (Gamboa et al., 2017). Sediments from cores 05JPC and 02PC are dominantly composed of detrital material, which is similar to an average shale (Pourmand et al., 2012). However, sediments from core 02PC are slightly enriched in Al and depleted in Si in both the bulk and clay fractions compared to core 05JPC. In addition, the clay fraction of core 02PC is also enriched in Al and K, whereas core 05JPC is enriched in Mg and Fe (Fig. 35C). Likewise, bulk sediments from cores 02PC and 05JPC have a similar chemical composition to the sediments of the Mackenzie River and Chukchi Shelf/Eurasian Rivers, respectively. In the bulk sediments, the IRD layers showed higher Ca contents (dolomite) and plot along the mixing line from average shale to the detrital carbonate end-member (Fig. 35A). These Ca-rich IRD layers have a similar composition to the Canadian Arctic Archipelago sediments (including Banks and Victoria islands; Darby et al., 2011; Gamboa et al., 2017).

Based on all the results discussed above, we selected the log(Ca/Al), log(Mg/Al), log(Zr/Al) and log(Fe/Al) ratios to reconstruct downcore changes in sediment provenance and transport on the Chukchi-Alaskan and Canadian Beaufort margins since the last deglaciation (Figs. 37-38). Indeed, the grain-size changes could be investigated with log(Zr/Al), because Zr is concentrated in zircon grains in the coarser fraction and Al is preferentially associated with clay minerals and aluminosilicates in the fine-grained fractions (Von Eynatten et al., 2012). As discussed in Bischof and Darby (1999) and Gamboa et al. (2017), sediments derive from the Canadian Shield, the sedimentary platform along the Mackenzie Valley, and the Western Canadian Arctic Archipelago are characterized by high contents (up to 2 %) in iron-oxides, including hematite, goethite, pyrite, maghemite and magnetite. Thus, high log(Fe/Al) ratios could reflect a higher input of iron-oxides entrained by icebergs from the Laurentide and Innuitian ice sheets (Bischof and Darby, 1999). In addition, a high log(Ca/Al) and log(Mg/Al) ratio reflects a greater contribution from detrital carbonates (notably, dolomite), whereas low ratios suggest the input of aluminosilicates.

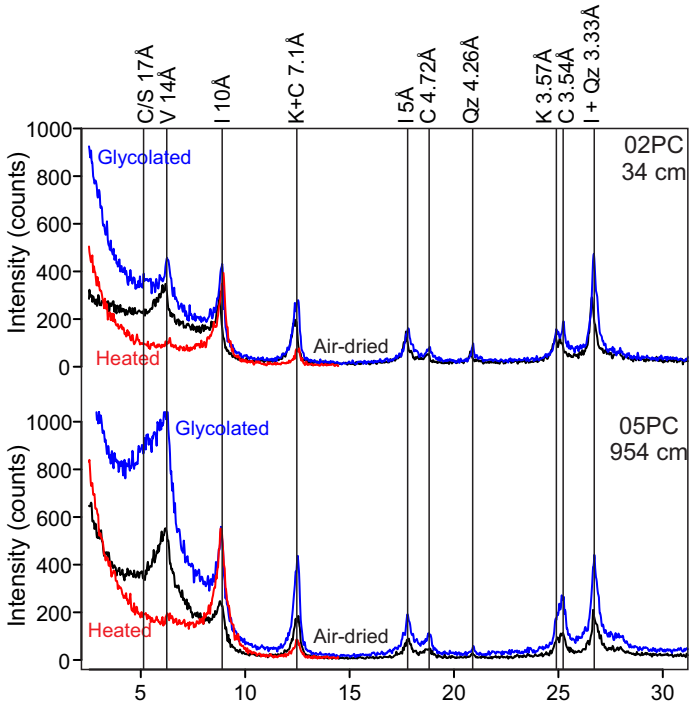

Figure 36: X-ray diffractograms of typical samples from cores 02PC and 05JPC showing interpretation of major clay mineral species from the three classical runs, i.e., in air-dried, glycolated, and heated conditions.

2.6.3 Bulk mineralogy

Stratigraphic distributions of the bulk mineralogical data from the two sedimentary cores in this study are shown in Fig. 45. The mineralogy of the bulk sediment fraction from the Canadian Beaufort and Chukchi-Alaskan margins is dominated by quartz (02JPC: 13–40 %; 05JPC: 12-39 %), phyllosilicates, which includes kaolinite, chlorite, illite, biotite, muscovite, smectite and vermiculite (02JPC: 47-80 %; 05JPC: 30-50 %), plagioclase (02JPC: 1-7 %; 05JPC: 4-11 %), K-feldspar (02JPC: 0-5 %; 05JPC: 1-6 %), dolomite (02PC: up to 28 %; 05JPC: up to 5 %), and lower proportions (< 1 %) of Fe-bearing, amphibole and pyroxene minerals. In general, quartz, phyllosilicates, plagioclase and K-feldspar represented more than 80 % of the overall mineral concentration in both sediment cores. However, K-feldspar, plagioclase, muscovite, chlorite and vermiculite are more abundant in core 05JPC, whereas quartz, illite and kaolinite are enriched in core 02PC (Figs. 35C-D). In both sed-

iment cores, intervals with punctuated enrichments of dolomite (up to 28 % for 02PC and up to 5 % for 05JPC), as well as in quartz (up to 40 % in both cores) are observed in the IRD layers (Fig. 45). Based on these results, we performed a ternary plot of illite+kaolinite, total feldspars, and dolomite (Fig. 35B) to obtain a general mineralogical discrimination of the potential source areas. The Bering Strait and Eurasian sources are characterized by a higher total feldspar proportion, the sediments from the Northern Alaska and Mackenzie River are related to higher illite+kaolinite contents, and the sediments from the Banks and Victoria Island are enriched in dolomite. The sediments of core 02PC are mostly related to the Mackenzie River as potential sources, whereas the sediments of core 05JPC seem to be composed by a mixture of sediments from the Eurasian margin, Bering Strait and Mackenzie River. The sediments in the IRD layers present higher dolomite contents. Overall, the relative abundance of dolomite, and the following ratios are used to trace sediment provenance changes over time : log[quartz/(K-feldspar+plagioclase)] or log(Qz/Fsp), log[phylosillicates/(K-feldspar+plagioclase)] or log(Phy/Fsp), and log(illite+kaolinite/chlorite+muscovite) or
log(I+K/C+Ms).

2.6.4 Clay mineralogy

Stratigraphic distributions of clay mineralogical data from the two sedimentary cores studied here are shown in Fig. 46. The clay mineral assemblage consists mainly of illite, kaolinite, chlorite and vermiculite in both cores (Fig. 36). Indeed, core 02PC consists of illite (55-70 %), kaolinite (10-30 %), chlorite (10-25 %), vermiculite (0-20 %) and a scarce abundance of a smectite/chlorite mixed layer (0-8 %, average, 1 %) (Fig. 46). The clay mineral assemblage for core 05JPC consists of illite (30-70 %), chlorite (10-20 %), kaolinite (5-15 %), vermiculite (5-55 %) and smectite/chlorite mixed layer (0-20 %), which is present in much less abundance, with average contents of 1 % (Fig. 46). Thus, as also shown in the bulk qXRD data, the major clay mineralogical difference between the two sediment cores is

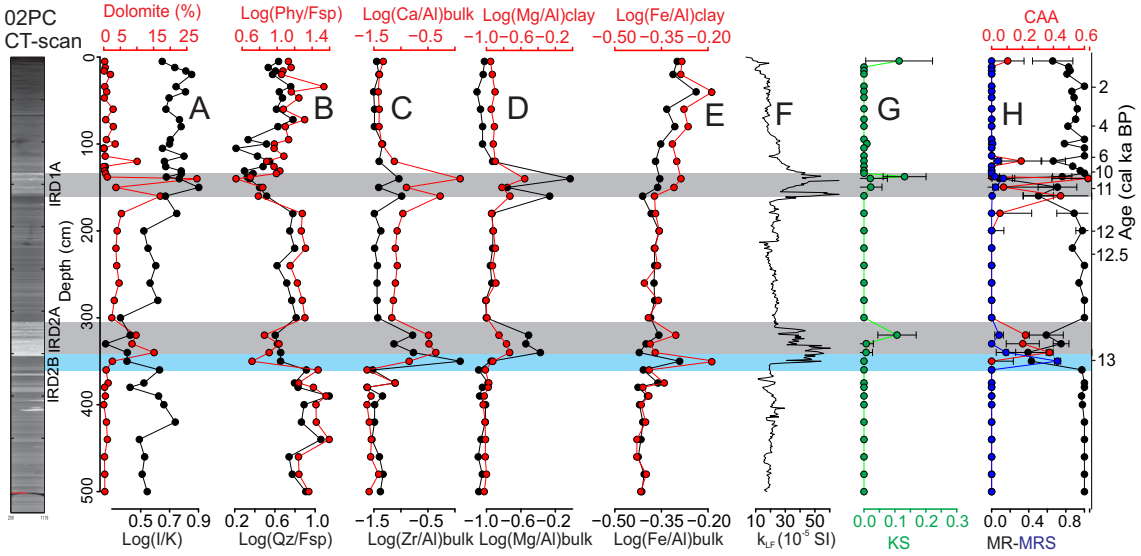

Figure 37: Downcore variations of core 02PC showing (A) log-ratio illite/kaolinite and dolomite content (red). (B) Log-ratios quartz/feldspar (black) and phyllosilicates/feldspar (red). (C) Log-ratio Zr/Al (black) and Ca/Al (red). (D) Log-ratio Mg/Al for the bulk (black) and clay (red) fractions. (E) Log-ratio Fe/Al for the bulk (black) and clay (red) fractions. (F) Magnetic susceptibility, k_{LF} (Deschamps et al., 2018b). (G) Proportion of sediment from the Kara Sea (black). (H) Proportion of sediment from the Mackenzie River (black), Mackenzie River sand (blue) and CAA (red). IRD layers rich in dolomite and quartz are highlighted in gray and blue, respectively.

the higher illite-kaolinite proportion in core 02PC, whereas core 05JPC is relatively enriched in chlorite (see Supplementary Material). These results are consistent with those reported for modern surface sediments on the Chukchi Shelf and Beaufort Shelf (Kalinenko, 2001; Krylov et al., 2014; Naidu et al., 1982; Naidu and Mowatt, 1983; Wahsner et al., 1999). Thus, we used the log(illite+kaolinite/chlorite+vermiculite) ratio or log(I+K/C+V) to derive changes in transport pathways (e.g., Bering Strait inflow) and the log(illite/kaolinite) ratio or log(I/K) to reconstruct changes in sediment inputs within the Canadian Beaufort Shelf.

2.7 Discussion

Long-term changes in sediment sources were explored using the program SedUnMixMC (Andrews and Eberl, 2012). As summarized in Asahara et al. (2012), modern sediment inputs in the Chukchi Sea are mainly derived from northeastern Siberia and Bering Strait

inflow, and accessorily from the Mackenzie River. Based on this premise, we ran the SedUnMixMC on sediment core 05JPC using the following sediment sources: Bering Strait, Northern Alaska, Eastern Siberian-Laptev Seas, Mackenzie Trough-Canadian Beaufort Shelf and detrital carbonates from the Canadian Arctic Archipelago, including the Banks/Victoria Islands (See Supplementary Material). In core 02PC, we ran SedUnMixMC using surface samples from the following sources: Mackenzie Trough-Canadian Beaufort Shelf, Canadian Arctic Archipelago, Kara Sea and bed sands from the Mackenzie River basin (see Supplementary Material). The boxplot based on principal component scores of geochemical and mineralogical data (See Supplementary Material), ternary plot illite+kaolinite-total feldspars-dolomite (Fig. 35B), the log(Qz/Fsp)/log(I+K/C+Ms) crossplots (Fig. 35B), and the discriminant and membership probability analyses based on log ratio mineral data (Fig. 34), indicates that these potential source regions have mineral and chemical compositions that allow a reasonable degree of sediment discrimination as indicated by their relatively high membership value (up to 90 %).

In this context, the long-term variations observed in our mineralogical and geochemical records are discussed below in terms of glacial and postglacial changes in detrital sediment supply, provenance and transport and their possible relations with both the deglacial/Holocene climate variability and relative sea-level variations.

2.7.1 Deglacial/Holocene sediment dynamics (14 to 10.5 cal ka BP)

Canadian Beaufort Sea

SedUnMixMC modelling indicated that the fine-grained feldspar, quartz and Zr-rich layer in core 02PC (IRD2B) dated at ~13 cal ka BP is mainly derived from the Mackenzie River (40 %, Fig. 37H). Optically stimulated luminescence ages from the Mackenzie drainage basin suggest a major routing of deglacial meltwaters from Lake Agassiz into the Arctic Ocean at 13±0.2 cal ka BP, near the onset of the Younger Dryas (Murton et al., 2010).

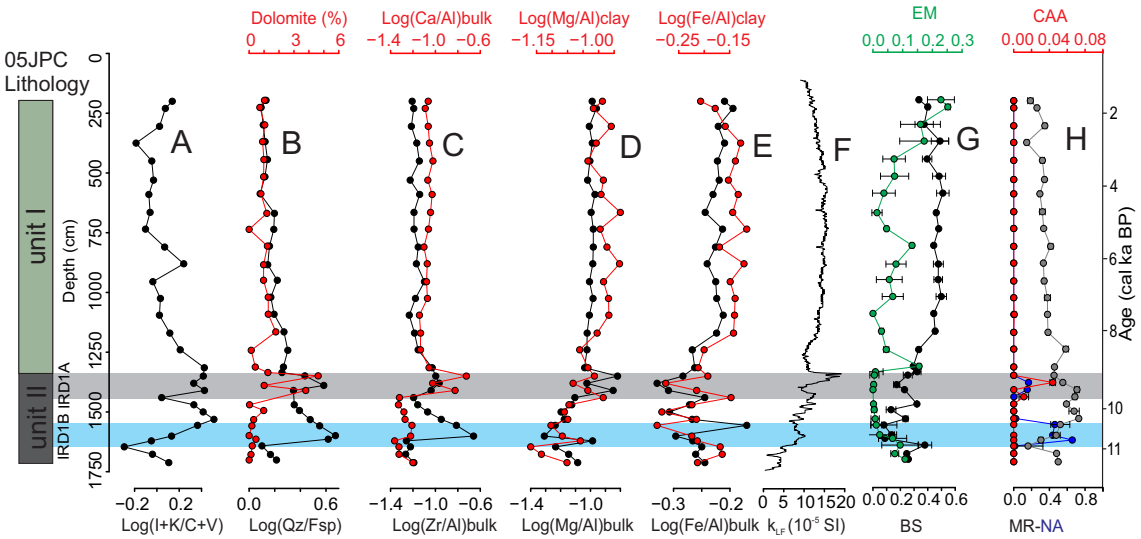

Figure 38: Downcore variations of core 05JPC showing (A) log-ratio illite+kaolinite/chlorite. (B) Log-ratio quartz/feldspar (black) and proportion of dolomite (red). (C) Log-ratio Zr/Al (black) and Ca/Al (red). (D) Log-ratio Mg/Al for the bulk (black) and clay (red) fractions. (E) Log-ratio Fe/Al for the bulk (black) and clay (red) fractions. (F) Magnetic susceptibility, k_{LF} (Barletta et al., 2008). (G) Proportion of sediment from the Eurasian margin (EM), which includes Kara Sea and Eastern Siberian Sea in green and proportion of sediment from the Bering Strait in black. (H) Proportion of sediment from the Mackenzie River (black), North Alaska (blue) and CAA (red). IRD layers rich in dolomite and quartz are highlighted in gray and blue, respectively.

This observation concurred to highlight that the quartz and feldspars-rich layers observed at ~13 cal ka BP in the Canadian Beaufort margin may be related to an outburst flood from Lake Agassiz. We hypothesize that meltwaters from the Lake Agassiz remobilized rock flour deposits that are characterized by an abundance of quartz and feldspars from the northwest part of the Mackenzie River watershed (Fig. 39). Furthermore, SedUnMixMC modelling also indicated that dolomite-rich (Ca-Mg) IRD layers (IRD1A and IRD2A) dated at 11 and 12.8 cal ka BP were originated from the Canadian Arctic Archipelago (Fig. 37H). Similar dolomite-rich IRD have been found on the Lomonosov Ridge and in Fram Strait during the Younger Dryas chronozone (Hillaire-Marcel et al., 2013; Maccali et al., 2013; Not and Hillaire-Marcel, 2012). Major purge from the M'Clure and Amundsen Gulf ice stream was previously suggested by isotope data (Hillaire-Marcel et al., 2013; Maccali et al., 2013), paleogeography study (Stokes et al., 2009) and numerical model (Tarasov and Peltier, 2005) between 13 and 12.7 cal ka BP and may have played a role in the slowdown of the Atlantic

meridional overturning circulation at the onset of the Younger Drays (Condron and Winsor, 2012). Overall, our results support the hypothesis that large meltwater and iceberg discharges from the Lake Agassiz outburst and Amundsen Gulf ice stream were more likely to have triggered the Younger Dryas cooling by inhibited deep water formation in the subpolar North Atlantic and weakened the strength of the Atlantic Meridional Overturning Circulation (Condron and Winsor, 2012; Hillaire-Marcel et al., 2013; Lakeman et al., 2018; Maccali et al., 2013; Not and Hillaire-Marcel, 2012; Tarasov and Peltier, 2005).

In core 02PC, the high quartz/total feldspars and phyllosilicates/total feldspars ratios observed during the Younger Dryas interval suggest that the detrital sediments mainly originated from the northern tributaries of the Mackenzie River (Figs. 37-39A). Wickert (2016) suggested that meltwater inputs to the Mackenzie River ended no later than 11 cal ka BP, when its eastern tributaries were temporarily rerouted eastward due to a combination of ice retreat and glacial isostatic depression. The age of 11 cal ka BP coincides with the decrease of the sedimentation rates from 50 cm.ka^{-1} to 2 cm.ka^{-1} (Fig. 42). In addition, the low foraminifera abundance and high terrestrial organic matter content observed in the nearby core 750PC (Scott et al., 2009) also suggest higher Mackenzie River discharge to the Canadian Beaufort margin during this time, providing support to our interpretations. Finally, in agreement with Stokes et al. (2005, 2006, 2009) and Dyke and Savelle (2000), we suggest that the IRD1A layers dated at 11 cal ka BP may be linked to a retreat phase of the Amundsen Gulf Ice Stream occurring during the Meltwater pulse 1B (Fig. 39B).

Chukchi-Alaskan margin

The overall mineralogical and geochemical signatures characterizing core 05JPC around 11 cal ka BP point to a detrital input from the Bering Strait and Eurasian margin (~30 % each; Fig. 38G). However, the increase of vermiculite and mixed-layer chlorite/smectite recorded in the clay fraction in this interval together with lower log(EM1/EM2) ratio suggest that most of the sediments are mainly derived from the Bering Strait and redistributed by bottom (nepheloid) currents to the shelf and continental slope (Figs. 40-44). In addition, amorphous silica

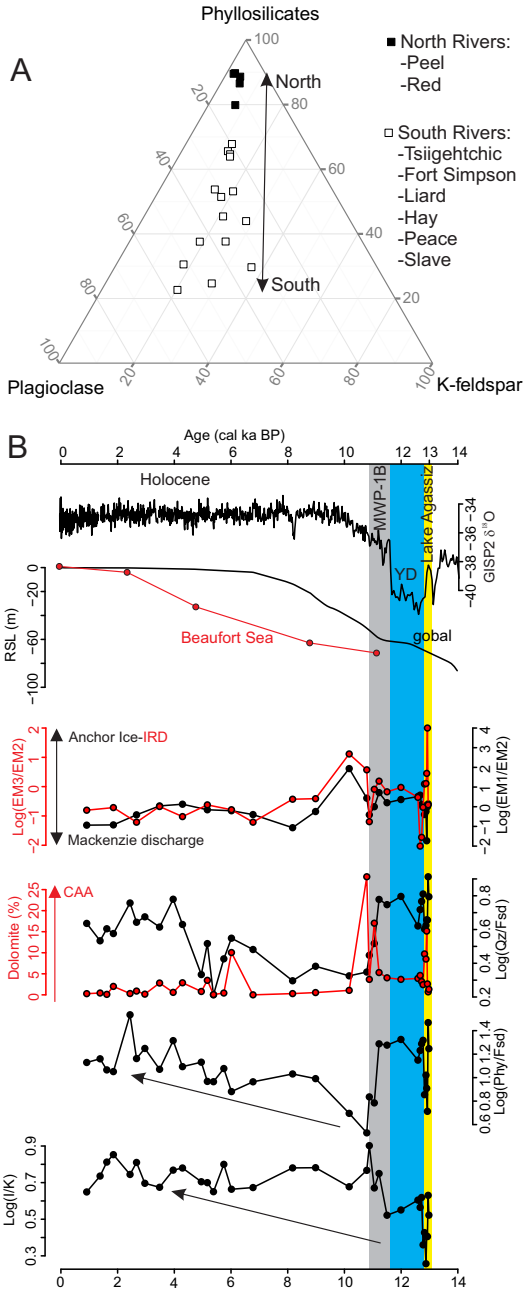

Figure 39: (A) Phyllosilicates-plagioclase-K-feldspar ternary plot of sand samples from the main tributaries of the Mackenzie River (Gamboa, 2017). Note that the northern tributaries are enriched in phyllosilicates while the southern tributaries are enriched in total feldspars. (B) Comparison of log(EM3/EM2), log(EM1/EM2), log(Qz/Fsd), dolomite content, log(Phy/Fsd) and log(I/K) from core 02PC with global eustatic sea level variations (Lambeck et al., 2014) and relative sea level from the Beaufort Sea (Héquette et al., 1995).

concentrations, derived from qXRD analysis also depict a sharp increase (up to 25 %) in the same interval (Fig. 40). High amorphous silica concentrations in the Chukchi Sea sediments are interpreted to represent times when biosilica-rich Pacific waters flowed through the Bering Strait (Jakobsson et al., 2017). Indeed, the presence of amorphous silica, including diatoms, radiolarians, siliceous sponges and silicoflagellates, is a characteristic signature of Pacific waters today, and therefore, this proxy may also be used to track Pacific waters inflow in the western Arctic Ocean (Jakobsson et al., 2017; Stein et al., 2017). Thus,we hypothesize that sediments in this interval may be related to the initial opening of the Bering Strait at ~11 cal ka BP (Jakobsson et al., 2017).

SedUnMixMC results from core 05JPC suggest that the fine-grained quartz and Zr-rich IRD layers and dolomite-rich (Ca-Mg) IRD layers originate from the Northwest Alaska and the Canadian Arctic Archipelago, respectively (Fig. 38H). The quartz and Zr-rich, but carbonate-poor sediment record at ~10.6 cal ka BP (IRD1B) is more consistent with a northwestern Alaskan source (Polyak et al., 2007). Indeed, high-resolution seismic reflection data in conjunction with sedimentological data from piston cores from the outer Chukchi margin are evidence of the occurrence of iceberg and meltwater discharge from the Brooks Range to the shelf occurring between 10 and 13 cal ka BP (Hill and Driscoll, 2008, 2010). At the opposite, the carbonate rich layers dated at 9.5 cal ka BP is more consistent with the Canadian Archipelago source. We infer that the dolomite-rich IRD (IRD1A) layer at 9.5 cal ka BP may be related to the final retreat phase of the Amundsen Gulf Ice Stream which ceased operating by ~9.5 cal ka BP (Stokes et al., 2009). However, this carbonate rich layer is missing in the Canadian Beaufort margin, as such layer was not identified in core 02PC at this time (Fig. 38). A plausible explanation for this could be the presence of a hiatus in the early to middle Holocene transition (Fig. 42). This observation is supported by the fact that sedimentation rates in core 02PC show a distinct decrease from 50 $cm.ka^{-1}$ to 2 $cm.ka^{-1}$ between 6 and 11 cal ka BP, which appears very large and abrupt. However, the accumulation is thought to have been continuous because of the lack of sharp lithological changes or sedimentological indicators of hiatus or mass flow transport in this part of the core (Deschamps et al., 2018b).

In addition, this abrupt decrease in sedimentation rates is consistent with major reduction of meltwater flow derived from the Mackenzie River (Wickert, 2016). Alternatively, as ages after 8.5-9 cal ka BP in core 05JPC were extrapolated, and the IRD1A in cores 05JPC and 02PC show similar mineralogical and geochemical signatures which are consistent with a common source area (Fig. 35). We thus hypothesize that the dolomite-rich IRD1A in core 05JPC could be dated at 11 cal ka BP similar to IRD1A from core 02PC (Fig. 42). This IRD correlation would imply that the age for the opening of the Bering Strait may be older than 11 cal ka BP (Jakobsson et al., 2017) as previously suggested by Keigwin et al. (2006) and England and Furze (2008). Further investigations are required to gain a more precise chronology of the age constraint for the Bering Land Bridge flooding.

2.7.2 Holocene sediment dynamics (10.5 cal ka BP to present)

Canadian Beaufort Sea

In the Canadian Beaufort margin, the log(EM1/EM2) ratio from the core 02PC showed few variations upwards from 10 cal ka BP to present, supporting the idea that stable sedimentation dynamics predominate through the Holocene (Fig. 39B). Likewise, the sediment unmixing model suggests that Holocene detrital sediments are derived primarily from the Mackenzie River (> 80 %; Figs. 39H-41). However, the slight changes observed in bulk and clay mineralogical signatures during the mid-Holocene relative to the deglacial interval (i.e., relatively enriched in total feldspars and illite; Fig. 39B), may reflect changes in sediment provenance within the Mackenzie River basin. Indeed, the watershed lithology of the main Mackenzie River tributaries is composed of a mixture between shale and igneous rocks having granodioritic to granitic compositions (Dellinger et al., 2017; Millot et al., 2003). More specifically, the northern tributaries of the Mackenzie River (such as the Peel and Red Rivers) drain almost exclusively weathered marine sedimentary rocks (e.g., Cambrian to Cretaceous limestones and shales), which are enriched in phyllosilicates, quartz, and detrital carbonates, whereas granitic source rocks outcropping in the North American Cordillera (including the

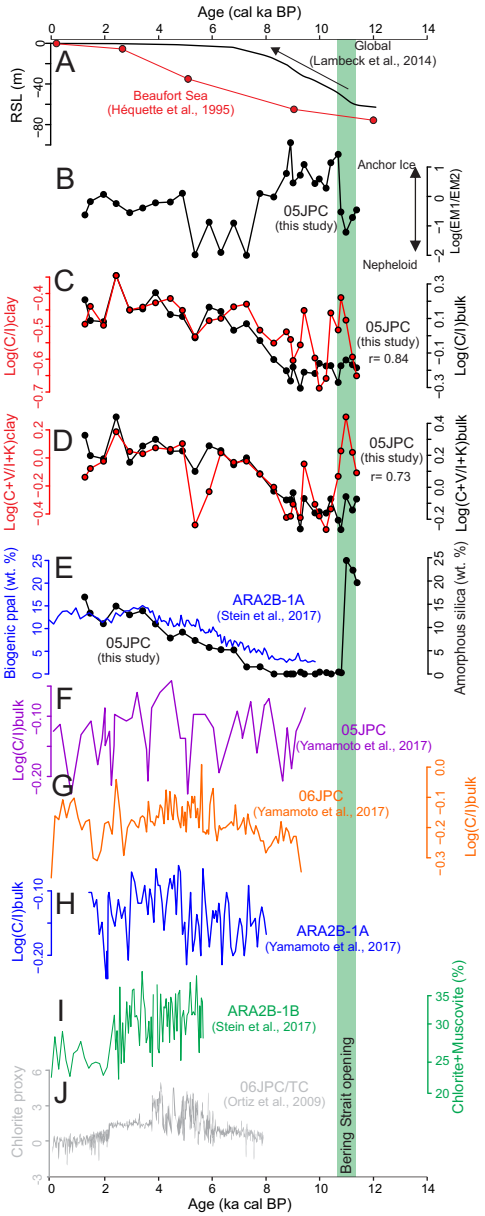

Figure 40: Comparison of (A) global eustatic sea level changes and relative sea level variation in the Beaufort Sea, (B) log(EM1/EM2) for cores 05JPC, (C) log-ratio chlorite/illite based on bulk (black) and clay mineralogy (red) from core 05JPC, (D) log-ratio chlorite+vermiculite/illite+kaolinite based on bulk (black) and clay mineralogy (red) from core 05JPC, (E) amorphous silica from core 05JPC (black) and biogenic opal for the core ARA2B-1A (blue), (F) log-ratio chlorite/illite derived of the bulk mineralogy from core 05JPC, (G) log-ratio chlorite/illite of the bulk mineralogy from core 06JPC, (H) log-ratio chlorite/illite of the bulk mineralogy from core ARA2B-1A, (I) chlorite+muscovite contents from core ARA2B-1B, and (J) chlorite proxy obtained by diffusive spectral reflectance analysis from cores 06JPC/TC. Enhanced Bering Strait inflow is highlighted in gray and opening of the Bering Strait is highlighted in light green.

Rocky and the Mackenzie Mountains) and Canadian Shield are drained by the southern tributaries (such as the Liard and Slave Rivers), which are characterized by an abundance of total feldspars (Gamboa, 2017; Fig. 39A). All these observations suggest that the proportion of sediment derived by the southern tributaries increased during the mid-Holocene. Thus, we hypothesized that the final recession of the LIS in the Mackenzie Valley after ~11-10.5 cal ka BP (Dyke, 2004) promoted a major remobilization of glaciogenic sediments derived from crystalline rocks as the Mackenzie River adjusted to the postglacial hydrologic regime. Alternatively, we cannot rule out the possibility that Holocene changes in relative sea level could also influence sedimentation in the Canadian Beaufort margin. The sea level rise resulted in coastal retreat and likely exerted significant control on the sedimentation on the Mackenzie Shelf during the early- to mid-Holocene (Deschamps et al., 2018b; Héquette et al., 1995). We thus hypothesize that a minor proportion of fine silt detrital sediments in core 02PC during the mid-Holocene may have also been supplied from sea level rise-induced coastal erosion of fine-grained Pleistocene quartz- and feldspar-rich glacial tills outcropping along the Tuktoyaktuk Peninsula (Gamboa et al., 2017; Vogt, 1997; Fig. 39B). However, sediments from the southern Mackenzie River tributaries and Tuktoyaktuk Peninsula are both characterized by similar mineralogical signatures (Gamboa, 2017), and therefore, we cannot estimate the proportion of sediment derived from coastal erosion. Additional information could be gained by consideration of other provenance indicators such as radiogenic isotopes (Fagel et al., 2014).

Chukchi-Alaskan margin

SedUnMixMC modelling and the mineralogical ratios log(I+K/C+V) and log(Qz/Fsp) from core 05JPC indicate that during the early Holocene (10.5–8 cal ka BP), the predominant sediment source on the Chukchi-Alaskan margin was from the Mackenzie River (up to 92 %). In addition, log(EM1/EM2) ratios revealed the dominance of clay- to fine silts-sized particles during the early Holocene, suggesting that sediment transport by sea ice predominates at this time (Figs. 38h-40B). In accordance with previous sedimentological studies (Darby et al., 2012; Not and Hillaire-Marcel, 2012; Yamamoto et al., 2017), we hypothesize

that sediment-laden meltwater plumes derived from glacial erosion on the Mackenzie River basin were incorporated on the shelf by sea ice. Sea ice was thus transported westwards along the Chukchi-Alaskan margin by an enhanced BG during the early Holocene (Fig. 41). Note that the BG strengthening during the early Holocene is likely driven by a maximum boreal summer insolation (Gajewski, 2015; Yamamoto et al., 2017).

During the Holocene, the log(EM1/EM2) ratio reached minimum values between 8 and 6 cal ka BP, suggesting that sediment transport during the mid-Holocene was dominated by bottom currents (Fig. 40B). In addition, the end-member EM3 (10 to 30 μm) records from both margins during the deglacial interval are clearly associated with the IRD events (Fig. 34B). However, this end-member is still present during the Holocene interval for cores located in the Chukchi-Alaskan margin (01JPC and 05JPC), while it did not influence the Holocene sedimentation in the Canadian Beaufort shelf (Fig. 34B). In agreement with previous late Quaternary sedimentological and geochemical studies from the western Arctic (Darby et al., 2009), we hypothesize that end-member EM3 recorded in the Holocene sediments from the Chukchi-Alaskan margin may reflect suspended load and winnowed silts deposited by down-welling of brine-enriched shelf waters. Moreover, the SedUnMixMC modelling reveals that sediment provenance in core 05JPC was mainly derived from the Bering Strait, Mackenzie River and Eurasian margin (Figs. 38G-H). The proportion of sediment derived from the Mackenzie River gradually decreases up-core (60 to 30 %), whereas the Bering Strait and Eurasian margin sources show a long-term increase (10 to 60 % and 0 to 30 %; Figs. 38I-J). Indeed, decreases of quartz, kaolinite, illite, aluminum and potassium contents most likely reflect a decline in sediment inputs from the Mackenzie River (Fig. 38), while an increase of total feldspars, chlorite, muscovite, and vermiculite, as well as magnesium and iron contents in the clay fraction reflect higher Bering Strait sediment inputs (Figs. 38D-E, 44). Thus, the Holocene variations observed in the detrital proxies from core 05JPC are likely related to a long-term decline in both the Mackenzie River discharge (Wagner et al., 2011) and anchor ice transported by weaker BG (Yamamoto et al., 2017). In addition, the increased proportion of sediment coming from the Kara Sea observed in core 05JPC between 4 and 2 cal ka BP

(15-30 %; Fig. 38G) suggests that a strong positive mode of the AO was predominant at this time (Darby et al., 2012). In fact, based on iron oxide grain provenance on the Chukchi shelf and slope sediments, Darby and Bischof (2004) and Darby et al. (2012) suggested a weaker BG during the late Holocene, which also occurs today during the positive phase of the AO (Fig. 41) in agreement with our interpretations.

As shown in Figs. 38A-B-G and Figs 40C-D, the proportion of chlorite, vermiculite, total feldspars, amorphous silica and sediments derived from the Bering Strait showed a gradual increase between 10 and 2 cal ka BP, with maximum values recorded between 7.5 and 2 cal ka BP, suggesting an enhanced increase in the Bearing Strait inflow into the Chukchi Sea. This increased Bearing Strait inflow trend shows a parallel temporal evolution with regional sea level variations and increasing bottom current redistribution (Figs 34-40). In agreement with Keigwin et al. (2006), we hypothesize that the progressive and rapid relative sea-level rise observed during 10 and 7.5 cal ka BP in the western Arctic Ocean not only promoted the widening and deepening of the Bering Strait, but also the subsequent remobilization of sediments stored on the Chukchi Shelf and the enhanced sediment transport from the Pacific towards the western Arctic Ocean (Fig. 41). Our findings are consistent with palynological (dinocyt, pollen and spores) and organic matter geochemistry data from the same sediment core (Faux et al., 2011; Khim, 2003; McKay et al., 2008; Polyak et al., 2016), indicating that full marine continental shelf setting was established in the Chukchi-Alaskan margin between 7 and 8 cal ka BP. Overall, these observations suggest that regional sea level variations have exerted a significant control on sedimentation in the western Arctic Ocean during the early- to mid-Holocene.

As a whole, although the variations in the previously published mineralogical proxy records of the Bearing Strait inflow are not identical among the different sediment cores from the Chukchi Sea (Figs. 40E-I), there is a common enhancement in the Bering Strait inflow between 7.5 and 2 cal ka BP, followed by a decrease during the last 2 cal ka BP (Ortiz et al., 2009; Stein et al., 2017; Yamamoto et al., 2017). Holocene changes in the Bering

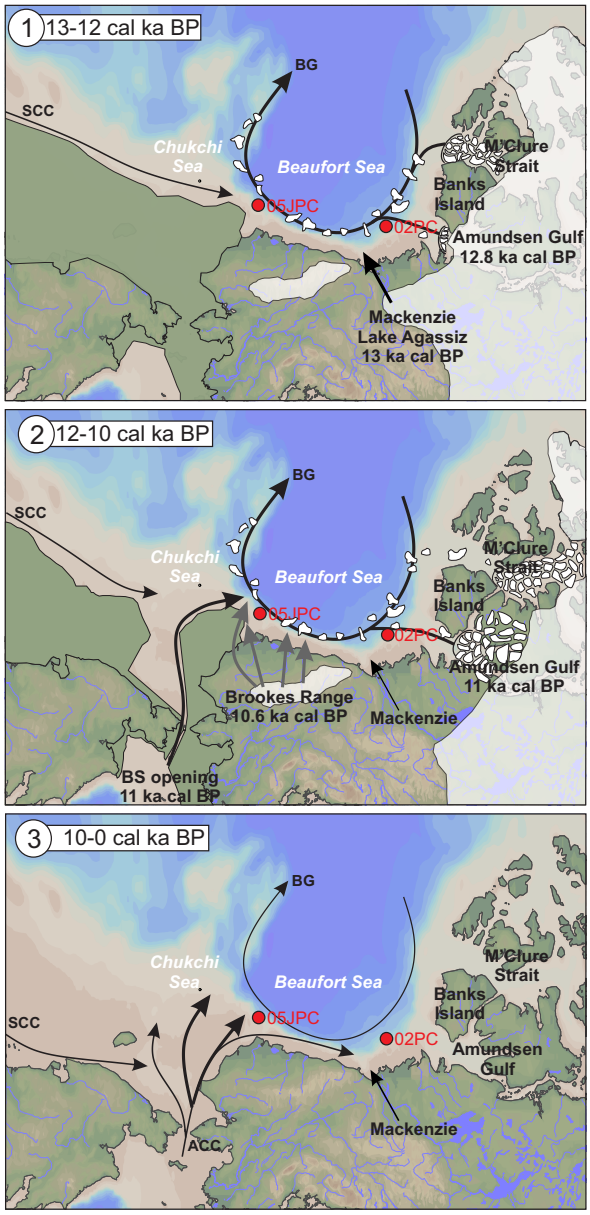

Figure 41: Evolution of sedimentary dynamics in the western Arctic Ocean during the last 13 cal ka BP.

Strait inflow have been attributed to changes in the Aleutian Low pressure system, which is located in the North Pacific (Yamamoto et al., 2017). This Aleutian Low is sensitive to tropical Pacific sea surface temperature (SST) anomalies (Anderson et al., 2016; Trenberth and Hurrell, 1994). In general, warm eastern Pacific SST conditions are characterized by a stronger and southeastward-shifted Aleutian Low, while cool eastern Pacific SST conditions

are associated with a weaker and northwestward-shifted Aleutian Low. In this context, the Holocene paleoenvironmental records across eastern Beringia (Alaska, westernmost Canada and adjacent seas) suggest that the Aleutian Low was weaker during the middle Holocene than during the late Holocene (Barron and Anderson, 2011). This configuration is thought to promote a major Bering Strait inflow into the Chukchi Sea during the middle Holocene and a weak inflow during the late Holocene. Finally, as discussed in Darby and Bischof (2004) and Yamamoto et al. (2017), sediments transported by the inflowing Pacific waters into the Bering Strait might be diverted west towards Herald Canyon by the western Bering Sea branches, and thus missing the Chukchi-Alaskan margin (Yamamoto et al., 2017). This redistribution of the Bering Strait inflow between the different current branches may be a plausible explanation for the spatial and temporal differences observed between the Pacific inflow proxies from the Chukchi Sea cores (Fig. 40).

2.8 Summary and conclusions

Geochemical and mineralogical compositions of two sediment cores recovered on the Canadian Beaufort (core 02PC) and Chukchi-Alaskan (core 05JPC) margins highlight the evolution of the origin, transport, and dynamics of the detrital sediments in the western Arctic Ocean since deglaciation. Overall, the results of this research yield the following generalizations and conclusions:

1. The end-member modelling analysis of grain-size data indicate that sea ice and nepheloid current are factors controlling sediment redistribution in the Chukchi-Alaskan margin, whereas sea ice and the Mackenzie River sediment plume influenced sedimentation in the Canadian Beaufort margin.

2. The mineralogical and geochemical data from the bulk and clay fractions corroborate that log(I+K/C+V), log(Qz/Fsp), dolomite, log(Ca/Al), log(Mg/Al), and log(Fe/Al), together with a discriminant diagram based on Al-Si-Ca and I+K-total feldspars-dolomite, can be suc-

cessfully used to track changes in detrital sediment provenance on the Chukchi and Beaufort continental margins.

3. The sediment unmixing model, together with specific mineralogical and geochemical signatures, indicates that the North American margin (including the Mackenzie River, Northern Alaska and Canadian Arctic Archipelago) is the major source of sediment during the deglaciation at the coring sites of cores 05JPC and 02PC.

4. The dolomite-rich IRD layers dated to 12.8 cal ka BP and 11 cal ka BP in core 02PC and 9.5 cal ka BP in core 05JPC are related to the debacle of the M'Clure and Amundsen Ice Streams. The quartz and feldspar-rich IRD intervals dated to 13 cal ka BP in core 02PC and 10.7 cal ka BP in core 05JPC are likely related to meltwater events, and are derived from the Mackenzie River and the Brooks Range glaciers in the northwestern Alaska, respectively.

5. Mineralogical and geochemical signatures of deglacial sediments from core 02PC support the hypothesis that large meltwater and iceberg discharges from the Lake Agassiz outburst through the Mackenzie Valley may have triggered the Younger Dryas cooling.

6. During the Holocene, the detrital sediment supply in the Canadian Beaufort margin remains controlled mainly by the Mackenzie River. In the Chukchi margin, the proportion of sediment derived from the Mackenzie River gradually decreased during the early to late Holocene.

7. The opening of the Bering Strait at 11 cal ka BP is typified in core 05JPC by a sharp increase in vermiculite, mixed-layer chlorite/smectite and amorphous silica. In addition, bulk mineralogical data, together with high log(Mg/Al) and log(Fe/Al) ratios from the clay fraction, supports the notion that an enhanced Bearing Strait inflow into the Chukchi Sea occurred between 7.5 to 2 cal ka BP.

8. The similar trends observed between the regional sea-level curves and our mineralogical and geochemical data suggest that the relative sea-level changes in the western Arc-

tic Ocean have an important influence on the western Arctic sedimentary dynamics during the early to mid-Holocene.

2.9 Acknowledgments

We sincerely thank the captains, officers, crew and scientists on board the USCGC Healy and the CCGS Amundsen for the recovery the cores used in this study. These cores were collected as part of the HOTRAX expedition (USCGC Healy), as well as the CASES and ArcticNet (CCGS Amundsen) programs. We also thank Quentin Beauvais (UQAR-ISMER), Mathieu Babin (UQAR-ISMER), and Adriana Gamboa (UQAR-ISMER and UDO) for their technical support and advice in the laboratory. This research was funded ArcticNet and by the Natural Sciences and Engineering Research Council of Canada (NSERC) through Discovery Grants to J.-C. Montero-Serrano and G. St-Onge, as well as through ship time support for several expeditions (J.-C. Montero-Serrano and G. St-Onge).

2.10 Supporting information

2.10.1 Age model

Contemporaneous IRD peaks have been identified in magnetic susceptibility profiles in cores from the Canadian Beaufort Sea. We then used the correlation between the magnetic susceptibility profiles of cores 56PC (Lakeman et al., 2018), 750PC (Scott et al., 2009) and 02PC (Deschamps et al., 2018b) in order to transfer 6 radiocarbon ages to core 02PC (Fig. 42). However, most available ΔR values for the Arctic are derived in regions south of 81°N using mollusks found in coastal regions (Coulthard et al., 2010; McNeely et al., 2006). Furthermore, reduced entry of Atlantic waters to the Arctic Ocean during marine isotope stage 2 (MIS2) with thick multi-year sea ice has resulted in depleted ^{14}C inputs and therefore a greater reservoir age in the Arctic Ocean waters (Hanslik et al., 2010). Thus, based

on numerical simulations of oceanic radiocarbon since the last glacial interval (Butzin et al., 2005), Hanslik et al. (2010) used marine reservoir ages of 400 years (ΔR = 0), 700 years (ΔR = 300), 1050 years (ΔR = 650), and 1400 years (ΔR = 1000) to observe the better fit between foraminiferal abundance and the Younger Drays period in sediment cores located on the Lomonosov Ridge. Their results suggest that better environmental interpretations are obtains by using a regional reservoir age of 700 years (ΔR = 300) for the Holocene and 1400 years (ΔR = 1000) for the Late glacial. Thus, as suggested in Hanslik et al. (2010) and other Late Quaternary paleoenvironmental studies from Arctic (Coulthard et al., 2010; Not and Hillaire-Marcel, 2012; Hillaire-Marcel et al., 2013), we applied a ΔR= 335±85 for the Holocene interval and a ΔR= 1000 for the deglacial interval to construct the age model of core 02PC (Fig. 42, Table 5). Finally, we used a Bayesian approach to estimate the best fit or weighted mean age for each depth with a 95 % confidence interval with the R software package BACON (Blaauw and Christen, 2011).

2.10.2 Sediment unmixing model

As suggested by Andrews and Eberl (2012), we prepared a series of known mixtures similar to the Arctic source areas to demonstrate the degree to which we could differentiate between them using SedUnMixMC. Pulverized granite, limestone, shale and Fe-rich glacial till end-members from Eastern Canada were as follows: (1) mixed in varying known proportions, (2) processed for qXRD, and (3) estimates of the end-member fractions were calculated using SedUnMixMC. The results (Fig. 47) showed a reasonable agreement between the known percentage of the four source mixtures and the estimated fractions ($r > 0.92$ and $p < 0.0001$), thus validating the use of this sediment provenance approach.

2.10.3 Sediment unmixing model

Previous sedimentological studies (Astakhov et al., 2013; Darby et al., 2011; Dong et al., 2017; Fagel et al., 2014; Gamboa et al., 2017; Gordeev et al., 2004; Holemann et al., 1999; Rachold, 1999; Rachold et al., 1996; Stein et al., 2017; Viscosi-Shirley et al., 2003a,b; Vogt, 1997; Yamamoto et al., 2017) have synthesized the distribution of the main bulk and clay mineral assemblages, as well as some chemical elements in the modern sediments deposited on continental shelves and adjacent coasts that surround the Arctic Ocean (Table 5). The following is noteworthy: (1) very few published records are based on multi-elemental data (including major, minor, and trace elements), and (2) these studies have used different methodological approaches. Considering this, we performed a principal component analysis (PCA) of bulk mineralogical and elemental geochemical data available in the literature, together with our data, to observe the relative differences between the sediment composition in the potential source areas of the circum-Arctic and our sediment core (Fig. 48; Tables 6-7). Prior to PCA, a log-centered (clr) transform was applied to the dataset (Aitchison, 1990). PCA was conducted with "CoDaPack" software (Thió-Henestrosa and Martín-Fernández, 2005).

As shown in Figure 48, quartz-carbonates, illite, kaolinite and Al contents are dominant along the North American margin where Paleozoic-Mesozoic sedimentary rocks and Pleistocene glacial till outcrop (Darby et al., 2011; Dong et al., 2017; Gamboa et al., 2017; Naidu and Mowatt, 1983). Dolomite and Mg, Cr, and V are particularly enriched in the Canadian Arctic Archipelago (e.g., Banks and Victoria Islands), where Paleozoic-Mesozoic sedimentary rocks from the Sverdrup Basin and Tertiary-Quaternary glacial deposits are carbonate-rich (Gamboa et al., 2017; Phillips and Grantz, 2001). In addition, higher illite+kaolinite and chlorite contents have been found along the North American margin and Bering Strait, respectively. Indeed, sediments delivered by the Mackenzie River are enriched in illite and kaolinite and show a high K/C ratio than sediments from the Bering Strait (Naidu and Mowatt, 1983). The total feldspar, amphiboles, and smectite and Ti, Fe, and Ca are the dominant min-

erals and elements, respectively, in the Eurasian shelf sediments, where rivers drain large basaltic provinces (e.g., Putorana Plateau, Anabar massif, Verkhoyansk Fold Belt; Viscosi-Shirley et al., 2003a,b). In addition, sediment from the middle Chukchi Sea (including Herald Banks and Canyon) contains intermediate total feldspar contents, high illite content, substantial chlorite and less smectite and kaolinite compared to Eurasian sediments. This sediment also has the highest contents of Al, Fe, and Ca. Sediment inputs in this area originated mainly from the Anadyr River drainage basin where volcanic, granite and granodiorite rocks from the Okhotsh-Chutoka volcanic belt outcrop (Kobayashi et al., 2016). Likewise, sediments in the eastern Chukchi Sea are rich in quartz, feldspars, chlorite, muscovite, smectite, and vermiculite and are most likely derived from the Bering Sea coasts of Alaska (notably from the Yukon and Kuskokwim Rivers; Naidu and Mowatt, 1983) and the Aleutian arc. Suspended matter from these source regions are transported to the eastern Chukchi shelf by the Alaska Coastal Current (Eberl, 2004). Bering Strait inflow sediments are characterized by high contents of chlorite (Kobayashi et al., 2016; Ortiz et al., 2009; Stein et al., 2017; Yamamoto et al., 2017). In addition, the south Bering Strait sediments consist of mafic material enriched in vermiculite from the Aleutian Arc (Gardner et al., 1980). Furthermore, the boxplots of PC scores also confirms that geochemical and mineralogical signatures of cores 02PC (generally negative scores) and 05JPC (positive scores) are similar to the Mackenzie River/Canadian Arctic Archipelago and Bearing Strait/Chukchi Sea sediment composition, respectively (Figure 48, Table 7).

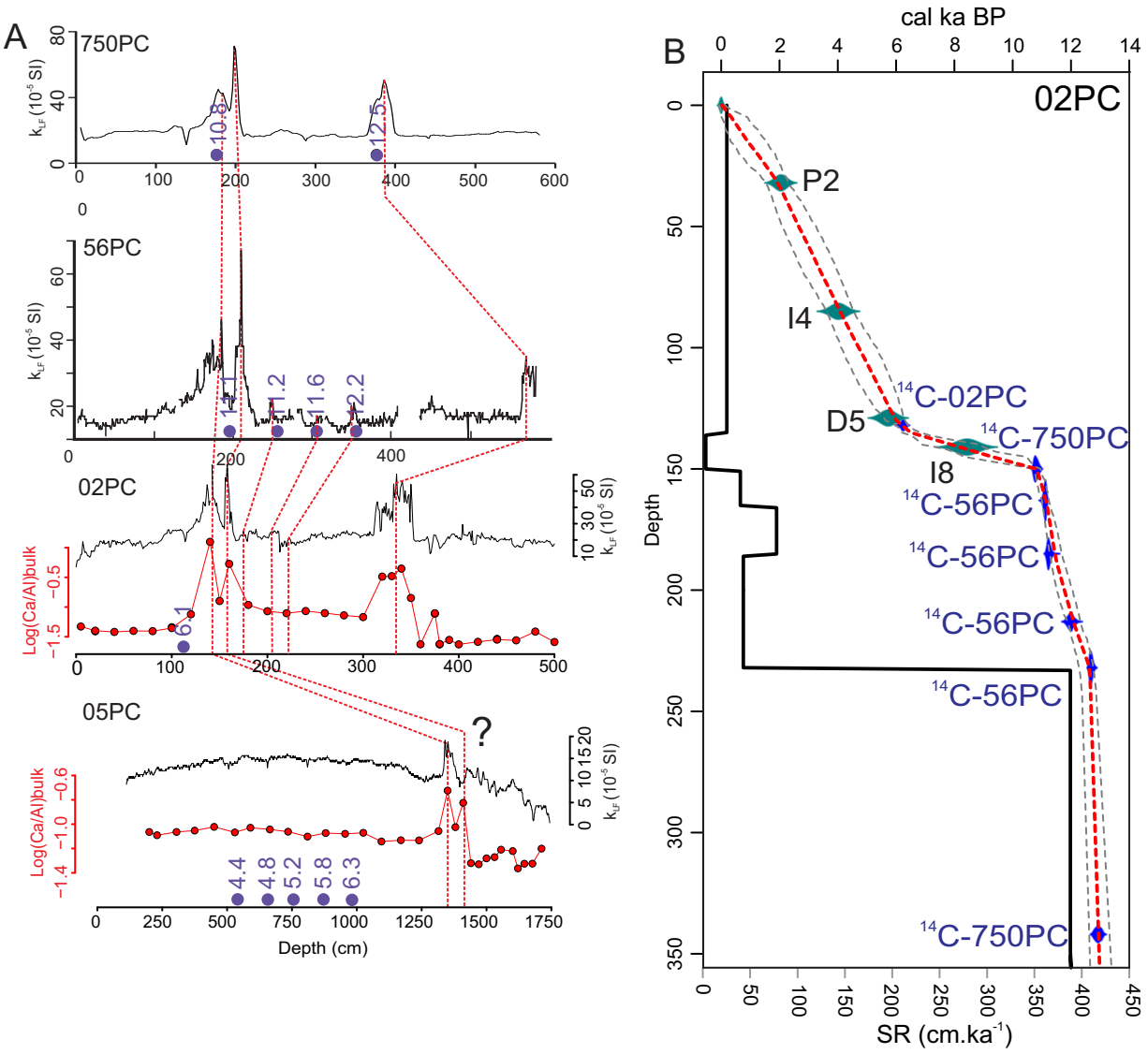

Figure 42: (A) Proposed correlations between cores 750PC (Scott et al., 2009), 56PC (Lakeman et al., 2018), 02PC (this study) from the Beaufort Sea as well as core 05JPC (this study) from the Chukchi Sea. (B) Age model and sedimentation rates of core 02PC based on the correlations in figure (A) and the paleomagnetic tie-points from Deschamps et al. (2018b).

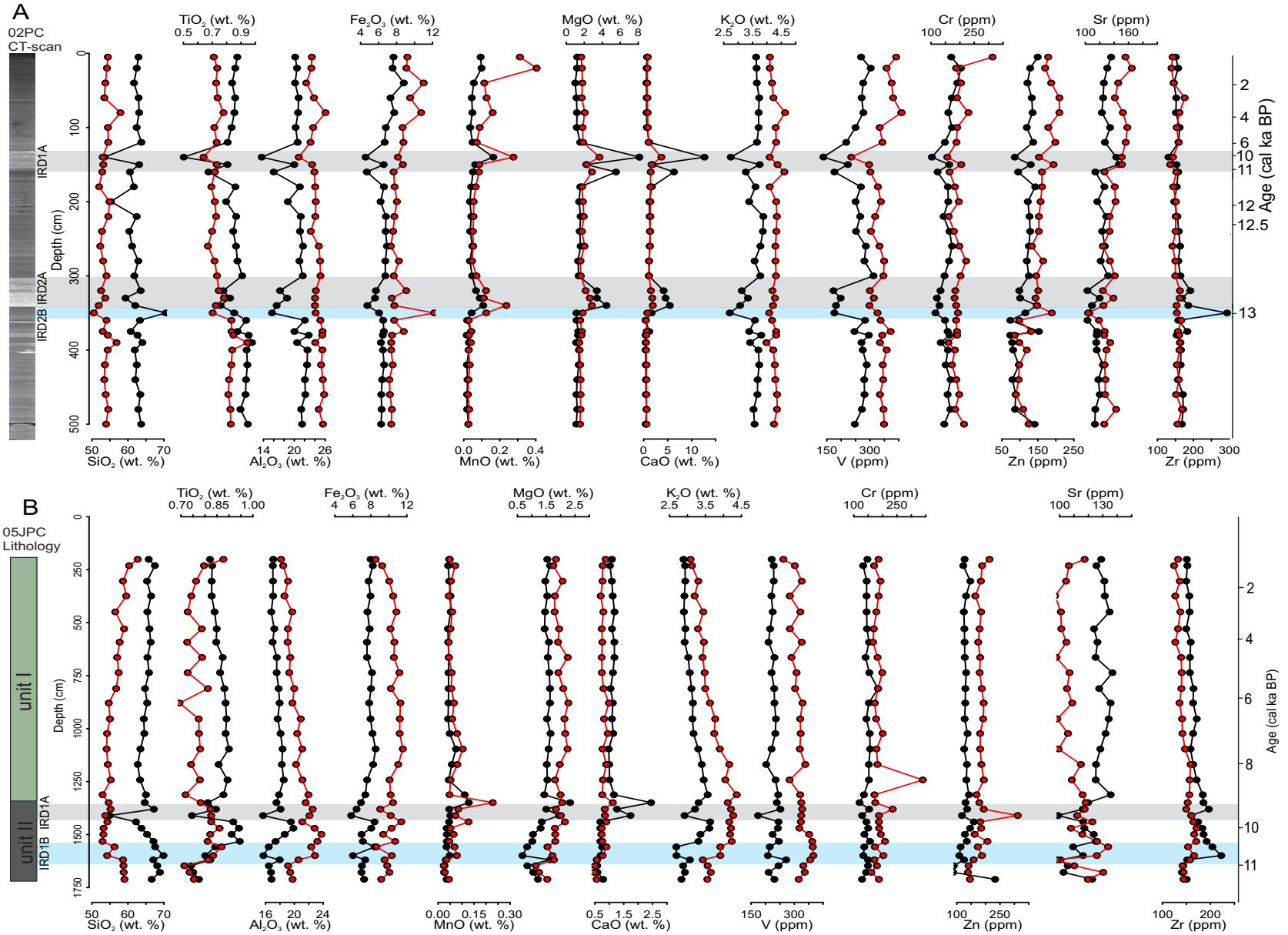

Figure 43: Downcore variations of the major-, minor-, and trace-elements measured on the bulk (square) and clay (diamond) fractions for cores (A) 02PC and (B) 05JPC. IRD layers rich in dolomite and quartz are highlighted in gray and blue, respectively.

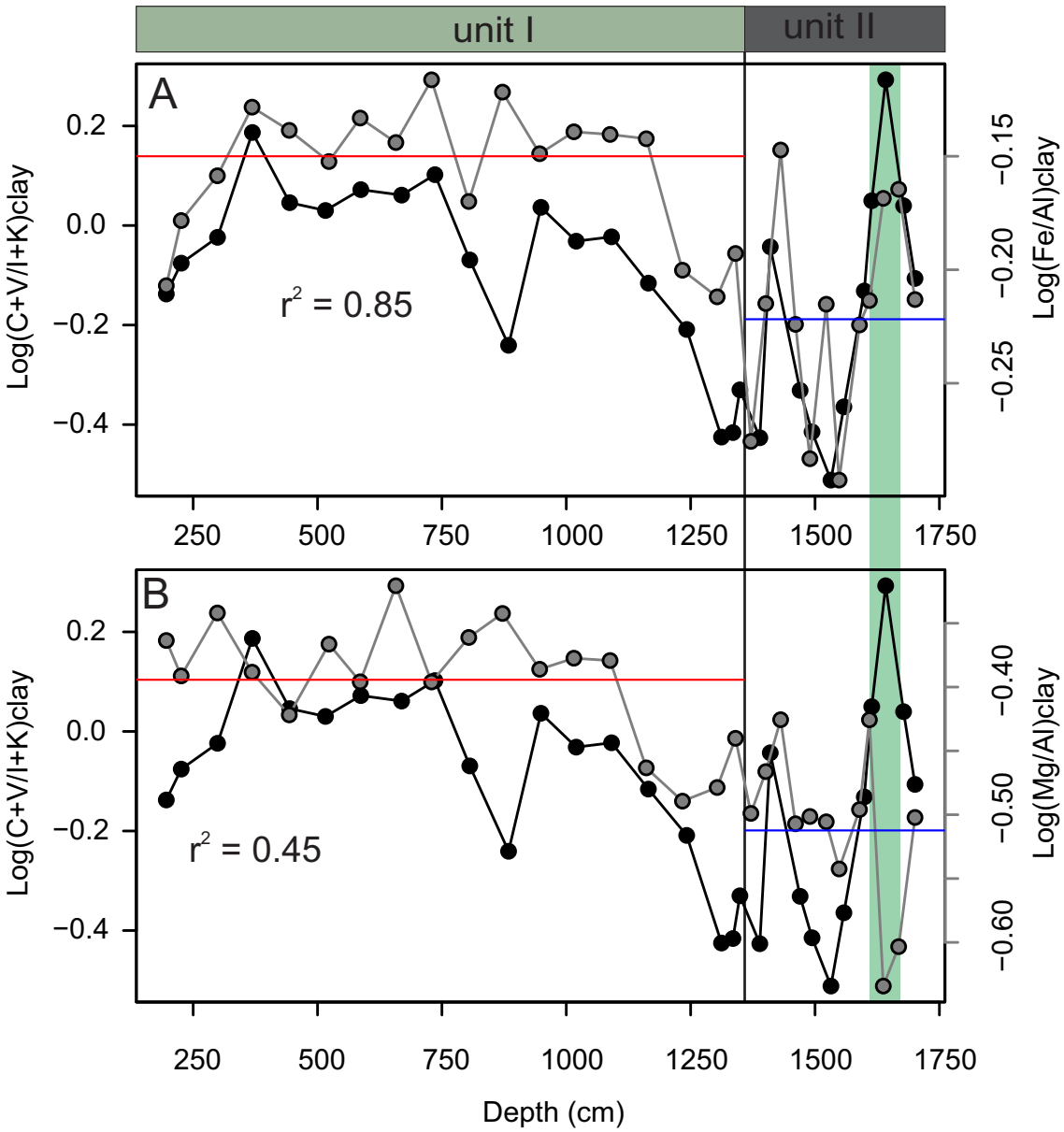

Figure 44: Relationship between (A) log-ratio chlorite+vermiculite/illite+kaolinite (black) and log-ratio Fe/Al (grey) and (B) log-ratio chlorite+vermiculite/illite+kaolinite (black) and log(Mg/Al) derived from the clay fraction of the core 05JPC. The correlation was performed using the software Analyseries (Paillard et al., 1996). Red and blue lines are the mean values for the log-ratio Fe/Al and log-ratio Mg/Al for Unit I and II respectively. The increase of Fe and Mg in unit I are significant ($p < 0.05$) based on a Student's t-test.

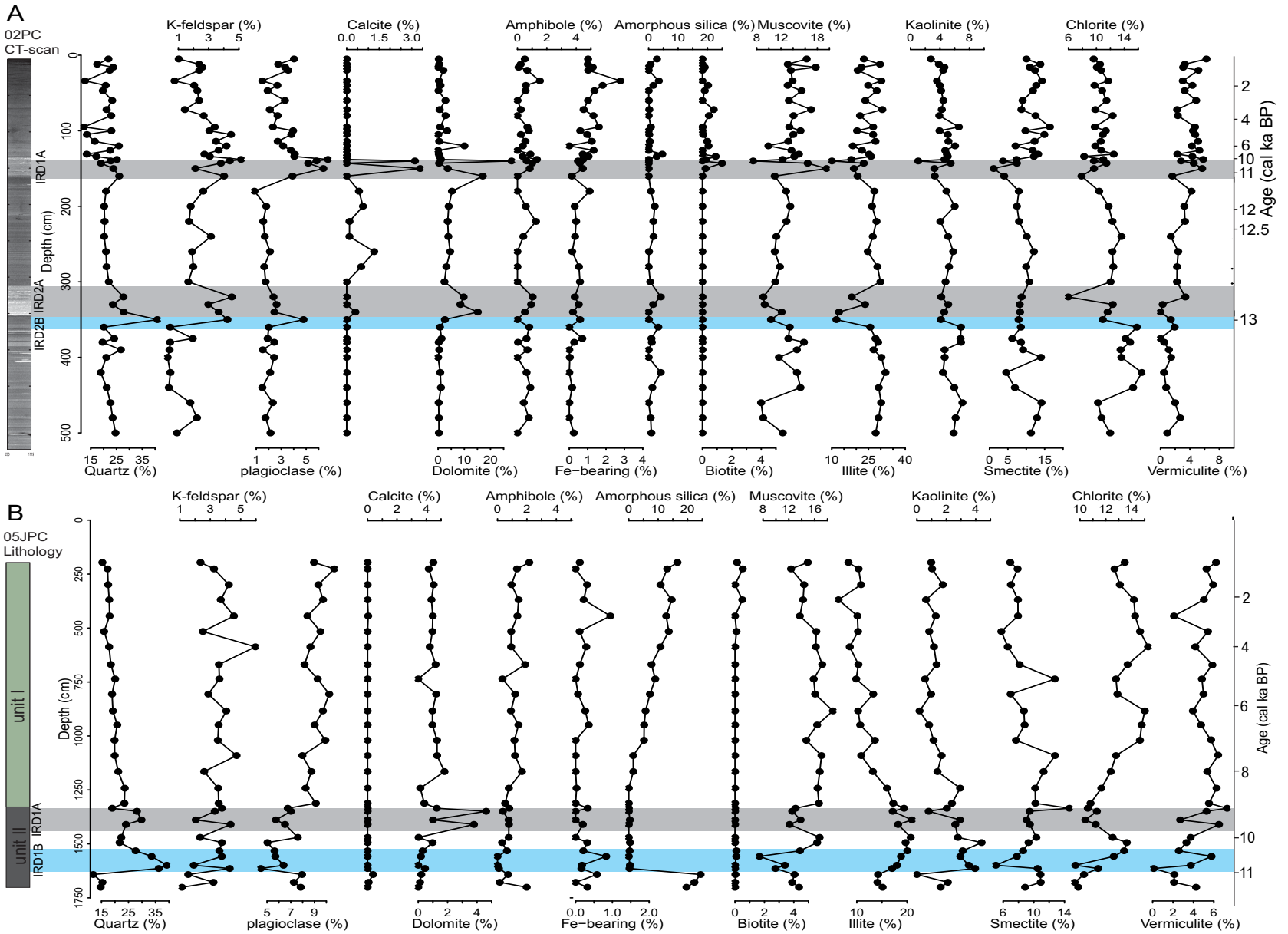

Figure 45: Downcore variations of the major mineralogical components determined for the cores (A) 02PC and (B) 05JPC. IRD layers rich in dolomite and quartz are highlighted in light and dark gray, respectively.

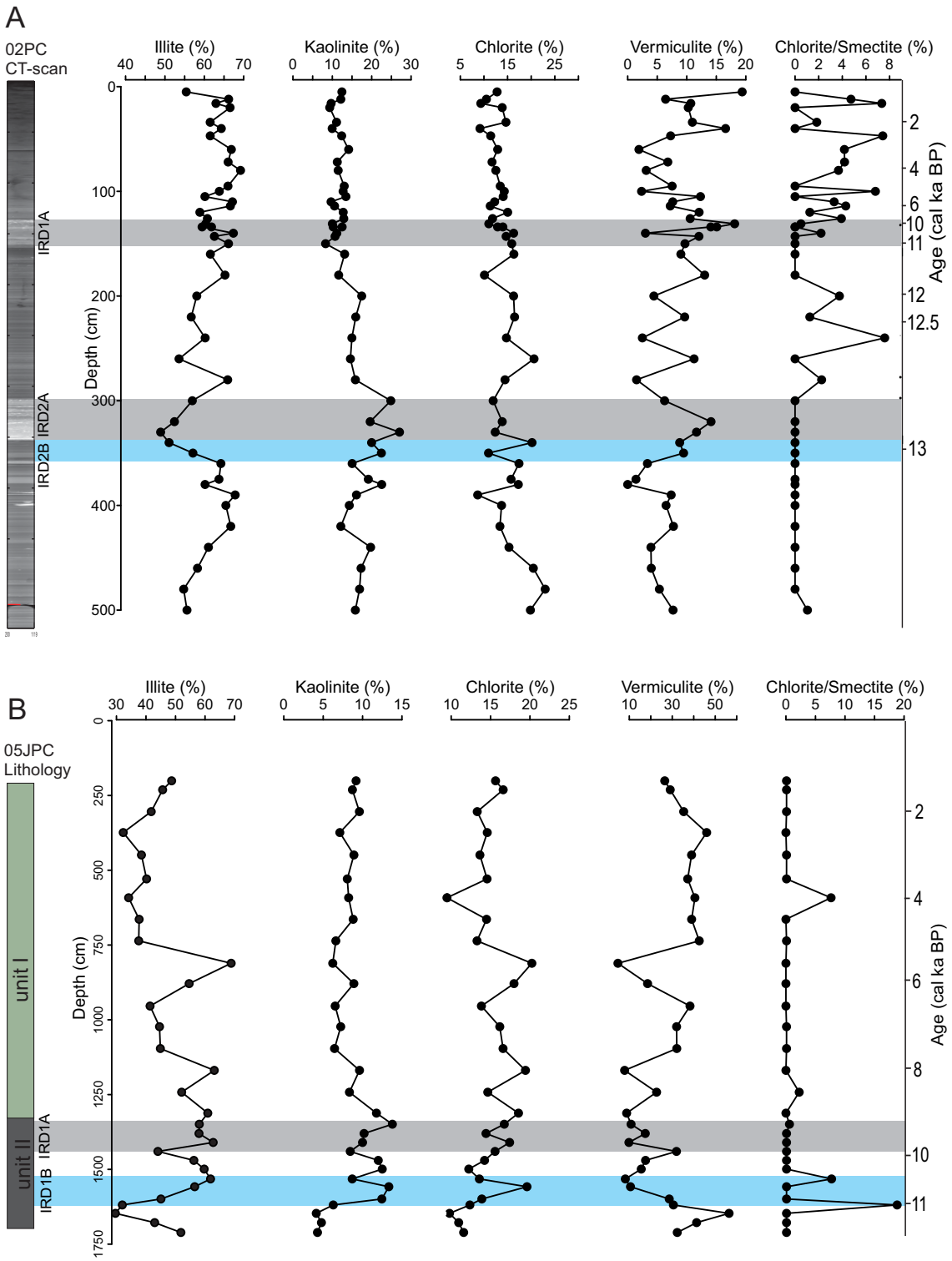

Figure 46: Downcore variations of the clay minerals assemblages identified in the cores (A) 05JPC and (B) 02PC. IRD layers rich in dolomite and quartz are highlighted in light and dark gray, respectively.

	Calculated (%)			
Mixed sample name	Source1	Source2	Source3	Source4
M1 - granite	100	0	0	0
M2	86	18	0	0
M3	68	7	14	0
M4	53	4	14	26
M5	68	0	27	9
M6	41	15	14	32
M7	12	4	8	79
M8	22	80	0	0
M9	11	54	24	22
M10 - shale	0	100	0	0
M11 - limestone	0	0	100	0
M12 - red sediment	0	0	0	100

	Measured (%)			
Mixed sample name	Source1	Source2	Source3	Source4
M1 - granite	100	0	0	0
M2	80	20	0	0
M3	69	10	10	11
M4	59	10	10	20
M5	59	0	20	21
M6	40	20	10	30
M7	10	5	5	79
M8	20	80	0	0
M9	0	39	21	40
M10 - shale	0	100	0	0
M11 - limestone	0	0	100	0
M12 - red sediment	0	0	0	100

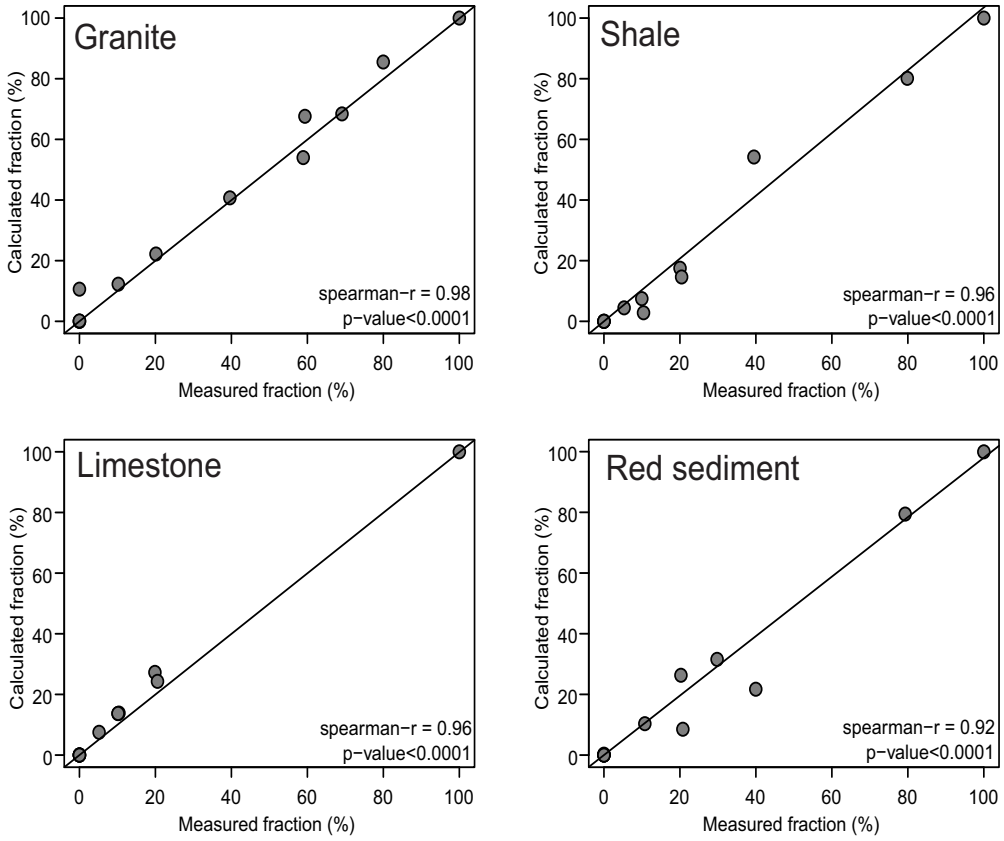

Figure 47: SedUnMixMC results of measured (known) and calculated (estimated) fractions of a series of mixed samples from 4 different sources bedrock and sediments. The samples used are granite from Canadian Shield, shale from the Appalachian Mountains, limestone from Quarry Island (Mingan Archipelago) and Fe-rich glacial till from SW Gulf of Saint Lawrence. The null hypothesis of no association between the known and calculated fractions is rejected at the $p<0.0001$ level ($r > 0.96$).

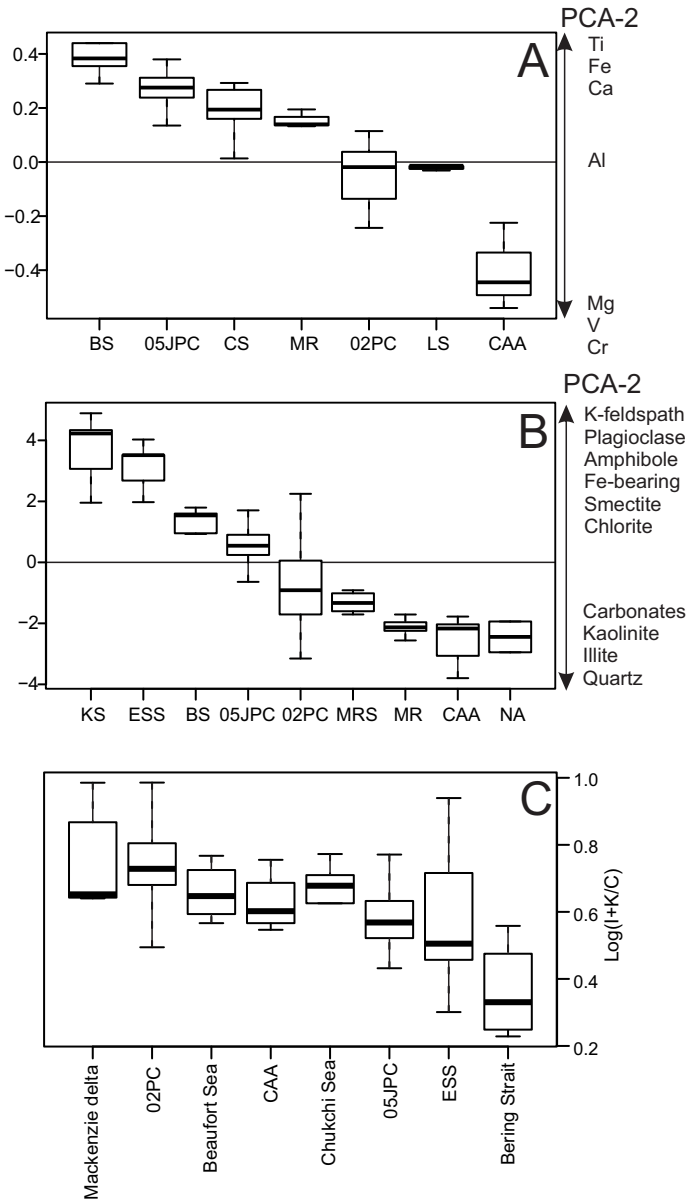

Figure 48: PC2 scores derived from (A) some major and minor elements and (B) bulk minerals of cores 02PC and 05JPC, as well as the circum-Arctic source areas. (C) Box-plot of the log-ratio I+K/C showing the relative composition of the sediment from cores 05JPC and 02PC, in comparison with some circum-Arctic sources (Beaufort Sea, Mackenzie Delta and CAA: Gamboa (2017), Chukchi Sea: Khim (2003), Bering Strait: Kalinenko (2001), Eastern Siberian Sea: Khim (2003) and Viscosi-Shirley et al. (2003a)).

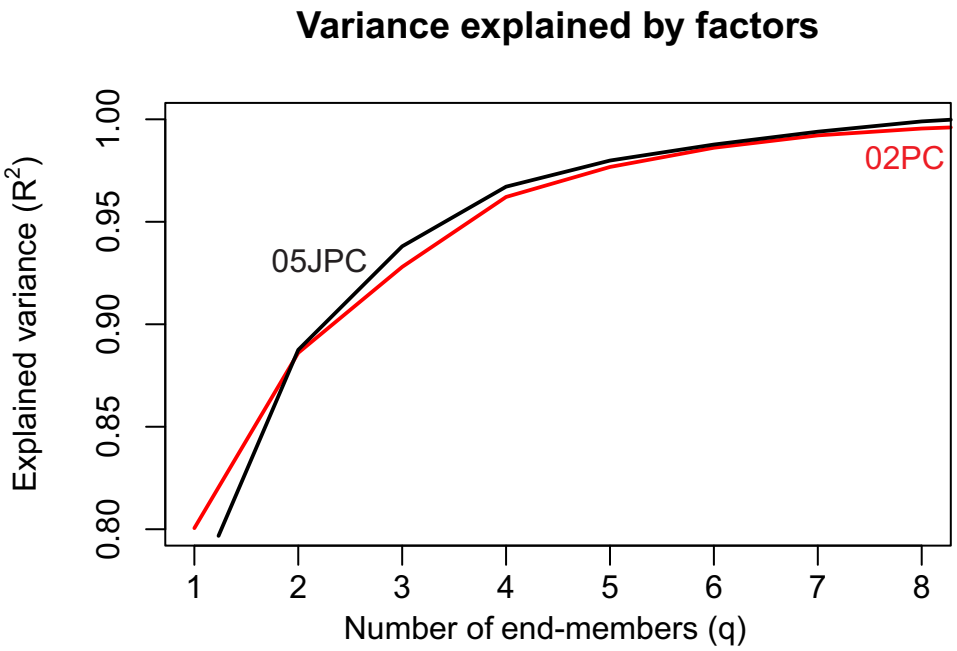

Figure 49: The explained cumulative variance as function of the number of potential end-members q for core 02PC (red) and core 05JPC (black).

Table 5: Conventional ^{14}C ages (half-life 5568 years) calibrated with Marine13 (Reimer et al., 2013) using Calib software (v7.1; http://calib.org/calib/) for core 18TC, 750PC, 56PC and 02PC for three different marine reservoir ages.

Core	Species	Depth (cm)	^{14}C age years BP	SD	$\Delta R=0$ (2σ) years BP	$\Delta R=335$ (2σ) years BP	$\Delta R=1000$ (2σ) years BP	Reference
18TC	N.pachyderma	15.2	10,240	100	11,260 (11,019-11,699)	10,865 (10,611-11,123)	10,025 (9,690-10,253)	Hanslik et al. (2010)
18TC	N.pachyderma	17.7	11,480	110	12,956 (12,709-13,192)	12,656 (12,460-12,887)	11,642 (11,239-12,036)	Hanslik et al. (2010)
18TC	N.pachyderma	21.7	11,890	120	13,353 (13,115-13,612)	13,027 (12,757-13,276)	12,365 (12,000-12,645)	Hanslik et al. (2010)
18TC	N.pachyderma	25.7	11,720	120	13,194 (12,913-13,426)	12,864 (12,642-13,120)	12,133 (11,658-12,562)	Hanslik et al. (2010)
18TC	N.pachyderma	27.7	12,535	110	14,027 (13,729-14,424)	13,654 (13,407-13,909)	13,009 (12,753-13,246)	Hanslik et al. (2010)
750PC	Mixed	170.5	10,865	30	12,412 (12,205-12,564)	11,779 (11,459-11,977)	10,803 (10,678-10,968)	Scott et al. (2009)
750PC	Mixed	381	12,450	90	13,937 (13,717-14,144)	13,569 (13,367-13,787)	12,922 (12,709-13,130)	Scott et al. (2009)
56PC	Mixed	195.5	11,100	35	12,626 (12,551-12,709)	12,217 (12,034-12,434)	11,114 (10,989-11,207)	Lakeman et al. (2018)
56PC	Mix benthic	256	11,250	60	12,727 (12,609-12,870)	12,462 (12,198-12,695)	11,242 (11,094-11,477)	Lakeman et al. (2018)
56PC	Mix benthic	306	11,650	55	13,144 (12,973-13,285)	12,778 (12,654-12,918)	11,995 (11,738-12,282)	Lakeman et al. (2018)
56PC	Mix benthic	356	12,200	65	13,562 (13,469-13,828)	13,331 (13,193-13,466)	12,690 (12,577-12,827)	Lakeman et al. (2018)
02PC	Mixed	122	6160	30	6,596 (6,450-6,680)	6,245 (6,176-6,302)	5,526 (5,455-5,584)	Deschamps et al. (2018b)

Table 6: List of references for the (A) geochemical and (B) mineralogical database used in this study. SPM = suspended particular matter.

A Area	References	Lithology
Laptev Sea	Holemann et al. (1999)	Surface sediment
Ob River	Gordeev et al. (2007)	SPM
Yenisey River	Gordeev et al. (2007)	SPM
Lena River	Rachold et al. (1996)	SPM
Yana River	Rachold (1999)	SPM
Khatanga River	Rachold (1999)	SPM
Banks Island	Gamboa et al. (2017)	Surface sediment
Mackenzie slope	Gamboa et al. (2017)	Surface sediment
Bering Strait	Astakhov et al. (2013)	Surface sediment
Chukchi Sea	Astakhov et al. (2013)	Surface sediment
B Area	References	Lithology
North Alaska	Darby et al. (2011)	Surface sediment
Mackenzie River	Gamboa et al. (2017)	Surface sediment
Mackenzie River sand	Gamboa (2017)	Surface sediment
Mackenzie tributaries	Gamboa (2017)	Surface sediment
Banks Island	Gamboa et al. (2017)	Surface sediment
	Belt et al. (2010)	Arc-4
	Lakeman et al. (2018)	44PC
Bering Strait	Stein et al. (2017)	core ARA2B-1B
Eastern Siberian Sea and Laptev Sea	Darby et al. (2011)	Surface sediment
Kara Sea	Andrews et al. (2016)	Surface sediment

Table 7: Loadings derived from the principal component analysis of core 05JPC geochemical and mineralogical data, illustrating the weight of each (A) element (bulk and clay fraction) and (B) mineral in the definition of each PC score.

A	clr.Qz	clr.Feld-K	clr.pla	clr.Ca	clr.Amp	clr.Fe-b	clr.Ka	clr.Ch	clr.Ill	clr.Mu	clr.Sm	Cum. prop. exp.
PC1	0.12	0.25	0.21	0.35	0.34	0.16	-0.48	-0.04	-0.48	-0.04	-0.44	0.37
PC1	-0.04	0.22	0.27	-0.84	0.31	0.12	-0.20	0.06	-0.05	0.04	0.12	0.81

B	clr.Mg	clr.Al	clr.Ca	clr.Ti	clr.V	clr.Cr	clr.Fe	Cum. prop. exp.
PC1	0.32	-0.19	0.77	-0.09	-0.34	-0.31	-0.16	0.83
PC2	-0.65	0.01	0.22	0.57	-0.21	-0.23	0.30	0.90

ARTICLE 3

PROVENANCE DES SÉDIMENTS POSTGLACIAIRES DES MARGES CANADIENNE DE BEAUFORT ET DES TCHOUKTCHES (ARCTIQUE DE L'OUEST): UNE PERSPECTIVE GÉOCHIMIQUE

3.1 Résumé en français du troisième article

Les concentrations en éléments majeurs, traces et terres rares ont été mesurées sur les fractions totales et argileuses de deux carottes sédimentaires récupérées le long des marges continentales de la mer Beaufort canadien (02PC) et d'Alaska (05JPC). Ces carottes ont été étudiées pour mieux comprendre l'évolution de la provenance des sédiments détritiques et le transport lié aux changements climatiques et océaniques depuis la dernière déglaciation. Les corrélations significatives observées entre les terres rares (REE) avec la distribution granulométrique, les ratios élémentaires et minéralogiques suggèrent que la granulométrie et les minéraux argileux sont les deux facteurs contrôlant la composition en REE dans les carottes sédimentaires. Les profils des REE normalisés, combinés aux diagrammes discriminants basés sur les éléments majeurs et les REE, suggèrent que les sédiments de la carotte 02PC sont composés principalement de matériel felsique provenant du fleuve Mackenzie. Tandis que dans la carotte 05JPC, les sédiments sont de composition felsique durant la déglaciation, reflétant un transport plus important des sédiments provenant du fleuve Mackenzie associé à une gyre de Beaufort plus intense. Cependant, la proportion de sédiments de source felsique diminue graduellement au cours de l'Holocène. Au contraire, les sédiments de source mafique provenant du détroit de Béring augmentent durant la même période. Cette étude démontre que les REE peuvent être utilisées pour observer les changements de provenance des sédiments dans l'Arctique de l'ouest.

Le troisième article de cette thèse intitulé "*Provenance of postglacial sediments from the Canadian Beaufort and Chukchi-Alaskan margins (western Arctic Ocean): a geochemical perspective*" a été rédigé par moi-même sous la supervision de mon directeur et mon co-directeur soit Jean-Carlos Montero-Serrano (UQAR-ISMER) et Guillaume St-Onge (UQAR-ISMER). L'article sera soumis prochainement dans la revue *Journal of Quaternary Science*.

Ma contribution à ce travail fut la rédaction de l'article en tant que premier auteur. J'ai aussi réalisé la majorité des analyses effectuées dans ce chapitre. Les co-auteurs de l'article ont contribués à l'interprétation des données et à la rédaction de l'article. Une version abrégée de ces travaux de recherche ont été présenté sous la forme de présentation orale au congrès des étudiants du GEOTOP en 2016 et au congrès Arctic Change à Québec en 2017.

3.2 Provenance of postglacial sediments from the Canadian Beaufort and Chukchi-Alaskan margins (western Arctic Ocean): a geochemical perspective

Major, trace and rare earth element (REE) concentrations on bulk and clay fractions of two sediment piston cores, recovered from the Canadian Beaufort (02PC) and Chukchi-Alaskan (05JPC) margins, were investigated to better constrain the evolution of detrital sediment provenance and transport related to ocean-climate changes since the last deglaciation. The significant correlation observed between REE versus grain-size distribution, elemental and mineralogical ratios suggest that grain-size and clay minerals are the two most important factors that control the REE composition in the sediment cores. The shale-normalized REE patterns, combined with discriminant plots based on major elements and REE, suggest the following: (1) felsic sediments derived from the Mackenzie River are dominant in core 02PC, and (2) felsic sources are dominant in core 05JPC during the deglaciation, which likely reflects the enhanced transport of the Mackenzie River sediments linked to an intensified Beaufort Gyre. However, the proportion of this felsic source derived from the Mackenzie River gradually decreases during the early to late Holocene, whereas sediments of mafic composition from the Bering Strait increase. This study demonstrates that REE can be successfully used to track Late Quaternary sediment provenance changes in the western Arctic Ocean.

3.3 Introduction

Detrital inputs to the Arctic Ocean are mainly derived from the surrounding continents that have different mineral assemblages and geochemical signatures (Fagel et al., 2014). These land-derived, terrigenous materials originated in a cold climate under conditions of minimal chemical weathering. Therefore, these sediment inputs consist of weakly altered detrital particles from the original source rocks. This allows good correlations between the mineralogical and geochemical signatures preserved in Arctic shelf sediments, as well as the

petrographic composition of surrounding continents (Gamboa et al., 2017).

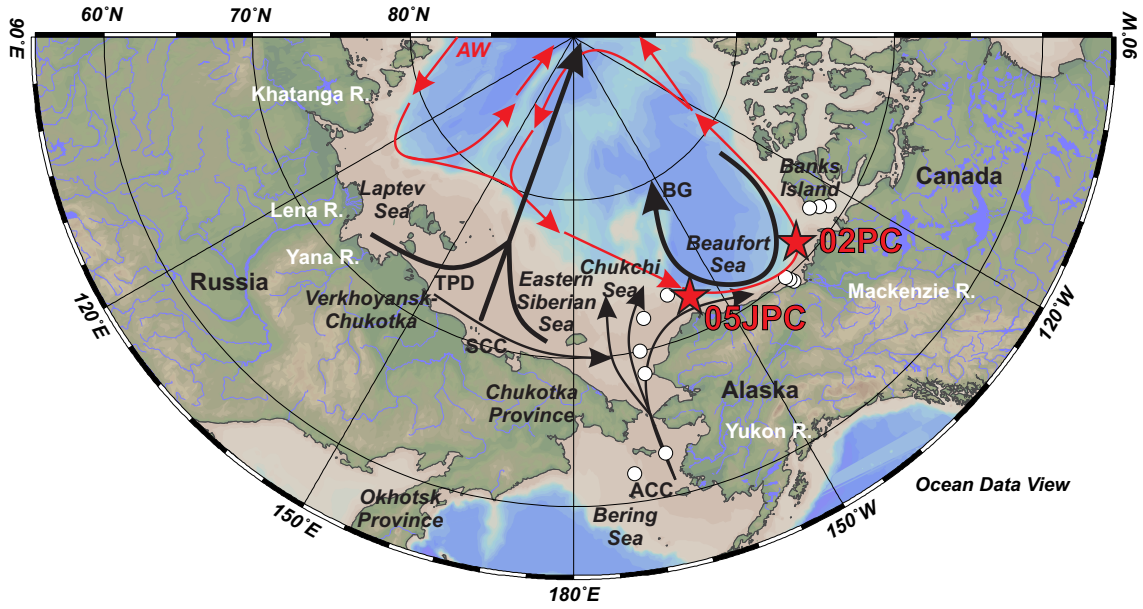

Figure 50: Location of coring sites 02PC and 05JPC (red stars). The white circles represent the REE datasets used in this study (Beaufort Sea: this study; Chukchi Sea: Asahara et al. (2012) and Chen et al. (2003); Bering Sea: Asahara et al. (2012). Data from the Aleutian volcanic arc are from the GEOROC database (http://georoc.mpch-mainz.gwdg.de). SCC: Siberian Coastal Current; ACC: Alaska Coastal Current; BG: Beaufort Gyre: TPD: Transpolar Drift; AW: Atlantic Water.

Rare earth elements (REE) have geochemical characteristics (e.g., similar ionic radii and electrical charges) that leave them relatively unaffected by secondary processes such as weathering, preserving the relative abundances of these elements given by the source rocks from which they originate (McLennan, 1989; McLennan and Taylor, 2012). Their distribution in marine sediments is mainly linked to the competing influences of source rock composition, sediment sorting and to a lesser degree, to chemical weathering intensity (McLennan, 1989; McLennan and Taylor, 2012). Thus, REE compositions have been used to determine variations in detrital particle provenance, weathering conditions in drainage basins, changes in sediment propagation and ocean-current pathways (Armstrong-Altrin et al., 2015; Asahara et al., 2012; Martinez et al., 2009).

Under this framework, several studies have used REE composition of sediments in the Arctic Ocean in order to determine sediment provenance. For example, Chen et al. (2003)

have characterized REE compositions of surface sediment from the Chukchi Sea to document modern sediment dynamics in the western Arctic Ocean. Martinez et al. (2009) have examined the REE composition of a sediment core located on the Lomonosov Ridge to trace sediment sources throughout the Cenozoic. Asahara et al. (2012) have studied the REE composition of surface sediments along the Bering and Chukchi Seas to investigate the regional and temporal changes in the inflow and transportation of terrigenous material over the past 100 years. Fagel et al. (2014) have studied the REE distributions of circum-Artic source provinces and in a sediment core from the Northern Mendeleev Ridge to document the Late Quaternary evolution of sediment provenances. Overall, REE data generated from these previous studies allow the characterization of the regional patterns in geochemical composition related to the main circum-Artic sources. Deschamps et al. (*under review*) have characterized major elements and mineralogy (bulk and clay fraction) composition of the detrital sediments along the Canadian Beaufort and Chukchi-Alaskan margins in order to document changes in detrital sediment provenance and transport related to climate variability since the last deglaciation. However, there is a lack of REE data for modern and past records within the Beaufort margin compared to other Arctic continental shelf regions as well as on the factors controlling their distribution in this area. Such geochemical data may provide valuable information to better interpret the sediment dynamics and climate change in the southern Beaufort Sea.

Here, we present major and trace element compositions (including REE) from both bulk and clay fractions of two sediment piston cores recovered from the Canadian Beaufort (02PC) and Chukchi-Alaskan (05JPC) margins to better constrain the long-term changes in sediment provenance related to ocean-climate changes since the last deglaciation. In the present study, the geochemical features of cores 02PC and 05JPC are compared with grain size and bulk and clay mineralogical data previously published from the same cores. The objective of the study was to assess major controlling factors for REE concentrations and the applicability of potential REE signatures for understanding of sediment origin in the western Arctic Ocean since the last deglaciation.

3.4 Regional Setting

3.4.1 Oceanic circulations

The Arctic surface oceanic circulation is related to two main, wind-driven circulation systems, which are the anticyclonic Beaufort Gyre (BG) in the western Arctic and the Transpolar Drift (TPD; Darby et al., 2012). On the Chukchi Shelf, oceanic circulation is controlled by an inflow of Pacific waters via the Bering Strait (referred to as the Bering Strait inflow), the Siberian coastal current, and the Atlantic intermediate water, which affects the northern margin (Weingartner et al., 2005). The Pacific inflow could be divided into 3 major branches (Fig. 50). The first branch turns westward around Herald Canyon. The third branch flows into Barrow Canyon, and the second branch flows between the first and third branches (Weingartner et al., 2005). The Bering Strait inflows are mainly controlled by the strength and position of the Aleutian Low on an interannual time scale (Yamamoto et al., 2017). On the other hand, oceanic circulation in the southeastern Beaufort Sea is dominated by the anticyclonic BG, which pushes both surface currents and sea ice westward at the shelf break (Fig. 50).

3.4.2 Sediment dynamics

The margins of the shallow Beaufort and Chukchi seas were last flooded during the glacial/Holocene transition (Keigwin et al., 2006). Modern sediment in the Chukchi Sea is believed to be derived mainly from northeastern Siberia, Bering Strait inflow (especially from the Yukon River) and Mackenzie River, whereas the Canadian Beaufort margin sediment originates primarily from the Mackenzie River basin (Deschamps et al., *under review*; Gamboa et al., 2017). Smaller Alaskan rivers have a more local impact, but these rivers may have been a more important sediment source during the early stages of the last transgression (Hill and Driscoll, 2008). During deglaciation and the early Holocene, sediment inputs to the Chukchi and Beaufort margins were presumably higher due to the rising sea level as-

sociated with meltwater and iceberg discharge from the retreating Laurentide Ice Sheet or LIS (**?**). However, sea ice, bottom currents and ice rafted debris (IRD) in the Arctic Ocean could also influence redistribution and act as a sediment carrier. During the Holocene, interglacial sediment redistribution was strongly controlled by bottom currents, whereas during the deglacial/glacial period, sea ice and IRD strongly affected sediment dispersal and deposition (Darby et al., 2009). Several IRD have been recorded in the sedimentation along the North American margin during the last deglacial, which is linked to the debacle of the Laurentide and Innuitian Ice Sheets (Darby and Zimmerman, 2008).

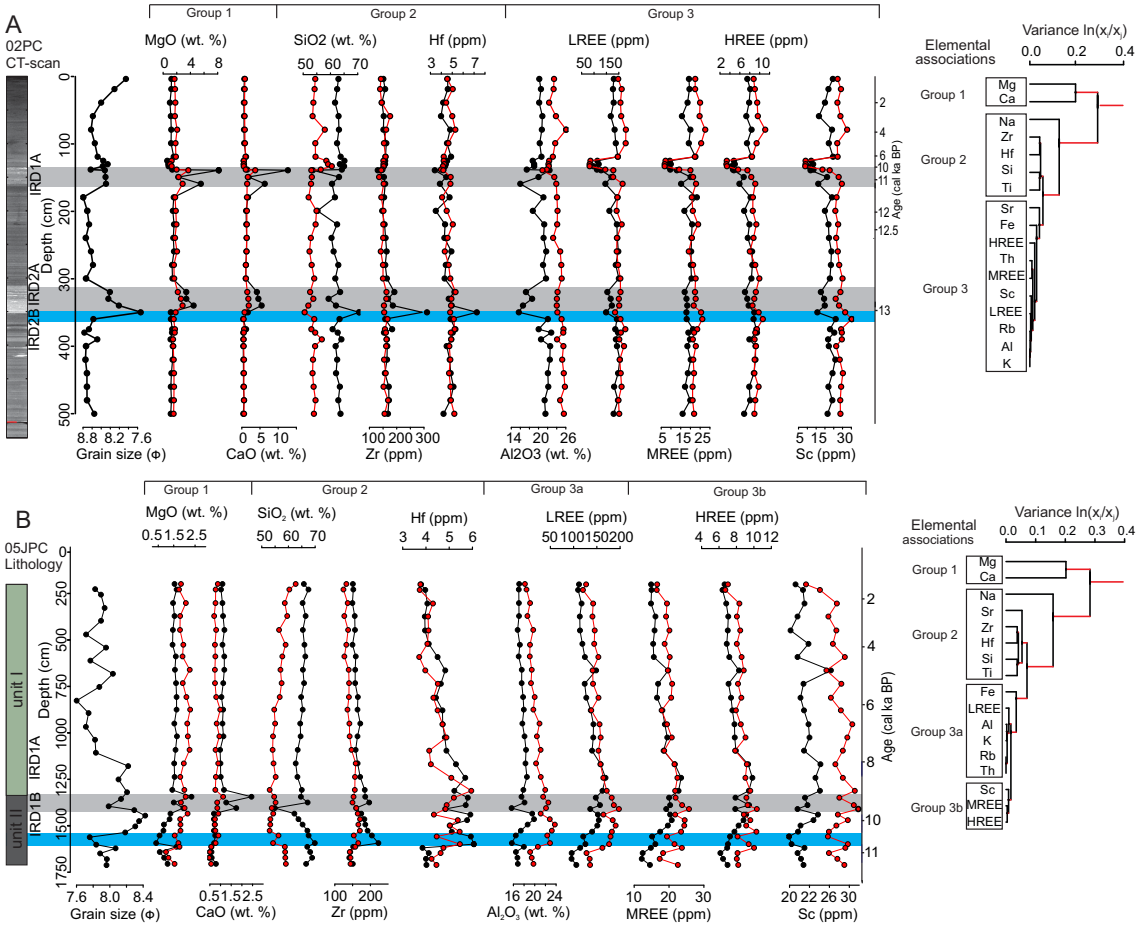

Figure 51: Stratigraphic profiles of the mean grain size and major geochemical associations obtained through the compositional Q-mode cluster analysis of cores (A) 02PC and (B) 05JPC. Dendrogram of the association of variables was obtained by applying the Ward clustering algorithm based on the variation matrix of the elemental geochemical dataset. The black and red lines represent the bulk and clay fractions studied here. IRD layers rich in dolomite and quartz are highlighted in gray and blue, respectively.

3.4.3 Surrounding geology

Circum-Arctic source areas have variable geological ages and tectonic settings and are therefore characterized by different petrographic signatures (Fagel et al., 2014). The Canadian Arctic Archipelago and Mackenzie Delta region were constituted by shale and sandstones from marine and non-marine sedimentary rocks (Harrison et al., 2011). In addition, the Banks and Victoria Islands are composed of shale and sandstones rich in dolomite clasts, as well as quartz and feldspar grains (Bischof and Darby, 1999). As part of the North American margin, the Canadian Shield is made of Archean plutonic and metamorphic rocks (Padgham and Fyson, 1992). Alaskan terrains include the Canadian–Alaskan Cordillera, Brooks Range, and part of the North American platform containing mostly metamorphic and clastic rocks (Hamilton, 1986). The Siberian platform is composed of Precambrian and Cambrian limestones, Jurassic to Cretaceous terrigenous sediments and Quaternary alluvial material (Harrison et al., 2011). The volcanic areas can be separated into different zones: the intraplate Okhtosk-Chukotka, which is composed of acidic to intermediate rocks predominating in the west and intermediate to basic rocks in the east (Viscosi-Shirley et al., 2003b), as well as the Bering Sea Basalt Province, Permian and Triassic volcanic rocks of Siberian traps, and convergent margins of the Pacific Aleutian (Harrison et al., 2011).

3.5 Material and Methods

The sediment core AMD0214-02PC (hereinafter referred to as core 02PC; location: 71°22.910'N, 133°34.040'W) was collected on the Canadian Beaufort margin on board the CCGS Amundsen during the 2014 ArcticNet expedition (Montero-Serrano et al., 2014; Fig. 50). Core HLY0501-05JPC (hereinafter referred to as core 05JPC; location: 72°51.618'N, 158°25.26'W) was recovered in the Chukchi-Alaskan margin on board the USCGC Healy as part of the 2005 Healy-Oden Trans-Arctic Expedition (Darby et al., 2005; Fig. 50). Note that cores 02PC and 05JPC were raised from the continental slope at 415 m and 998 m depth,

respectively, where sediment deposition was not interrupted by sea-level changes. The age model and physical properties of the sediment cores 02PC and 05JPC have been described in Deschamps et al. (2018b) and Barletta et al. (2008), respectively. The age model for core 02PC used in this study was developed in Deschamps et al. (2018a) using a ΔR=335 years for the Holocene and a ΔR=1000 years for the deglacial units, respectively (Coulthard et al., 2010; Hanslik et al., 2010). The sedimentation rate for core 02PC was lower in the postglacial parts (2-20 cm.ka^{-1}) and higher in the glacial parts (50-380 cm.ka^{-1}). The linear age model for core 05JPC is based on radiocarbon dating and using a ΔR=460 years (Barletta et al., 2008; Darby et al., 2009). Furthermore, the paleointensity data for this core shows several features that can be correlated to other independently dated paleointensity records from high latitudes (Barletta et al., 2008). Ages below 8.5-9 were extrapolated, and therefore, our interpretations remain hypothetic.

Detailed descriptions of the methods are given as Supporting Information and all analytical data presented are available electronically in the PANGAEA database (https://www.pangaea.de/). The chemical index of alteration, defined as: CIA = 100 $\times$ $Al_2O_3/(Al_2O_3 + CaO^* + Na_2O + K_2O)$ in molar proportions (Nesbitt and Young, 1982), was used as a proxy to the degree of weathering in the source areas. The fractionation of REE in the sediment samples were determined by normalizing REE concentrations to Post Archaean Australian Shale (PAAS, Pourmand et al., 2012). Thus, the subscript "n" indicates PAAS-normalized abundances. Fractionation between light REE (LREE: La–Nd) and heavy REE (HREE: Tm–Lu) was investigated using the following ratio: LREE/HREE ratio [(La+Ce+Pr+Nd)/(Tm+Yb+Lu)]. Likewise, because titanium (Ti) is a relatively immobile element in the chemical weathering (Nesbitt, 1979), total REE (ΣREE) are normalized to Ti to reduce or remove the grain-size effects on the REE distributions so that changes in the composition of the lithogenous material can be discerned.

3.6 Results

The vertical distribution of major, trace and REE elements of bulk and clay-sized fractions together with mean grain size from both cores are shown in Fig. 51. Downcore variations are quite constant throughout core 02PC with the exception of the two IRD intervals (IRD1: 130-150 cm; IRD2; 320-350 cm), which show lower concentrations of Sc, Th and LREE. Conversely, core 05JPC displays long-term elemental variations throughout the core. In Unit II of this core, all measured elements globally increase to reach a maximum at the deglacial/Holocene interval (1700-1400 cm; Fig. 51). Unit I is characterized by a decrease in trace (e.g., Th-Hf-Sc-Zr) and REE elements (1400-200 cm; Fig. 51). The PAAS-normalized REE patterns of bulk and clay-sized fractions from both sediment cores display homogeneous and flat distributions, which are similar to PASS (Fig. 52). However, shale-normalized patterns in both cores display subtle differences. In core 02PC, REE distributions are characterized by light fractionated patterns with moderate LREE enrichment and slightly depleted to flat HREE, which is mostly marked in the clay-sized fraction. Conversely, in core 05JPC, REE patterns of bulk and clay-sized fractions exhibit a slight LREE depletion with a progressive HREE enrichment. Likewise, a flat pattern is apparent in the comparison between REE contents in the bulk and clay fractions (Fig. 53).

In addition, the compositional Q-mode cluster analysis of cores 02PC and 05JPC revealed three major elemental geochemical associations (Fig. 51): Group 1 includes Ca and Mg; Group 2 is composed of Na, Sr, Zr, Hf, Si, and Ti; and Group 3, which can be divided into two subgroups, is composed of Fe, LREE, Al, K, Rb, Th (Group 3a) and Sc, MREE, HREE (Group 3b). Group 1 consists of elements related to detrital carbonates (notably, dolomite). Group 2 consists of elements associated with silt particles, mainly as chemical constituents of detrital mineral grains (e.g., quartz, feldspars, rutile, zircon). Group 3 consists of elements that are found mainly in fine-grained particles, as chemical constituents of the clay minerals (e.g., illite, kaolinite) and Fe-oxides or adsorbed on their surface (e.g., Montero-Serrano et al., 2010). Variations in Group 3 variables reflect the interplay of felsic (Group 3a) and

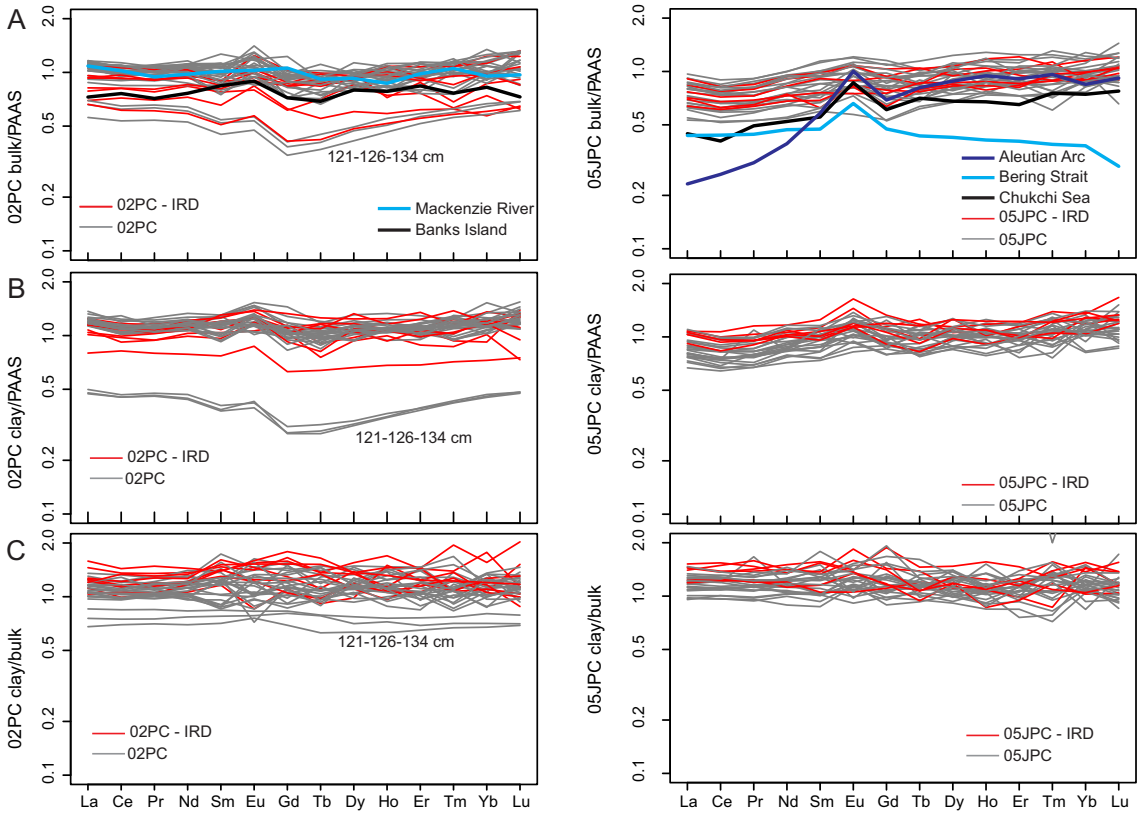

Figure 52: PAAS-normalized REE patterns for bulk (A) and clay (B) fractions of cores 02PC and 05JPC. (C) PAAS-normalized REE distribution patterns of clay versus corresponding bulk fractions. PAAS values by Pourmand et al. (2012) are used for normalization. For comparison, we also included average PAAS-normalized REE patterns from the Mackenzie Trough and Southwestern Banks Island (this study), as well as the Chukchi Sea and Bering Strait (Asahara et al., 2012; Chen et al., 2003).

mafic (Group 3b) sources in the provenance of detrital sediments.

Based on the information extracted from the compositional Q-mode cluster results (Fig. 51), we selected the log(LREE/HREE) and log(La/Sc) ratios, together with the composite variable given by the geometric mean of Group 1 and Group 3, to reconstruct down-core changes in sediment provenance and transport in the Chukchi-Alaskan and Canadian Beaufort margins since the last deglaciation (Fig. 54 and 54). The log(LREE/HREE)n and log(La/Sc) ratios reflect sediment sources based on the preferential La and LREE concentrations in felsic rocks, whereas Sc and HREE are more concentrated in mafic rocks (Armstrong-Altrin et al., 2015; Cullers, 1994). In addition, the changes observed in the REE distributions

will be discussed below together with variations in the log[quartz/(K-feldspar+plagioclase)] or log(Qz/Fsp), log(K-feldspar/Plagioclase) or log(Kfeld/Pla) and log(illite+kaolinite/chlorite+vermiculite) or log(I+K/C+V) ratios as well as the dolomite contents, which were previously published by Deschamps et al. (2018a). The combination of these different detrital proxies will favor (1) a better discrimination between the sediments from the North American and Canadian Arctic Archipelago sources and those from the Eurasian Shelf and Bering Strait (Gamboa et al., 2017; Kobayashi et al., 2016; Vogt, 1997; Yamamoto et al., 2017), and (2) highlight the evolution of the sedimentary dynamics since the last deglaciation. In fact, total feldspars are more abundant along the Eurasian margin and Bering Strait, whereas quartz-illite-kaolinite are more common along the North American margin, and sediments from the Canadian Arctic Archipelago are enriched in dolomite. Kobayashi et al. (2016) and Deschamps et al. (2018a) also indicate that chlorite and vermiculite are more abundant in the Bering Sea and Chukchi-Alaskan margin. In addition, the discriminant diagram based on major elements developed in Roser and Korsch (1988), which consists of four provenance fields i.e., mafic, felsic, intermediate and quartzose-recycled, was used to infer provenance in the western Arctic Ocean.

3.7 Discussion

3.7.1 Sedimentary processes

The chemical composition of siliciclastic sediments on most continental margins reflects cumulative effects such as the following: (1) sediment grain-size and hydraulic sorting of minerals during sedimentary processes (Garzanti et al., 2010), (2) source rock composition, i.e., mineralogical composition (McLennan, 1989), and (3) intensity of chemical weathering (McLennan, 1993). The hydraulic sorting and grain-size effect has been widely accepted because trace elements including REE tend to be enriched in fine-grained sediments and depleted in most coarse fractions, which is mostly because of dilution by quartz and carbonate minerals (Von Eynatten et al., 2016). Furthermore, REE fractionations in sediments have re-

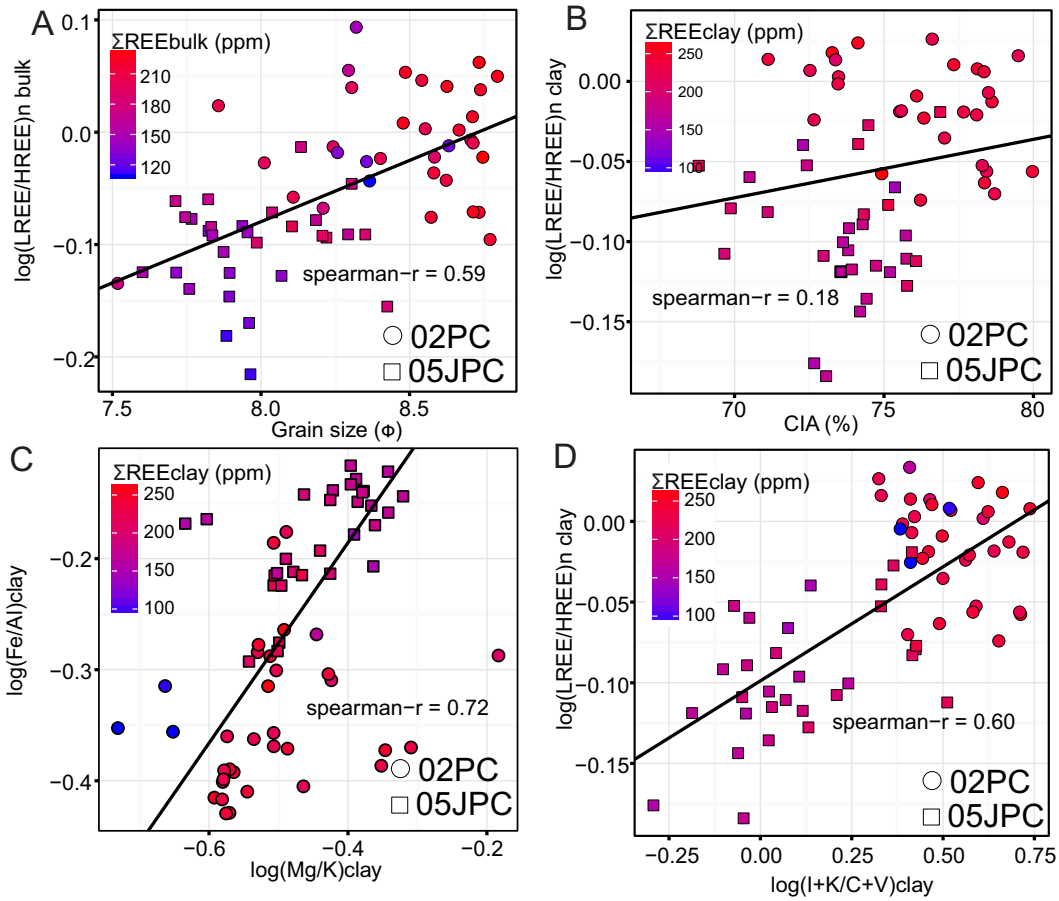

Figure 53: Correlation plots of (A) log(LREE/HREE)n from the bulk fraction with mean grain-size (phi-scale), (B) log(LREE/HREE)n with CIA from the clay fractions, (C) log(Fe/Al) with log(Mg/K) from the clay fractions, (D) log(LREE/HREE)n compared to log(I+K/C+V) from the clay fractions. The ΣREE are shown using a gradient color from high (red) to low (blue) values.

mained controversial, whereas several mineral phases including heavy phosphatics, Fe-oxides and clay minerals were proposed as the main host phases (Song and Choi, 2009). Thus, REE host minerals consequently vary based on sources rocks and weathering conditions within a drainage basin.

The correlation between the log(LREE/HREE)n ratio and mean grain-size composition in sediments may help with evaluating the effects of hydrodynamic sorting during sediment transport on geochemical compositions (Dou et al., 2015). In general, the log(LREE/HREE)n ratio, as well as the ΣREE content, gradually increases from core 05JPC to 02PC, with a de-

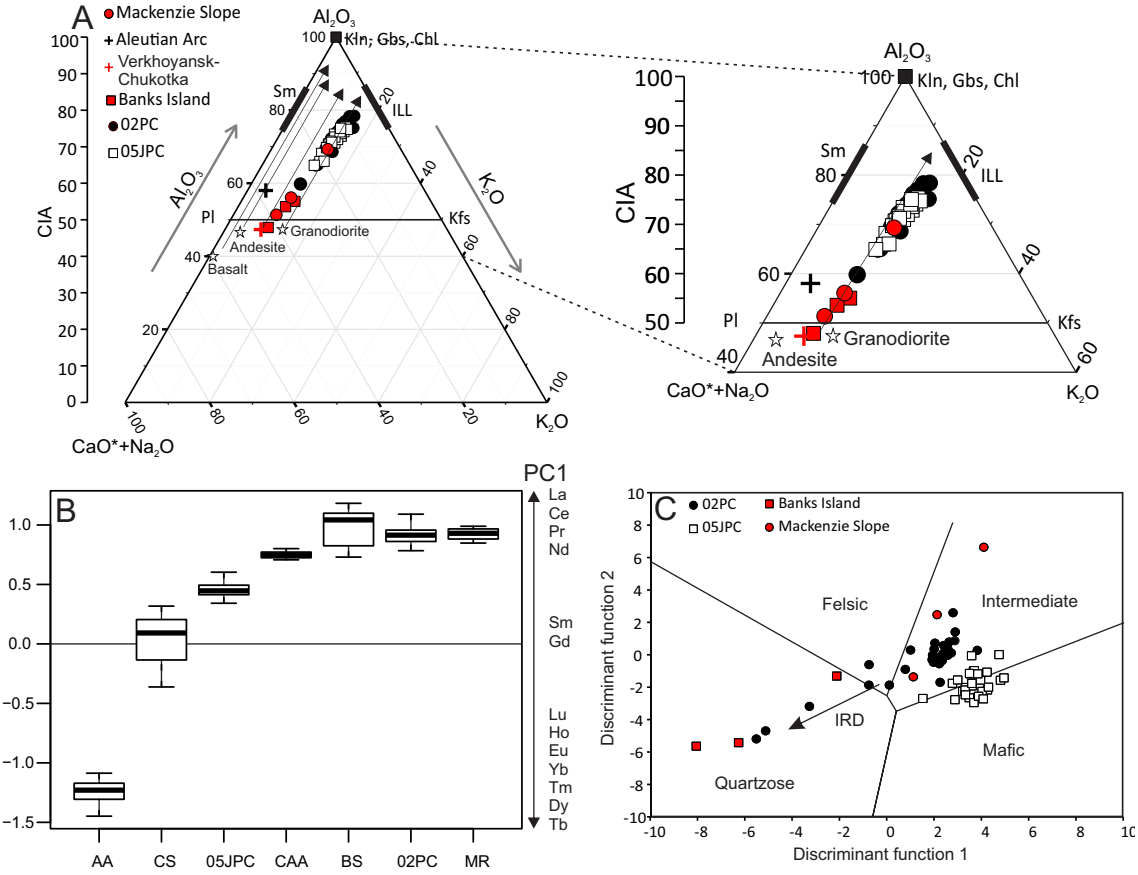

Figure 54: (A) Al_2O_3–(CaO^* + Na_2O)–(K_2O) ternary diagram (Nesbitt and Young, 1982). (B) PC1 scores obtained from the log-centered transformation of REEs from cores 02PC and 05JPC, as well as the circum-Arctic source areas (Table 9). AA: Aleutian volcanic arc; CS: Chukchi Sea; CAA: Canadian Arctic Archipelago; BS: Bering Strait; MR: Mackenzie River. (C) Discriminant function diagram based on major elements from sediment cores 02PC and 05JPC, as well as surface sediments from the Mackenzie Trough and Southwestern Banks Island. The discriminant functions are from Roser and Korsch (1988): DF1= (-1.773 TiO_2) + (0.607 Al_2O_3) + (0.760 Fe_2O_3) + (-1.500 MgO) + (0.616 CaO) + (0.509 Na_2O) + (-1.224 K_2O) + (-9.090); DF2= (0.445 TiO_2) + (0.070 Al_2O_3) + (-0.250 Fe_2O_3) + (-1.142 MgO) + (0.438 CaO) + (1.475 Na_2O) + (-1.426 K_2O) + (-6.861).

creasing grain-size from fine silt (7.5 phi) to clay (9 phi) (Fig. 53A). This significant positive correlation (r = 0.65, n = 61) suggests that grain-size is one of the major factors controlling REE concentrations in bulk sediments. On the other hand, weathering (as shown by the CIA) does not play an important role in the REE distribution of sediments along the North American margin (r = 0.22; Fig. 53B). Next, to identify possible relationships between the element concentrations and mineral compositions in the clay-sized fractions, we

used the log(Mg/K) and log(Fe/Al) ratios together with REE concentrations. Deschamps et al. (2018a) suggest that Al, K, Mg and Fe are the major elements controlling the variations in clay-sized fractions relative to their host minerals (Al and K for illite and kaolinite, Mg and Fe for chlorite and vermiculite). The REE concentrations increase towards higher values of K and Al from core 05JPC to 02PC (Fig. 53C). Likewise, we used log(LREE/HREE)n vs log(I+K/C+V) to observe the relationship between clay minerals and REE concentrations. The log(LREE/HREE)n-log(I+K/C+V) crossplot reveals that LREE and ΣREE contents in the clay fraction increase with the proportion of kaolinite and illite from core 05JPC to 02PC and decrease towards higher chlorite and vermiculite content (Fig. 53D).Total REE contents depict a clear and positive correlation with aluminosilicate clays, which suggests that REE are lodging in clay minerals structure, more specifically, in illite and kaolinite. Overall, our results indicate that grain-size and clay minerals, as well as the relative contribution of different sediment sources (e.g., Bering Strait vs. Mackenzie River) are the most important factors controlling REE composition in the sediments from the Chukchi-Alaskan and Canadian Beaufort margins.

Furthermore, the ternary plot Al_2O_3 – (CaO* + Na_2O) – K_2O (Fig. 54A) illustrates that surface sediments from the Mackenzie Trough and Southwestern Banks Island, as well as the Chukotka source rocks, are close to the plagioclase/K-feldspar line, suggesting a low degree of chemical weathering from granodioritic sources. The Aleutian Arc source rocks are close to the weathering trends from basaltic and andesitic rocks. Sediment samples of bulk and clay-sized fractions of both cores follow a trend to potassium aluminosilicates (illite) with CIA values raging between 64 and 78 % in both cores (Fig. 51), which reflects a moderate to high degree of alteration in the source area. Note that illite, a typical clay mineral in cold regions, is delivered in all shelf areas surrounding the circum-Arctic basin and represents the dominant clay mineral in sediments (> 50 %; Naidu et al. 1982).

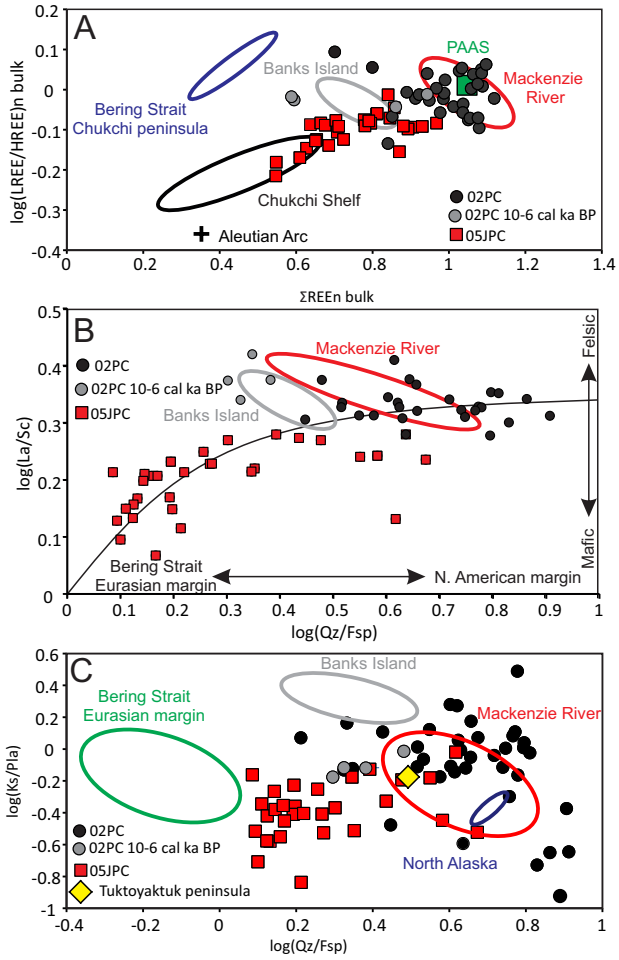

Figure 55: (A) Log(LREE/HREE)n vs. ΣREE, (B) Log(La/Sc) vs log(Quartz/Feldspars) and (C) Log(Qz/Fsp) vs. Log(K-feldspar/Plagioclase) variation plots for sediment cores 02PC and 05JPC and the potential sources (see Fig. 50).Mackenzie and CAA geochemical data are from this study. Bering Strait and Chukchi shelf geochemical data are from Asahara et al. (2012) and Chen et al. (2003). Mineralogical data from core 02PC and 05JPC are from Deschamps et al. (2018a); Mackenzie River and Banks Island data are from Gamboa et al. (2017); Tuktoyaktuk peninsula data is from Vogt (1997); North Alaska and Eurasian margin data are from Darby et al. (2011).

3.7.2 REE compositions of potential sedimentary sources

Previous geochemical studies (Asahara et al., 2012; Bayon et al., 2015; Chen et al., 2003; Fagel et al., 2014) have synthesized the distribution of REE in the sediments deposited on continental shelves and adjacent coasts that surround the Arctic Ocean. Considering this, we performed a principal component analysis on the log-ratio of REE data available in the

literature together with our data to observe the relative differences between sediment composition in potential source areas of the circum-Arctic and our sediment core (Fig. 54B; Table 9). As shown in Fig. 54B, LREE (La-Ce-Nd-Pr) are dominant along the North American margin where Paleozoic-Mesozoic sedimentary rocks and Pleistocene glacial till outcrop, which is also characterized by high Al-K-Ti-Fe-Cr-V-Zn and quartz-carbonate-illite-kaolinite contents (Deschamps et al., 2018a; Gamboa et al., 2017; Fig. 54B). In addition, using the discriminant diagram developed in Roser and Korsch (1988), Mackenzie River sediment could be classified with an intermediate composition between felsic and mafic source rocks (Fig. 54C-B). This interpretation is in agreement with Mackenzie River REE patterns, which display relatively homogeneous and flat PAAS-normalized patterns that are typical of large river draining igneous/metamorphic rocks (Bayon et al., 2015; Fig. 52A). On the other hand, the Canadian Arctic Archipelago is composed of Paleozoic and Mesozoic sedimentary rocks which are made up of sand and fine-grained terrigenous material (shale or mudstone), and thus reflect quartzose signatures (Patchett et al., 2004; Fig. 54B). Likewise, MREE (Sm-Eu-Gd-Tb-Dy) and HREE (Ho-Er-Tm-Yb-Lu) are dominant in the Chukchi Sea, as well as in the Aleutian volcanic arc (Fig. 54B). The REE patterns for the Chukchi Sea, Bering Strait and Aleutian volcanic arc displayed an LREE depletion, which is typical of volcanic river sediment inherited from the depleted nature of their source rocks (Bayon et al., 2015; Fig. 54A). Distribution of the detrital sediments in the Bering Sea is controlled mainly by two components: the continental material from the Yukon River basin, which is underlain mainly by Mesozoic and Paleozoic rocks on the Alaskan mainland, and the andesitic material from the Aleutian volcanic arc (Asahara et al., 2012; Gardner et al., 1980).

3.7.3 Postglacial sediment dynamics in the western Arctic Ocean

Canadian Beaufort margin

In core 02PC, excluding the IRD intervals, the major sediment source was linked to the Mackenzie River input since the last deglaciation (Fig. 56). The PAAS-normalized REE

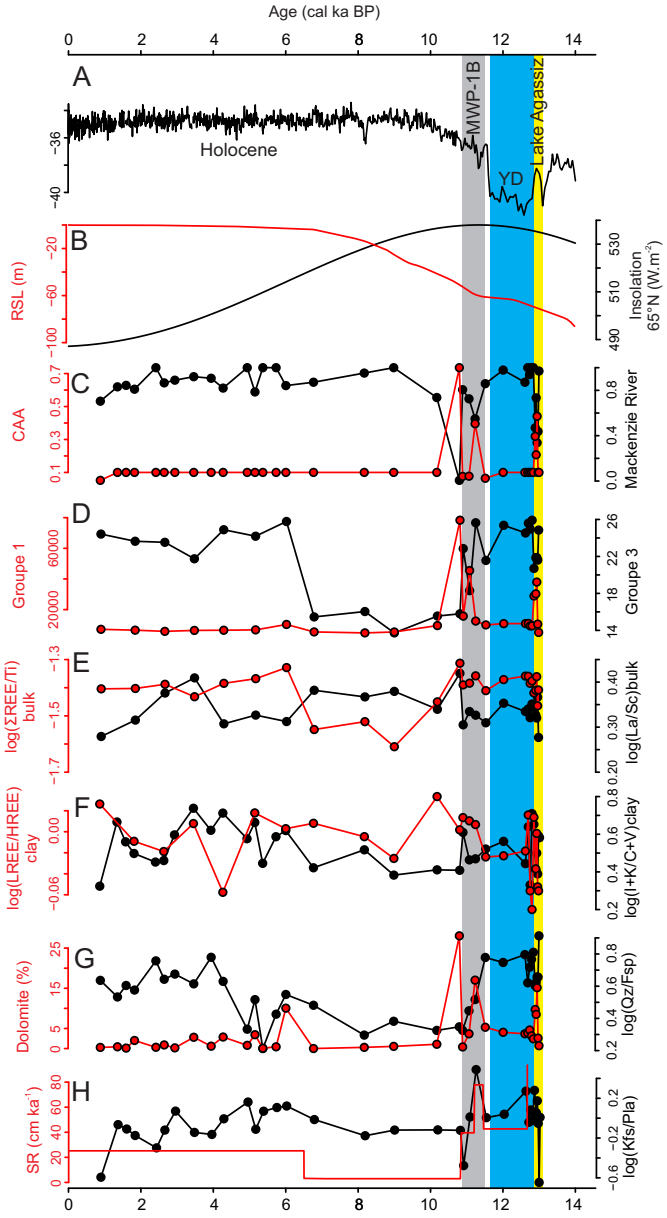

Figure 56: (A) GISP2 δ^{18}O (Grootes and Stuiver, 1997), (B) June insolation at 65°N (Berger and Loutre, 1991) and global eustatic sea level changes (Lambeck et al., 2014). (C) Downcore variations in core 02PC showing proportion of sediment from the Mackenzie River (black) and Canadian Arctic Archipelago (red), (D) Group 1 and Group 3 composite variables, calculated by computing the geometric mean of the elemental associations (see details in Fig. 51A), (E) log(ΣREE/Ti) and log(La/Sc), (F) log(LREE/HREE)n and log(Illite+Kaolinite/Chlorite+Vermiculite) based on clay mineralogy, (G) proportion of dolomite and log(Quartz/Feldspars), and (H) log(K-feldspath/plagioclase) and sedimentation rates.

patterns of the bulk fraction are similar to Mackenzie River signatures. Banks Island REE patterns show a slight REE depletion and relatively homogeneous and flat PAAS-normalized patterns, which is similar to the IRD intervals (Fig. 52). In addition, the relationship between ΣREE concentrations and log(La/Sc) and log(Qz/Fsp) ratios reveals that sediments in core 02PC are related mainly to felsic source materials derived from two end-members: the Mackenzie River and Canadian Arctic Archipelago (Fig. 55). The quartz and feldspars-rich layer observed at ~13 cal ka BP (IRD2B) in the Canadian Beaufort margin is characterized by lower LREE and high Si-Zr-Hf-Sc-MREE-HREE contents (Fig. 51B). Optically stimulated luminescence dates from the Mackenzie drainage basin suggest a major routing of deglacial meltwater from Lake Agassiz into the Arctic Ocean at 13±0.2 cal ka BP, near the start of the Younger Dryas (Murton et al., 2010) . Thus, we hypothesize that this event promoted the remobilization of rock flour deposits from the northwest part of the Mackenzie River watershed, which are characterized by an abundance of quartz and feldspar and likely by high Si-Zr-Hf-Sc-MREE-HREE contents (Fig. 56). The major changes in sediment provenance in core 02PC are related to IRD events rich in dolomite (IRD1A and IRD2A; Fig. 51), which occurred at 12.8 and 11 cal ka BP and are linked to the collapse of the Amundsen Gulf Ice Stream (Stokes et al., 2009). During these dolomite-rich IRD, the ΣREE content together with log(La/Sc) in both clay and bulk fractions decreased (Fig. 56). We infer that this decrease in the REE contents may likely be the result of a dilution by higher dolomite (Ca-Mg rich) inputs (Fig. 56).

In core 02PC, the detrital proxies show high quartz/total feldspars and lower LREE/HREE ratios observed during the Younger Drays (spanning ~12.8 to ~11.7 cal ka BP; Rasmussen et al., 2006). The mineralogical difference was attributed to the increase contributions from the northern tributaries of the Mackenzie River (Deschamps et al., 2018a). Indeed, (Wickert, 2016) suggested that meltwater inputs to the Mackenzie River ended no later than 11 cal ka BP, when its eastern tributaries were temporarily rerouted eastward due to a combination of ice retreat and glacial isostatic depression. The age of 11 cal ka coincide with the decrease of the sedimentation rates from 50 $cm.ka^{-1}$ to 2 $cm.ka^{-1}$ (Deschamps et al., 2018a). In this

context, we hypothesize that the recession of the LIS in the Mackenzie River drainage basin before ~11-10.5 cal ka BP (Dyke, 2004) remobilized MREE-HREE-rich sediments from the northwest part of the Mackenzie Basin.

Furthermore, during the early- to mid-Holocene (10-6 cal ka BP), sediments in core 02PC are characterized by lower log(ΣREE/Ti) and log(I+K/C+V) and showed an increase in the feldspars proportion notably in plagioclase, likely suggesting a mixed provenance of detrital particles, that is, mainly from the southern of the Mackenzie Basin with a minor influence from the northern tributaries (Figs. 55 and 56). The northern tributaries of the Mackenzie River (such as the Peel and Red Rivers) drain weathered marine sedimentary rocks (e.g., Cambrian to Cretaceous limestones and shales) almost exclusively, which are enriched in clay minerals, quartz, and detrital carbonates (and likely also in REE). Conversely, granitic source rocks outcropping in the North American Cordillera (including the Rocky and the Mackenzie Mountains) and Canadian Shield are drained by the southern tributaries (such as the Liard and Slave Rivers), which are characterized by an abundance of feldspars (Gamboa, 2017). Alternatively, because the sea level exerted significant control on the sedimentation of the Mackenzie Shelf during the early- to mid-Holocene (Deschamps et al., 2018a), we cannot rule out the possibility that Holocene changes in relative sea level also influenced sedimentation in the Canadian Beaufort margin. Indeed, the change in sediment provenance recorded between 10 and 6 cal ka BP in core 02PC coincides with lower sedimentation rates (2 $cm.ka^{-1}$) and a relative sea level rising (Fig. 56). Such conditions probably promoted an increase in coastal erosion of fine-grained feldspar-rich Pleistocene glacial tills, which outcrop along the Tuktoyaktuk Peninsula (Gamboa et al., 2017; Vogt, 1997) and, therefore, a larger sediment supply from this area (Figs. 55 and 56).

Chukchi-Alaskan margin

In general, sediment provenance in core 05JPC displayed a mroe prononced variability over time compared to core 02PC (Fig. 51). Shale-normalized REE patterns for core 05JPC displayed slight LREE depletion and HREE enrichment, which is similar to Aleutian

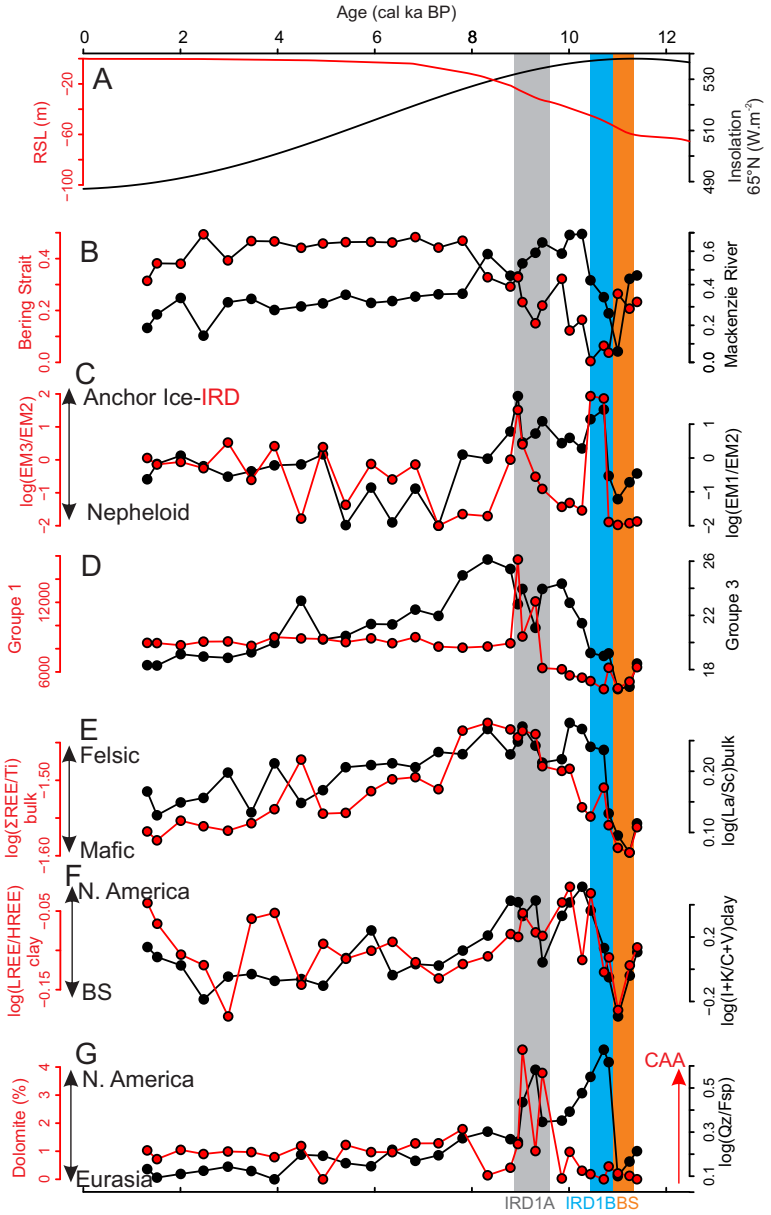

Figure 57: Downcore variations in core 05JPC showing (A) June insolation at 65°N (Berger and Loutre, 1991) and global eustatic sea level changes (Lambeck et al., 2014), (B) proportion of sediment from the Bering Strait and Mackenzie River, (C) log(EM1/EM2) and log(EM3/EM2) based on grain size analyses from Deschamps et al. (2018a), (D) Group 1 and Group 3 composite variables, calculated by computing the geometric mean of the elemental associations(see details in Fig. 51B), (E) log-ratios ΣREE/Ti and La/Sc, (F) log(LREE/HREE)n and log(illite+kaolinite/chlorite+vermiculite) based on clay mineralogy, and (G) proportion of dolomite and log(Quartz/Feldspars)

and Chukchi Sea sediments (Fig. 52). Likewise, the relationship between ΣREE concentrations and log(La/Sc) and log(Qz/Fsp) ratios in core 05JPC reveals provenance changes between two end-members since the last deglaciation (Fig. 55). The first one is related to a predominant felsic source during the deglacial/Holocene interval and is characterized by high quartz-La-LREE contents derived mainly from the North American margin (including the Mackenzie River and Canadian Arctic Archipelago), and the second is related to a more mafic source predominant during the mid-to-late Holocene, which is typified by high feldspars-Sc-HREE contents derived mainly from Bering Strait inflow (Figs. 51, 54B-C and 54). Thus, the low log(La/Sc) and log(LREE/HREE) and log(ΣREE/Ti) ratios observed at 11 cal ka BP may be interpreted as a major input of mafic material coming from the Aleutian Arc via the Bering Strait (Fig. 57). In agreement with a sedimentological study on the post-glacial flooding of the Beringia Land Bridge (Jakobsson et al., 2017), we hypothesize that sediments in this interval may be related to the initial opening of the Bering Strait, which is dated to around 11 cal ka BP. On the other hand, the quartz-rich and dolomite-rich layers observed in core 05JPC at ~10.6 (IRD1B) and 9.5cal ka BP (IRD1A), respectively, are characterized by high log(La/Sc) and log(LREE/HREE) ratios, which suggests a relative increase in the input of a more felsic source coming from the North American margin (Fig. 51A and 57). High-resolution seismic reflection data in conjunction with piston coring from the outer Chukchi margin have evidenced the occurrence of iceberg discharge from the Brooks Range to the shelf between 13 and 10 cal ka BP (Hill and Driscoll, 2008, 2010). Therefore, we hypothesize that the quartz-rich but carbonate-poor sediment records at ~10.7 cal ka BP in core 05JPC are most likely related to a meltwater event derived from northwestern Alaska. Similar to core 02PC, the dolomite-rich sediments recorded at 9.5 cal ka BP (IRD1A) are supplied by sea ice and icebergs from the Canadian Arctic Archipelago via an active Beaufort Gyre (Phillips and Grantz, 2001) and are probably related to the final collapse of the Amundsen Gulf Ice Stream (Stokes et al., 2009). However, based on similarities in the geochemical and mineralogical signatures of the IRD1A in cores 05JPC and 02PC, Deschamps et al. (2018a) suggested they were related to the same event dated at 11 cal ka BP. This IRD correlation

would imply that the age for the opening of the Bering Strait may be older than 11 cal ka BP (Jakobsson et al., 2017) as previously suggested by (Keigwin et al., 2006).

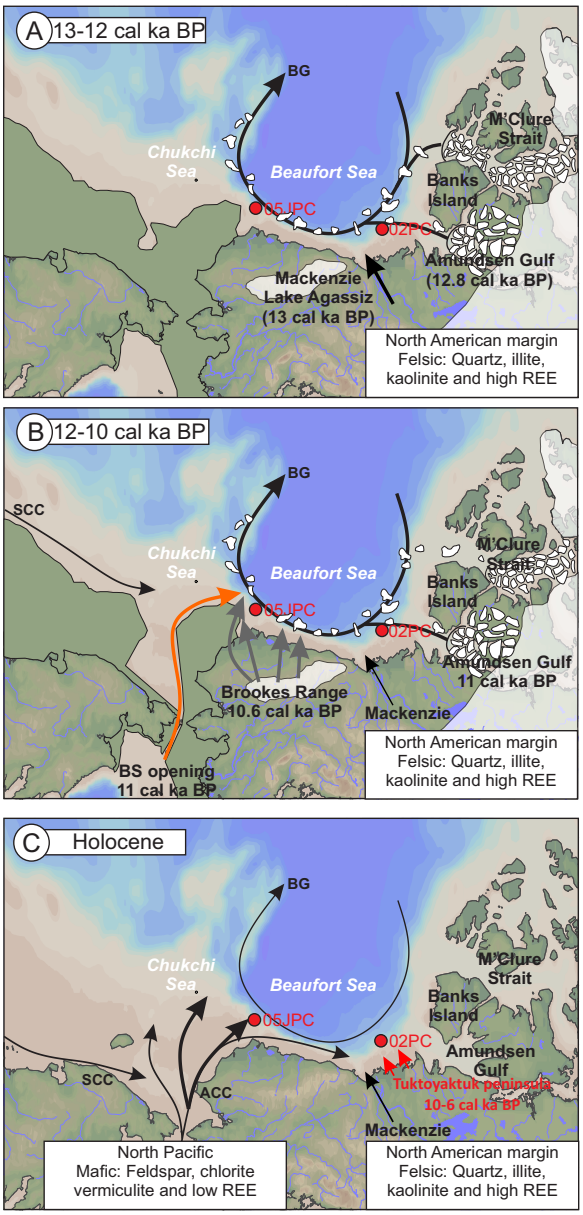

Figure 58: Evolution of sedimentary dynamics in the western Arctic Ocean during the last 13 cal ka BP. LIS position is from Dyke (2004) and sea level stages are from Manley (2002). SSC: Eastern Siberian Coastal Current; ACC: Alaskan Coastal Current; BG: Beaufort Gyre.

Previous sedimentological studies have shown the importance of sea ice transport along the Chukchi-Alaskan margin during the last deglacial-Holocene period (Darby et al., 2012;

Yamamoto et al., 2017). Thus, as the LREE are lodged in clay mineral structures (notably in illite and kaolinite; Fig. 53D) in the fine fraction, we hypothesize that sediment-laden meltwater plumes derived from glacial erosion in the Mackenzie River basin during the early Holocene were incorporated on the shelf by sea ice and subsequently transported westward through an enhanced BG (Fig. 57). The BG strengthening during the early Holocene is likely driven by a maximum boreal summer insolation (Gajewski, 2015; Yamamoto et al., 2017). During the early to late Holocene, the progressive decrease observed in the log(La/Sc), log(LREE/HREE) and log(ΣREE/Ti) ratios, together with low illite and kaolinite contents, suggest a long-term decrease in the Mackenzie-derived sediments and an increase in Bering Strait sediment sources (Fig. 57). We infer that this long-term decrease in the North American margin sediment input in core 05JPC is related to a progressive weakening of the BG strength, which was driven by decreasing summer insolation (Yamamoto et al., 2017). These observations are also supported by an increase in the proportion of chlorite, vermiculite and feldspar contents and sediment derived from the Bering Strait (Fig. 57), which also suggests an enhanced increase in Bering Strait inflow into the Chukchi Sea during the early to late Holocene (Deschamps et al., 2018a). Furthermore, this increased Bering Strait inflow trend shows a parallel temporal evolution with regional sea level variations between 10.5 and 7 cal ka BP (Fig. 57). Thus, increasing sea level most likely promoted the remobilization of sediments stored on the Chukchi Shelf and the subsequent sediment transport from the Pacific towards the western Arctic Ocean, and therefore, exerted significant control on sedimentation in the western Arctic Ocean during the early to mid-Holocene (Deschamps et al., 2018a; Keigwin et al., 2006).

3.8 Conclusion

The elemental geochemical signatures obtained from both the bulk and clay fractions of two sediment cores recovered on the Canadian Beaufort (core 02PC) and Chukchi-Alaskan (core 05JPC) margins highlight the evolution of the origin, transport, and dynamics of de-

trital sediments in the western Arctic Ocean since the last deglacial period (summarized in Fig. 58). These data provide additional information related to mineralogical and elemental geochemical records, which were previously published by (Deschamps et al., 2018a). The comparison of these studies robustly confirms that grain-size, clay minerals (notably, illite and kaolinite) and the relative contribution of different sediment sources (e.g., Bering Strait *vs*. Mackenzie River) are the most important factors that control the REE composition in western Arctic sediments.

In the Canadian Beaufort margin, excluding the IRD intervals, the major sediment source in core 02PC was related mainly to the input of felsic material coming from the Mackenzie River since the last deglacial period. The dolomite-rich IRD are related to the debacle of the Amundsen Ice Stream, whereas the quartz and feldspar-rich IRD is linked to the outburst flooding from Lake Agassiz. Our detrital proxies suggest an enhanced detrital input from the northern tributaries of the Mackenzie River during the Younger Drays probably linked to the final recession of the LIS.

In the Chukchi-Alaskan margin, geochemical signatures in core 05JPC suggest that a felsic source primarily from the Mackenzie River was dominant during the deglacial/Holocene interval, whereas with the rapid postglacial transgression, a more mafic source coming from the Bering Strait was dominant during the mid to late Holocene. The opening of the Bering Strait at ~11 cal ka BP is typified in core 05JPC by a marked decrease in log(La/Sc) and log(REE/Ti) ratios, which is related to the depleted nature of the mafic sediment source. Furthermore, the felsic source composition of sediments in the dolomite-rich and quartz-rich IRD support the idea that these IRD are derived mainly from North American sources (notably from the Amundsen Gulf Ice Stream) and Brooks Range glaciers in northwestern Alaska, respectively.

Finally, discriminant plots based on major elements and REE appear to be useful tools to discriminate between different continental sources which delivered sediment to the western Arctic Ocean, and to determinate of possible oceanographic and/or climatic forces acting on

sedimentation during the Late Quaternary.

3.9 Acknowledgments

We sincerely thank the captains, officers, crew and scientists on board the USCGC Healy and the CCGS Amundsen for the recovery the cores used in this study. These cores were collected as part of the HOTRAX expedition (USCGC Healy), as well as the CASES and ArcticNet (CCGS Amundsen) programs. We also thank Quentin Beauvais (UQAR-ISMER), Mathieu Babin (UQAR-ISMER), and Adriana Gamboa (UQAR-ISMER and UDO) for their technical support and advice in the laboratory. This research was funded by the Natural Sciences and Engineering Research Council of Canada (NSERC) through Discovery Grants to J.-C. Montero-Serrano and G. St-Onge, as well as through ship time support for several expeditions (J.-C. Montero-Serrano and G. St-Onge).

3.10 Supporting Material

3.10.1 Sediment cores and sampling

The sediment cores 02PC and 05JPC present two distinct sedimentary units. Core 02PC consists of homogeneous olive-brown to dark-gray for the upper unit, while the second unit consists of dark-gray with the presence of white clasts interpreted as IRD (Deschamps et al., 2018b). According to Barletta et al. (2008), the upper unit in core 05JPC is composed of olive-gray mud, and the second unit is characterized by dark-gray mud with sandy layers and IRD. The sediment core 02PC was sampled systemically every 10 cm in the IRDs intervals and every 20 cm in the remaining intervals for a total of 31 samples. The sediment core 05JPC was sampled every 80 cm for the first 11 meters (corresponding to the Holocene sediments) and every 30 cm for the remaining sections (corresponding to the deglacial sediments) for a total of 30 samples. Furthermore, six surface samples from the Mackenzie Trough and the

Southwestern Banks Island samples were also measured to observe the relative differences between the sediment compositions within the Canadian Beaufort margin.

3.10.2 Geochemical analysis

Before the geochemical analysis, the sediment samples were rinsed five times with distilled water after the removal of organic matter and biogenic carbonate fractions with 10 mL of hydrogen peroxide (30 % H_2O_2) and 10 mL of hydrochloric acid (0.5 N), respectively. Next, an aliquot of these sediment samples was used as bulk fraction, whereas another aliquot was used to separate the clay-size fraction (< 2 μm). A centrifuge based Atterberg method according to Stoke's Law was used to separate the clay-size fraction. Subsequently, aliquots of the bulk and clay-size-separated samples were oven dried overnight at about 60°C and then slightly homogenized with an agate mortar. These homogenized sediment fractions were used for geochemical analysis.

A total of 9 elements (Al, Si, K, Mg, Ca, Ti, Fe, P, and Zr) were analyzed on both bulk and clay-size fractions by energy dispersive X-ray fluorescence (EDXRF) spectrometry using a PANalytical Epsilon 3-XL. Around 0.6 g was mixed with ~0.6 g of lithium borate with lithium bromide flux (CLAISSE, pure, 49.75 % LiB4O7, 49.75 % LiO2, 0.5 % LiBr). The mixtures were melted in Pt-Au crucibles and after fusion in a CLAISSE® M4 Fluxer. The melts were cast to flat disks in Pt–Au moulds. Analytical accuracy and precision was found to be better than 1-5 % for major elements and 5-10 % for the other elements, as checked by an international standard (USGS SDC-1) and analysis of replicate samples.

Abundances of REE and further major and trace elements (e.g., Na, Sc, Rb, Hf, Th; Table 12-13) were analyzed by laser ablation inductively coupled plasma mass spectrometry (LA-ICP-MS) as described in previous studies (Jackson, 2001; Leite et al., 2011; Wegner et al., 2015). A NewWave UP213 196 nm excimer ablation system interfaced to an inductively coupled plasma-quadrupole mass spectrometer (ICP-QMS Agilent 7500c) was used

for the ablation of the lithium tetraborate discs previously analyzed by XRF. Operating conditions of the ablation system included a 10 Hz repetition rate, 100 μm spot size, 5 μm.s^{-1} scanning velocity, and 10 J.cm^{-2} on-sample energy density. Helium was used as a carrier gas; the make-up gas argon was admixed after the ablation cell and the aerosole carried to ICP-QMS. The acquisition times for the background and the ablation interval were 170 and 370 s, respectively. Dwell times per isotope ranged from 10 ms for major elements to 30 ms for trace and REE, and peak hopping mode was employed. The ICP-QMS system was tuned using a NIST SRM 612 synthetic glass standard to ensure robust plasma conditions, while maximizing signal to background intensity ratio and retaining low oxide production levels (< 0.5 % ThO). Bracketed external standardization used NIST SRM 612 glass. Aluminum content obtained by XRF was used for internal standardization. Data reduction for concentration and limit of detection calculation was undertaken off-line using the software LAMTRACE (Jackson, 2008). Procedural blanks always accounted for less than 1 % of the lowest concentration measured in the samples. The analytical accuracy and precision were found to be better than 10 % for all REE, as checked by NIST SRM 612 and USGS SBC-1 standards and analysis of replicate samples (Table 8). In addition and for comparison, abundances of REE and further trace elements (e.g., Sc, Rb, Hf, Th; Table S1) for 4 sample in core 02PC (126, 131, 134, 139 cm) including the bulk and clay fractions were analyzed at Geoscience Laboratories (Ontario, Canada). Sample were digest using a multi-acid digestion (HF+HNO_3+$HClO_4$) in close vessel and then analyzed on a ICP-MS Perkin Elmer Elan 9000. The analytical accuracy and precision were found to be better than 3% for all REE, as checked by USGS SBC-1 standards. Procedural blanks always accounted for less than 0.6% of the lowest concentration measured in the samples. Fig. 59 shows similar PAAS-normalized REE patterns for samples obtained by LA-ICP-MS on fused-beads with those obtained by ICP-MS on multi-acid digests solution, thus validating by an independent method the LA-ICP-MS methodology used here.

A compositional Q-mode cluster analysis (Egozcue and Pawlowsky-Glahn, 2005) and principal component analyses (PCA) was performed on our elemental geochemical dataset

with the goal of finding elemental associations with similar relative variation patterns that may be interpreted from a palaeoenvironmental standpoint (Montero-Serrano et al., 2015). This analysis was carried out using a log-ratio approach (Aitchison, 1990). Likewise, as measure of dissimilarity we use the variation array, and as clustering criterion the Ward method. Q-mode cluster analysis were conducted with "R" software using the packages "StatDA" (Reimann et al., 2008) and "compositions" (Van Den Boogaart and Tolosana-Delgado, 2008). PCA was performed using "CoDaPack" software (Thió-Henestrosa and Martín-Fernández, 2005). Loadings derived from the principal component analysis are shown in Table 9.

The chemical index of alteration, defined as: CIA = 100 × Al_2O_3/(Al_2O_3 + CaO* + Na_2O + K_2O) in molar proportions (Nesbitt and Young, 1982), was used as a proxy to the degree of weathering in the source areas. This index essentially describes the weathering degree of aluminum silicate minerals especially from feldspar to clays. CaO* is restricted to the CaO present in silicate minerals, i.e. excluding calcite, dolomite and apatite (McLennan, 1993). Thus, in this study, CaO was corrected (CaO*) for phosphate using P_2O_5. If the remaining number of moles is less than that of Na_2O, this CaO value was adopted. If the number of moles is greater than Na2O, CaO* was assumed to be equivalent to Na_2O.

Table 8: Major, trace, REE composition of reference glass bead USGS SBC-1 and NIST SRM 612. Reference values are from GEOREM (http://georem.mpch-ainz.gwdg); SD and RSD are standard deviation and relative standard deviation, respectively; Diff. = ((Reference value – measured value)/ reference value)*100.

LA-ICP-MS	Na_2O (wt%)	Al_2O_3 (wt%)	CaO (wt%)	Sc (ppm)	Co (ppm)	Rb (ppm)	La (ppm)	Ce (ppm)	Pr (ppm)	Nd (ppm)	Sm (ppm)	Eu (ppm)
SBC-1 ref	0.35	22.60	Nd.	23.80	24.60	156.00	60.70	121.00	13.20	54.00	10.80	2.26
SBC-1 (n=5)	1.35	22.80	3.42	25.34	21.91	128.60	58.60	107.40	13.22	53.70	10.85	2.00
SBC-1 SD	0.23	0.00	0.13	1.83	0.87	4.51	4.31	4.16	0.38	3.01	1.14	0.14
SBC-1 RSD (%)	16.81	0.00	3.94	7.22	3.95	3.50	7.35	3.87	2.90	5.60	10.55	6.94
NIST612 ref	13.30	1.99	11.90	41.00	35.30	31.60	35.80	37.11	35.20	36.70	34.40	
NSIT612 (n=40)	13.29	1.99	11.84	41.00	35.22	31.60	35.73	38.30	37.11	35.20	36.68	34.39
NIST612 SD	0.13	0.03	0.14	0.68	0.50	0.40	0.55	0.61	0.46	0.61	0.69	0.55
NIST612 RSD (%)	1.01	1.28	1.16	1.66	1.43	1.25	1.55	1.59	1.25	1.74	1.88	1.60
LA-ICP-MS	Gd (ppm)	Tb (ppm)	Dy (ppm)	Ho (ppm)	Er (ppm)	Tm (ppm)	Yb (ppm)	Lu (ppm)	Hf (ppm)	Ta (ppm)	Th (ppm)	U (ppm)
SBC-1 ref	7.89	1.56	7.46	1.60	4.09	0.57	4.33	0.50	3.92	0.92	16.80	6.32
SBC-1 (n=5)	9.37	1.33	8.04	1.63	4.52	0.66	4.64	0.61	4.09	1.22	17.96	5.57
SBC-1 SD	0.30	0.10	0.36	0.10	0.40	0.10	0.36	0.09	0.31	0.10	1.17	0.20
SBC-1 RSD(%)	3.18	7.81	4.53	6.01	8.86	18.51	7.70	14.35	7.63	7.79	6.52	3.56
NIST612 ref	37.00	35.90	36.00	37.90	37.40	37.60	40	37.70	34.80	39.80	37.20	37.20
NIST612 (n=40)	36.91	35.88	35.93	37.82	37.39	37.50	39.90	37.67	34.73	39.72	37.18	37.11
NIST612 SD	0.67	0.66	0.69	0.66	0.59	0.66	0.67	0.72	0.68	0.49	0.56	0.60
NIST612 RSD (%)	1.80	1.83	1.91	1.76	1.59	1.76	1.67	1.92	1.95	1.23	1.51	1.61
ICP-MS	Na_2O (wt%)	Al_2O_3 (wt%)	CaO (wt%)	Sc (ppm)	Co (ppm)	Rb (ppm)	La (ppm)	Ce (ppm)	Pr (ppm)	Nd (ppm)	Sm (ppm)	Eu (ppm)
SBC-1 ref	-	-	-	23.80	24.60	156.00	60.70	121.00	13.20	54.00	10.80	2.26
SBC-1 (n=2)	-	-	-	20.7	22.85	146.87	50.95	106.2	12.97	50.06	9.94	1.97
SBC-1 SD	-	-	-	0.14	0.02	1.87	1.00	3.79	0.17	1.13	0.06	0.01
SBC-1 RSD (%)	-	-	-	13.03	7.09	5.85	16.07	12.24	1.78	7.30	7.97	13.00
ICP-MS	Gd (ppm)	Tb (ppm)	Dy (ppm)	Ho (ppm)	Er (ppm)	Tm (ppm)	Yb (ppm)	Lu (ppm)	Hf (ppm)	Ta (ppm)	Th (ppm)	U (ppm)
SBC-1 ref	7.89	1.56	7.46	1.60	4.09	0.57	4.33	0.50	3.92	0.92	16.80	6.32
SBC-1 (n=2)	8.13	1.22	7.15	1.37	3.90	0.56	3.64	0.54	3.74	1.09	15.01	5.80
SBC-1 SD	0.01	0.02	0.10	0.02	0.05	0.01	0.00	0.00	0.01	0.01	0.37	0.05
SBC-1 RSD (%)	3.08	22.11	4.19	14.21	4.71	2.48	15.91	7.26	4.72	18.97	10.63	8.28

Table 9: Loadings derived from the principal component analysis of REE from the database and cores 05JPC and 02PC, which illustrates the weight of each element in the definition of each PC score.

	clr.La	clr.Ce	clr.Pr	clr.Nd	clr.Sm	clr.Eu	clr.Gd	clr.Tb	clr.Dy	clr.Ho	clr.Er	clr.Tm	clr.Yb	clr.Lu	Cum.Prop.Exp.
PC1	0.43	0.44	0.34	0.26	0.11	0.04	0.00	-0.17	-0.19	-0.25	-0.20	-0.24	-0.22	-0.35	0.55
PC2	-0.26	-0.18	-0.09	-0.02	0.17	0.55	0.32	0.23	0.12	0.01	0.00	-0.08	-0.21	-0.55	0.75

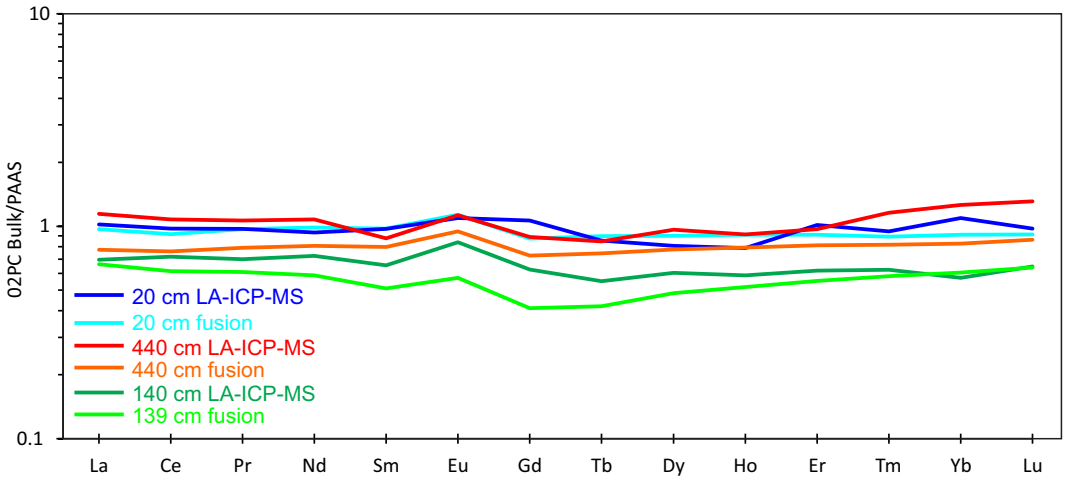

Figure 59: Comparison of PAAS-normalized REE patterns obtained by LA-ICP-MS on fused-beads with those obtained by ICP-MS on multi-acid digests solution ($HF+HNO_3+HClO_4$) for 4 samples in core 02PC (126, 131, 134, 139 cm).

ARTICLE 4

CHANGEMENTS HOLOCÈNES DANS LA CIRCULATION EN EAU PROFONDE DANS L'OCÉAN ARCTIQUE OCCIDENTAL À PARTIR DES ISOTOPES RADIOGÉNIQUES DU ND ET DU HF

4.1 Résumé en français du quatrième article

La concentration en terres rares (REE), la mesure des isotopes radiogéniques du Sr-Nd-Hf dans les lixiviats des sédiments ainsi que les signatures minéralogiques, ont été étudiées sur deux carottes sédimentaires récupérées sur la marge canadienne de Beaufort (AMD0214-02PC) et la marge d'Alaska (HLY0501-01JPC). Ces données ont permis d'étudier les changements des régimes d'altération et de la circulation en eau profonde pendant l'Holocène. Les évolutions couplées des compositions isotopiques du Nd et Hf (exprimées en unités epsilon: εNd et εHf) sont similaire avec les données modernes des eaux du Pacifique, de l'Atlantique et du fleuve Mackenzie. Ces résultats suggèrent que la formation de saumure joue un rôle important dans les signatures εNd et εHf des eaux de fond dans l'océan Arctique occidental. Les signatures εNd et εHf dans les marges canadiennes de Beaufort et des Tchouktches changent vers des valeurs plus radiogéniques au cours de l'Holocène. D'après les enregistrements εNd et εHf, les valeurs moins radiogéniques ne sont pas contrôlées par la provenance et le mélange des masses d'eau, mais plutôt par la provenance et un changement du régime d'altération dans les bassins versants des fleuves Mackenzie et du Yukon au début et au milieu de l'Holocène. Cependant, les valeurs plus radiogéniques en εNd et εHf, couplées avec les enregistrements minéralogiques à la fin de l'Holocène, sont principalement contrôlés par une augmentation de l'afflux d'eau via le détroit de Béring, résultant des changements des modes de variabilités climatique du Pacifique (tels que PNA/PDO/ENSO).

Le second article de cette thèse intitulé "*Holocene changes in deep water circulation in the western Arctic Ocean inferred from authigenic Nd and Hf isotopes* " a été rédigé par moi-même sous la supervision de mon directeur et mon co-directeur soit Jean-Carlos Montero-Serrano (UQAR-ISMER), Guillaume St-Onge (UQAR-ISMER) mais aussi André Poirier (UQAM-GEOTOP). L'article sera soumis prochainement dans la revue *Paleoceanography and Paleoclimatology*.

4.2 Holocene changes in deep water circulation in the western Arctic Ocean inferred from authigenic Nd and Hf isotopes

Rare earth element (REE) concentrations and radiogenic isotopes (Sr-Nd-Hf) retrieved from bulk sediment leachates, together with bulk and clay mineralogical signatures, were studied on two piston cores recovered in the Canadian Beaufort (AMD0214-02PC) and Chukchi-Alaskan (HLY0501-01JPC) margins to investigate changes in the weathering regimes and deep-water circulation during the Holocene. The coupled evolutions of the Nd and Hf isotopic compositions (expressed in epsilon unit: εNd and εHf, respectively) are in good agreement with modern seawater and bulk sediment leachate data from Pacific water, Atlantic water and the Mackenzie River and support the idea that brine formation plays a significant role in the εNd and εHf signatures of the bottom waters in the western Arctic Ocean. The εNd and εHf signatures in the Canadian Beaufort and Chukchi-Alaskan margins reveal changes towards more radiogenic values from the early- to late-Holocene. Based on the εNd and εHf records, we suggest that the unradiogenic values are not controlled by water mass provenance and mixing but rather by provenance and a change in the weathering regime over the Mackenzie and Yukon drainage basins during the early- to mid-Holocene. However, more radiogenic εNd and εHf, combined with mineralogical records in the late-Holocene, has primarily been controlled by an increase in the Bering Strait inflow, which is likely related to major changes in the atmospheric climate mode (such as PDO/PNA/ENSO).

4.3 Introduction

The Arctic Ocean plays an important role in regulating Earth's climate because (1) its perennial sea ice cover modulates the atmospheric and oceanic heat budget since it reflects a large part of the incoming solar radiation during the summer (albedo) and acts as an insulating shield during the winter (Serreze et al., 2007) and (2) the export of freshwater into the North Atlantic affects the Atlantic meridional overturning circulation by changing the deep-

water convection (Dickson et al., 2007). The northward flows of Atlantic and Pacific waters are the major sources of heat advection toward the Arctic Ocean and strongly affect sea ice distribution (Kinnard et al., 2011; Polyakov et al., 2017). Indeed, the increase in warm Atlantic water over the past 2 000 years seems to be the main factor in sea ice decline induced by retroaction from sea ice (Kinnard et al., 2011). Likewise, the advection of warm Pacific water into the Arctic Ocean induces a greater supply of heat in the western Arctic Ocean and acts as a trigger for sea ice decline in the Chukchi Sea (Shimada et al., 2006). In this context, paleoceanographic and paleoclimate proxy records from marine sediment cores can provide evidence for the large-scale natural variability in the Arctic deep-water circulation during the Late Quaternary against which recent changes can be compared. A better understanding of the past variation in the deep-water circulation may help to decipher the processes controlling Arctic climate and sea ice variability.

The content of dissolved trace elements in the oceans mainly derives from riverine and eolian inputs determined by weathering processes on the adjacent continents, as well as from shelf exchange processes (Frank, 2002; Jeandel et al., 2007). Water masses of different origins therefore acquire distinct elemental and radiogenic isotope compositions in their source areas (Frank, 2002). In particular, neodymium ($^{143}Nd/^{144}Nd$) and hafnium ($^{176}Hf/^{177}Hf$) can be used as sensitive tracers for water mass mixing and provenance (Chen et al., 2012; Rickli et al., 2009; Stichel et al., 2012) and past continental weathering (Gutjahr et al., 2014; Rickli et al., 2010) at different time scales. The Nd and Hf isotope compositions are expressed in epsilon units, which correspond to the relative deviation of the $^{143}Nd/^{144}Nd$ and the $^{176}Hf/^{177}Hf$ of a sample from the Chondritic Uniform Reservoir (CHUR: $^{143}Nd/^{144}Nd$=0.512638 (Jacobsen and Wasserburg, 1980) and $^{176}Hf/^{177}Hf$= 0.282769 (Nowell et al., 1998)) in parts per 10,000. Because dissolved trace elements are incorporated by co-precipitation processes during early burial in the top few centimeters of the sediments (Haley et al., 2004; Bayon et al., 2004), the authigenic Nd and Hf signatures can be extracted from ferromanganese (Fe-Mn) oxyhydroxide coatings on marine sediment samples (Bayon et al., 2004; Gutjahr et al., 2007). The Nd and Hf isotope compositions of rocks largely depend on the lithology and the crustal

age. For example, low $^{143}Nd/^{144}Nd$ values (εNd of -40) reflect old continental crust, while high $^{143}Nd/^{144}Nd$ values (εNd of +20) reflect young mantle derived rocks (Frank, 2002). The variability in the Hf isotope composition in terrestrial rocks is larger than the Nd, ranging from the most unradiogenic values of εHf ~ -50 in Archean rocks to values as high as +25 in the mid-ocean ridge basalt (Zimmermann et al., 2009b). Based on these findings, the analysis of εNd and εHf signatures of authigenic fractions in marine sediments is a powerful tool for assessing Late Quaternary changes in water mass provenance and transport.

Taking this into account, a number of studies have investigated the seawater Nd and Hf isotope compositions of past Arctic Intermediate Water extracted from the authigenic Fe-Mn oxyhydroxide fraction of late Tertiary (mid-Miocene) to Quaternary sedimentary records (Chen et al., 2012; Haley et al., 2008; Meinhardt et al., 2016) to decipher changes in the weathering regimes and water mass mixing. Likewise, modern Nd and Hf isotope compositions of seawater in Arctic Ocean basins (Porcelli et al., 2009; Zimmermann et al., 2009a), and pre-modern authigenic Nd isotope signatures of surface sediments from the Arctic Ocean seafloor (Haley and Polyak, 2013) have been investigated to better present the Arctic Ocean's circulation patterns. Nonetheless, the Holocene variability in the contributions of different water masses to the deeper parts of the western Arctic Ocean is as yet not completely understood. Thus, authigenic Nd and Hf isotopic compositions retrieved from sediment cores may provide new clues concerning the evolution of the Holocene deep circulation and climate in the western Arctic Ocean, which may then help to place modern environmental changes in perspective. Such studies may provide new clues concerning the evolution of the past deep circulation and climate in the western Arctic Ocean, which may then help to place modern environmental changes in perspective.

In this context, the Nd and Hf isotope signatures and the REE concentrations obtained from the authigenic Fe-Mn oxyhydroxide fractions, together with the bulk and clay mineralogical analysis, of two sediment piston cores recovered from the Chukchi-Alaskan (core HLY0501-01JPC) and Canadian Beaufort (core AMD0214-02PC) margins are used here to

(1) assess changes in the deep water masses provenance, (2) interpret variations in the dynamics of deep water circulation in terms of paleoenvironmental changes since the last deglaciation, and (3) provide new insights on the potential relationships between changes in erosional inputs and oceanic circulation variations in the western Arctic Ocean since the last deglaciation.

4.4 Regional Setting

4.4.1 Oceanic circulations

The Arctic surface oceanic circulation is related to two main, wind-driven circulation systems, which are the anticyclonic Beaufort Gyre (BG) in the western Arctic and the Transpolar Drift (TPD; Darby and Bischof, 2004). On the Beaufort Shelf, the anticyclonic BG pushes both surface currents and sea ice westward at the shelf break. Conversely, closer to shore around the 50-m isobath, the Beaufort Undercurrent transports both Pacific and Atlantic waters eastward along the continental margin and into the Amundsen Gulf (Forest et al., 2011). The Atlantic waters (AW) flow through the Fraim Strait and the Barents Sea. The depth of the Atlantic waters is between 200 and 1000 m and has a temperature above 0°C (Rudels et al., 2004). The AW circulation is counterclockwise along the margins of the Arctic Ocean. It begins along the Eurasian margin and then separates at the level of the Lomonosov Ridge. A branch of the AW circulation diverges towards the eastern face of the Lomonosov Ridge, and the other branch continues in the Canadian basin (Poirier et al., 2012; Fig. 60). The modern Nd and Hf isotope signatures of the AW in Arctic Ocean basins have been studied in Zimmermann et al. (2009a), Porcelli et al. (2009) and Haley et al. (2008), and the results showed εNd and εHf values of -9 and 1.6, respectively.

The Chukchi Shelf circulation is controlled by an inflow of Pacific waters via the Bering Strait (referred as the Bering Strait inflow), the Siberian coastal current, and the Atlantic Intermediate Water affecting the northern margin (Pickart, 2004; Weingartner et al., 2005). Warm

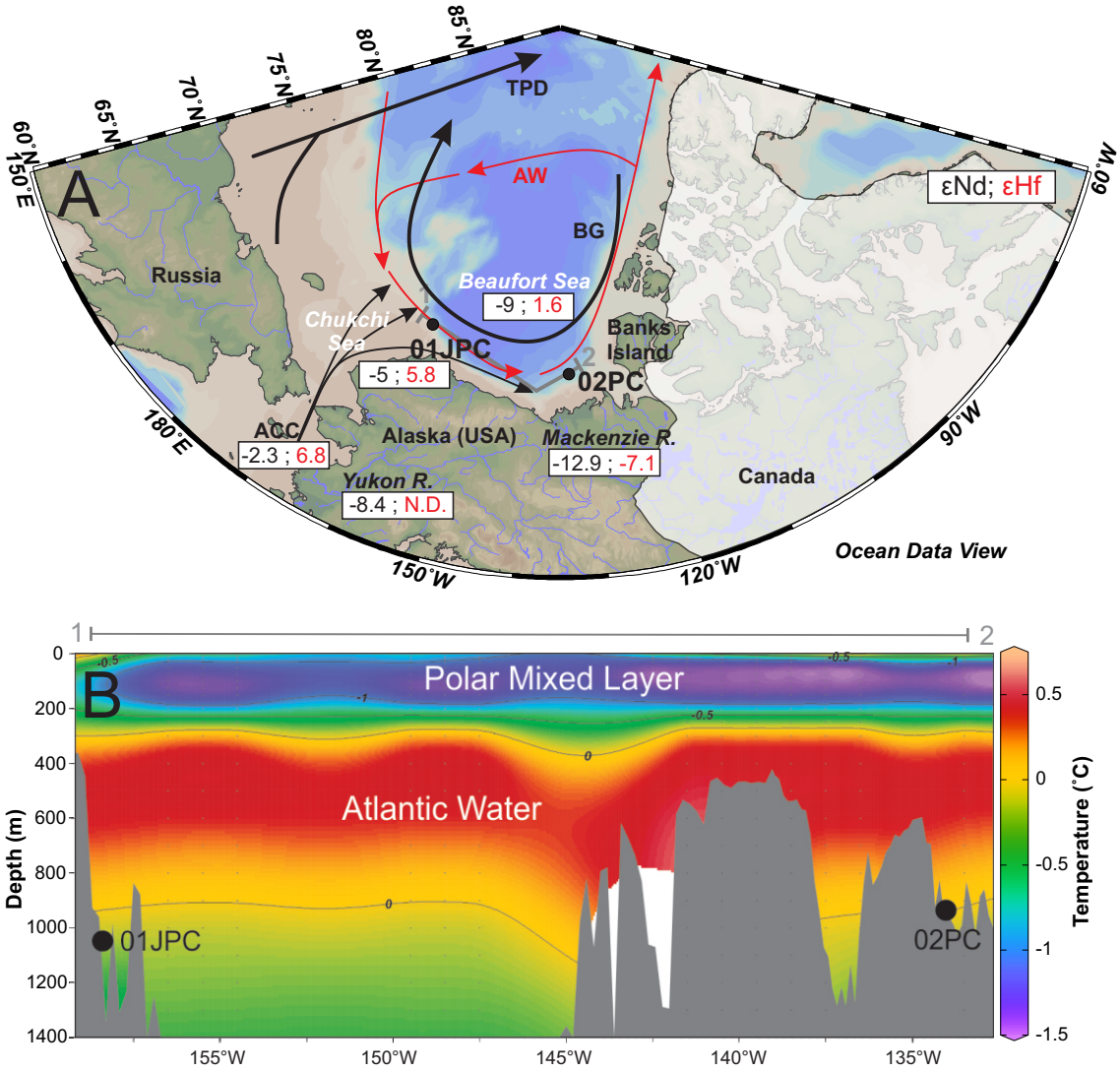

Figure 60: (A) Schematic map of Atlantic water (AW), Pacific water (PW), Transpolar Drift (TPD) and Beaufort Gyre (BG) circulation in the Arctic Ocean and locations of cores 01JPC and 02PC (black circles). The Pacific water drifts eastward in the Beaufort Sea and is known as the Alaskan Coastal Current (ACC). The εNd and εHf values are shown in the map. Also shown the Laurentide Ice Sheet at 11.5 cal ka BP (Dyke, 2004). (B) East-west mean annual temperature profile across the Beaufort-Chukchi slope (transect 1-2 in gray). Core sites are marked by black circles. Temperature data are from Polar Science Center Hydrographic Climatology (PHC, http://psc.apl.washington.edu/Climatology.html).

Pacific water from the Bering Sea flows into the Chukchi Sea in three major branches (Fig. 60). The first branch turns westward around Herald Canyon. The third branch flows into Barrow Canyon following the northwestern Alaskan coast in the eastern Chukchi Sea (known as the Alaska Coastal Current or ACC; Okkonen et al., 2009), whereas the second branch flows

between the first and the third branches (Weingartner et al., 2005). The Bering Strait inflows are controlled mainly by the Aleutian Low pressure center's strength and position at the inter-annual time scales (Yamamoto et al., 2017). Indeed, periods of strengthening of the Aleutian Low pressure center, located over the eastern North Pacific, induce an increase in the Bering Strait inflow into the Arctic Ocean (Danielson et al., 2014). According to modern hydrographic observations, dense waters (brines) generated at the Chukchi-Alaskan margin during the fall/winter sea-ice formation can descend to the pycnocline depth of up to 200 m (Pickart et al., 2005; Weingartner et al., 2005). Corlett and Pickart (2017) have shown that Pacific water flows into the Barrow Canyon and forms a slope current they have called the Chukchi Slope current. The Chukchi Slope current can transport 0.50 Sv of Pacific water westward of Barrow Canyon and can extend into the Atlantic layer (Corlett and Pickart, 2017). The isotopic signature of the Pacific water before entering the Chukchi Sea has been described in Zimmermann et al. (2009b) with εNd values of approximately -2.3 and εHf values ranging from 3.5 to 8.6 with a mean value of 6.8. The isotopic signature of the Pacific throughflow water in the Chukchi Sea is εNd= -5 and εHf= 5.8 (Haley and Polyak, 2013; Porcelli et al., 2009; Zimmermann et al., 2009b). The change in terms of the isotopic signature of the Pacific water before and after the Bering Strait is possibly due to the influence of runoff from the Yukon and Anadyr rivers and/or "boundary exchange" with Bering Strait sediments (Haley and Polyak, 2013; Porcelli et al., 2009) (Haley and Polyak, 2013; Porcelli et al., 2009). The εNd signature of the Yukon River is εNd= 8; however, its Hf isotopic signature is still unknown (Horikawa et al., 2010).

4.4.2 Sedimentation

On the Canadian Beaufort shelf, most of the surficial seabed sediments are predominantly composed of Holocene marine olive-gray silts and clays (Gamboa et al., 2017). Surface sediments from the Chukchi Sea are composed of bioturbated gray to clayey silts (Kobayashi et al., 2016). The modern sedimentation in the Chukchi Sea is believed to be mainly derived

from northeastern Siberia, the Bering Strait inflow (especially from the Yukon River) and the Mackenzie River, whereas the Canadian Beaufort margin sediment originates primarily from the Mackenzie River basin (Darby et al., 2011; Gamboa et al., 2017; Kobayashi et al., 2016). Smaller Alaskan rivers have a more local impact but may have been a more important sediment source at the early stages of the last transgression (Hill and Driscoll, 2008). During deglaciation and the early Holocene, sediment inputs to the Chukchi-Alaskan and Beaufort margins were presumably higher due to the rising sea level associated with meltwater and iceberg discharge from the retreating of large ice sheets (Deschamps et al., 2018a). During the Holocene or interglacial period, sediment redistribution is strongly controlled by bottom currents, while during the deglacial/glacial period, sea ice and ice rafted debris (IRD) strongly affected sediment dispersal and deposition (Darby et al., 2009). In fact, several IRD have been recorded in the sedimentation along the North American margin during the last deglaciation that are linked to the debacle of the Laurentide and Innuitian Ice Sheets (Darby and Zimmerman, 2008).

4.5 Material and methods

4.5.1 Sample and chronology

The sediment core HLY0501-01JPC (hereinafter referred to as core 01JPC; water depth: 1163 m; location: 72°90'N, 158°42'W) was recovered in the Chukchi-Alaskan margin on board the USCGC Healy as part of the 2005 Healy-Oden Trans-Arctic Expedition (Fig. 60). Core AMD0214-02PC (hereinafter referred as core 02PC; water depth: 998 m; location: 71°22.910'N, 133°34.040'W) was collected on the Canadian Beaufort margin on board the CCGS Amundsen during the 2014 ArcticNet expedition (Fig. 60). Age models and physical properties of the 01JPC and 02PC sediment cores have been described in Deschamps et al. (2018b). The sedimentation rate for core 02PC ranged from 2-20 cm.ka^{-1} in the postglacial parts, whereas the sedimentation rate in core 01JPC is constant in the postglacial unit (60

cm.ka^{-1}). The core 01JPC is characterized by a hiatus in the sedimentary sequence at approximately 6 cal ka BP and the deglacial parts of the core Deschamps et al. (2018b). For this reason, only the Holocene parts of the core 01JPC have been sampled (n=11, resolution of 500 years). The core 02PC spans the last 13.5 cal ka BP and is characterized by two IRD interval between 140 and 160 cm (IRD1) and 320 and 360 cm (IRD2) (Deschamps et al., 2018b). In this study, we focus on the last 11.5 cal ka BP (n= 22, resolution of 500 years).

4.5.2 Radiogenic isotopes and REE analyses

Bulk sediment leaching

Seawater Sr, Nd and Hf isotopic signatures from authigenic Fe-Mn coatings of the bulk sediment were extracted applying the leaching protocol of Chen et al. (2012). Briefly, 1 g of dried and powdered sediments was rinsed three times with Milli-Q water. Next, Sr, Nd and Hf contained in the sediment oxyhydroxide fraction were leached for approximately 1h in a single step using a dilute reducing and complexing solution consisting of 0.005 M hydroxylamine hydrochloride (HH), 1.5 % acetic acid, and 0.03 M Na-EDTA, buffered to pH = 4 with suprapur®NaOH. A buffered acetic acid leach step was omitted since biogenic carbonates are negligible in all sediment samples (Deschamps et al., 2018a). The hydroxylamine hydrochloride and acetic acid mixture was 10-fold diluted compared with the method of Gutjahr et al. (2007) to avoid any potential contamination caused by the leaching of clay minerals. During treatment, the sediment samples were gently shaken to enhance the reaction. After centrifugation, the leach solution was decanted, evaporated and re-dissolved in 2 mL of 2.5 M HCl. This last solution was divided into two aliquots of 1 mL, one for the REE concentration analyses and the other one for the Nd and Sr chromatographic extraction. The aliquot for REE concentration analysis was evaporated almost to dryness, and the residue was re-dissolved in 1 mL of concentrated HNO_3 and subsequently diluted with Milli-Q water to a total volume of 5 mL.

Sr, Nd and Hf separation: column chemistry

The Sr, Nd and Hf were separated from the other elements by applying a single-step ion chromatographic separation (Li et al., 2014). Briefly, the leaching solutions obtained from the previous steps were centrifuged at 5000 rpm for 8 min. Then, 1 mL of the supernatant solution was passed through a two-layered mixed resin column (70 mm length, 6 mm diameter) with the upper layer containing 1.5 mL of Biorad®AG50W-X12 (200–400 mesh) resin and the bottom layer containing 0.45 mL of Eichrom®LN Spec resin (100–150 μm). Before sample loading for the separation of Sr–Nd–Hf from the sample matrix, the mixed resin column was pre-washed with 18 mL of 6 M HCl, 8 mL of 3 M HF, and 4 mL of H_2O in turn. After sample loading and rinsing four times with 0.5 mL of 2.5 M HCl, the column was washed with 13.5 mL of 2.5 M HCl. Most matrix elements (K, Ca, Na, Mg, Al, Fe, Mn, Ti) and Rb were removed during this step. Then, the Sr fraction was stripped with 5.5 mL of 2.5 M HCl. Part of the HREE (Dy, Ho, Er, Tm, Yb, Lu) and Ba were then washed out with 3 mL of 2.5 M HCl. Next, the Nd was then isolated from the other REE with 8 mL of 6 M HCl. Finally, the Hf was isolated with 5 mL of 3 M Hf. Then, the Sr, Nd, and Hf fractions were dried on a hotplate at 120°C to dryness and prepared for isotope measurements.

3.2.3 REE concentrations and Sr-Nd-Hf analysis

The REE concentrations (La, Ce, Pr, Nd, Sm, Eu, Gd, Tb, Dy, Ho, Er, Tm, Yb and Lu) were determined using an inductively coupled plasma-quadrupole mass spectrometer (ICP-QMS Agilent 7500c) at ISMER. Procedural blanks always accounted for less than 1 % of the lowest concentrations measured in the samples. An in-house internal standard was used to monitor the external reproducibility and system drift. The analytical accuracy and precision were found to be better than 5 % for all of the REE (Table 12). The REE abundances were normalized to Post-Archean Australian Shale (PAAS; Taylor and McClennan, 1985) in order to evaluate the REE patterns as given in Maccali et al. (2013) and Du et al. (2016). The fractionation between the light REE (LREE: La–Nd), medium REE (MREE: Sm–Dy) and heavy REE (HREE: Tm–Lu) was investigated using the following indices: HREE/LREE

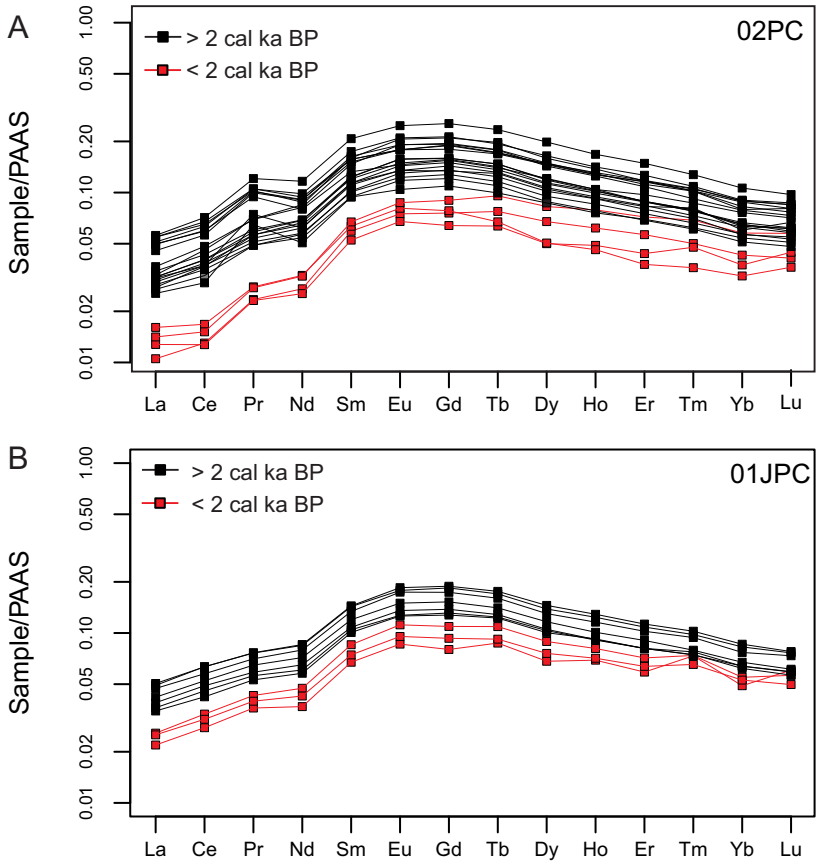

Figure 61: REE patterns normalized to PAAS (Taylor and McClennan, 1985) for the bulk sediment leachates samples of (A) core 01JPC (Chukchi-Alaskan margin) and (B) core 02PC (Canadian Beaufort margin).

([Yb + Lu]/[Pr + Nd] and MREE* (2[Tb + Dy]/[Pr + Nd + Yb + Lu]) to investigate the fractionation between LREE, MREE, and HREE (Du et al., 2016; Molina-Kescher et al., 2014).

The Sr isotopic ratios ($^{88}Sr/^{86}Sr$) were measured in dynamic mode on a Thermo Scientific Triton Plus™ multicollector thermal ionization mass spectrometer (TIMS) at GEOTOP (Montreal, Canada). The Sr samples were loaded and analyzed on a single zone-refined Re filament. Repeated analyses of the NIST-987 standard (n=6) yielded values of 0.710276 (±0.000021, 2σ reproducibility). This mean value compares well to its certified value of 0.710248 (Weis et al., 2006). The total procedural blanks for Sr were less than 0.5 ng, which is considered negligible compared to the sample yields (> 100 ng).

The Nd and Hf isotopic ratios ($^{143}Nd/^{144}Nd$ and $^{176}Hf/^{177}Hf$) were analyzed on a Nu Plasma II instrument, a Multi-Collector Inductively Coupled Plasma Mass Spectrometer (MC-ICP-MS), also at GEOTOP. The mass-bias correction was made by monitoring $^{146}Nd/^{144}Nd$ (taken to be equal to 0.7219) and $^{176}Hf/^{177}Hf$ (taken to be equal to 0.7325) and by applying an exponential beta factor correction to the other ratios. The external reproducibility was provided by the repeated measurements of the JNdi-1 (from 0.1 to 0.3 ε units, 2σ; n=31) and JMC 475 (0.5 to 1.3 ε units, 2σ; n=31) standards at the same concentration as the samples. The results were normalized to the accepted $^{143}Nd/^{144}Nd$ of 0.512115 for the JNdi-1 standard (Tanaka et al., 2000) and $^{176}Hf/^{177}Hf$ of 0.282160 for the JMC 475 (Nowell et al., 1998). Thus, the analytical error associated to each sample analysis is taken as the external reproducibility of the JNdi-1 and JMC 475 standard for each session. However, uncertainties estimated for Nd and Hf from some samples are artificially higher (up to 0.4 ε units for Nd and up to 9 ε units for Hf ; Table 11) than those of the Nd and Hf standards, due to use of a measurement method optimized for samples with low Nd-Hf concentration. The procedural blank values were < 0.5 ng for Nd and for Hf and were therefore neglected as they represented less than 0.1 % of the Nd and Hf analyzed per sample, respectively. The $^{143}Nd/^{144}Nd$ and $^{176}Hf/^{177}Hf$ isotopic ratios are expressed in ε units (εNd and εHf).

4.5.3 Bulk and clay mineralogical analyses

Complementary bulk mineral associations were studied by quantitative X-ray diffraction (qXRD) following the method developed by Eberl (2003). Briefly, ~1 g of each sample was spiked with 0.25 g of corundum, and the powder samples were scanned from 5° to 65° two-theta in steps of 0.02° two-theta on a PANalytical X'Pert Powder diffractometer. For the quantification of the major mineralogical components, sediment XRD scans obtained were converted into mineral weight percent (wt. %) using the Excel macro program ROCKJOCK v11 (Eberl, 2003). Then, we used the non-linear unmixing Excel macro program SedUnMixMC (Andrews and Eberl, 2012) to gain a quantitative understanding of the downcore

changes in bulk sediment provenance. In addition, clay mineral associations were studied using XRD following established protocols (Bout-Roumazeilles et al., 1999). The separated clay-sized fraction was concentrated by centrifugation and oriented by wet smearing on glass slides. The analyses were run from 2.49° to 32.49° two-theta on a PANalytical X'Pert Powder diffractometer. Three X-ray diagrams were performed, and after the sample was air-dried, ethylene glycol vapor saturation was completed for 12 h, followed by heating at 490°C for 2 h. A semi-quantitative estimation of clay mineral abundances (smectite, illite, chlorite, kaolinite, vermiculite and a chlorite/smectite mixed layer) based on peak areas was performed using the MacDiff 4.2.5 software (Petschick, 2000). Similar to other Arctic clay mineral studies (Schoster et al., 2000; Wahsner et al., 1999), the clay mineral contents were calculated by using the weighting factors introduced by Biscaye (1965) and calculated to a sum of 100 %. Note that bulk and clay mineralogical analyses on sediments for the core 02PC were reported previously (Deschamps et al., 2018a). In this study, based on a previous sediment provenance study in the western Arctic Ocean (Deschamps et al., 2018a), we used the proportion of sediments derived from the Bering Strait and Mackenzie River (SedUnMixMC results), as well as the amorphous silica contents and log(illite+kaolinite/chlorite+vermiculite) ratio or log(I+K/C+V) to trace sediment provenance changes over time. The high amorphous silica concentrations in the Chukchi Sea sediments are interpreted to show when biosilica-rich Pacific waters flowed through the Bering Strait (Jakobsson et al., 2017; Stein et al., 2017). Likewise, the log(I+K/C+V) ratio allowed us to discriminate between sediments from the Bering Strait (rich in chlorite and vermiculite) and sediments from the Mackenzie River (rich in illite and kaolinite).

4.6 Results

4.6.1 Authigenic REE distribution

The REE concentrations are presented in Table 10. The PAAS-normalized REE of the bulk sediment leachates from both cores reveals an MREE bulge-type pattern (Fig. 61), with an enrichment of MREE compared to HREE and LREE, which is often found for leachates (Du et al., 2016; Gutjahr et al., 2007). Likewise, in order to further evaluate the efficiency of our procedure to extract the authigenic phase, we compared the HREE/LREE ratio to the MREE* (Fig. 62B). The HREE/LREE-MREE* cross-plots reveal that all our bulk sediment leachates plot on the Fe-Mn leachate array (Du et al., 2016; Gutjahr et al., 2010). This indicates that authigenic Fe–Mn oxyhydroxide coatings control the Nd and Hf signals in our bulk sediment leachates. Furthermore, the significant negative correlation observed between the ΣREE content and εNd values in core 01JPC (r= -0.75) and 02PC (r= -0.59) suggests an enrichment in ΣREE towards more unradiogenic values (Fig. 62C).

4.6.2 Sr, Nd and Hf isotope signatures

The Sr, Nd, and Hf isotope data obtained from the leachates are provided in Table 11. The $^{87}Sr/^{86}Sr$ values obtained from the bulk sediment leachates in cores 01JPC and 02PC range from 0.70922 to 0.71066, with a mean value of 0.70933 ± 0.00004 (Fig. 62A). These values are characteristic of the present-day sea water values recorded in the western Arctic Ocean (0.70920; Asahara et al., 2012).

In core 01JPC, the εNd values ranged from -3.7 to -5.7, while the εHf values ranged from 4.1 to 9.2 (Fig. 62D). In general, the Nd and Hf isotopic signatures in core 02PC are less radiogenic than in core 01JPC. The εNd ranged from -7.6 to -16.8, while the εHf values ranged from 4.8 to -10.4 (Fig. 62D). As shown by Fig. 62D, Nd-Hf isotopes values of core 01JPC fall into the sea water array, whereas data from core 02PC range from sea water array

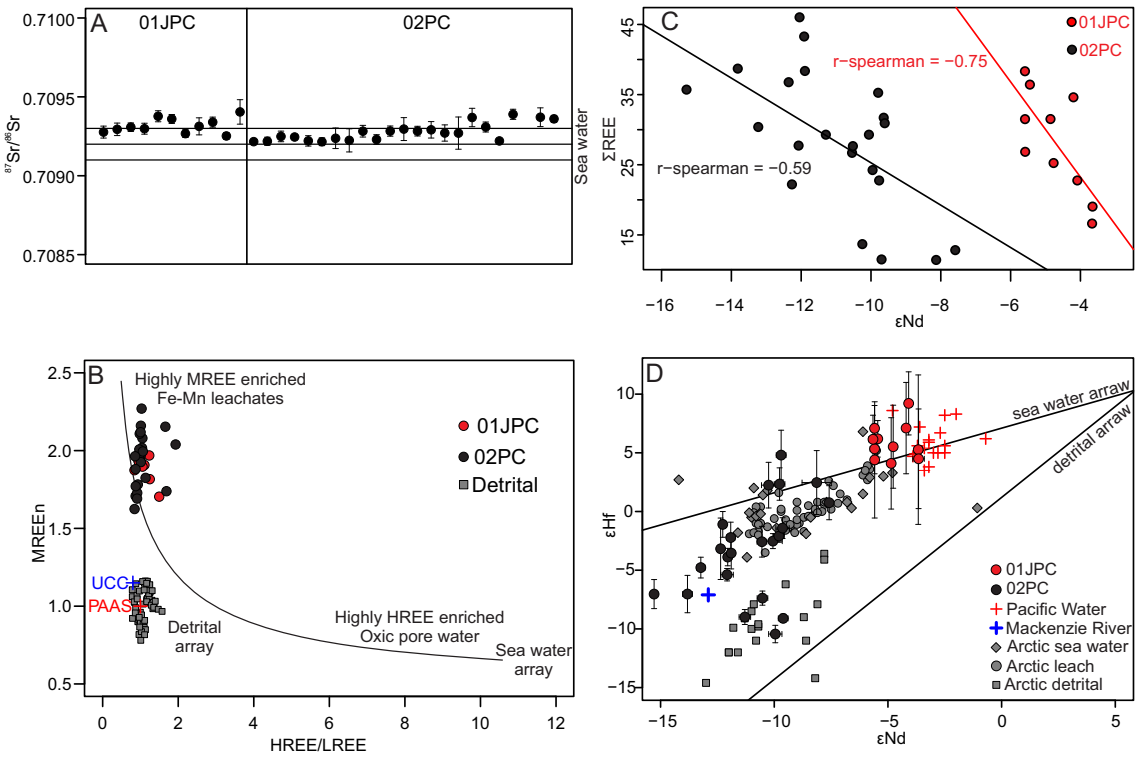

Figure 62: (A) $^{87}Sr/^{86}Sr$ isotope ratio for the bulk sediment leachates sample of cores 01JPC and 02PC; sea water values in the Arctic ocean are shown by the black lines (Asahara et al., 2012). (B) Bi-plot HREE/LREE vs. MREE. A mixing line between the most MREE enriched leachates and the most HREE enriched oxic pore water reflects the "authigenic-pore water array" (Gutjahr et al., 2010). Detrital REE compositions of cores 02PC and 05JPC are also shown (Deschamps et al, *in preparation*). (C) Spearman correlation between ΣREE contents and the authigenic εNd values from the cores 01JPC and 02PC. (D) Hafnium–neodymium isotope systematics of the bulk sediment leachates obtained in this study together with previously published data and εNd-εHf correlation lines from the literature. Terrestrial and seawater arrays are from Vervoort et al. (1999) and Albarède et al. (1998), respectively. Pacific water, Mackenzie River and Arctic Sea water values are from Zimmermann et al. (2009a) and Zimmermann et al. (2009b), and leach and detrital values are from Chen et al. (2012).

to the detrital array.

The Nd signature in core 01JPC is very similar to the Arctic Pacific water signatures between -6 and -4 cal ka BP (εNd= -5.5; Haley and Polyak, 2013; Zimmermann et al., 2009a). From 1 to 4 cal ka BP, the Nd signature becomes more radiogenic (εNd=-4) towards the modern North Pacific water signature (εNd=-2; Zimmermann et al., 2009b). Despite the large uncertainties in the Hf isotopic composition, the global signature in core 01JPC matches with the overall Hf isotopic signatures of the Pacific waters (Zimmermann et al., 2009a,b;Fig. 63).

However, the large external uncertainties that show the Hf isotopic signatures in core 01JPC do not allow deciphering Holocene changes in Pacific waters signatures (Fig. 66).

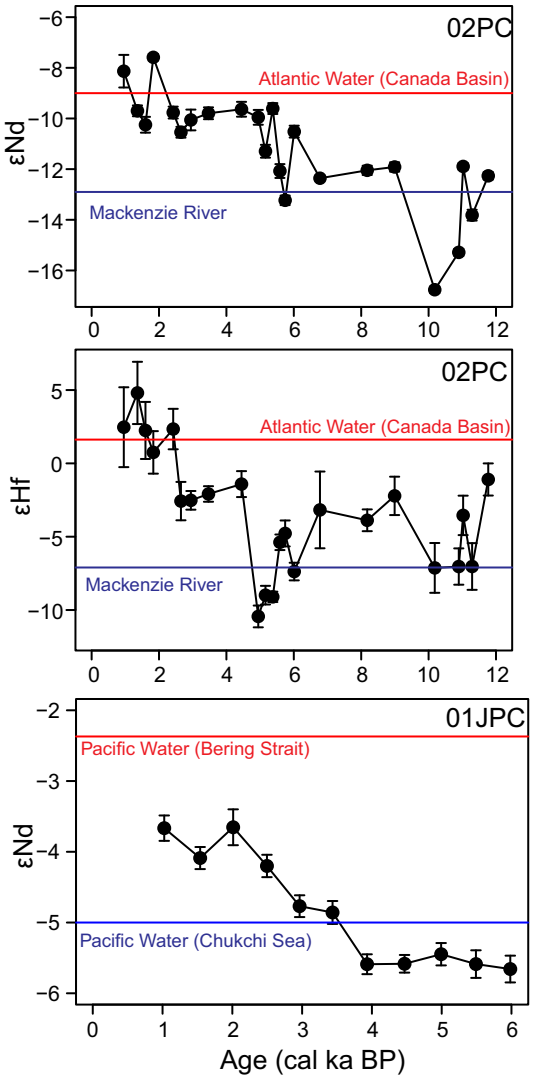

Figure 63: Nd and Hf isotopic evolution of the Arctic deep-waters obtained from the cores 02PC and 01JPC. Horizontal blue and red lines show modern values of the North Pacific water (Zimmermann et al., 2009a,b), Atlantic water and Mackenzie River (Porcelli et al., 2009; Zimmermann et al., 2009a,b).

As shown by Fig. 63, core 02PC displayed high variations and ranged between the Atlantic water (εNd: -9, εHf: 1.6; Zimmermann et al., 2009a) and modern Mackenzie River signatures (εNd: -12.9, εHf: -7.1; Zimmermann et al., 2009a). Indeed, from 12 to 6 cal ka BP, the εNd in core 02PC shows a clear isotopic signature similar to the Makenzie River, whereas

between 6 and 2 cal ka BP, the Nd isotopic signature became more radiogenic and reflected a mixed value between the Atlantic water and Mackenzie River. After 2 cal ka BP, the εNd signatures matched that of the Atlantic water. Similar to Nd isotope compositions, the εHf isotopic signatures in core 02PC showed a higher variability between a clear Mackenzie River signature (12-8 cal ka BP), a mixed signature between the Mackenzie River and the Atlantic water (8-2 cal ka BP), and a greater Atlantic water signature after 2 cal ka BP (Fig. 63).

4.6.3 Bulk and clay mineralogical data

Stratigraphic distributions of the bulk and clay mineralogical data from core 02PC have been shown in Deschamps et al. (2018a). The mineralogy of the bulk sediment fraction of core 02PC is dominated by quartz (22%) and phyllosilicates (72%). The clay mineral assemblage of core 01JPC consists of illite (60%), kaolinite (14%), chlorite (14%), vermiculite (8%) and chlorite/smectite mixed layers (2%). Based on SedUnMixMC results, the major source of sediment for core 02PC is related to the Mackenzie River (¿ 80%), whereas the secondary source is the Canadian Arctic Archipelago (up to 60%). The mineralogy of the bulk sediment fraction of core 01JPC is dominated by quartz (~20 %), phyllosilicates (52 %), plagioclase (11 %), K-feldspar (5 %) and amorphous silica (3-14 %). The clay mineral assemblage of core 01JPC consists of illite (27-45 %), kaolinite (5-10 %), chlorite (10-15 %), vermiculite (7-50 %) and chlorite/smectite mixed layers (0-40 %). Based on SedUnMixMC results, the major source of sediment for core 01JPC is related to the North Pacific (40-60 %), while the secondary source is the Mackenzie River (10-30 %).

4.7 Discussion

The REE distribution,$^{87}Sr/^{86}Sr$, εNd and εHf from sediment leachates accurately represent the bottom seawater signatures in the western Arctic Ocean, with Pacific and Atlantic waters and Mackenzie River end members clearly distinguishable (Fig. 62D and 63). Thus,

the long-term Nd-Hf isotope variations observed in our bulk sediment leachates, the proportion of sediments derived from the Bering Strait and Mackenzie River (SedUnMixMC results), and the amorphous silica contents and log(I+K/C+V) ratio are discussed below in terms of changes in water sources, shelf-seawater interaction, brine formation, continental input, and their possible relationships with both the deglacial/Holocene climate variability and relative sea-level variations.

4.7.1 Role of weathering regime changes in the Nd and Hf isotopic evolution

Seawater εNd and εHf values are essentially determined by the mixing of different water masses in the open ocean, whereas the interaction between dissolved and particulate fractions is significant near the river mouths and continental margins (Chen et al., 2012). Several studies (Lacan and Jeandel, 2005; Pearce et al., 2013; Tachikawa et al., 1999) have discussed the exchange of material between particulates and seawater along the continental margins, a process commonly referred to as boundary exchange, which is thought to play a significant role in controlling the Nd and Hf isotopic and REE composition of the oceans. In the Arctic Ocean, the authigenic Nd and Hf isotopic records of a core recovered on the Lomonosov Ridge that spans the last 14 Myr showed more radiogenic values compared to the Atlantic water under glacial conditions and compared to during the interglacial periods (Chen et al., 2012; Haley et al., 2008). These authors interpreted the more radiogenic values as reflecting higher weathering during glacial periods associated with reduced Atlantic water inflow into the Arctic. Likewise, as described in Porcelli et al. (2009), deep waters in the Canada Basin have been enriched in Nd, apparently by addition of Nd to waters from the shelves. Similarly, the Hf concentration variations in the Canada Basin clearly reflect the additions of river-derived Hf from the Mackenzie River and may be responsible for increasing the Hf budget over much of the western Arctic Ocean (Zimmermann et al., 2009a). In addition, detrital εNd in the Bering Strait showed the most radiogenic ($\sim$ -7) value, probably influenced by the Aleutian arc volcanism, whereas detrital εNd in the Mackenzie area

showed the most unradiogenic (~ -15) value, reflecting material from the North American Craton (Maccali et al., 2018). In this context, the concentrations of ΣREE derived from the bulk sediment leachates in cores 02PC and 01JPC are higher towards unradiogenic εNd and εHf values between 12 and 4 cal ka BP, probably reflecting major influence from the Mackenzie and Yukon rivers, respectively (Fig. 62). We hypothesize that the major Nd and Hf input associated with enhanced weathering on the Mackenzie (εNd ~ -12.9; εHf ~ -8.1) and Yukon (εNd ~ 8.4) rivers watershed likely contributed to a decrease in the εNd and εHf signatures in cores 02PC and 01JPC during the early- to mid-Holocene. Assuming that the addition of Nd and Hf by the rivers could be applied to all of the REE, a period of intense weathering from the Mackenzie and Yukon drainage basin may increase the input of the dissolved ΣREE, with mostly unradiogenic Nd and Hf isotopic signatures into the shelf. At the opposite, the ΣREE concentration decreased for the last 2 cal ka BP when the Hf and Nd isotopic compositions reflected more radiogenic values derived from North Atlantic and Pacific waters (Fig. 62).

4.7.2 Origin of deglacial-Holocene seawater εNd and εHf variations

Canadian Beaufort margin

Modern monitoring data have shown that vigorous ice production within coastal polynyas may result in the production of brine shelf waters in the Beaufort Sea (Forest et al., 2015). In the Canadian Beaufort margin, the Nd and Hf isotopic signatures from core 02PC (located at ~1000 m deep) exhibited a large range, from -16 to -8 for εNd and from -10 to 5 for εHf, implying major changes in the seawater εNd and εHf since the deglaciation. Based on previous radiogenic isotopes studies (Chen et al., 2012; Porcelli et al., 2009; Zimmermann et al., 2009a), we suggest that seawater εNd and εHf variation records in the core 02PC can be interpreted mainly as the mixing of two dominant isotopic end members between the Mackenzie River and Atlantic water (Fig. 62D). The clear Mackenzie River signature in the early Holocene suggests that slope convection from brine enriched shelf waters to the deep waters and/or downwelling current supporting shelf-slope sediment transfer (Forest et al.,

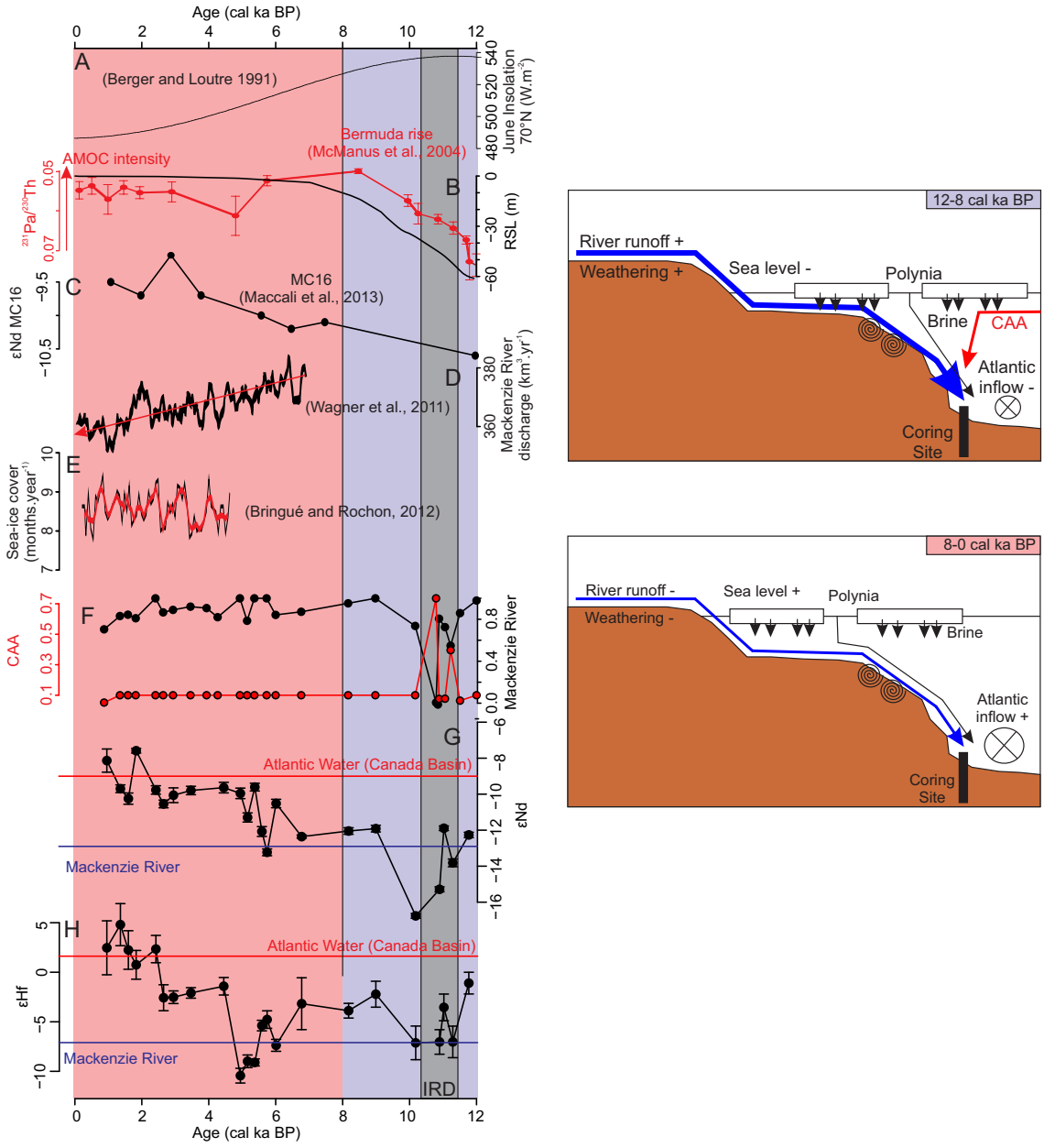

Figure 64: On the left: (A) Mean summer insolation at 70°N (Berger and Loutre, 1991). (B) Global sea level curve (Lambeck et al., 2014) and $^{231}Pa/^{230}Th$ curve showing the intensity of the Atlantic meridional overturning circulation (McManus et al., 2004). (C) Authigenic εNd records from the Fram Strait (Maccali et al., 2013). (D) Holocene Mackenzie River discharge based on numerical models (Wagner et al., 2011). (E) Mackenzie River sediment provenance proportion (Deschamps et al., 2018a) (F) Authigenic εNd and (G) εHf evolution for the core 02PC (this study). On the right: schematic illustration depicting the changes in authigenic εNd and εHf variations in core 02PC before 8 cal ka BP (light blue) and after 8 cal ka BP (light red).

2015; Rudels, 2012) played a significant role in the distribution of the Nd-Hf signature of the deep water between 8 and 12 cal ka BP. In addition, the most unradiogenic values at approximately 11 ka cal BP coincide with the IRD originating from the Canadian Arctic Archipelago (Deschamps et al., 2018a; Fig. 64). We suggest that weathering over the Canadian Arctic Archipelago at this time may also have contributed to the release of unradiogenic Nd because the geological terrain over the Canadian Arctic Archipelago displayed the most unradiogenic Nd isotopes values (-14 to -16) in this area (Maccali et al., 2018).

Any major modification in detrital inputs troughs the Mackenzie River that occurred during the early to middle Holocene cannot be driven by the LIS that was considerably reduced by this time (Dyke, 2004). Wickert (2016) suggested that meltwater inputs to the Mackenzie River ended no later than 11 cal ka BP, when its eastern tributaries were temporarily rerouted eastward due to a combination of ice retreat and glacial isostatic depression. Based on permafrost studies in the Canadian Arctic (Burn, 1997; Dallimore et al., 1996), we hypothesize that the very unradiogenic εNd and εHf values recorded in core 02PC during the early to middle Holocene are more likely the result of readily erodible rock flour and unconsolidated sediments derived from glacially deformed terrain on the Mackenzie Rivers watershed. The permafrost degradation in the western Canadian arctic correlates with an enhanced boreal summer insolation during the early Holocene that would increase soil moisture storage and thus facilitate its erosion (Burn, 1997). Furthermore, the sedimentation in the Beaufort Sea is strongly influenced by sea level variations (Deschamps et al., 2018b,a). Recently, Cornuault et al. (2018) have shown that the εNd record can be influenced by sea level variation.Similarly, during the early to middle Holocene, the unradiogenic Nd and Hf isotopic values recorded in core 02PC showed a parallel evolution together with the intensity of the Atlantic Meridional Overturning Circulation and relative sea level variations (Fig. 64). At the same time, the ^{231}Pa/^{230}Th ratio has been used as a tracer for the intensity of the Atlantic Meridional Overturning Circulation (McManus et al., 2004). In this context, we hypothesize that a reduced contribution of Atlantic waters to the Arctic Ocean, in relation to low global sea level conditions, can enhance the influence of the Mackenzie River (and

hence that of isotopic exchange with particles; Pearce et al., 2013) on the Canadian Beaufort Shelf during the early to middle Holocene, leading to more unradiogenic Nd and Hf isotopic signatures.

Numerical models of the regional hydrologic responses of the Mackenzie River to large-scale atmospheric circulation patterns suggest a decreasing trend in the freshwater discharges to the Canadian Beaufort margin associated with a greatly reduced moisture transport over North America during the mid- to late Holocene, likely driven by a diminution in the boreal summer insolation (Wanner et al., 2008; Wagner et al., 2011; Fig. 64). In this context, we suggest that this decreasing discharge of the Mackenzie River also reduced the inputs of the dissolved ΣREE with the most unradiogenic Nd and Hf isotopic signatures to the Canadian Beaufort Shelf. After 8 cal ka BP, the isotopic record of core 02PC increases towards more radiogenic values (εNd: -9.5; εHf: 2), similar to the modern values of the Atlantic water recorded in the Canada Basin (Porcelli et al., 2009; Zimmermann et al., 2009a; Fig. 64). However, the εNd values observed in the Canada Basin are slightly higher than those of the waters entering from the North Atlantic (εNd of ~10.7; Porcelli et al., 2009). This difference in εNd values probably reflects the influence of the Pacific waters. A value of εNd between -9.6 and -9.1 can be obtained by the mixing of 20 % Pacific inflow water and 80 % Atlantic water (Porcelli et al., 2009). Similar trends have been observed in the Nd isotopic signatures of a core located in the Fram Strait and attributed to Pacific water influence (Maccali et al., 2013). Thus, the changes observed in the authigenic Nd and Hf isotope signatures in core 02PC after 8 cal ka BP most likely reflect the combination of both decreasing in the Mackenzie River discharge and the relative increase of the Atlantic inflow through the Arctic with some noticeable contribution of Pacific waters. The foraminifera assemblage in the Beaufort slope also suggests an increase in the Atlantic water inflow after 7.5 cal ka BP (Andrews and Dunhill, 2004), and quantitative mineralogical data form the Chukchi Sea displayed an enhanced Bering Strait inflow after 8 cal ka BP (Deschamps et al., 2018a), in agreement with our results. Furthermore, quantitative reconstructions of past sea-surface conditions (temperature, salinity, and the duration of sea-ice cover), based on dinoflagellate cyst assemblages

and transfer functions, reveal relatively long-term stable oceanographic conditions during the late Holocene (Bringué and Rochon, 2012). However, the lower resolution of our results prevent any linkage with the short term variation of past sea-surface conditions in the Beaufort Sea. Finally, these results, together with the concomitant dominance of Atlantic and Pacific waters, suggest that the modern oceanographic conditions in the Canadian Beaufort Shelf were established during the late Holocene.

Chukchi-Alaskan margin

In the Chukchi-Alaskan margin, our bulk sediment leachates data from core 01JPC (located at > 1000 m deep) show εNd values between -6 and -4, similar to the Pacific water signatures (Fig. 65). Core 01JPC is located in the area of enhanced slope convection from brine enriched shelf waters to the deep ocean (Rudels, 2012). In fact, using the εNd distribution on the Chukchi Shelf, Haley and Polyak (2013) have found a modern to pre-modern distinct radiogenic εNd signal observed on the slopes of the Chukchi margin and adjacent borderland, indicative of Pacific water convection (e.g., via brine rejection) and/or persistent sediment redistribution from the shelf. The convection by brine rejection has been found in the εNd isotope records in the Eurasian shelf (Haley et al., 2008). Thus, our result supports the notion that slope convection from brine enriched shelf waters to the deep waters plays a significant role in the distribution of the homogeneous Nd isotope composition in western Arctic seawater for the last 6 cal ka BP.

The Nd and Hf isotopic records from the Chukchi-Alaskan margin allow a close look at the changes in the relative contributions between the two potential endmembers: (1) brines formed with more unradiogenic values derived from the weathering of the Yukon drainage basins and (2) Bering Strait inflow. Atmospheric climate modes on interannual to multi-decadal times-scales, such as the El Niño Southern Oscillation (ENSO), the Pacific North American (PNA) pattern, and the Pacific Decadal Oscillation (PDO), provide a potential mechanistic explanation for correlations between changes in the precipitation patterns over North America and the position of the Aleutian Low in the North Pacific, as well as the Bering

Strait inflow (Anderson et al., 2016; Yamamoto et al., 2017). The winter precipitation patterns result from the strength and position of the Aleutian Low, which is strengthened and/or located further to the east of the North Pacific during a positive PDO phase and weakened and/or located more to the west of the North Pacific during a negative PDO (Barron and Anderson, 2011). The increased sea surface temperature in the North Pacific leads to enhanced water vapor transportation over the continent, thus increasing precipitation on western North America (Anderson et al., 2016). In addition, modern data from the Yukon River suggest a positive trend in the annual flow during the positive PDO phases, perhaps reflecting the increases in annual precipitation in the interior of Alaska (Brabets and Walvoord, 2009).

The transition between the middle to late Holocene (4 cal ka BP) was characterized by a decrease in the boreal summer insolation, which affected the Northern Hemisphere climate system (Wanner et al., 2008). Several paleoclimate studies based on Alaskan terrestrial records (Anderson et al., 2005, 2016; Barron and Anderson, 2011) and Bering Shelf marine records (Harada et al., 2014; Katsuki et al., 2014) suggest that this transition was characterized by: (1) changes between PDO+ to a strong PDO- state, and (2) enriched to depleted precipitation that was linked to a major change in the Aleutian Low intensity and position on the North Pacific. Likewise, a decrease in the boreal summer insolation also affected the PNA states with a transition from a more negative to a positive PNA-like climate during the mid- to late Holocene, respectively (Liu et al., 2014). These changes have been inferred to be caused by Pacific Ocean–atmospheric dynamics that are attributed to an increase in El Niño frequency and a warm eastern tropical Pacific sea surface (Anderson et al., 2016; Liu et al., 2014). Within this context, we hypothesize that the wetter conditions associated with weak PDO-, PDO+ and PNA- states during the middle Holocene (Anderson et al., 2016; Liu et al., 2014) may have promoted higher weathering rates over the Yukon drainage basin, which is consistent with the most unradiogenic εNd values recorded in core 01JPC. Conversely, during the late Holocene, the drier conditions in western North America associated with strong PDO- and PNA+ states likely reduced the weathering rates on the Yukon drainage basin and also promoted an increase in the Bering Strait inflow (Yamamoto et al., 2017). Likewise,

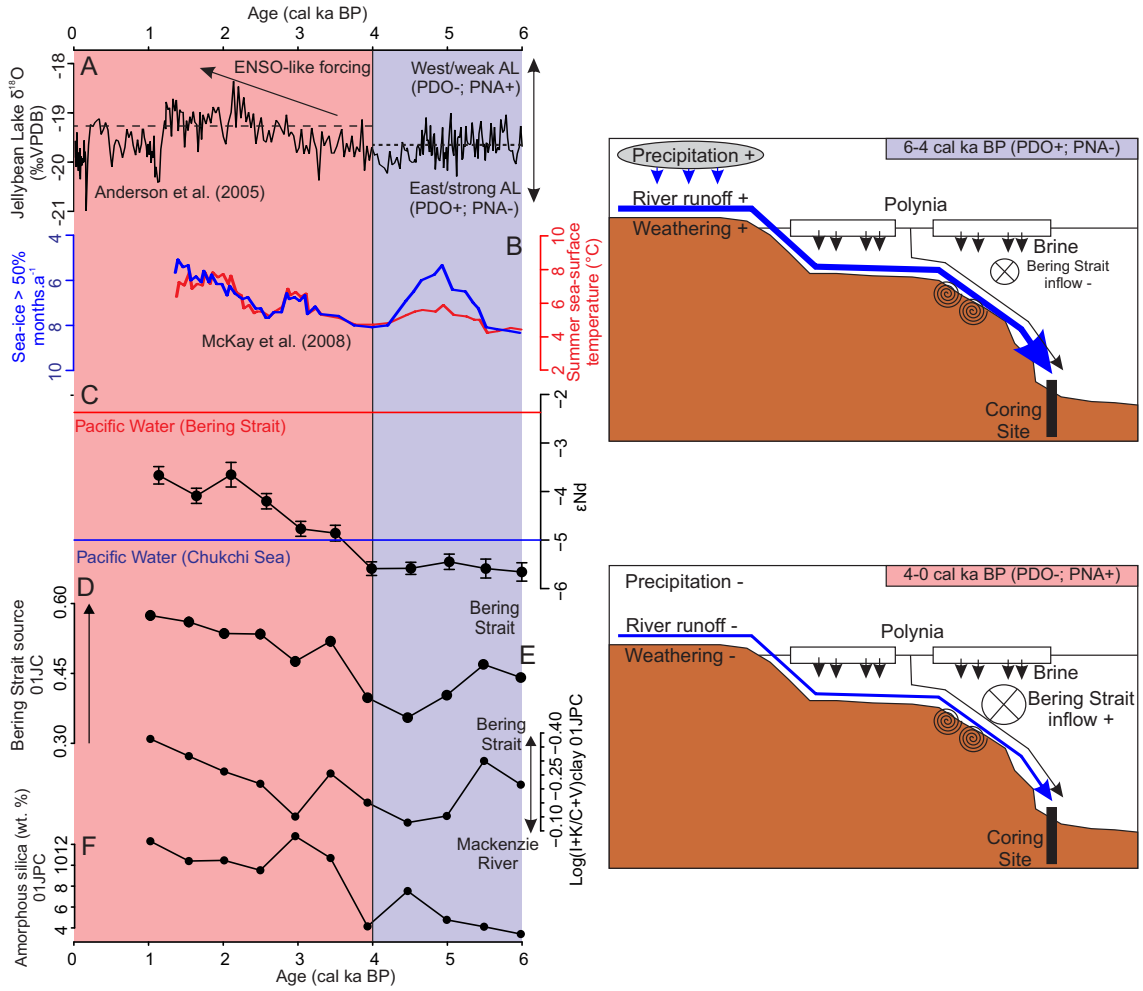

Figure 65: On the left: (A) δ^{18}O records from Jellybean Lake used as a PDO index (Barron and Anderson, 2011). (B) Quantitative reconstruction of past sea surface temperature (red) and sea-ice cover (blue) based on dinoflagellate cyst assemblages (McKay et al., 2008). (C) Authigenic εNd evolution for the core 01JPC (this study). (D) proportion of Bering Strait source and (E) Log(I+K/C+V) ratio in core 01JPC (this study). (F) Amorphous silica content in core 01JPC (this study). On the right: schematic illustration depicting the changes in authigenic εNd and εHf variations in core 01JPC before 4 cal ka BP (light blue) and after 4 cal ka BP (light red).

the log(I+K/C+V), the relative proportion of the Bering Strait sediment (SedUnMix results) as well as the proportion of amorphous silica are used as proxies for the Bering Strait inflow (Deschamps et al., 2018a; Jakobsson et al., 2017; Stein et al., 2017). The mineralogical proxies, including amorphous silica in core 01JPC are in agreement with increases in the Bering Strait inflow during the late Holocene (Fig. 65). Increase in the Bering Strait inflow

into the Chukchi Sea would lead to a reduced sea-cover as well as an increase in sea surface temperature (Shimada et al., 2006). Indeed, transfer functions based on dinoflagellate cyst assemblages from the nearby core 05JPC (McKay et al., 2008) suggest a decrease in the duration of sea-ice cover and an increase in summer sea-surface temperature after 4 cal ka BP. These results show a parallel temporal evolution with our detrital and isotopic proxies, and therefore, supporting our interpretation for an increase in the Bering Strait inflow during the late Holocene (Fig. 65).

Overall, our results show that long-term PDO and PNA states conditions, have a significant influence on the oceanic circulation in the Chukchi Sea. However, a study with a higher temporal resolution coupling quantitative mineralogy and radiogenic isotope data during this period needs to be performed to provide a better understanding between the atmospheric climate mode (PDO/PNA), continental weathering and the Bering Strait inflow.

4.8 Conclusion

Using a combined Nd and Hf isotopic record of bulk sediment leachates from two piston cores recovered in the Canadian Beaufort (02PC) and Chukchi-Alaskan (01JPC) margins, we have investigated changes in weathering regimes and deep water circulation during the Holocene. The coupled evolutions of these two isotopic records are in good agreement with modern seawater and leachate data from Pacific water, Atlantic water and the Mackenzie River. . Overall, our mineralogical and Nd-Hf isotopic data, together with modelled Holocene Arctic river discharges (Wagner et al., 2011), quantitative reconstructions of past sea-surface conditions (McKay et al., 2008) and hypothesized changes in atmospheric circulation (Barron and Anderson, 2011), reveals that:

(1) A clear Mackenzie River and Pacific water isotopic signature at a coring site at approximately 1000 m suggests that brine rejection during sea ice formation plays a significant role in εNd and εHf signatures of the bottom waters in the western Arctic Ocean.

(2) The Nd and Hf isotopic composition of bulk sediment leachates in the Beaufort Sea varies from the Mackenzie River to Atlantic water end members since the last deglacial period. These variations are linked to the remobilization of rock flour from glacially deformed terrain on the Mackenzie River watershed, lower sea level, and reduced Atlantic inflow through the Arctic Ocean during the early Holocene. In the middle to late Holocene, change towards Atlantic water isotopic signatures was inferred to be the result of an increase in the Atlantic inflow and decrease in the Mackenzie River discharge.

(3) The Nd and Hf isotopic composition of bulk sediment leachates in the Chukchi-Alaskan margin is controlled by (1) more intense precipitation and weathering over the drainage basin of the Yukon River during the middle Holocene, and (2) drier conditions and an increase in the Bering Strait inflow during the late Holocene. This transition has been inferred to result from major changes in atmospheric climate modes induced by an ENSO-like forcing.

4.9 Acknowledgments

We sincerely thank the captains, officers, crew and scientists on board the USCGC Healy and the CCGS Amundsen for the recovery the cores used in this study. These cores were collected as part of the HOTRAX expedition (USCGC Healy), as well as the CASES and ArcticNet (CCGS Amundsen) programs. We also thank Quentin Beauvais (UQAR-ISMER) and Mathieu Babin (UQAR-ISMER) for their technical support and advice in the laboratory. This research was funded by the Natural Sciences and Engineering Research Council of Canada (NSERC) through Discovery Grants to J.-C. Montero-Serrano and G. St-Onge, as well as through ship time support for several expeditions (J.-C. Montero-Serrano and G. St-Onge).

4.10 Supporting Material

Table 10: REE and trace elements concentrations (ppm) of cores 02PC et 01JPC leachates.

Core	Depth (cm)	La	Ce	Pr	Nd	Sm	Eu	Gd	Tb	Dy	Ho	Er	Tm	Yb	Lu	Hf	Th	U
01JPC	5	0.84	2.21	0.32	1.25	0.37	0.09	0.37	0.07	0.32	0.07	0.17	0.03	0.14	0.03	2.20	0.42	0.06
01JPC	30	0.98	2.65	0.38	1.60	0.47	0.12	0.51	0.08	0.42	0.08	0.20	0.03	0.15	0.02	2.37	0.37	0.14
01JPC	55	0.96	2.47	0.35	1.44	0.41	0.10	0.43	0.07	0.36	0.07	0.18	0.03	0.15	0.02	1.84	0.38	0.17
01JPC	86	1.80	4.58	0.62	2.69	0.74	0.19	0.81	0.12	0.61	0.11	0.29	0.04	0.22	0.03	4.14	0.75	0.22
01JPC	115	1.33	3.35	0.47	1.96	0.56	0.14	0.59	0.09	0.47	0.09	0.23	0.03	0.18	0.03	2.24	0.66	0.29
01JPC	144	1.60	4.17	0.57	2.43	0.66	0.16	0.71	0.11	0.55	0.10	0.26	0.03	0.19	0.03	3.10	0.59	0.17
01JPC	172	1.93	5.03	0.68	2.90	0.80	0.20	0.88	0.14	0.68	0.13	0.32	0.04	0.24	0.03	3.07	1.05	0.59
01JPC	203	1.39	3.63	0.50	2.05	0.58	0.14	0.61	0.10	0.48	0.09	0.23	0.03	0.18	0.03	2.41	0.78	0.37
01JPC	234	1.88	5.04	0.67	2.87	0.79	0.19	0.86	0.13	0.65	0.12	0.31	0.04	0.23	0.03	3.30	0.80	0.21
01JPC	265	1.49	3.90	0.52	2.20	0.60	0.15	0.64	0.10	0.49	0.09	0.23	0.03	0.17	0.02	2.62	0.83	0.12
01JPC	295	0.24	0.56	0.11	0.34	0.13	0.02	0.09	0.02	0.07	0.01	0.03	0.00	0.02	0.00	0.40	0.20	0.02
02PC	6	0.40	1.04	0.21	0.92	0.33	0.08	0.35	0.06	0.32	0.06	0.16	0.02	0.12	0.02	2.28	0.50	0.14
02PC	12	0.49	1.01	0.20	0.86	0.29	0.07	0.30	0.05	0.23	0.05	0.12	0.02	0.11	0.02	2.14	0.26	0.22
02PC	16	0.61	1.33	0.25	1.10	0.35	0.09	0.36	0.05	0.24	0.05	0.11	0.01	0.09	0.02	1.78	0.11	0.18
02PC	20	0.54	1.21	0.24	1.09	0.37	0.09	0.42	0.07	0.39	0.08	0.20	0.03	0.16	0.02	2.96	0.51	0.16
02PC	34	1.03	2.58	0.43	1.93	0.57	0.14	0.63	0.10	0.48	0.09	0.23	0.03	0.16	0.02	3.31	0.60	0.11
02PC	47	1.06	2.93	0.50	2.26	0.68	0.17	0.74	0.11	0.56	0.10	0.25	0.03	0.18	0.03	4.61	0.98	0.12
02PC	60	1.21	3.21	0.52	2.33	0.69	0.17	0.74	0.11	0.55	0.10	0.25	0.03	0.18	0.03	5.40	1.01	0.11
02PC	72	1.25	3.66	0.62	2.87	0.89	0.22	0.98	0.15	0.74	0.14	0.33	0.04	0.23	0.03	6.93	1.28	0.14
02PC	84	1.40	3.84	0.61	2.77	0.82	0.21	0.90	0.14	0.67	0.12	0.31	0.04	0.22	0.03	6.52	1.16	0.12
02PC	95	1.10	2.80	0.43	1.84	0.52	0.13	0.56	0.08	0.41	0.08	0.20	0.02	0.14	0.02	4.92	0.85	0.11
02PC	100	1.17	3.06	0.48	2.10	0.62	0.15	0.67	0.10	0.50	0.09	0.24	0.03	0.18	0.03	5.43	0.89	0.12
02PC	105	1.32	3.43	0.53	2.34	0.67	0.16	0.73	0.11	0.53	0.10	0.25	0.03	0.18	0.03	6.22	1.05	0.12
02PC	110	1.14	2.96	0.45	1.95	0.56	0.13	0.60	0.09	0.44	0.08	0.21	0.03	0.16	0.02	5.23	0.85	0.08
02PC	114	1.22	3.19	0.50	2.18	0.63	0.16	0.70	0.11	0.53	0.10	0.25	0.03	0.19	0.03	5.13	0.90	0.10
02PC	119	1.20	2.96	0.66	2.10	0.63	0.15	0.62	0.10	0.49	0.09	0.24	0.03	0.17	0.03	4.43	0.86	0.10
02PC	126	1.74	4.48	0.88	3.06	0.91	0.21	0.91	0.14	0.70	0.13	0.32	0.04	0.22	0.03	6.80	1.31	0.11
02PC	131	2.14	5.68	1.07	3.95	1.15	0.27	1.19	0.18	0.93	0.17	0.42	0.05	0.30	0.04	10.45	1.63	0.10
02PC	134	1.95	5.03	0.93	3.34	0.97	0.23	0.99	0.15	0.77	0.14	0.36	0.04	0.25	0.04	7.01	1.20	0.09
02PC	138	2.09	5.36	0.93	3.19	0.87	0.19	0.88	0.13	0.69	0.13	0.34	0.04	0.25	0.04	7.68	1.32	0.16
02PC	143	1.89	4.76	0.83	2.71	0.74	0.16	0.72	0.11	0.57	0.10	0.28	0.04	0.21	0.03	7.33	1.23	0.22
02PC	148	2.09	5.17	0.90	2.98	0.84	0.19	0.84	0.13	0.68	0.13	0.33	0.04	0.25	0.04	7.68	1.52	0.15
02PC	164	1.91	4.71	0.90	3.08	0.87	0.19	0.89	0.13	0.69	0.13	0.33	0.04	0.25	0.03	9.28	1.53	0.41
02PC	190	0.97	2.34	0.57	1.71	0.52	0.11	0.51	0.08	0.41	0.08	0.20	0.03	0.15	0.02	3.30	0.57	0.17

Table 11: Nd-Hf-Sr isotopes from leachates of core 01JPC and 02PC.

Sample	Depth (cm)	Age (cal BP)	$^{143}Nd/^{144}Nd$	2σ	εNd	$^{176}Hf/^{177}Hf$	2σ	εHf	$^{87}Sr/^{86}Sr$	2σ
01JPC	5	1024	0.512450	0.00002	-3.7	0.282918	0.00036	5.3	0.70928	0.00004
01JPC	30	1539	0.512428	0.00002	-4.1	0.283029	0.00015	9.2	0.70929	0.00004
01JPC	55	2012	0.512451	0.00003	-3.7	0.282896	0.00024	4.5	0.70931	0.00003
01JPC	86	2496	0.512423	0.00002	-4.2	0.282970	0.00022	7.1	0.70930	0.00003
01JPC	115	2964	0.512394	0.00002	-4.8	0.282925	0.00020	5.5	0.70938	0.00003
01JPC	144	3436	0.512389	0.00002	-4.9	0.282885	0.00022	4.1	0.70936	0.00003
01JPC	172	3931	0.512351	0.00001	-5.6	0.282969	0.00011	7.1	0.70927	0.00002
01JPC	203	4468	0.512352	0.00001	-5.6	0.282893	0.00028	4.4	0.70931	0.00005
01JPC	234	4992	0.512359	0.00002	-5.4	0.282944	0.00009	6.2	0.70934	0.00003
01JPC	265	5491	0.512352	0.00002	-5.6	0.282920	0.00012	5.3	0.70925	0.00002
01JPC	295	5983	0.512348	0.00002	-5.7	0.282943	0.00012	6.2	0.70940	0.00008
02PC	6	707	0.512221	0.00003	-8.1	0.282839	0.00015	2.5	0.70922	0.00002
02PC	12	990	0.512141	0.00002	-9.7	0.282905	0.00012	4.8	0.70922	0.00003
02PC	16	1175	0.512113	0.00003	-10.2	0.282832	0.00011	2.2	0.70925	0.00003
02PC	20	1362	0.512249	0.00001	-7.6	0.282790	0.00008	0.7	0.70925	0.00002
02PC	34	2029	0.512137	0.00002	-9.8	0.282835	0.00008	2.3	0.70922	0.00003
02PC	47	2658	0.512098	0.00002	-10.5	0.282696	0.00007	-2.6	0.70922	0.00002
02PC	60	3286	0.512122	0.00004	-10.1	0.282698	0.00004	-2.5	0.70924	0.00007
02PC	72	3829	0.512136	0.00002	-9.8	0.282710	0.00003	-2.1	0.70922	0.00007
02PC	84	4404	0.512144	0.00003	-9.6	0.282729	0.00005	-1.4	0.70928	0.00004
02PC	95	4918	0.512128	0.00003	-10.0	0.282474	0.00004	-10.4	0.70923	0.00003
02PC	100	5153	0.512059	0.00003	-11.3	0.282515	0.00004	-9.0	0.70928	0.00003
02PC	105	5382	0.512146	0.00002	-9.6	0.282512	0.00002	-9.1	0.70930	0.00007
02PC	110	5617	0.512019	0.00003	-12.1	0.282617	0.00003	-5.4	0.70928	0.00003
02PC	114	5809	0.511960	0.00002	-13.2	0.282634	0.00005	-4.8	0.70929	0.00005
02PC	119	6039	0.512099	0.00002	-10.5	0.282560	0.00003	-7.4	0.70927	0.00005
02PC	126	6507	0.512004	0.00001	-12.4	0.282679	0.00015	-3.2	0.70927	0.00010
02PC	131	7254	0.512020	0.00002	-12.0	0.282659	0.00004	-3.9	0.70937	0.00006
02PC	134	7878	0.512027	0.00002	-11.9	0.282706	0.00007	-2.2	0.70931	0.00003
02PC	138	8526	0.511779	0.00001	-16.8	0.282567	0.00010	-7.1	0.70922	0.00002
02PC	143	9433	0.511854	0.00001	-15.3	0.282570	0.00007	-7.0	0.70939	0.00003
02PC	148	10227	0.512028	0.00001	-11.9	0.282669	0.00008	-3.5	0.71066	0.00014
02PC	164	10815	0.511930	0.00002	-13.8	0.282570	0.00009	-7.0	0.70937	0.00006
02PC	190	11253	0.512009	0.00002	-12.3	0.282738	0.00006	-1.1	0.70936	0.00002

Table 12: REE composition of reference QC used for ICP-MS measurements; SD and RSD are standard deviation and relative standard deviation, respectively; Diff. = ((Reference value – measured value)/ reference value)*100.

	La	Ce	Pr	Nd	Sm	Eu	Gd	Tb	Dy	Ho	Er	Tm	Yb	Lu	Hf	Th	U
QCmean(n=3)	3.78	3.78	3.75	3.79	3.75	3.84	3.82	3.90	3.74	3.84	3.81	3.93	3.81	3.85	23.33	3.12	3.87
QC SD	0.12	0.12	0.11	0.10	0.09	0.10	0.12	0.08	0.07	0.08	0.07	0.08	0.06	0.07	0.31	0.35	0.25
QC RSD (%)	3.16	3.06	2.84	2.53	2.52	2.65	3.11	2.04	1.87	2.17	1.94	1.98	1.69	1.79	1.33	11.24	6.38

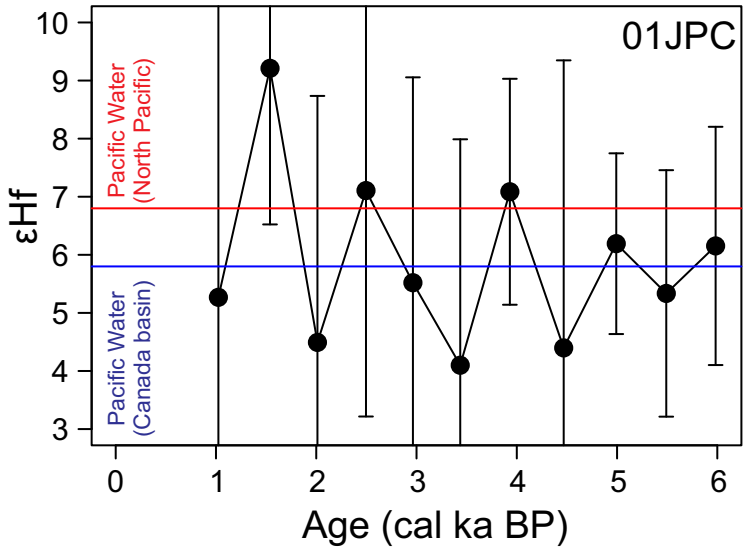

Figure 66: εHf signature of core 01JPC. Horizontal blue and red lines illustrate modern values of the North Pacific water. Due to the large uncertainties, εHf signature of core 01JPC cannot be used to observe Holocene changes in εHf Pacific signature.

CONCLUSION GÉNÉRALE

Cette étude combine une approche multi-traceur comprenant les propriétés sédimentologiques, physiques, magnétiques, minéralogiques (fraction totale et argileuse) et géochimiques (éléments majeurs, traces, REE et rapports isotopiques du Nd et du Hf). Ces données ont été obtenues sur un ensemble de carotte sédimentaire recueillies sur les marges continentales canadienne de la mer de Beaufort et de la mer des Tchouktches. Cette approche combinant plusieurs traceurs a permis de répondre à l'objectif général de la thèse qui consistait à reconstituer la variabilité des sources sédimentaires et la circulation océanique dans l'ouest de l'océan Arctique depuis la dernière déglaciation. La réalisation des trois objectifs spécifiques de recherche a mené à l'accomplissement de l'objectif principal. Ces objectifs spécifiques étaient : (1) établir la chronostratigraphie de trois carottes sédimentaires en utilisant les variations du champ magnétique terrestre, (2) déterminer les changements de provenance des sédiments marins et leurs caractéristiques minéralogiques et géochimiques et (3) de tracer les variations de la circulation profonde et le régime d'altération continentale à partir de la composition isotopique en Nd et Hf des lixiviats.

Objectif 1 : chronostratigraphie

L'ensemble des données paléomagnétiques et de datations radiocarbones obtenues a permis de réaliser le premier objectif de cette thèse, c'est-à-dire, établir la chronologie de trois carottes sédimentaires situées dans les marges continentales des mers des Tchouktches (01JPC) et de Beaufort (03PC et 02PC). La comparaison des PSV avec des enregistrements provenant des mers de Tchouktches et de Beaufort (Barletta et al., 2008; Darby et al., 2012; Lisé-Pronovost et al., 2009), ainsi qu'avec le modèle CALS10k (Korte et Constable, 2011) pour la mer de Beaufort a permis l'identification de 14 marqueurs chronostratigraphiques permettant ainsi à la fois, d'augmenter la résolution et de diminuer l'erreur sur les modèles d'âge. Finalement la carotte 01JPC recouvre les derniers 6000 ans et les carottes 03PC et 02PC recouvrent respectivement les derniers 10 500 et 13 500 ans. Ces séquences sédimentaires

constituent ainsi trois nouvelles archives paléomagnétiques à haute résolution couvrant la période Holocène en Arctique de l'ouest. Dans la mer de Beaufort, les taux de sédimentation sont très variables, avec des valeurs supérieures à 40 cm.ka^{-1} et 2-20 cm.ka^{-1} en fonction de la distance avec le fleuve Mackenzie. La variabilité des taux de sédimentation a des conséquences sur la résolution des enregistrements des PSV. En effet, les forts taux de sédimentation dans la 03PC en comparaison avec ceux de la 02PC permettent d'obtenir les PSV à plus haute résolution. **Les résultats obtenus sur les carottes 03PC et 02PC permettront d'établir plus facilement la chronostratigraphie des carottes marines prélevées le long de la marge canadienne de la mer de Beaufort à haute et faible résolution pour les études ultérieures.**

La compilation des données magnétiques issues des études ultérieures nous ont permis d'observer les différences inter- et intra-marges. Le paramètre montrant le plus de variation correspond à la granulométrie des grains magnétiques. Durant la déglaciation, on observe des grains magnétiques plus grossiers résultant des IRD provenant de la calotte Laurentidienne. Durant l'Holocène, les courants de fond et la glace de mer jouent un rôle important sur la distribution des grains magnétiques dans la marge des Tchouktches (grains plus fin aux niveaux des sites de carottage plus profond et inversement). **Ces résultats démontrent le rôle du type de transport sur la dynamique sédimentaire et les variations des propriétés magnétiques le long de la marge nord-américaine.**

L'ensemble de cette étude montre l'utilité du paléomagnétisme pour améliorer la datation des matériaux géologiques de l'Arctique. Finalement, la chronologie des séquences sédimentaires obtenues dans ce chapitre fournit les bases pour mener à terme une étude sur les variations de la dynamique sédimentaire depuis la dernière déglaciation en Arctique de l'ouest.

Objectif 2 : dynamique sédimentaire depuis la dernière déglaciation

Le chapitre deux de cette thèse est celui qui comporte le plus de traceurs permettant

de déterminer la provenance des sédiments depuis la déglaciation en fonction de la variabilité climatique depuis la dernière déglaciation. En effet cette étude combine des analyses de granulométrie, modélisation des groupes granulométriques, géochimie (éléments majeurs, traces et terres rares) sur la fraction détritique totale et la fraction des argiles, minéralogie (totale et des argiles) et finalement la quantification des sources basée sur la minéralogie totale. L'approche multi-traceurs a permis de mieux caractériser d'un point de vue géochimique et minéralogique les sédiments des marges continentales de Beaufort et des Tchouktches et correspond à l'approche la plus complète réalisée sur des carottes sédimentaires dans l'Arctique de l'ouest.

Les résultats obtenus ont permis de mettre en évidence que la marge nord-américaine est une source de sédiments felsiques, enrichis en quartz, illite, kaolinite, Al, LREE. La dolomite, Mg, Ca, et LREE sont particulièrement enrichis dans les sédiments de l'archipel arctique canadien (incluant les îles de Banks et de Victoria), où les roches sédimentaires paléozoïques-mésozoïques du bassin Sverdrup et des dépôts glaciaires du Tertiaire-Quaternaire sont riches en carbonates. Dans le cas des sources de sédiments mafiques, les feldspaths totaux, les amphiboles et la smectite ainsi que Ti, Fe et Ca sont les minéraux et éléments dominants dans les sédiments de la marge eurasienne, où les rivières drainent de grandes provinces basaltiques. De même, les sédiments de la mer des Tchouktches sont riches en quartz, feldspaths, chlorite, muscovite, smectite, vermiculite et HREE et pauvres en ΣREE provenant des côtes de la mer de Béring en Alaska. Ces différences géochimiques et minéralogiques régionales nous ont permis d'utiliser des ratios géochimiques et minéralogiques permettant de discriminer la provenance des sédiments. **Les ratios tels que : quartz/feldspath, illite kaolinite/chlorite vermiculite, Mg/Al, Ca/Al, Zr/Al, La/Sc, ΣREE/Ti, LREE/HREE peuvent donc être utilisés dans des études ultérieures pour déterminer la provenance des sédiments dans l'Arctique de l'ouest.**

Au cours de la déglaciation, l'IRD enrichie en feldspaths, quartz et Zr dans la carotte 02PC (IRD2B) daté à 13 cal ka BP a pour origine le fleuve Mackenzie. Nous suggérons que

cet couche correspondrait à l'évidence sédimentologique de la vidage du lac Agassiz vers 13 cal ka BP (Murton et al., 2010). D'après des études antérieures sur la paléogéographie des langues glaciaires de l'archipel Arctique canadien (Darby et Zimmerman, 2008; Stokes et al., 2005, 2006), les IRD riches en dolomite (IRD1A et IRD2A), datés respectivement à 12,8 et 11 cal ka BP, pourraient être reliés aux différentes phases de recul de la langue glaciaire du golfe d'Amundsen. L'intervalle froid du Dryas récent (Younger Dryas ; ~12,8 à ~11,7 ka cal BP ; Rasmussen et al., 2006) est relié à une diminution du taux de formation des eaux profondes dans l'Atlantique Nord et à un affaiblissement de la circulation méridienne de retournement Atlantique en raison d'un apport important d'eau douce provenant de l'Arctique (Condron et Winsor, 2012). Nos résultats montrent que la vidange du lac Agassiz vers 13 cal ka BP et la débâcle de la langue glaciaire du golfe d'Amundsen serait responsable du déclenchement du Dryas récent en accord avec des études ultérieures (Hillaire-Marcel et al., 2013; Murton et al., 2010; Stokes et al., 2009; Tarasov et Peltier, 2005). La couche riche en chlorite, vermiculite et silice amorphe identifié à la base de la carotte 05JPC peut être liée à l'ouverture initiale du détroit de Béring vers 11 cal ka BP (Jakobsson et al., 2017). Les similitudes entre la composition géochimique et minéralogique entre les IRD1A des carottes 02PC et 05JPC suggèrent un même événement daté vers 11 cal ka BP. Cette corrélation entre ces IRD impliquerait que l'ouverture du détroit de Béring soit plus ancien que 11 cal ka BP (Jakobsson et al., 2017) comme suggéré précédemment par Keigwin et al. (2006) et England et Furze (2008). L'assemblage minéralogique de l'IRD1B (enrichi en feldspaths, quartz et Zr) retrouvé uniquement dans la carotte 05JPC, suggère un évènement local plutôt que régional. En s'appuyant sur plusieurs études sédimentologiques (Hill et Driscoll, 2008, 2010), nous proposons l'hypothèse que l'IRD1B résulte d'un événement d'eau de fonte provenant de la chaîne de Brooks (nord-ouest de l'Alaska). **L'approche multi-traceur nous a permis de mieux caractériser les couches associées à l'histoire déglaciaire contenant des IRD dans l'Arctique de l'ouest de la calotte de glace Laurentidienne et de déterminer leur provenance (Fig. 67).**

Durant l'Holocène, la principale source de sédiments pour la marge canadienne de la

mer de Beaufort est le fleuve Mackenzie. Malgré une source sédimentaire unique, les variations du niveau marin contrôlent le taux de sédimentation dans la partie orientale de la marge canadienne (**?**). Au contraire, dans la marge continentale de la mer des Tchouktches, les variations du niveau marin jouent un rôle important sur la provenance des sédiments. En effet, la remontée rapide du niveau marin enregistré entre 10,5 et 7 cal ka BP induit une submersion du détroit de Béring. Nous proposons l'hypothèse que l'élargissement et l'approfondissement du détroit de Béring a favorisé la remobilisation des sédiments stockés sur le plateau des Tchouktches ainsi que l'augmentation du transport de sédiment du Pacifique vers l'océan Arctique. Les enregistrements détritiques montrent une stabilité dans les apports de sédiments provenant du détroit de Béring après 6 cal ka BP, une fois le niveau marin stabilisé. Ces résultats suggèrent un changement de contrôle entre le niveau marin et les oscillations climatiques vers 6 cal ka BP sur les apports sédimentaires provenant du détroit de Béring. Durant l'Holocène, le déclin à long terme du débit du fleuve Mackenzie et de la glace d'ancrage transportée par la gyre de Beaufort a entrainé une diminution des apports sédimentaires provenant du fleuve Mackenzie sur la marge continentale de la mer des Tchouktches. **Au cours de l'Holocène, les variations de l'insolation et du niveau marin sont les principaux facteurs contrôlant les variations à long terme de la provenance sédimentaire et de la circulation océanique dans l'Arctique de l'ouest (Fig. 67).**

Objectif 3 : variations de la circulation profonde depuis la dernière déglaciation

Les signatures isotopiques en Nd et Hf (exprimées en εNd et εHf) extraites des oxyhydroxides de fer et de manganèse des sédiments (lixiviats) de la mer de Beaufort montrent une signature isotopique variant entre le fleuve Mackenzie et les eaux atlantiques depuis la dernière déglaciation. Ces variations résultent (1) de la diminution de l'altération continentale dans le bassin versant et du débit du fleuve Mackenzie, (2) de l'intensité des apports d'eau atlantique dans l'océan Arctique et (3) des variations du niveau marin. Les modifications des signatures en εNd et εHf dans la mer des Tchouktches résultent d'un changement majeur dans le climat mondial contrôlé par la diminution de l'insolation entre le l'Holocène

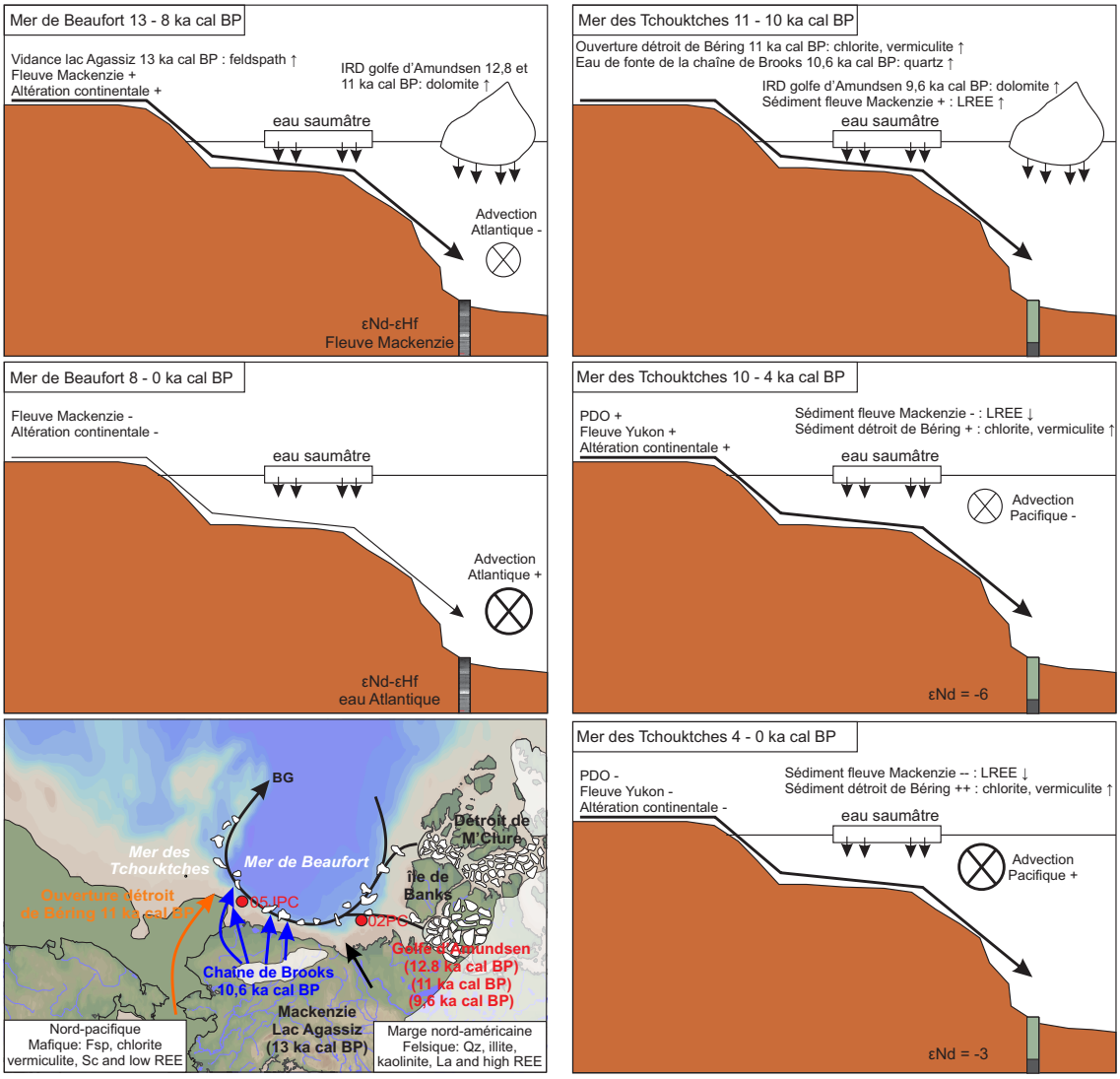

Figure 67: Figure schématique montrant la provenance des sédiments et les changements de la circulation océanique de surface et profonde depuis 13 ka cal BP.

moyen et l'Holocène tardif (Liu et al., 2014). Enfin, nous suggérons que les conditions plus humides associées aux indices PDO+ et PNA- au cours de l'Holocène moyen pourraient favoriser les précipitations sur le bassin versant du Yukon, ce qui est cohérent avec les valeurs moins radiogéniques dans la carotte 01JPC. À l'opposé, à la fin de l'Holocène, les conditions plus sèches associées à des indices PDO- et PNA+ réduisent les précipitations dans le bassin versant du Yukon et augmentent l'afflux d'eau Pacifique *via* le détroit de Béring

et conduisent à des valeurs plus radiogéniques dans la carotte 01JPC. Dans l'ensemble, nos résultats démontrent que les téléconnections à grande échelle telles que PDO, PNA et ENSO ont une influence significative sur la circulation océanique dans la mer des Tchouktches. **Au cours de l'Holocène, les variations de l'intensité des précipitations, de l'altération continentale, des apports d'eaux atlantiques et pacifiques, ainsi que les variations du niveau marin sont les principaux facteurs contrôlant les variations à long terme des signatures isotopiques en Nd et Hf authigène.**

Dans son ensemble, le travail de recherche réalisé dans cette thèse a permis de mieux documenter les processus contrôlant la variabilité des sources sédimentaires et la circulation océanique dans l'ouest de l'océan Arctique depuis la dernière déglaciation. En outre, les vêlages d'icebergs, la glace de mer et les courants marins jouent un rôle important sur le transport sédimentaire dans l'Arctique de l'ouest. D'une manière plus globale, les variations du niveau marin et les changements climatiques à long et court terme tels que l'insolation et les oscillations climatiques (PDO, PNA et ENSO) influencent à la fois la circulation océanique et le régime d'altération continentale de l'Arctique depuis la dernière déglaciation (Fig. 67).

PORTÉE ET PERSPECTIVE DE L'ÉTUDE

Chronostratigraphie

Le développement de la chronostratigraphie permet de mieux dater les enregistrements sédimentaires marins dans l'Arctique de l'ouest. Cependant la résolution de l'enregistrement des PSV peut être améliorée, notamment en changeant l'approche méthodologique sur la carotte 03PC. L'utilisation de cubes de 1 x 1 cm prélevés tous les 1 ou 2 cm sur la carotte permettrait (1) d'augmenter la résolution de l'enregistrement en effaçant l'effet de lissage lors des mesures avec un u-channel et (2) de pouvoir comparer les résultats des deux approches méthodologiques. D'une manière plus générale, les hautes latitudes de l'hémisphère nord et de l'hémisphère sud sont des zones manquant d'enregistrement des PSV. Le développement

de la reconstruction des PSV dans ces régions permettrait l'amélioration des modèles géomatiques tels que CALS10k (Korte et Constable, 2011). De plus, une grande partie des enregistrements de la variation séculaire paléomagnétique sur la période Holocène provienne principalement des sédiments continentaux des lacs de l'hémisphère nord et les reconstitutions provenant de séquences sédimentaires utilisant des compilations de données paléomagnétiques sont encore rares (Barletta et al., 2010). Étant donné la complexité d'obtenir des datations indépendantes sur les enregistrements sédimentaires marins (^{14}C), il est nécessaire de continuer le développement de la magnétostratigraphie dans l'Arctique. La compilation des données paléomagnétiques provenant de nombreux enregistrements PSV présente l'avantage de réduire les effets lithologiques locaux, améliorant ainsi le vrai signal géomagnétique. Finalement, une plus grande couverture spatiale d'enregistrements paléomagnétiques dans l'océan Arctique pourrait permettre le développement de courbes paléomagnétiques de référence (inclinaison, déclinaison et paléointensité) pour l'ensemble de l'Arctique.

Le développement de la magnétostratigraphie a très nettement contribué à l'amélioration des modèles d'âges Holocène dans l'Arctique de l'ouest. Cependant, les modèles d'âges sont souvent un point de controverse important dans les projets de recherche dans l'océan Arctique et notamment durant la déglaciation. L'intervalle froid du Dryas récent (~12,8 to ~11,7 cal ka BP) a été relié à une diminution du taux de formation des eaux profondes dans l'Atlantique Nord et à un affaiblissement de la circulation méridienne de retournement Atlantique en raison d'un apport important d'eau douce (Broecker et al., 1988). Au début du Dryas récent, les modèles numériques de Tarasov et Peltier (2005) révèlent que la plus grande décharge d'eau de fonte provenant du lac Agassiz était dirigée vers l'océan Arctique. De plus, en se basant sur des datations par luminescence sur le bassin versant du fleuve Mackenzie, Murton et al. (2010) émettent l'hypothèse d'un relargage de centaines de kilomètre-cube d'eau de fonte provenant du lac Agassiz dans l'océan Arctique à travers le fleuve Mackenzie vers 13 cal ka BP, soit avant le début du Dryas récent. Maccali (2012) observe dans ces résultats la vidange du lac Agassiz durant la période du Dryas récent mais ne peut conclure si la vidange en est une cause ou une conséquence en raison de l'erreur sur le modèle d'âge et des faibles taux

de sédimentations. Pour réaliser le modèle d'âge de la carotte 02PC, nous utilisons les datations obtenues sur des carottes dans la même zone d'étude (Scott et al., 2009; Lakeman et al., 2018). Scott et Lakeman utilisent des âges réservoirs pour calibrer les ages ^{14}C respectivement de 400 et 335 ans. Ces âges réservoirs actuels ont été déterminés à partir de datation radiocarbone sur des mollusques modernes (Coulthard et al., 2010; McNeely et al., 2006). Cependant, la présence de glace de mer limiterait les échanges de CO_2 entre l'océan et l'atmosphère et l'entrée réduite d'eau Atlantique dans l'océan Arctique aurait entrainé un appauvrissement des apports en ^{14}C. En effet, plusieurs études montrent que l'âge réservoir change durant la dernière période glaciaire et la déglaciation, avec des âges réservoirs allant de 800 à 2000 ans (Hutchinson et al., 2004; Sikes et al., 2000). Dans l'océan Arctique, Hanslik et al. (2010) ont utilisé plusieurs âges réservoirs pour observer le meilleur ajustement entre l'abondance des foraminifères et la période du Dryas récent. Ils ont finalement utilisé un réservoir régional de 300 ans pour l'Holocène et de 1000 ans pour la déglaciation en accord avec les modèles numériques de Butzin et al. (2005). Plusieurs publication utilisent un âge réservoir de 1000 ans durant la déglaciation (Hillaire-Marcel et al., 2013; Maccali et al., 2012, 2013). Pour ces raisons, nous utilisons un âge réservoir de 335 ans pour l'Holocène et de 1000 ans pour la déglaciation pour réaliser le modèle d'âge de la 02PC. De nombreuses incertitudes restent néanmoins quant à la valeur des âges réservoirs. En effet, l'âge réservoir de 335 ans provient de mollusques situés dans l'archipel arctique canadien et non de la mer de Beaufort (Coulthard et al., 2010). De plus, l'âge réservoir dans la mer de Beaufort varie entre 1000 et 1300 ans durant la déglaciation selon les modèles numériques de Butzin et al. (2005). En appliquant, un âge réservoir de 1300 ans dans le modèle d'âge de la 02PC au lieu de 1000 ans, les âges calibrés deviennent plus jeunes. La couche riche en quartz et felspar dans la carotte 02PC identifié comme l'évidence de la vidange du Lac Agassiz pourrait être daté à 12,7 cal ka BP au lieu de 13 cal ka BP. De même, l'IRD riche en dolomite daté à 12,8 cal ka BP serait daté vers 12,5 cal ka BP. En utilisant donc un âge réservoir plus vieux, la vidange du lac Agassiz et la débâcle de la calotte Laurentidienne ne seraient plus une cause mais une conséquence du Dryas récent. **Cette mise en perspective dans la chronologie déglaciaire**

montre bien à quel point nous devons améliorer nos connaissance sur les âges réservoirs durant la déglaciation dans l'océan Arctique.

Provenance sédimentaire et paléocéanographie dans l'Arctique de l'ouest depuis la déglaciation

Selon Hamilton (1982), la chaîne de Brooks (Alaska) est une zone dont l'extension des glaciers se terminerait vers 11,5 cal ka BP durant la déglaciation. Les données de sismiques combinées avec l'étude de carottes marines dans la marge continentale de la mer des Tchouktches ont montré l'occurrence de décharges d'icebergs et d'eau de fonte des glaciers provenant de la chaîne de Brooks entre 13 et 10 cal ka BP (Hill et Driscoll, 2008, 2010). La date de 10.7 cal ka BP pour l'IRD1B est cohérente avec l'événement daté entre 10.4 et 10.6 cal ka BP dans Hill et Driscoll (2010). Cependant, comment peut-on expliquer la variabilité dans la datation des décharges d'icebergs provenant de la chaîne de Brooks (~11,9, 10,6 et 9,8 cal ka BP). Les problèmes de datation sont l'une des possibles causes pouvant expliquer la variabilité des âges. L'autre hypothèse est la succession d'événements indépendants qui sont canalisés par différents chenaux le long de la marge continentale de la mer des Tchouktches (Hill et Driscoll, 2008, 2010). **D'une manière plus globale, il est nécessaire de continuer d'étudier la stratigraphie de la marge Arctique d'Alaska pour mieux comprendre l'histoire glaciaire de la chaîne Brooks.**

Après l'ouverture du détroit de Béring vers 11 cal ka BP, l'augmentation des flux particulaires détritiques et d'eaux pacifiques sont contrôlés par l'augmentation du niveau marin. Après 7 cal ka BP, une fois le niveau marin relativement stable, les afflux pacifiques sont contrôlés par la position et la force de la dépression des Aléoutiennes (Yamamoto et al., 2017). Nous observons une concordance entre nos résultats et les études publiées concernant un maximum d'afflux d'eaux pacifiques entre 6 et 3 ka cal BP (Ortiz et al., 2009; Stein et al., 2017; Yamamoto et al., 2017). Au contraire, après 3 cal ka BP nous observons des divergences entre les résultats publiés mais aussi entre les résultats des carottes 05JPC et 01JPC. Les résultats des études de Stein et al. (2017) et Ortiz et al. (2009) mais aussi de la carotte

05JPC étudié ici montrent une diminution des afflux d'eaux pacifiques après 3 ka cal BP. L'étude de Yamamoto et al. (2017) ainsi que les données de la carotte 01JPC montrent une augmentation des afflux pacifiques jusqu'à 1 ka cal BP. De plus, les résultats des isotopes radiogéniques du Nd dans la 01JPC concordent avec des afflux d'eaux pacifiques plus important résultant d'une phase négative de la PDO et d'une dépression des Aléoutiennes plus faible et située plus vers l'ouest. Pour expliquer ces différences, Darby and Bischof (2004) et Yamamoto et al. (2017) proposent que les sédiments transportés par les eaux du Pacifique pénétrant dans le détroit de Béring puissent être déviés vers l'ouest en direction du canyon d'Herald et manquent ainsi la marge continentale de la mer des Tchouktches le long des côtes de l'Alaska. Cette redistribution de l'afflux du détroit de Béring entre les différentes branches peut être une explication plausible des différences spatiales et temporelles observées entre les différentes carottes de la mer des Tchouktches. De plus, nous montrons dans cette étude que les courants de fond (néphéloïdes) jouent un rôle sur la redistribution et la remobilisation des sédiments dans cette zone. L'effet des courants de fond est une autre possibilité expliquant les différences entre les enregistrements des carottes de la marge des Tchouktches. La dernière possibilité est liée à la résolution de nos analyses (un échantillon tous les 500 ans environ) ce qui nous permet d'étudier uniquement les variations à long terme. **L'analyse de la minéralogie et des isotopes du Nd à haute résolution au cours des deux derniers millénaires dans les canyons de Barrow et d'Herald permettrait de mieux comprendre la relation entre l'advection des sédiments provenant du détroit de Béring, l'afflux d'eau pacifique entre les différentes branches et les oscillations climatiques (PDO/PNA).**

Les isotopes du Nd-Hf dans la mer de Beaufort sont contrôlés par les variations du niveau marin, l'intensité des apports d'eaux atlantiques dans l'océan Arctique de l'ouest, mais aussi par l'altération du bassin versant du fleuve Mackenzie résultant des précipitations. Selon les modèles de Wagner et al. (2011), le débit du fleuve Mackenzie diminue au cours de l'Holocène en réponse à des conditions moins humides et une diminution des précipitations. Or, les données modernes montrent que le débit du fleuve Mackenzie répond directement aux précipitations et par conséquent aux conditions d'humidité (Déry et Wood, 2005). Les condi-

tions de précipitations sont corrélées avec des oscillations climatiques telles que la PDO (Déry et Wood, 2005). De plus, Durantou et al. (2012) montrent que l'évolution de la température, de la salinité, de la couverture de glace de mer et de la productivité des dinoflagellés dans la fosse du delta du Mackenzie peut être liée aux phases de la PDO à une échelle de temps décennale. Compte tenu du recul de la calotte laurentidienne, nous observons des différences minéralogiques dans la carotte 02PC. Nous avons interprété ces différences minéralogiques comme issue d'un changement dans la contribution sédimentaire des affluents du sud du fleuve Mackenzie. Ces légers changements dans la minéralogie permettraient-ils d'observer les changements dans le débit du fleuve Mackenzie et/ou les zones d'altération préférentielle dans le bassin versant du fleuve Mackenzie résultant des oscillations climatiques ? Pour répondre à cette question, la carotte 02PC présente un trop faible taux de sédimentation pour une étude à haute résolution sur le période Holocène. Au contraire, la carotte 03PC, possédant un taux de sédimentation de 40 à 70 cm.ka^{-1}, située à proximité de l'embouchure du fleuve Mackenzie répond aux critères pour cette étude. **L'étude à haute résolution de la granulométrie, de la géochimie, de la minéralogie et des palynomorphes de la carotte 03PC couplée à des analyses spectrales pourrait nous aider à mieux comprendre les variations dans les apports détritiques du fleuve Mackenzie et les oscillations climatiques.**

Changements climatiques modernes

L'élévation du niveau marin entre 10.5 et 7 cal ka BP peut servir d'analogue moderne à ce que l'on connaît actuellement dans le cas des changements climatiques anthropiques. Les données modernes montrent une augmentation de 2 mm.a^{-1} du niveau marin dans la mer des Tchouktches entre 1954 et 1989 (Proshutinsky et al., 2004). Selon les modèles, le niveau marin devrait augmenter de 1mm.a^{-1} jusqu'à 1 cm.a^{-}1 pour les scénarios les plus catastrophiques (Rahmstorf, 2007). Ces valeurs sont similaires, voire supérieures à celles qui ont eu lieu au début de l'Holocène (comprises entre 1 et 20 mm.a^{-1} ; Lambeck et al., 2014). Or, dans cette étude nous démontrons justement que l'advection d'eaux pacifiques dans l'Arctique est contrôlée par les variations du niveau marin. Selon Shimada et al. (2006), l'advection d'eaux

chaudes pacifiques dans l'océan Arctique entraine une diminution du couvert de la glace de mer. Cette diminution du couvert de glace de mer pourrait contribuer à l'amplification du réchauffement en Arctique (Screen et Francis, 2016; Screen et Simmonds, 2010; Serreze et al., 2000, 2007; Vihma, 2014). **L'augmentation du niveau marin résultant des changements climatiques actuels va-t-il avoir comme conséquence une augmentation des flux d'eaux pacifiques dans l'océan Arctique ?**

Mot de fin

Les mers de Beaufort et des Tchouktches sont des sites d'études privilégiés pour étudier les variations paléocéanographiques et la déglaciation. La richesse et la quantité des données issues de ce projet de thèse contribuent fortement à (1) caractériser la géochimie et la minéralogie des sédiments, (2) mieux comprendre le "timing" de la déglaciation et (3) établir les variations paléocéanographiques résultant de la variabilité climatique à plus ou moins long terme. Finalement, ce travail s'inscrit dans une compréhension globale de la variabilité climatique naturelle de l'Arctique et de ses conséquences. La compréhension du climat passé va permettre de mieux comprendre et de modéliser le climat à venir résultant des changements climatiques actuels. Même si cette thèse contribue fortement à comprendre le système arctique, beaucoup de travail reste à faire pour comprendre les interactions entre variabilités climatiques, dynamiques sédimentaires et changements de la circulation océanique, que ce soit à l'actuel ou dans le passé.

ANNEXE I

PROFILES SISMIQUES

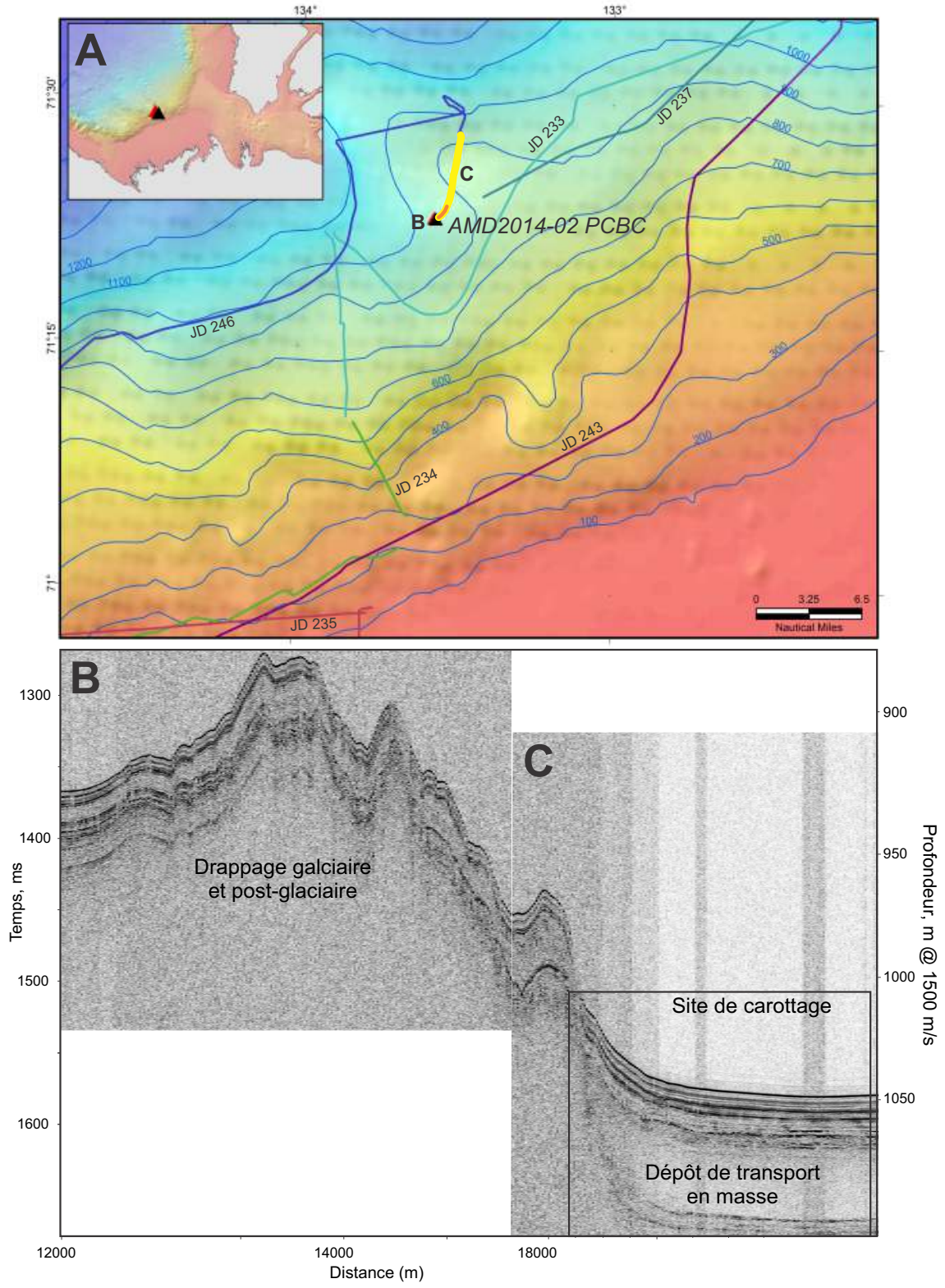

Figure 68: (A) Localisation du site de carottage AMD0214-02. (B) et (C) profils sismiques par acquisition à 3.5kHz. En (A) la ligne jaune représente (B) et la ligne orange représente (C)

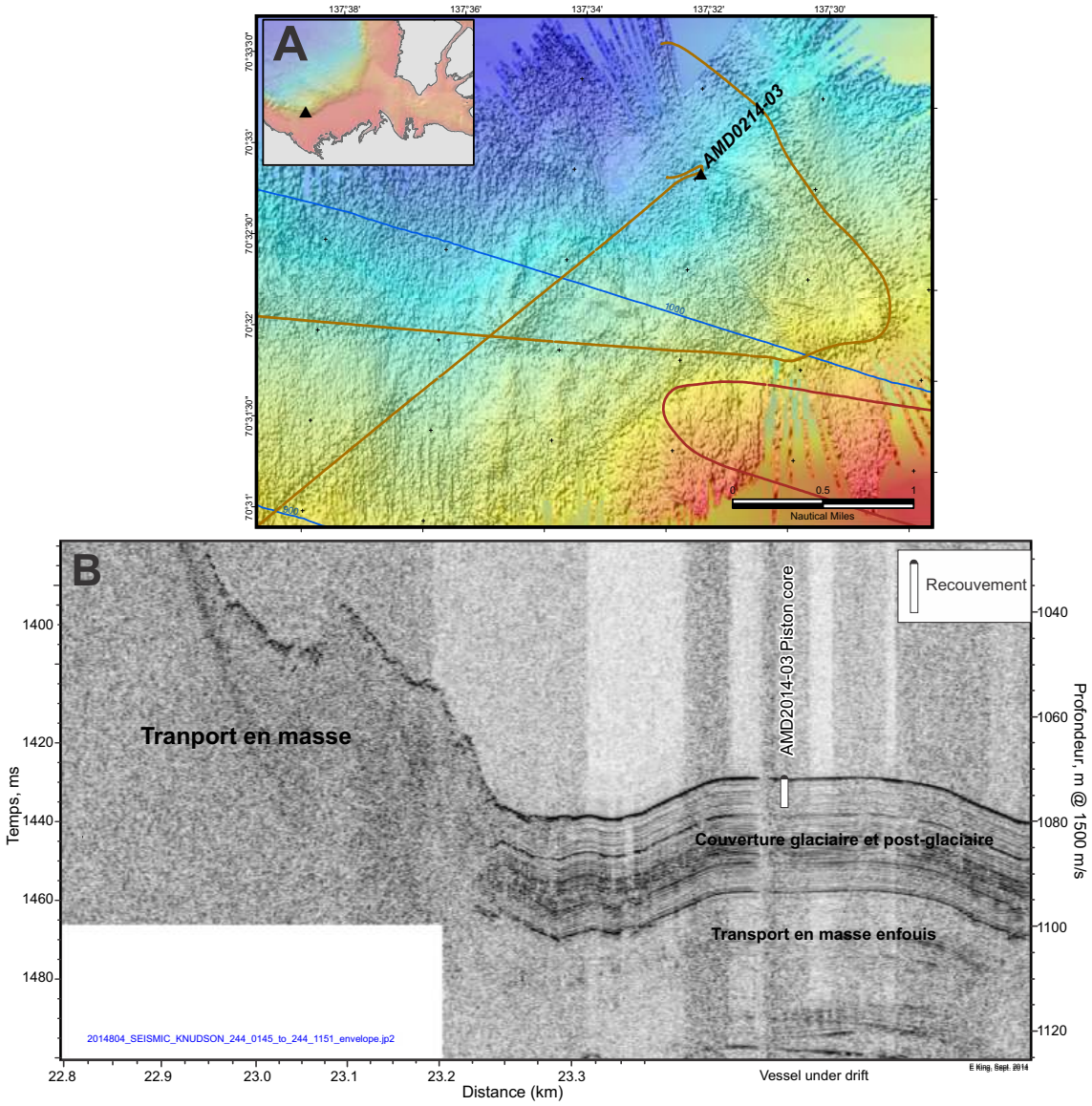

Figure 69: (A) Localisation du site de carottage AMD0214-03. (B) Profil sismique par acquisition à 3.5kHz.

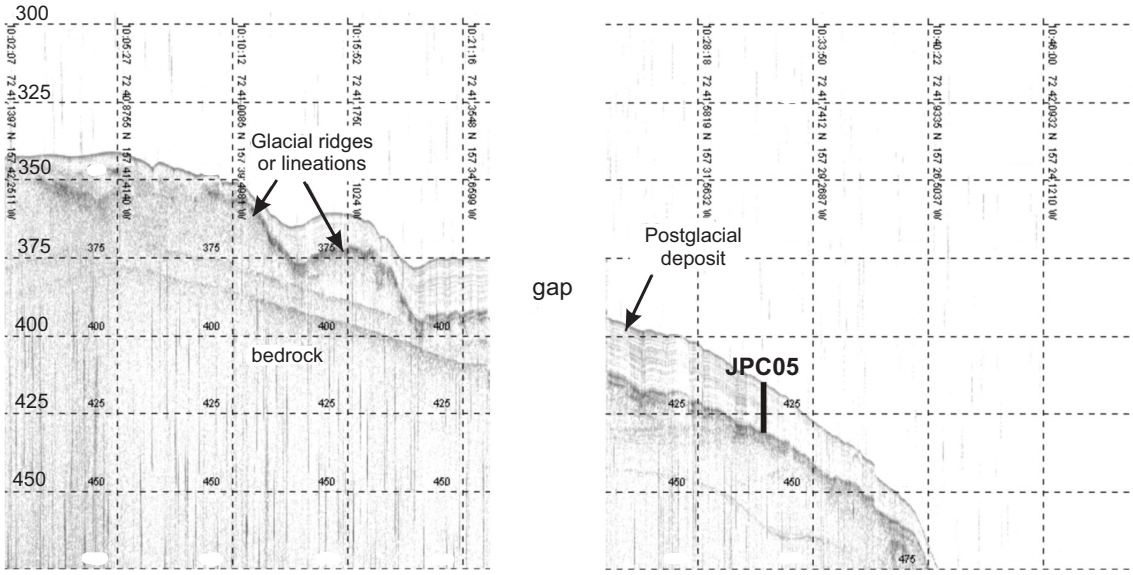

Figure 70: Profil sismique par acquisition à 3.5kHz de la carotte HLY0501-05JPC.

ANNEXE II

MSCL *WHOLE CORE* ET *SPLIT CORE*

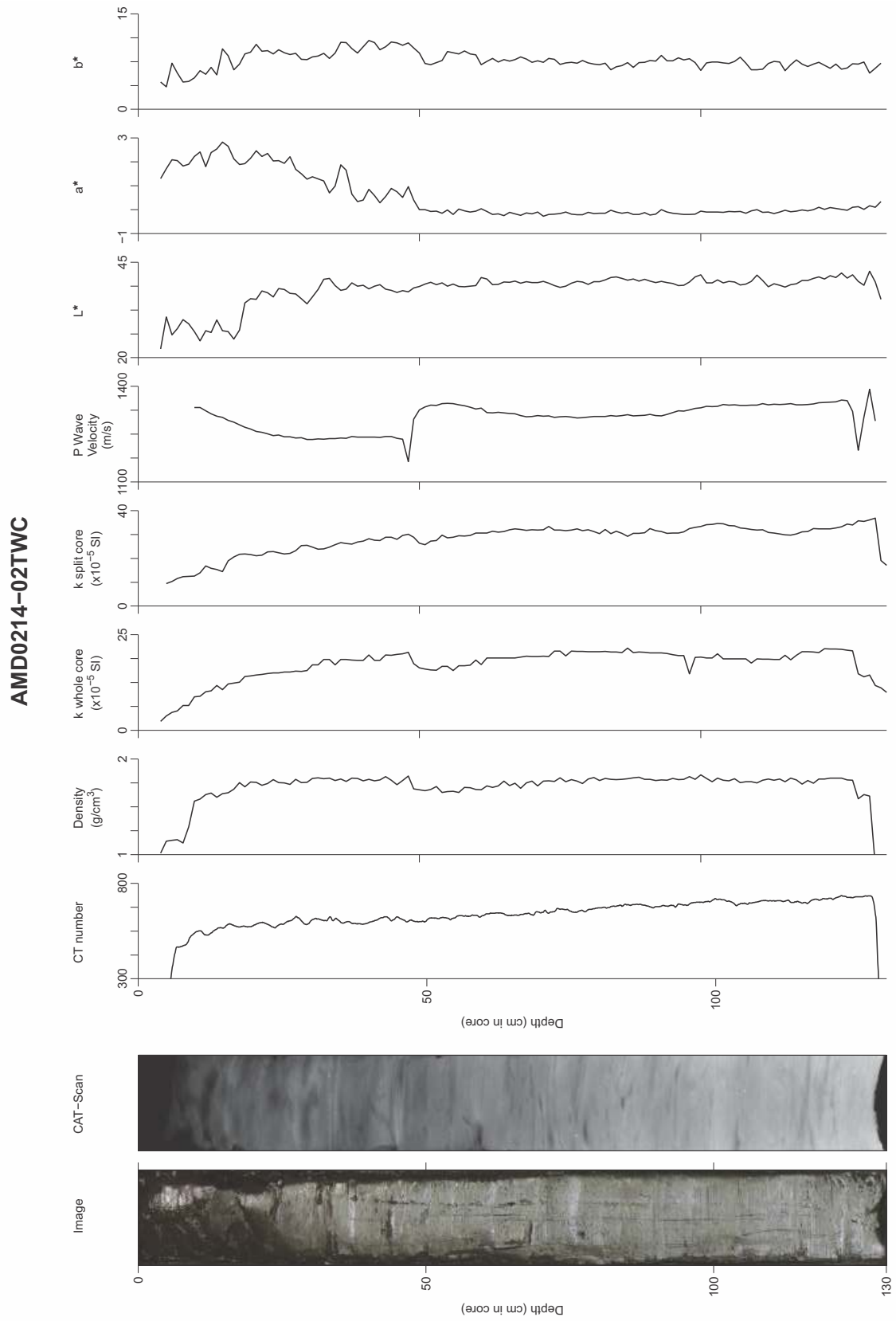

Figure 71: MSCL *whole* and *split core* pour la carotte AMD0214-02TWC

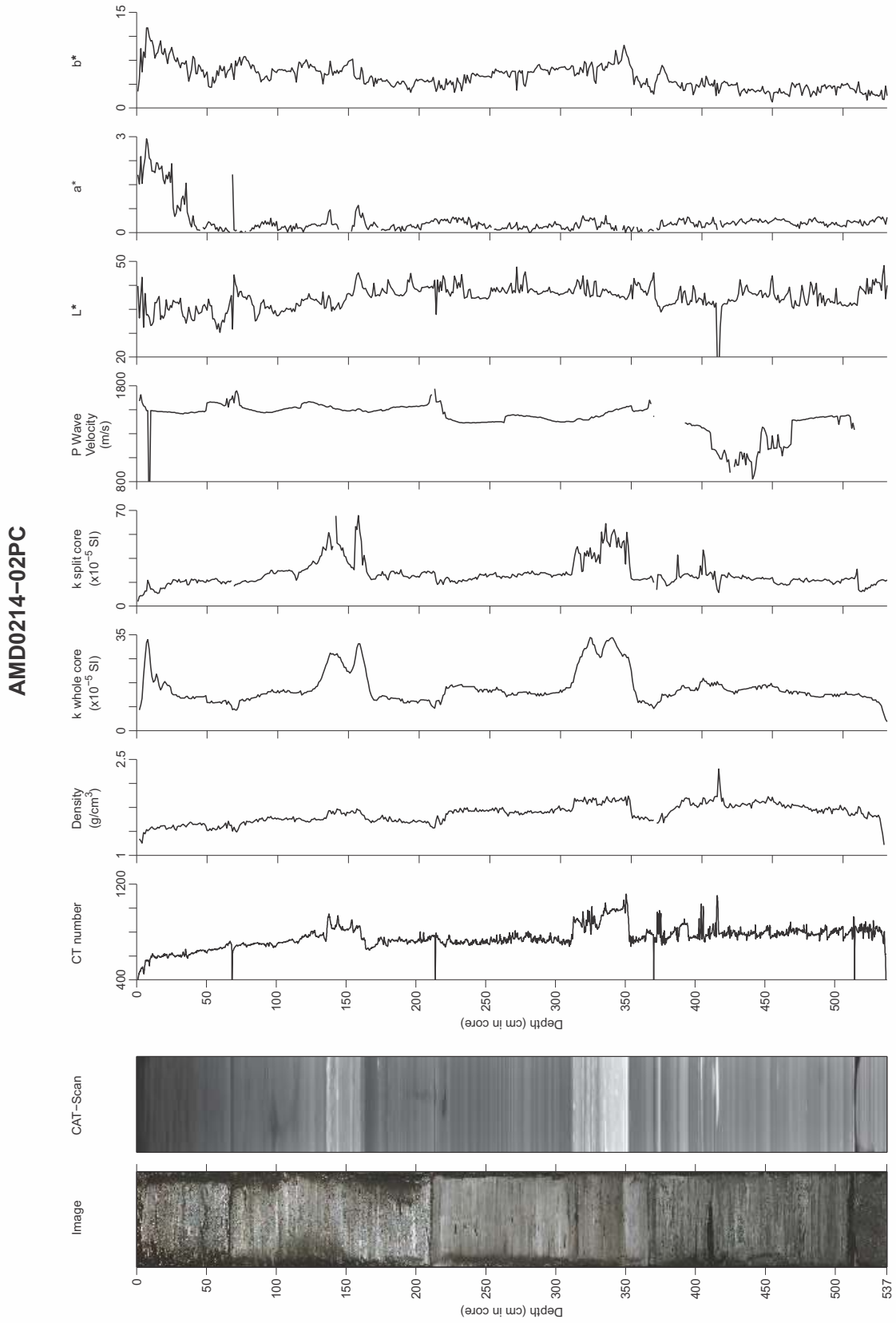

Figure 72: MSCL *whole* and *split core* pour la carotte AMD0214-02PC

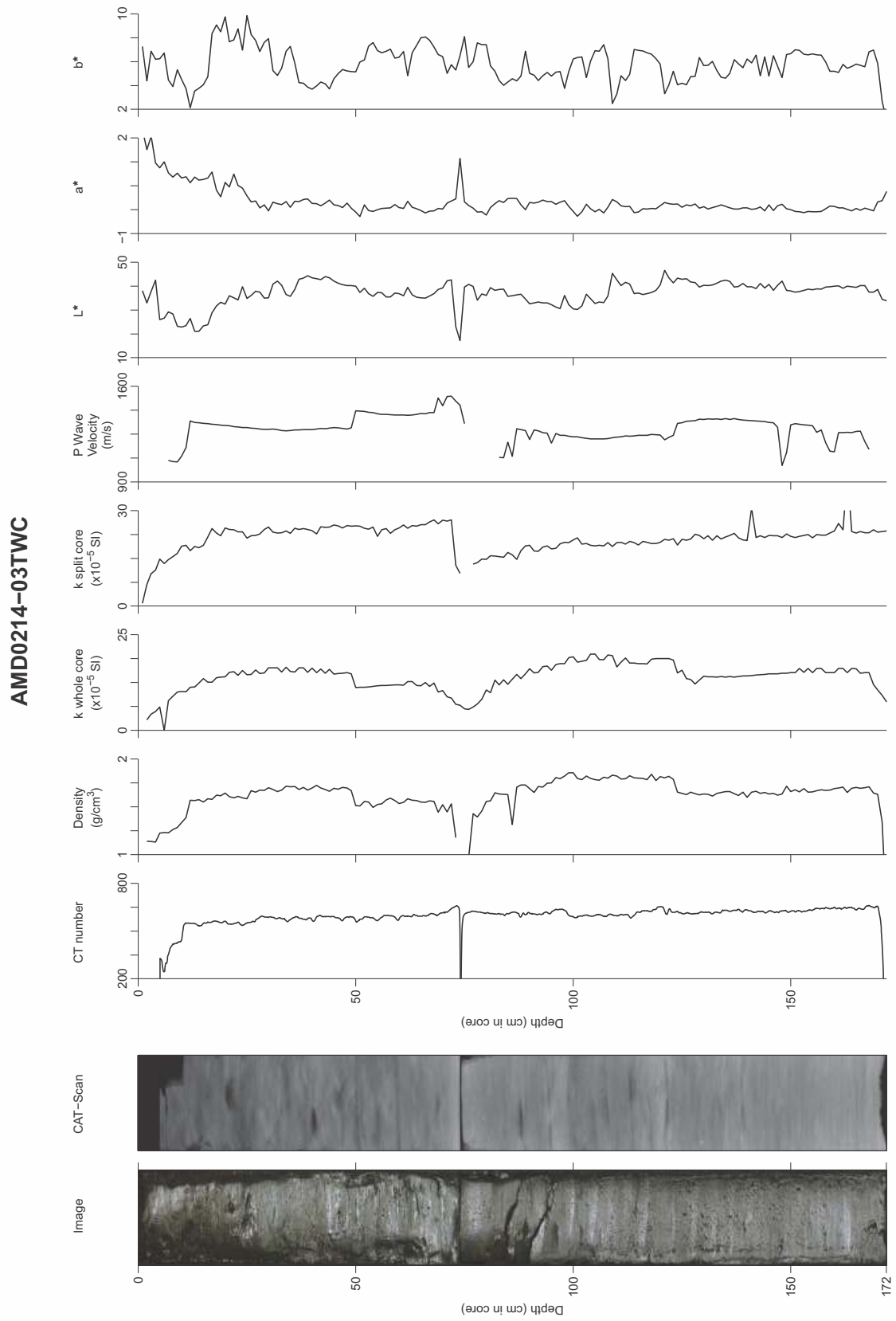

Figure 73: MSCL *whole* and *split core* pour la carotte AMD0214-03TWC

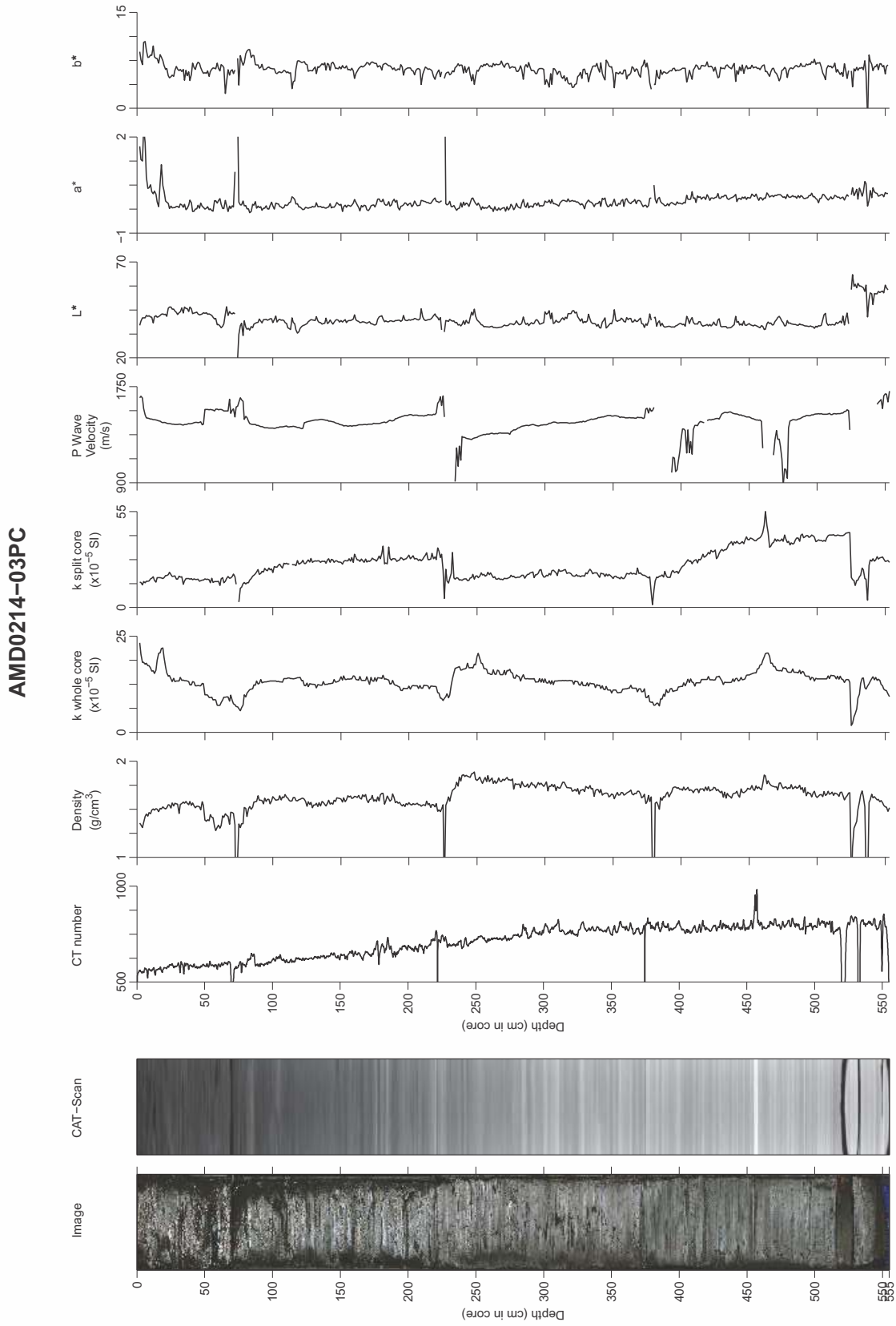

Figure 74: MSCL *whole* and *split core* pour la carotte AMD0214-03PC

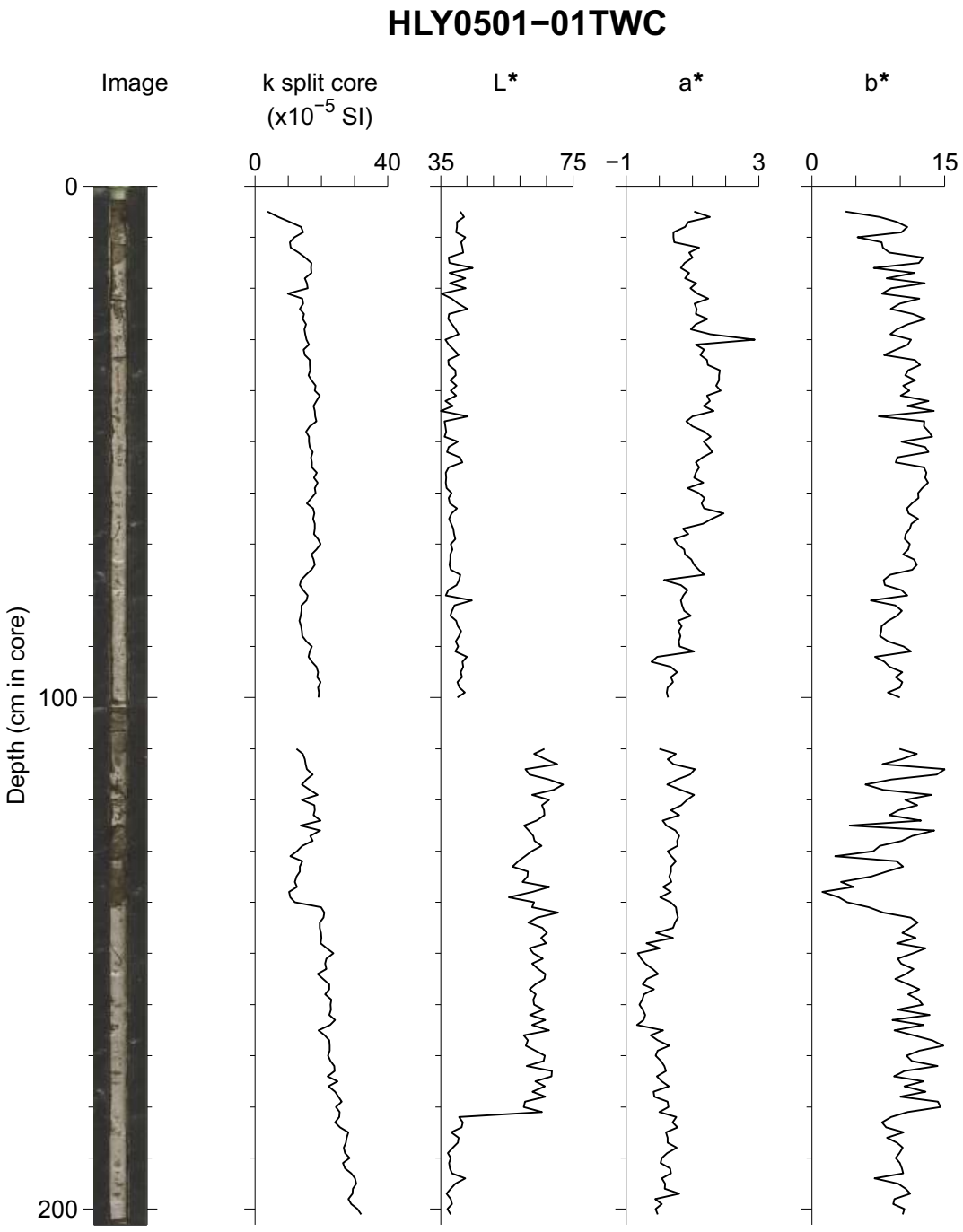

Figure 75: MSCL *split core* pour la carotte HLY0501-01TWC

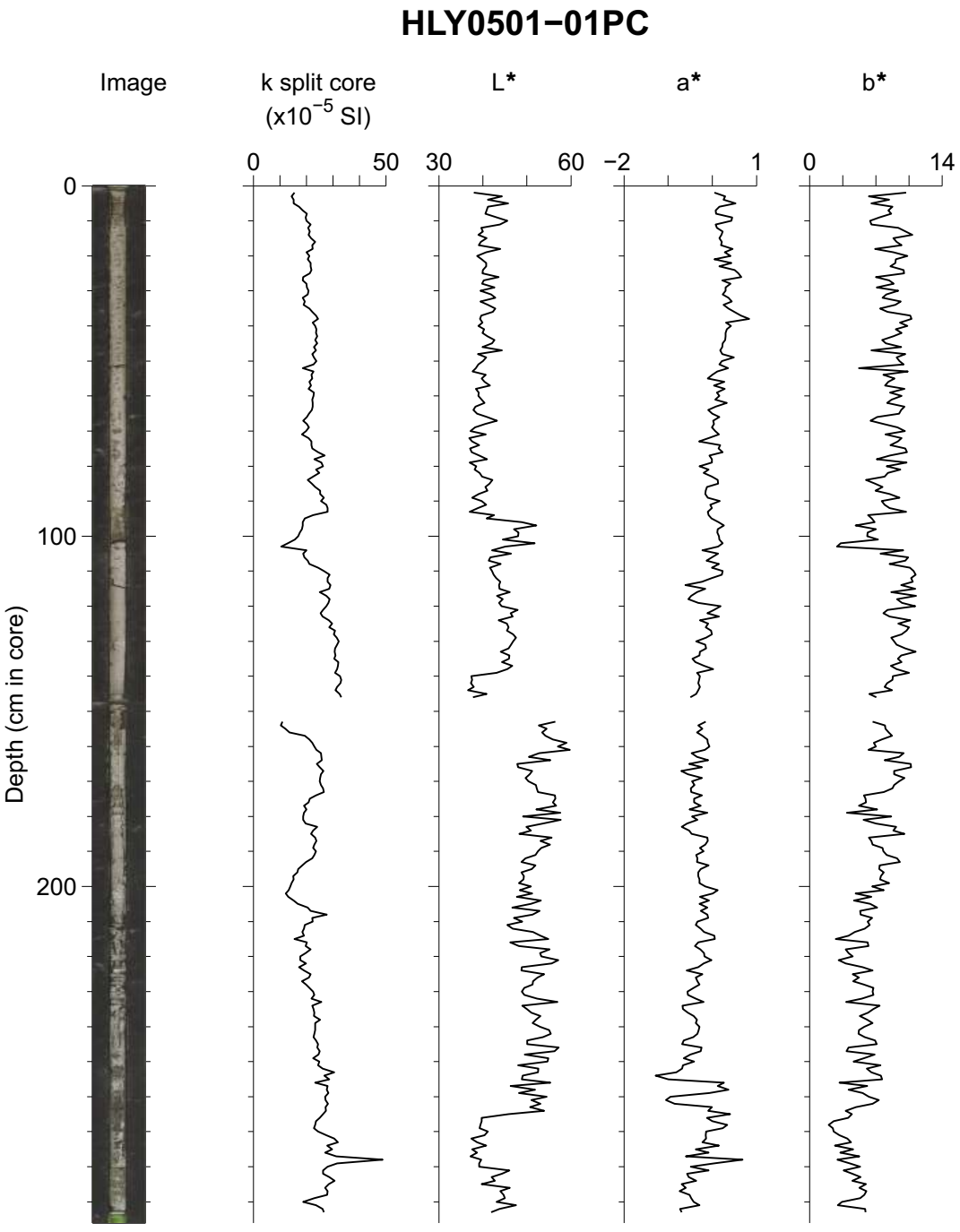

Figure 76: MSCL *split core* pour la carotte HLY0501-01PC

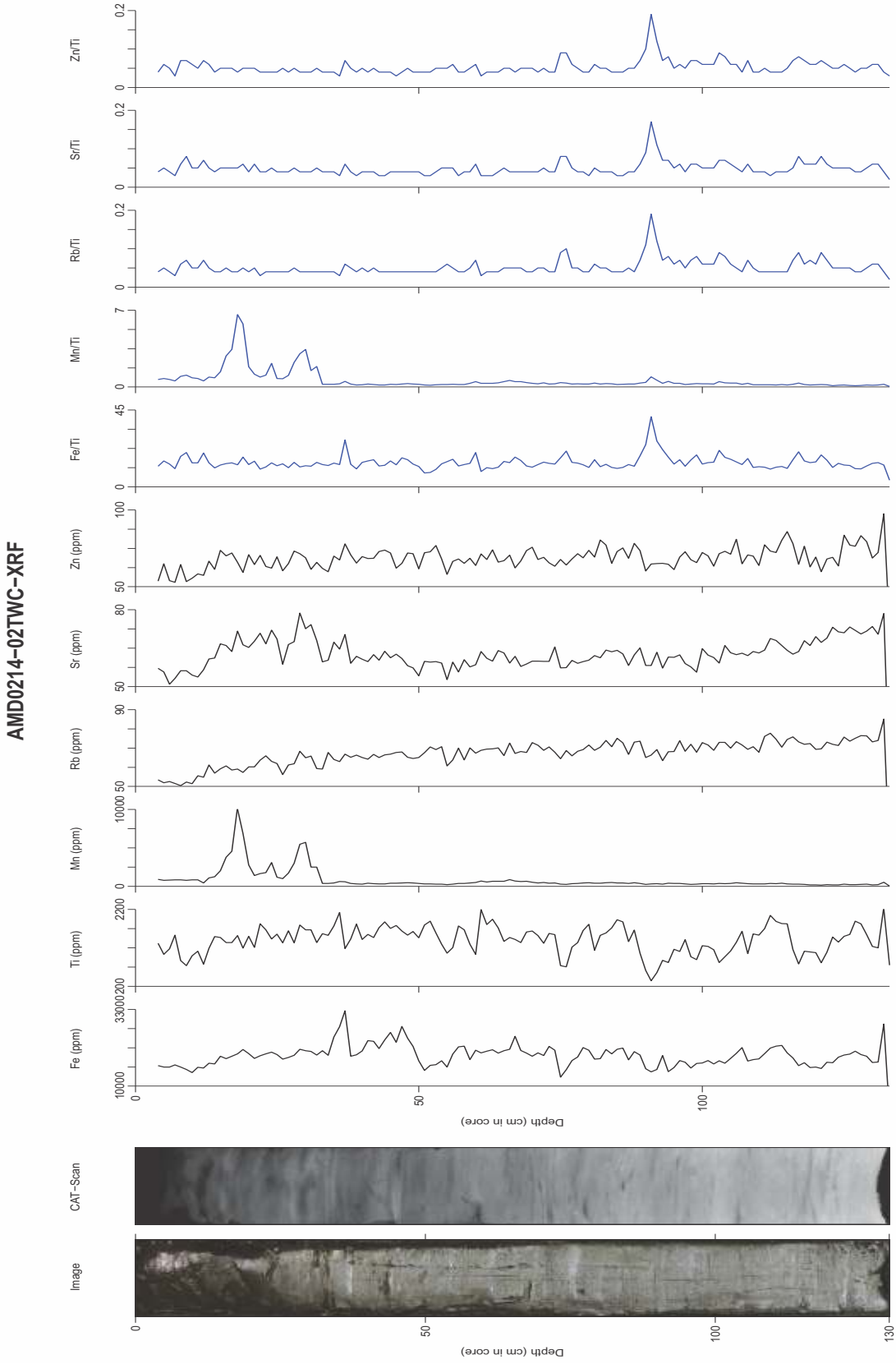

Figure 77: XRF pour la carotte AMD0214-02TWC

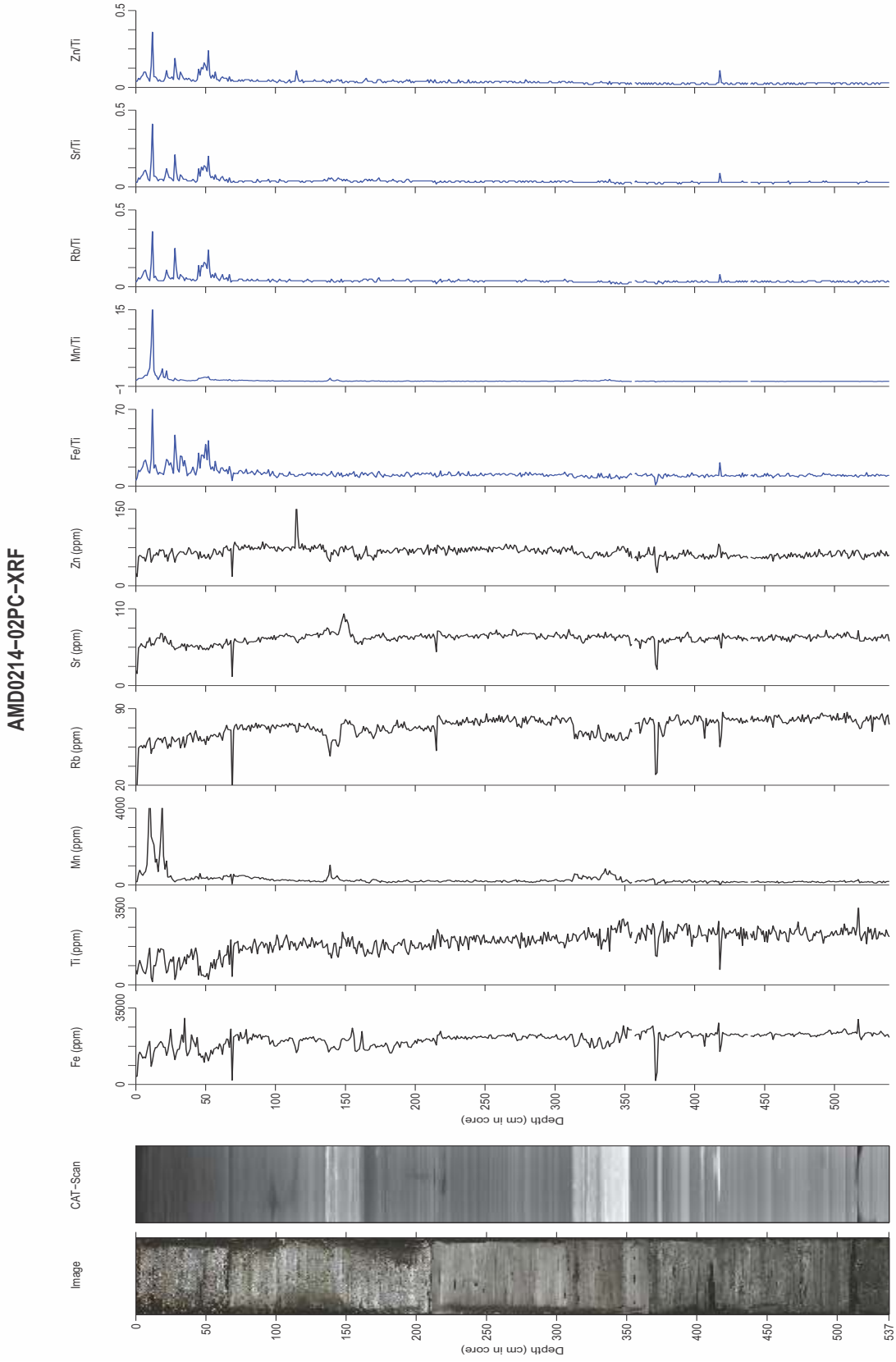

Figure 78: XRF pour la carotte AMD0214-02PC

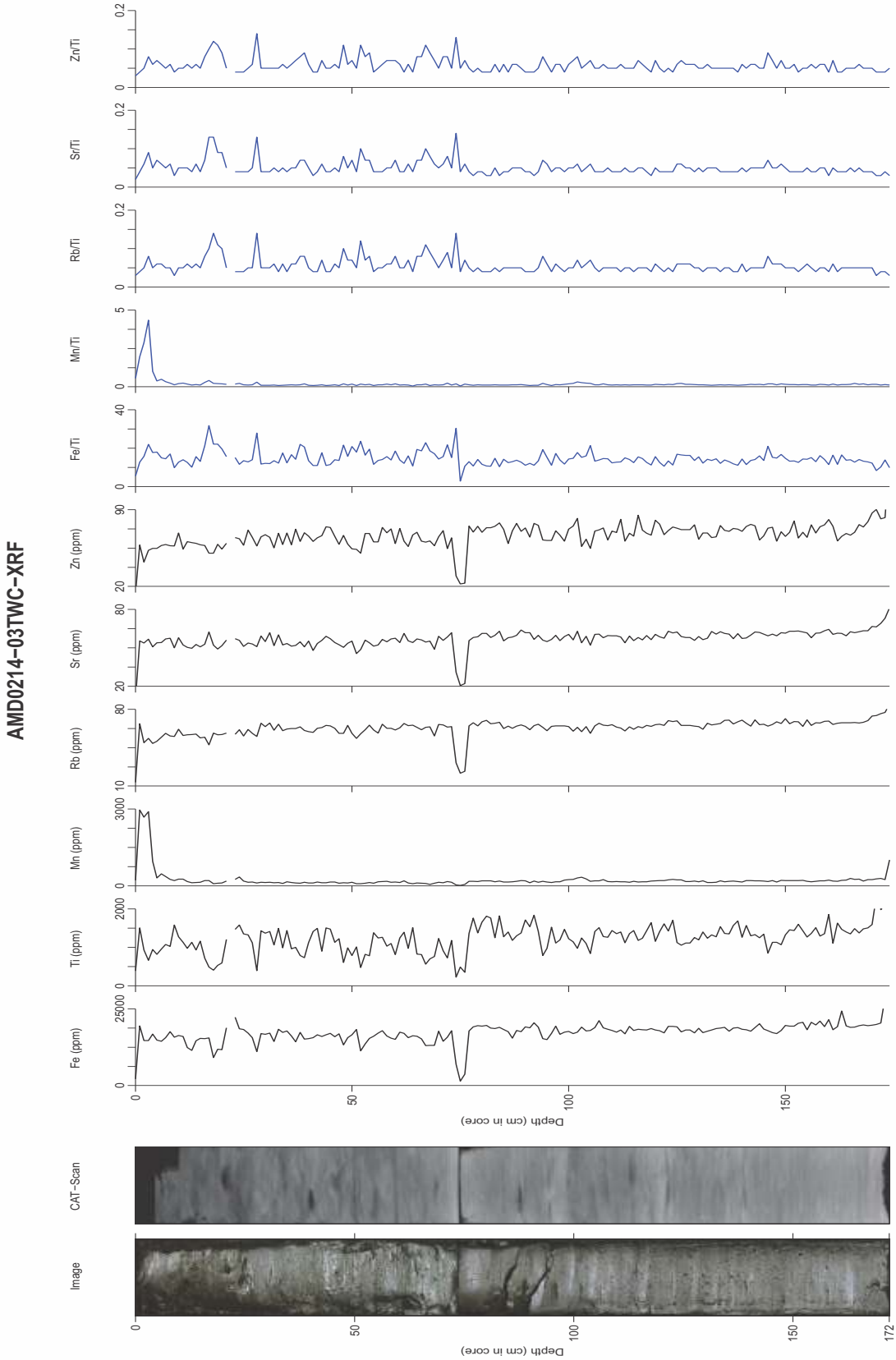

Figure 79: XRF pour la carotte AMD0214-03TWC

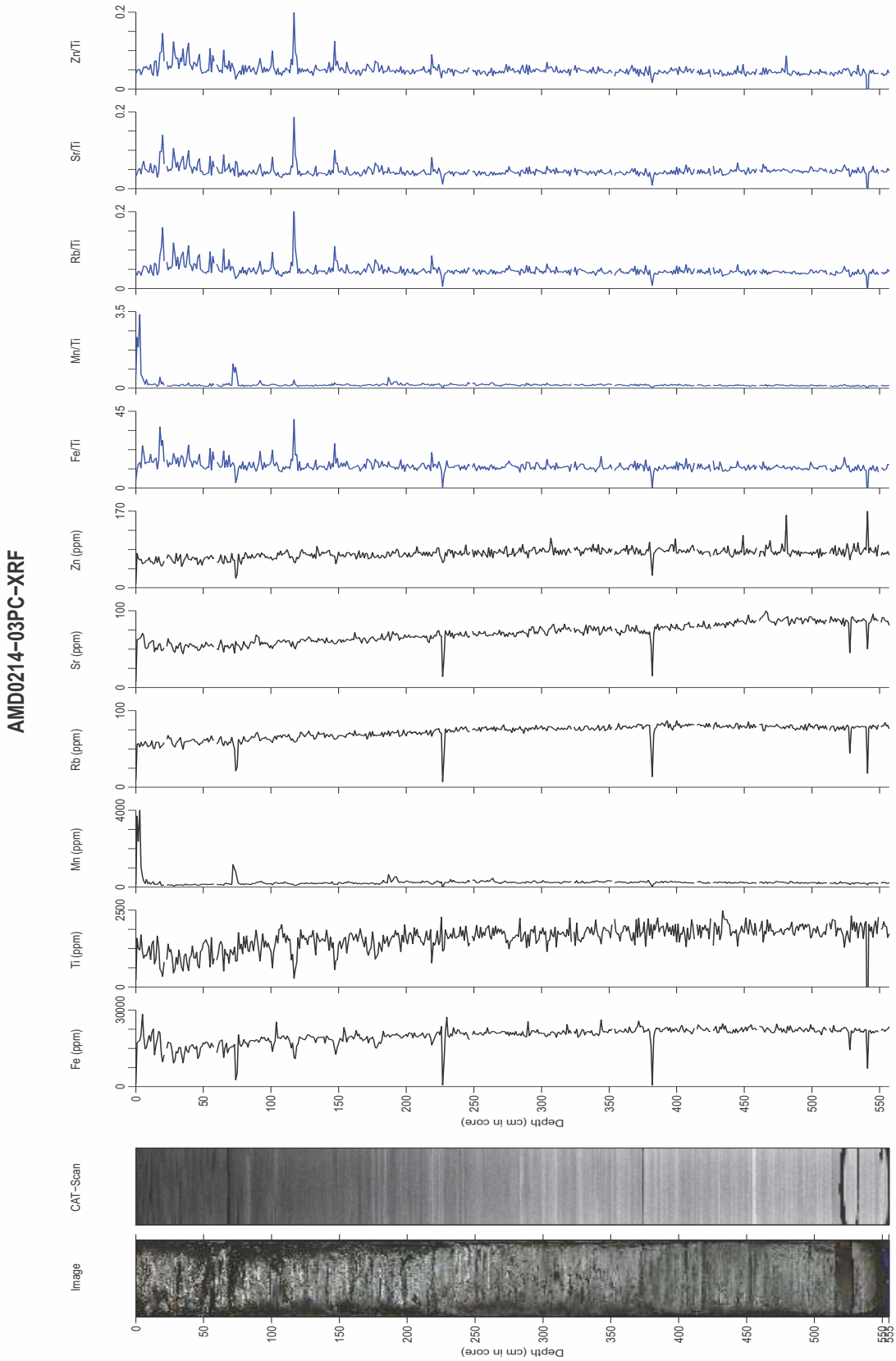

Figure 80: XRF pour la carotte AMD0214-03PC

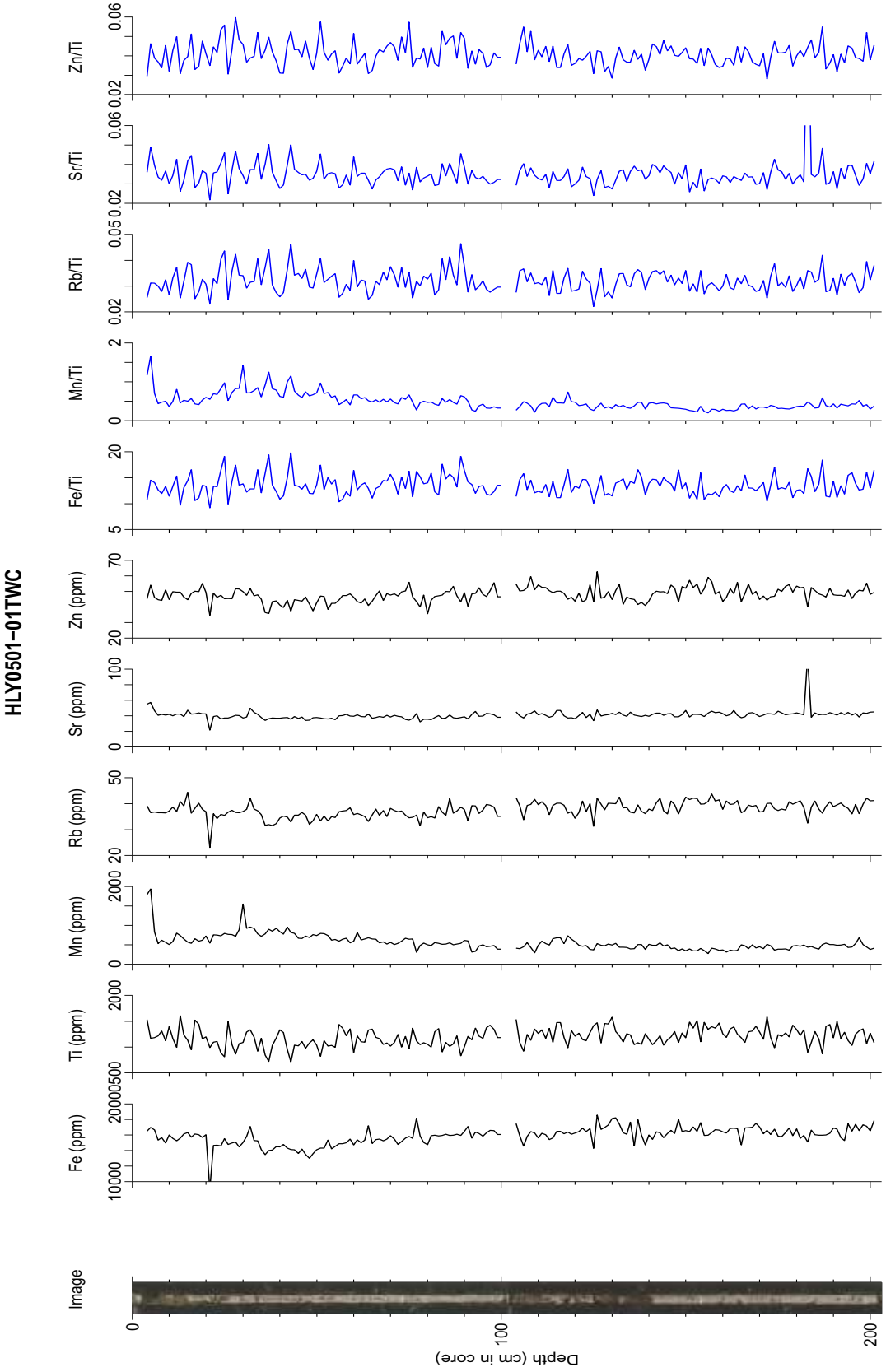

Figure 81: XRF pour la carotte HLY0501-01TWC

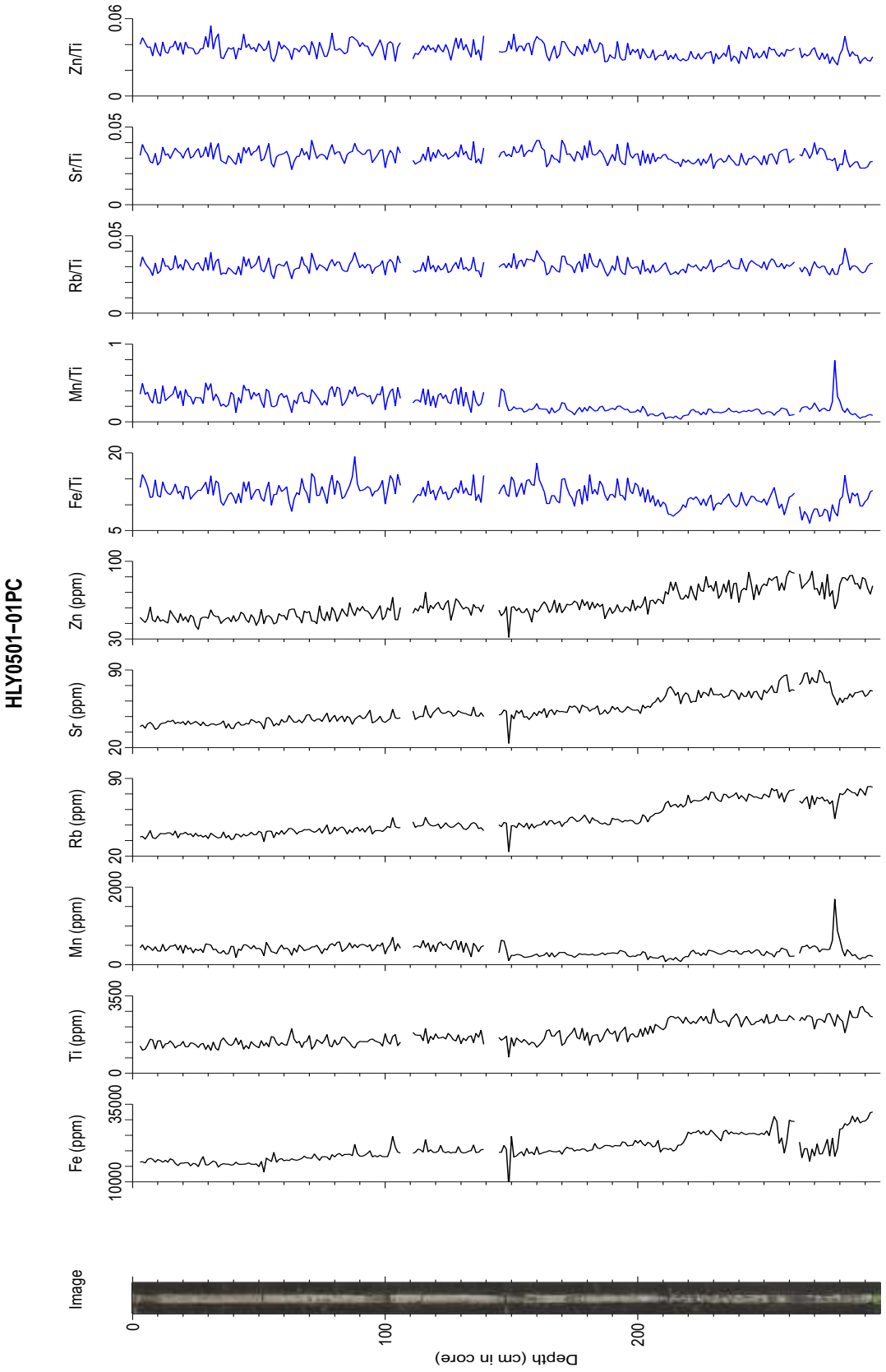

Figure 82: XRF pour la carotte HLY0501-01PC

ANNEXE III

DONNÉES

Tableau 13 – Éléments majeurs, traces et REE de la carotte 02PC. Oxydes exprimés en wt. % et les traces et REE en ppm.

	SiO_2		TiO_2		Al_2O_3		$Fe2O_3$		CaO		Na_2O		MgO		K_2O		P_2O_5		MnO		Sc		V	
Depth (cm)	Bulk	Clay	Bulk	Clay	Bulk	Clay	Bulk	Clay	Bulk	Clay	Bulk	Clay	Bulk	Clay	Bulk	Clay	Bulk	Clay	Bulk	Clay	Bulk	Clay	Bulk	Clay
5	62.93	54.42	0.87	0.71	20.17	23.41	7.66	9.21	0.70	0.85	2.54	1.40	1.22	1.67	3.63	4.10	0.86	1.59	0.09	0.31	25	27	269	391
20	62.45	54.18	0.86	0.74	20.53	23.32	7.56	9.09	0.61	0.80	2.00	1.17	1.20	1.74	3.64	4.10	0.81	0.68	0.10	0.41	22	29	303	358
40	61.68	53.74	0.84	0.73	20.14	22.33	8.80	11.01	0.57	0.74	2.19	1.56	1.00	1.79	3.65	4.18	0.91	1.67	0.06	0.11	20	27	276	375
60	62.96	53.45	0.86	0.74	20.84	23.83	7.33	9.52	0.61	0.77	1.75	1.15	1.13	1.72	3.73	4.23	0.80	1.66	0.04	0.13	17	29	271	380
80	63.11	57.92	0.85	0.78	20.73	26.07	7.74	10.74	0.60	0.82	0.72	1.72	1.19	2.05	3.71	4.63	0.76	0.85	0.05	0.16	24	33	277	409
100	62.42	54.44	0.83	0.71	20.26	23.67	6.81	8.67	0.66	0.86	1.94	1.80	1.16	1.81	3.71	4.30	0.79	0.77	0.04	0.09	22	27	250	334
120	63.73	54.52	0.81	0.73	20.64	23.15	6.68	8.77	1.15	1.02	1.86	1.43	1.55	1.87	3.65	4.32	0.65	0.73	0.05	0.07	25	27	218	343
126	65.12	58.49	0.85	0.82	18.71	22.34	4.82	7.40	0.53	0.55	-	-	0.60	1.24	3.52	4.16	0	0	0.02	0.03	12	9	248	325
131	63.44	59.11	0.82	0.82	19.03	22.18	5.26	6.73	0.58	0.51	-	-	0.77	1.04	3.51	4.06	0	0	0.02	0.03	13	9	240	292
134	64.98	60.50	0.84	0.83	19.04	22.26	5.01	6.70	0.61	0.54	-	-	0.80	1.25	3.47	4.06	0	0	0.02	0.03	10	9	231	307
139	64.17	56.45	0.72	0.72	17.41	21.81	5.38	8.04	1.46	1.08	-	-	1.34	1.97	3.39	3.99	0	0	0.04	0.05	13	19	203	261
140	53.51	52.99	0.50	0.64	13.65	20.86	4.56	8.15	12.66	3.68	1.01	1.75	8.17	3.70	2.75	4.10	0.59	0.62	0.16	0.28	12	23	137	235
150	63.13	53.17	0.81	0.73	19.99	23.47	6.57	8.71	1.87	1.64	2.31	1.15	2.23	2.27	3.75	4.37	0.60	0.72	0.06	0.09	21	28	223	297
160	60.56	52.88	0.67	0.72	15.99	23.90	4.70	7.67	6.31	1.46	0.54	0.61	5.53	2.86	3.27	4.61	0.76	0.58	0.05	0.08	16	30	176	301
180	61.64	52.00	0.86	0.69	21.08	24.06	6.60	7.78	1.69	1.41	1.75	1.59	1.56	1.76	3.60	4.10	0.79	0.70	0.04	0.07	24	27	269	328
200	55.26	54.88	0.80	0.72	18.74	24.18	6.23	8.04	1.18	1.39	1.44	1.43	1.42	1.85	3.38	4.32	0.63	0.66	0.03	0.06	20	26	250	338
220	62.43	54.55	0.87	0.73	21.25	24.10	6.82	7.76	1.24	1.39	3.41	0.84	1.60	1.95	3.88	4.35	0.67	0.72	0.04	0.05	22	28	266	318
240	60.39	52.80	0.85	0.70	21.11	23.21	6.78	7.62	1.34	1.33	1.36	0.86	1.49	1.74	3.86	4.33	0.73	0.69	0.04	0.05	22	26	252	304
260	61.16	52.33	0.87	0.67	21.69	24.76	6.94	7.37	1.27	1.30	1.98	0.53	1.59	2.03	3.77	4.30	0.61	0.56	0.05	0.05	24	27	286	333
280	62.87	53.11	0.88	0.72	20.99	25.01	6.75	8.26	1.13	1.11	1.51	0.68	1.31	1.58	3.57	4.30	0.70	0.71	0.03	0.05	23	28	281	349
300	61.78	54.04	0.91	0.73	21.65	25.09	6.75	7.70	1.09	1.12	2.12	0.98	1.37	1.62	3.77	4.32	0.53	0.69	0.05	0.07	23	30	312	347
320	63.53	52.55	0.78	0.75	17.23	24.18	5.71	9.09	4.15	1.50	2.52	1.83	3.39	2.15	3.13	4.19	0.59	0.65	0.07	0.12	18	29	173	300
330	59.31	53.72	0.82	0.78	18.59	24.04	5.61	7.47	4.56	1.79	1.24	0.77	3.40	2.62	3.34	4.28	0.71	0.59	0.09	0.11	20	26	198	313
340	62.03	51.88	0.76	0.73	16.58	24.01	4.75	7.75	5.44	1.91	1.15	1.25	4.47	2.85	3.07	4.21	0.55	0.59	0.11	0.24	20	28	182	298
350	70.53	50.52	0.85	0.70	15.66	24.15	6.06	12.18	1.65	0.75	1.17	0.88	1.13	1.82	2.71	4.08	0.75	0.75	0.04	0.13	16	32	176	326
360	63.33	54.05	0.94	0.83	22.05	25.07	6.51	7.73	0.39	0.49	1.71	0.85	1.14	1.55	3.58	4.18	0.61	0.73	0.02	0.03	26	35	283	337
375	60.78	53.01	0.88	0.83	20.03	25.49	6.59	8.80	1.16	0.64	1.21	2.09	1.33	1.73	3.39	4.32	0.63	0.70	0.04	0.04	23	29	246	372
380	62.65	54.40	0.95	0.85	22.79	25.44	6.48	7.49	0.40	0.54	2.34	1.03	1.30	1.70	3.80	4.32	0.65	0.60	0.02	0.03	25	30	296	343
390	64.01	56.83	0.98	0.94	20.55	24.07	6.26	7.41	0.43	0.49	1.85	1.33	1.09	1.45	3.42	3.98	0.62	0.65	0.03	0.04	22	30	270	335
400	61.90	54.37	0.94	0.84	22.56	25.47	6.48	7.41	0.39	0.51	2.71	2.33	1.41	1.49	3.70	4.22	0.58	0.60	0.03	0.03	22	26	275	358
420	62.46	53.60	0.94	0.83	22.48	25.21	6.62	7.58	0.43	0.59	1.55	1.11	1.39	1.55	3.73	4.28	0.76	0.64	0.02	0.03	26	28	289	345
440	62.05	53.43	0.94	0.82	22.05	25.55	6.41	7.20	0.46	0.57	1.88	1.10	1.22	1.59	3.68	4.29	0.71	0.60	0.02	0.03	24	30	280	346
460	63.45	53.82	0.93	0.81	22.14	25.80	6.30	7.26	0.45	0.57	2.17	1.08	1.13	1.59	3.67	4.35	0.69	0.55	0.02	0.02	22	29	281	335
480	62.88	54.52	0.90	0.83	21.34	24.76	6.35	7.48	0.61	0.59	1.38	0.81	1.22	1.58	3.54	4.35	0.60	0.59	0.02	0.03	24	29	272	347
500	63.68	53.94	0.95	0.83	21.52	25.57	6.29	7.41	0.41	0.60	1.63	1.07	1.12	1.53	3.57	4.25	1.14	0.63	0.03	0.03	22	29	248	349

Tableau 13 – Éléments majeurs, traces et REE de la carotte 02PC. Oxydes exprimés en wt. % et les traces et REE en ppm (suite).

	Cr		Co		Zn		Rb		Sr		Zr		La		Ce		Pr		Nd		Sm		Eu	
Depth (cm)	Bulk	Clay	Bulk	Clay	Bulk	Clay	Bulk	Clay	Bulk	Clay	Bulk	Clay	Bulk	Clay	Bulk	Clay	Bulk	Clay	Bulk	Clay	Bulk	Clay	Bulk	Clay
5	170	313	15	35	150	179	143	167	136	156	151	142	47	52	85	92	10	11	39	43	6.47	8.05	1.50	1.52
20	204	187	19	35	129	170	137	179	131	165	158	139	46	55	86	99	10	12	35	46	6.68	7.86	1.33	1.53
40	191	204	57	32	121	187	139	167	126	146	146	145	48	56	83	96	10	11	38	44	7.04	8.63	1.19	1.75
60	172	190	14	32	133	210	129	171	125	141	152	176	43	56	81	97	9	12	35	45	5.16	8.95	1.23	1.79
80	160	230	15	29	135	210	144	194	123	152	151	161	49	61	86	105	10	13	39	50	7.34	8.97	1.14	1.86
100	173	191	17	31	119	179	145	176	135	158	162	153	47	59	90	109	10	12	40	47	6.79	8.76	1.27	1.79
120	148	188	19	23	137	199	160	158	127	156	159	159	51	51	94	93	11	11	41	42	8.72	7.84	1.42	1.45
126	117	140	7	11	61	274	113	93	111	140	158	151	29	22	55	41	6	5	23	17	3.59	2.79	0.65	0.51
131	115	152	7	10	55	184	121	90	115	133	157	152	31	21	57	40	7	5	24	17	3.73	2.65	0.68	0.52
134	106	222	7	10	60	294	92	85	106	139	153	152	25	21	47	40	5	5	20	16	3.09	2.60	0.58	0.48
139	124	16	9	16	94	888	124	156	124	131	146	147	30	36	54	72	6	8	22	29	3.51	5.29	0.69	1.06
140	103	157	15	36	86	153	89	136	143	151	131	143	31	45	63	86	7	10	27	37	4.51	6.63	1.02	1.44
150	163	205	22	28	130	194	144	175	147	151	153	136	43	48	82	81	9	10	36	38	6.16	7.15	1.51	1.29
160	123	164	15	23	95	161	111	177	114	127	158	152	35	55	72	103	8	12	31	45	5.34	7.43	0.97	1.54
180	158	183	25	30	143	162	158	176	126	141	154	144	51	51	92	91	11	11	41	41	7.59	6.48	1.44	1.40
200	160	196	32	22	122	158	139	171	117	142	147	151	41	51	79	90	9	11	33	40	5.48	7.86	1.07	1.27
220	143	161	23	22	127	153	158	171	129	134	156	151	50	56	94	100	10	12	38	44	6.84	8.85	1.71	1.23
240	164	180	20	24	129	153	158	162	123	134	159	150	48	51	94	91	10	11	42	40	7.43	7.13	1.50	1.28
260	173	198	20	24	125	133	169	184	127	124	163	142	52	50	94	90	11	11	42	41	7.26	6.36	1.47	1.41
280	163	222	23	30	119	165	149	176	121	134	158	150	49	52	89	93	10	11	40	41	7.40	7.62	1.29	1.37
300	147	202	26	36	125	146	164	180	132	141	164	150	51	55	95	97	11	11	43	43	6.80	8.24	1.56	1.38
320	133	184	27	53	99	151	109	168	103	124	191	163	39	53	75	99	9	11	32	44	5.85	7.98	1.48	1.51
330	120	182	25	33	101	144	117	159	120	139	168	162	41	52	82	95	9	11	35	42	5.84	8.28	1.22	1.52
340	129	187	26	39	148	147	122	164	109	125	186	153	42	51	85	97	9	11	36	43	6.18	8.03	1.26	1.54
350	115	193	33	74	115	189	96	155	105	104	294	154	37	46	72	88	8	10	32	40	5.58	8.98	1.14	1.66
360	149	187	21	76	74	98	158	175	103	119	158	166	49	51	94	99	11	11	39	45	6.18	8.66	1.09	1.69
375	158	190	25	25	153	131	138	176	116	127	183	157	46	55	89	114	10	12	41	46	7.59	7.74	1.58	1.58
380	164	191	16	34	73	86	165	175	116	126	153	160	50	53	96	100	11	11	39	44	6.70	7.87	1.03	1.61
390	134	160	22	19	79	99	139	172	115	135	164	163	49	53	90	97	10	11	40	41	7.76	6.79	1.05	1.38
400	159	183	46	29	81	119	151	172	116	130	165	161	49	57	96	107	10	12	37	45	6.27	8.01	1.22	1.56
420	151	173	20	26	97	98	161	168	125	127	164	154	52	52	100	98	11	11	42	43	7.73	6.97	1.31	1.58
440	168	188	19	43	80	97	157	175	118	128	157	160	51	54	95	100	11	11	40	43	6.04	7.55	1.37	1.42
460	157	198	37	26	88	89	143	172	120	127	171	152	47	54	87	102	10	11	37	44	5.91	6.82	1.15	1.53
480	167	184	28	18	87	109	149	169	114	143	171	168	50	52	97	96	10	11	40	40	6.86	8.29	1.25	1.50
500	146	214	21	15	141	124	151	176	113	126	168	156	45	52	88	96	10	11	36	42	5.27	8.22	1.15	1.38

Tableau 13 – Éléments majeurs, traces et REE de la carotte 02PC. Oxydes exprimés en wt. % et les traces et REE en ppm (suite).

	Gd		Tb		Dy		Ho		Er		Tm		Yb		Lu		Hf		Ta		Th		U	
Depth (cm)	Bulk	Clay	Bulk	Clay	Bulk	Clay	Bulk	Clay	Bulk	Clay	Bulk	Clay	Bulk	Clay	Bulk	Clay	Bulk	Clay	Bulk	Clay	Bulk	Clay	Bulk	Clay
5	5.68	6.46	0.87	0.94	4.73	5.49	0.83	1.15	2.86	3.52	0.47	0.43	2.77	3.11	0.58	0.57	4.58	4.54	1.11	1.03	15.30	17.40	3.93	4.05
20	6.42	6.30	0.76	0.99	4.30	5.72	0.83	1.15	3.12	2.98	0.43	0.59	3.29	3.79	0.43	0.52	4.59	5.04	1.26	1.16	14.40	18.20	3.49	4.40
40	5.07	7.12	0.67	1.00	4.55	6.45	0.96	1.19	2.77	3.56	0.44	0.56	3.26	3.68	0.45	0.51	4.17	4.44	1.04	1.02	14.30	19.30	3.30	4.10
60	4.35	6.73	0.69	0.97	4.21	6.26	0.88	1.29	2.58	3.78	0.47	0.51	3.01	3.57	0.37	0.48	3.97	5.00	0.99	1.20	14.30	19.60	3.23	4.14
80	5.85	8.75	0.89	1.05	4.76	6.96	1.13	1.40	2.84	3.97	0.51	0.56	3.44	4.60	0.45	0.59	4.81	5.28	1.28	1.32	16.00	21.80	3.24	4.38
100	5.34	7.73	0.80	1.07	4.97	6.15	0.86	1.24	2.82	3.45	0.48	0.53	2.72	3.64	0.56	0.52	4.52	4.65	1.18	1.18	16.20	22.10	3.74	4.52
120	6.14	6.49	0.82	0.91	5.45	5.59	0.98	1.10	3.12	3.16	0.52	0.43	3.27	3.25	0.45	0.52	4.89	4.22	1.25	1.09	16.40	19.30	3.74	3.77
126	2.31	1.87	0.36	0.28	2.51	1.77	0.53	0.39	1.74	1.20	0.27	0.19	1.94	1.38	0.30	0.21	4.53	4.22	1.13	1.10	11.22	9.97	2.81	3.14
131	2.46	1.71	0.40	0.25	2.63	1.67	0.58	0.37	1.81	1.17	0.28	0.19	2.01	1.36	0.30	0.21	4.41	4.27	1.08	1.10	11.34	9.62	2.82	3.01
134	2.07	1.72	0.33	0.26	2.20	1.70	0.49	0.37	1.59	1.21	0.25	0.19	1.75	1.41	0.27	0.21	4.34	4.15	1.07	1.08	9.12	9.12	2.78	3.04
139	2.49	3.79	0.37	0.57	2.57	3.52	0.54	0.72	1.70	2.10	0.26	0.32	1.82	2.19	0.28	0.33	4.18	3.97	0.86	0.93	10.95	15.10	2.40	3.60
140	3.78	6.26	0.49	0.67	3.21	4.98	0.62	1.05	1.90	2.72	0.28	0.39	1.72	3.05	0.28	0.32	3.40	4.18	0.75	0.95	10.10	16.70	2.55	2.98
150	6.24	6.91	0.88	0.81	5.27	5.19	0.76	1.14	2.70	3.36	0.31	0.42	2.61	2.77	0.40	0.61	4.45	4.85	1.38	1.33	15.70	20.80	3.28	3.57
160	3.71	6.64	0.63	1.04	4.55	6.21	0.78	1.14	2.35	3.39	0.29	0.56	2.23	3.47	0.27	0.55	3.87	4.83	0.95	1.19	12.00	20.90	3.35	4.56
180	7.42	6.41	0.81	0.79	6.03	5.62	1.13	1.13	3.16	3.35	0.49	0.42	3.00	3.21	0.38	0.52	4.75	4.07	1.34	1.12	15.40	17.20	4.73	4.62
200	5.22	6.27	0.66	0.88	4.45	4.96	0.93	1.16	2.40	3.09	0.45	0.49	2.62	3.35	0.47	0.51	3.49	4.49	1.13	1.19	12.80	16.90	3.80	4.52
220	6.11	6.89	0.91	0.95	5.29	6.01	0.99	1.13	2.95	3.39	0.52	0.51	3.06	3.76	0.42	0.53	4.34	5.05	1.26	1.22	16.80	20.20	4.27	4.39
240	5.44	5.91	0.88	0.87	5.30	5.55	0.94	1.09	2.83	3.38	0.37	0.45	3.05	3.36	0.41	0.48	4.28	4.57	1.24	1.19	15.60	18.00	4.41	4.24
260	5.50	5.00	0.87	0.84	5.26	5.56	1.12	0.99	3.46	2.92	0.44	0.52	2.99	3.08	0.46	0.51	4.92	4.32	1.21	0.96	15.50	15.50	4.81	4.04
280	5.63	5.71	0.81	0.82	5.09	5.83	1.06	1.14	3.06	3.21	0.47	0.46	3.38	3.72	0.56	0.58	4.41	4.67	1.25	1.12	14.30	16.30	4.26	4.14
300	5.94	6.10	0.99	0.92	5.25	6.01	1.08	1.25	3.30	3.40	0.52	0.57	2.97	4.03	0.46	0.68	4.30	4.82	1.27	1.10	15.20	16.90	4.49	4.57
320	4.33	6.51	0.78	0.85	4.59	5.49	0.82	1.16	2.46	3.60	0.35	0.58	2.98	3.40	0.42	0.48	5.20	5.30	1.14	1.23	12.30	18.10	3.25	3.96
330	5.06	6.23	0.77	1.03	5.07	5.61	1.02	0.98	2.76	3.28	0.43	0.46	2.92	3.70	0.37	0.49	4.68	4.92	0.99	1.10	12.60	17.20	3.53	4.04
340	5.32	5.58	0.75	0.73	4.88	5.79	1.06	1.12	2.85	3.03	0.39	0.47	3.01	3.51	0.47	0.42	4.95	4.89	1.06	1.14	12.10	17.00	3.84	4.22
350	5.24	6.78	0.87	0.97	5.10	7.06	1.14	1.22	3.31	3.79	0.49	0.62	3.39	3.58	0.58	0.58	7.25	4.81	1.02	1.05	11.10	17.70	3.25	3.76
360	5.07	8.02	0.82	1.12	4.92	6.60	1.15	1.31	2.88	4.15	0.49	0.52	3.71	4.09	0.54	0.56	4.85	5.14	1.35	1.10	14.80	19.40	3.49	3.94
375	5.80	7.13	0.85	0.92	5.52	6.09	1.08	1.14	3.51	3.42	0.50	0.54	3.67	3.69	0.58	0.64	5.29	5.22	1.18	1.32	13.00	17.20	3.85	3.99
380	5.31	5.91	0.79	0.86	5.12	5.62	1.00	1.16	3.41	3.28	0.49	0.53	4.05	3.53	0.50	0.62	5.04	4.87	1.47	1.23	14.70	16.90	3.96	4.32
390	5.74	6.86	0.84	0.81	4.37	5.39	1.00	1.10	3.21	3.44	0.54	0.50	2.76	3.42	0.43	0.51	4.91	4.90	1.55	1.32	14.70	15.70	3.97	3.89
400	4.97	6.30	0.71	0.89	5.27	6.00	1.18	1.11	3.46	3.63	0.46	0.56	3.50	3.39	0.57	0.55	4.49	4.73	1.21	1.43	14.10	16.10	3.60	3.94
420	5.58	6.17	0.84	0.75	4.68	5.96	1.11	1.22	3.50	3.11	0.51	0.52	3.46	3.54	0.57	0.59	4.77	4.82	1.36	1.31	14.60	15.40	3.96	3.65
440	5.38	6.20	0.76	0.92	5.13	5.73	0.96	1.15	2.98	3.31	0.52	0.56	3.79	3.34	0.58	0.57	4.85	4.71	1.36	1.29	15.10	16.00	3.69	3.93
460	4.37	5.79	0.64	0.92	5.16	6.03	1.04	1.16	2.91	3.48	0.45	0.50	3.01	4.04	0.49	0.59	5.11	4.84	1.37	1.35	13.40	15.90	3.49	3.90
480	5.89	5.40	0.80	0.91	5.12	5.01	1.15	1.12	2.97	3.16	0.45	0.51	3.00	3.75	0.51	0.57	4.83	4.87	1.28	1.15	14.30	15.50	3.90	3.78
500	4.66	6.38	0.59	0.86	4.32	5.03	0.89	1.17	2.34	3.30	0.34	0.51	2.78	3.41	0.51	0.54	4.20	5.19	1.30	1.15	12.70	15.30	3.34	3.90

Tableau 14 – Éléments majeurs, traces et REE de la carotte 05JPC. Oxydes exprimés en wt. % et les traces et REE en ppm.

	SiO_2		TiO_2		Al_2O_3		$Fe2O_3$		CaO		Na_2O		MgO		K_2O		P_2O_5		MnO		Sc		V	
Depth (cm)	Bulk	Clay	Bulk	Clay	Bulk	Clay	Bulk	Clay	Bulk	Clay	Bulk	Clay	Bulk	Clay	Bulk	Clay	Bulk	Clay	Bulk	Clay	Bulk	Clay	Bulk	Clay
201	65.77	62.71	0.82	0.88	17.08	18.16	7.98	8.53	1.09	0.87	1.32	1.49	1.54	1.84	2.89	3.09	0.60	0.58	0.05	0.05	19	21	221	262
231	67.50	60.33	0.83	0.80	17.01	18.46	8.22	9.26	1.02	0.77	2.01	1.04	1.64	1.75	2.93	3.13	0.72	0.65	0.04	0.07	21	24	228	302
304	65.31	58.62	0.83	0.76	17.04	19.13	7.75	10.05	1.09	0.77	1.51	1.33	1.47	2.07	2.94	3.30	0.71	0.51	0.05	0.05	21	28	229	326
374	66.44	59.54	0.83	0.74	17.05	18.63	7.96	10.49	1.12	0.70	1.61	1.49	1.54	1.80	2.92	3.20	0.75	0.69	0.05	0.04	20	26	221	285
449	65.39	56.48	0.84	0.73	16.80	19.72	7.62	10.84	1.18	0.80	1.68	1.56	1.46	1.79	2.90	3.44	0.75	0.65	0.05	0.06	18	27	225	321
529	65.99	58.94	0.85	0.79	17.22	19.11	7.87	10.18	1.09	0.74	1.97	2.16	1.45	1.95	2.94	3.29	0.87	0.65	0.04	0.05	22	27	216	285
592	66.33	57.70	0.85	0.73	16.99	19.07	7.57	10.62	1.18	0.76	1.93	1.55	1.60	1.91	2.92	3.46	0.58	0.57	0.04	0.04	20	29	211	326
664	65.41	57.01	0.87	0.79	17.57	19.44	7.58	10.56	1.18	0.74	1.96	1.26	1.56	2.25	3.02	3.42	0.71	0.49	0.04	0.04	26	25	231	290
736	65.85	57.44	0.86	0.73	17.55	19.30	8.13	11.17	1.13	0.74	1.78	1.38	1.61	1.92	3.06	3.48	0.79	0.75	0.04	0.06	21	28	221	308
811	64.75	56.72	0.88	0.81	17.82	19.99	8.02	10.23	1.04	0.80	1.72	1.01	1.63	2.09	3.11	3.49	0.60	0.69	0.04	0.06	20	26	230	303
879	65.34	54.67	0.89	0.69	17.96	19.74	7.81	11.29	1.12	0.99	1.37	1.10	1.63	2.27	3.15	3.63	0.70	0.64	0.04	0.07	21	28	231	329
954	64.41	55.01	0.89	0.77	17.68	20.89	7.97	11.22	1.09	0.82	1.73	1.28	1.53	2.13	3.14	3.77	0.81	0.62	0.04	0.06	22	31	236	321
1023	64.55	54.21	0.89	0.78	18.09	20.40	8.18	11.20	1.14	0.95	1.38	0.96	1.65	2.16	3.17	3.75	0.54	0.64	0.05	0.08	22	30	234	322
1096	63.47	54.08	0.90	0.78	18.37	21.10	8.53	11.56	0.98	0.77	1.26	1.27	1.59	2.24	3.30	3.90	0.64	0.63	0.07	0.10	21	29	221	319
1169	62.72	54.41	0.86	0.74	18.26	20.25	8.26	11.04	1.00	0.89	1.80	0.87	1.52	1.97	3.40	4.16	0.69	0.58	0.06	0.08	24	27	203	338
1242	63.36	55.21	0.89	0.78	18.53	21.13	7.59	10.08	1.01	0.78	1.68	2.71	1.54	1.81	3.45	4.05	0.54	1.48	0.04	0.05	23	29	235	284
1312	65.00	52.96	0.88	0.72	17.87	21.96	7.39	10.20	1.16	0.76	1.41	2.31	1.43	2.00	3.56	4.37	0.70	0.61	0.11	0.05	24	31	244	321
1349	64.66	54.65	0.81	0.78	17.52	21.57	6.90	10.47	2.45	1.12	1.52	0.91	2.33	2.06	3.31	4.12	0.59	0.72	0.13	0.23	21	28	239	324
1380	67.19	55.17	0.85	0.82	18.09	22.55	6.41	9.05	1.27	0.84	1.92	2.80	1.50	1.84	3.21	4.21	0.74	0.66	0.05	0.08	22	31	252	328
1410	54.93	53.74	0.75	0.83	15.66	22.11	5.82	10.20	1.74	0.85	1.59	1.00	1.95	2.01	2.92	4.27	0.65	0.69	0.05	0.07	20	32	174	324
1440	62.23	54.30	0.92	0.83	19.53	21.11	8.41	11.38	0.69	0.90	1.64	1.77	1.35	2.15	3.63	4.16	0.61	0.66	0.05	0.13	24	28	245	323
1470	63.75	53.23	0.94	0.86	19.87	22.82	8.04	10.31	0.69	0.74	2.16	1.54	1.31	1.80	3.61	4.21	0.71	0.66	0.04	0.05	23	30	243	318
1499	65.30	53.19	0.91	0.82	18.67	23.77	6.96	9.37	0.72	0.74	1.27	1.06	1.04	1.82	3.36	4.19	0.76	0.65	0.04	0.06	20	27	225	352
1532	67.09	52.94	0.95	0.81	17.39	23.20	7.12	10.70	0.69	0.76	1.14	1.09	1.02	1.82	3.31	4.23	0.99	0.63	0.04	0.05	20	26	247	363
1558	67.55	56.27	0.84	0.87	16.45	22.35	8.41	8.62	0.75	0.90	1.15	1.35	0.84	1.55	2.69	3.91	0.70	0.61	0.04	0.07	18	26	215	364
1599	69.88	54.23	0.80	0.83	15.71	22.87	6.01	10.32	0.70	0.77	1.41	1.30	0.68	1.72	2.70	3.92	0.51	0.65	0.05	0.08	18	30	208	366
1619	67.05	58.66	0.82	0.81	17.97	20.59	7.37	9.53	0.58	0.57	1.25	2.00	1.63	1.77	3.07	3.43	0.62	0.57	0.03	0.03	21	29	272	356
1647	68.14	58.76	0.74	0.71	16.47	19.13	7.01	9.82	0.58	0.50	1.28	1.81	0.85	1.14	2.88	3.56	0.61	0.77	0.03	0.02	20	26	245	331
1678	68.88	58.82	0.75	0.74	16.76	19.43	6.96	10.07	0.59	0.47	1.71	1.26	1.05	1.25	2.93	3.65	0.56	0.66	0.03	0.03	20	28	211	336
1711	66.61	59.03	0.78	0.75	16.83	19.76	7.25	9.15	0.79	0.56	1.57	1.18	1.21	1.54	2.83	3.55	1.10	0.66	0.04	0.05	21	29	231	315

Tableau 14 – Éléments majeurs, traces et REE de la carotte 05JPC. Oxydes exprimés en wt. % et les traces et REE en ppm (suite).

	Cr		Co		Zn		Rb		Sr		Zr		La		Ce		Pr		Nd		Sm		Eu	
Depth (cm)	Bulk	Clay	Bulk	Clay	Bulk	Clay	Bulk	Clay	Bulk	Clay	Bulk	Clay	Bulk	Clay	Bulk	Clay	Bulk	Clay	Bulk	Clay	Bulk	Clay	Bulk	Clay
201	147	186	19	19	127	214	97	107	129	117	151	133	28	32	53	59	6	7	24	29	5.09	5.19	0.91	1.15
231	133	171	24	18	123	188	97	105	126	106	152	124	28	30	52	57	6	7	24	27	4.59	5.07	1.01	1.00
304	145	193	15	37	147	184	99	131	131	105	150	136	30	36	55	67	7	8	26	31	4.62	5.71	1.04	1.55
374	144	186	15	28	132	164	95	129	131	97	156	127	28	35	53	66	7	8	25	31	5.13	6.57	1.01	1.21
449	145	179	39	38	125	185	91	134	135	101	157	137	29	38	53	68	7	8	25	32	5.16	7.14	1.00	1.37
529	146	169	18	25	127	179	105	132	124	101	150	132	30	36	55	66	7	11	27	31	5.21	6.02	0.98	1.26
592	153	167	15	21	127	174	96	125	126	105	159	127	32	38	58	73	7	8	27	34	4.89	6.89	1.15	1.12
664	141	183	33	24	128	181	118	127	125	98	157	139	37	36	69	66	8	8	35	31	6.94	6.05	1.29	1.46
736	154	199	17	41	133	180	102	133	137	107	157	140	31	36	58	66	7	8	28	32	5.87	7.46	1.08	1.33
811	184	184	28	25	130	187	103	138	128	105	165	140	33	38	60	73	7	8	28	35	5.40	6.89	1.25	1.35
879	152	173	18	31	130	193	109	135	135	109	164	136	34	34	65	65	7	7	31	31	5.88	6.05	0.98	1.13
954	144	178	33	34	127	192	110	152	134	98	172	141	36	40	68	74	7	8	32	34	6.39	6.67	1.20	1.31
1023	155	200	20	28	137	181	113	145	132	106	164	142	35	40	67	73	8	9	32	37	6.83	7.06	1.34	1.46
1096	157	179	22	39	126	181	115	151	128	99	159	147	36	39	66	73	8	8	31	33	6.19	6.22	1.07	1.25
1169	152	182	20	28	135	186	123	145	125	115	164	159	41	39	73	73	9	9	36	37	6.92	7.04	1.37	1.25
1242	152	340	21	31	133	194	133	155	125	109	171	157	43	42	79	76	9	9	37	37	7.88	7.34	1.45	1.67
1312	135	172	22	38	142	169	129	171	136	116	184	156	41	43	75	80	9	10	37	40	7.72	6.98	1.47	1.51
1349	120	175	22	30	130	179	119	166	120	118	186	153	37	46	68	86	8	10	34	41	6.50	6.84	1.31	1.38
1380	153	235	30	38	136	194	131	175	116	117	197	150	41	48	72	88	9	11	35	40	6.74	7.77	1.31	1.76
1410	129	188	27	39	118	312	114	188	99	112	160	160	34	48	63	94	7	12	31	44	6.28	8.60	1.08	1.99
1440	144	187	33	30	159	182	129	152	116	123	174	164	39	42	71	78	8	9	34	35	6.74	6.87	1.18	1.52
1470	150	188	28	64	146	185	125	170	117	108	183	171	38	46	72	86	9	10	36	42	6.44	7.47	1.31	1.47
1499	137	194	19	27	128	162	114	163	124	116	186	166	38	49	69	88	8	10	35	43	6.52	7.97	1.19	1.60
1532	156	208	17	175	135	207	104	162	125	126	192	171	37	46	65	85	8	10	31	41	5.21	7.82	1.14	1.20
1558	136	173	23	64	113	173	85	149	109	134	204	153	31	47	55	85	7	10	28	38	4.29	6.60	1.01	1.38
1599	133	203	19	43	109	188	92	160	116	126	223	166	32	46	60	82	7	10	27	38	5.23	6.95	0.91	1.45
1619	149	172	17	30	125	159	106	146	101	98	152	158	28	41	54	74	6	9	25	38	4.73	7.39	1.00	1.40
1647	149	180	13	24	90	141	93	130	106	110	144	142	24	33	46	60	5	7	21	29	4.27	5.66	0.89	1.24
1678	143	161	22	24	88	139	97	129	103	130	141	144	24	35	46	63	5	7	20	30	4.10	5.24	0.70	1.06
1711	129	187	28	21	233	146	100	137	123	120	151	144	27	34	49	61	6	8	24	32	4.27	7.63	1.04	1.47

Tableau 14 – Éléments majeurs, traces et REE de la carotte 05JPC. Oxydes exprimés en wt. % et les traces et REE en ppm (suite).

	Gd		Tb		Dy		Ho		Er		Tm		Yb		Lu		Hf		Ta		Th		U	
Depth (cm)	Bulk	Clay	Bulk	Clay	Bulk	Clay	Bulk	Clay	Bulk	Clay	Bulk	Clay	Bulk	Clay	Bulk	Clay	Bulk	Clay	Bulk	Clay	Bulk	Clay	Bulk	Clay
201	3.80	4.82	0.61	0.73	4.44	4.71	0.79	0.85	2.78	2.76	0.35	0.52	2.30	2.50	0.42	0.39	3.79	3.76	0.85	0.94	10.10	12.10	2.53	2.24
231	4.80	5.17	0.62	0.71	3.96	4.52	0.79	0.83	2.24	2.60	0.33	0.46	2.64	2.46	0.40	0.38	3.97	3.73	0.83	0.79	10.20	12.40	2.29	2.20
304	3.95	5.92	0.68	0.86	4.54	5.37	0.88	1.18	2.65	3.11	0.42	0.41	2.49	3.20	0.39	0.44	4.06	4.30	0.92	0.76	11.00	14.40	2.47	3.03
374	4.22	5.62	0.60	0.69	5.14	5.06	1.03	1.10	2.61	2.75	0.32	0.44	2.72	3.31	0.38	0.46	3.95	4.09	0.85	0.76	10.60	13.90	2.61	2.57
449	4.99	5.20	0.72	0.95	3.98	5.45	0.86	0.97	2.64	2.50	0.41	0.53	2.73	4.01	0.36	0.42	3.96	4.11	0.79	0.84	10.20	14.80	2.41	3.06
529	4.37	5.39	0.67	0.74	4.22	5.33	0.87	1.17	2.60	2.93	0.38	0.40	2.65	3.09	0.38	0.46	4.12	4.06	0.96	1.15	10.90	14.50	2.36	3.04
592	4.49	5.83	0.80	0.91	4.30	5.44	0.92	1.06	2.85	3.53	0.46	0.56	2.47	2.83	0.48	0.61	4.50	3.71	0.94	0.81	11.10	14.40	2.69	3.70
664	5.55	5.73	0.84	1.05	5.16	5.36	1.13	1.08	3.03	3.40	0.45	0.43	3.18	3.44	0.50	0.49	4.83	3.97	1.09	0.93	12.50	14.20	3.22	2.73
736	5.02	5.47	0.74	0.82	4.15	5.82	0.91	0.95	2.55	3.19	0.40	0.49	2.78	3.06	0.45	0.48	4.64	4.51	0.85	0.79	11.70	14.50	2.91	2.84
811	4.79	6.12	0.77	0.87	4.34	5.38	0.95	1.05	2.69	3.01	0.35	0.47	2.93	3.54	0.46	0.49	4.43	4.32	1.07	0.96	12.10	15.60	2.64	3.19
879	5.36	4.78	0.84	0.78	5.04	5.13	1.05	0.96	2.72	2.93	0.47	0.50	2.88	3.06	0.41	0.48	4.71	4.50	1.00	0.85	12.10	15.50	2.89	4.03
954	5.69	5.41	0.69	0.75	4.83	5.29	1.02	1.04	3.01	3.22	0.45	0.48	3.00	3.26	0.29	0.50	4.72	4.71	0.86	1.05	11.80	17.10	3.07	3.74
1023	5.18	5.86	0.88	1.03	5.26	5.37	0.95	1.11	3.07	3.12	0.44	0.46	2.90	3.81	0.45	0.53	4.81	4.88	1.08	1.01	12.80	16.50	3.10	3.75
1096	5.36	5.66	0.75	0.76	5.06	4.72	0.98	1.02	3.10	2.35	0.47	0.37	2.92	3.62	0.47	0.49	4.88	4.14	1.08	0.91	12.20	16.80	2.73	2.92
1169	6.65	6.55	0.90	0.94	5.82	5.78	1.23	1.11	3.57	3.32	0.54	0.45	3.44	3.77	0.56	0.54	5.29	4.21	1.14	0.81	13.40	15.80	3.38	4.40
1242	6.56	6.43	1.02	0.97	6.56	5.99	1.35	1.14	3.82	3.22	0.56	0.40	3.54	3.70	0.56	0.57	5.69	5.09	1.24	0.98	14.20	16.30	3.52	3.29
1312	6.97	6.70	0.92	0.91	5.66	5.66	1.20	1.26	3.44	3.55	0.59	0.49	3.67	3.70	0.52	0.58	5.22	5.95	1.10	0.96	14.10	17.10	2.92	3.26
1349	6.24	6.91	0.93	1.12	5.03	5.63	1.06	1.15	3.17	3.12	0.51	0.44	2.68	3.89	0.46	0.54	5.80	5.20	1.08	1.01	12.80	17.10	2.89	3.15
1380	5.66	6.64	0.93	0.87	5.69	6.71	1.24	1.07	3.72	3.52	0.49	0.57	3.47	3.56	0.53	0.55	5.71	4.89	1.14	1.07	12.40	16.80	3.57	4.11
1410	5.60	8.01	0.76	1.05	5.47	6.07	1.10	1.24	2.93	3.68	0.40	0.63	2.96	4.06	0.47	0.73	4.83	4.84	0.91	1.02	11.70	17.90	2.88	4.19
1440	5.92	6.78	0.77	0.93	5.71	5.67	0.96	1.13	3.30	3.23	0.48	0.58	3.85	3.24	0.52	0.67	5.91	4.34	1.25	1.01	14.00	16.00	2.49	2.57
1470	6.22	7.87	0.85	1.02	5.96	6.66	1.13	1.21	3.24	3.65	0.46	0.61	3.35	3.54	0.63	0.58	5.77	5.37	1.25	1.09	13.00	17.90	2.33	2.82
1499	5.57	7.06	0.86	0.98	5.53	6.76	1.25	1.09	3.00	3.41	0.48	0.55	3.04	3.66	0.47	0.40	5.02	5.03	1.14	1.01	12.70	17.80	2.61	3.20
1532	4.85	7.51	0.87	0.86	5.39	6.07	0.87	1.32	3.12	3.58	0.45	0.57	2.80	4.21	0.53	0.61	5.11	5.45	1.10	0.81	11.80	16.30	2.55	3.35
1558	4.74	5.49	0.69	0.74	4.41	5.21	0.88	0.96	2.50	3.04	0.44	0.47	2.99	3.13	0.46	0.52	5.93	4.46	1.13	1.12	10.80	15.00	2.61	3.09
1599	4.56	6.41	0.77	0.82	4.61	5.93	0.92	1.15	2.63	3.01	0.40	0.55	2.68	4.15	0.39	0.54	6.06	5.46	1.06	1.08	10.20	16.10	2.79	3.38
1619	3.84	7.21	0.71	1.03	4.52	6.66	0.83	1.29	2.57	3.76	0.43	0.55	2.68	3.84	0.43	0.58	3.85	4.75	0.76	0.91	10.90	15.40	2.15	2.87
1647	3.18	6.11	0.55	0.69	3.56	4.59	0.78	0.95	2.24	2.96	0.27	0.34	2.47	3.34	0.39	0.53	4.12	4.63	0.80	0.62	9.73	12.70	1.76	3.12
1678	3.22	5.39	0.57	0.91	3.60	4.72	0.81	0.91	2.24	3.11	0.34	0.53	2.65	3.07	0.42	0.42	4.00	4.24	0.78	0.72	9.49	11.90	1.96	2.68
1711	4.34	6.63	0.62	0.86	4.25	5.95	0.91	1.05	2.43	2.98	0.38	0.50	2.85	3.20	0.40	0.47	4.02	4.45	0.71	0.74	10.10	13.60	2.53	2.86

Tableau 15 – Minéralogie totale de la carotte 02PC (exprimés en wt. %).

Depth (cm)	Quartz	Feldspath-K	Plagioclase	Calcite	Dolomite	Pyroxene	Amphibole	Fe-Bearing	Diatoms	Am. Silica	Kaolinite	Chlorite	Illite	Biotite	Smectite	Muscovite	Vermiculite
5	21.9	1.0	4.0	0.0	0.3	0.0	0.5	1.0	1.3	2.8	2.8	9.6	23.1	0.0	10.0	16.2	6.2
12	17.5	2.4	2.8	0.0	0.4	0.5	0.2	1.0	0.6	0.6	3.9	10.5	29.7	0.0	13.8	13.1	3.3
16	23.7	2.6	3.3	0.0	0.1	0.0	0.1	1.3	0.0	0.0	4.6	10.1	22.1	0.2	11.0	17.7	3.1
20	22.4	2.4	3.6	0.0	2.0	0.6	0.7	1.0	0.0	0.0	4.4	10.7	20.6	0.0	12.4	13.6	5.2
34	12.8	0.7	1.5	0.0	0.3	0.0	1.5	2.8	0.8	3.5	3.6	11.7	30.3	0.0	14.3	13.9	3.0
40	20.8	2.0	2.7	0.0	0.9	0.0	0.6	1.8	1.1	1.6	4.0	9.7	24.9	0.4	12.7	13.1	4.3
47	19.7	2.3	1.9	0.0	0.2	0.0	0.6	1.4	0.0	0.0	4.2	10.8	28.4	0.2	11.8	15.4	3.3
60	23.3	2.4	3.3	0.0	2.8	0.0	0.0	1.0	0.1	0.1	4.5	11.4	23.7	0.0	9.0	13.3	4.8
72	21.2	1.4	2.1	0.0	0.6	0.0	0.2	0.8	0.2	0.2	4.2	9.9	30.7	0.8	8.7	17.0	2.3
80	23.0	2.7	2.7	0.0	2.9	0.2	0.0	1.3	0.0	0.0	3.9	12.3	21.6	0.4	12.5	14.1	2.3
95	12.4	3.4	2.3	0.0	0.8	0.0	0.7	1.6	0.8	0.8	6.6	9.8	26.9	0.0	16.4	13.4	4.7
100	23.0	3.1	4.0	0.0	3.4	0.0	0.8	0.6	0.0	0.0	3.9	11.3	20.3	0.0	9.8	15.2	4.4
105	13.5	4.5	3.8	0.0	0.1	0.0	0.2	1.0	0.0	0.2	5.1	10.9	26.9	0.1	14.9	14.0	4.7
114	16.6	3.5	2.7	0.0	0.4	0.0	0.5	1.2	0.4	0.4	5.1	10.6	27.8	0.3	12.2	13.2	5.1
120	25.9	4.2	3.2	0.0	10.1	0.0	0.4	0.0	0.0	0.0	6.0	9.9	18.6	0.4	7.1	9.9	4.3
126	22.5	3.7	3.8	0.0	0.0	0.0	0.0	1.3	0.0	0.0	4.7	10.7	22.4	0.0	11.7	13.7	5.3
131	13.5	2.7	4.1	0.0	0.3	0.0	0.9	0.7	0.0	4.6	4.9	12.5	25.2	0.0	13.2	15.0	2.3
134	17.2	3.1	4.1	0.0	0.5	0.0	0.4	1.0	2.8	2.8	5.0	8.2	26.0	0.9	12.1	14.2	4.3
138	25.2	5.1	6.7	0.0	1.1	0.4	1.3	0.8	0.0	0.0	4.6	11.0	18.0	0.2	7.3	12.3	5.8
140	22.8	4.4	5.8	3.1	28.1	0.0	0.6	0.5	0.0	0.0	1.0	9.6	10.1	0.0	3.7	7.4	2.8
143	19.0	3.8	5.2	0.0	0.4	0.1	1.0	0.6	0.0	0.0	5.4	11.4	23.1	1.3	7.4	16.4	4.5
150	23.8	2.1	6.4	3.4	3.7	0.4	0.8	0.7	0.0	0.0	3.2	9.7	19.0	0.2	1.1	19.5	5.7
160	26.1	4.0	3.9	0.0	17.0	0.2	0.0	0.1	0.0	0.0	3.3	7.9	20.6	0.0	4.0	11.0	1.6
180	21.0	2.6	0.9	0.6	5.3	0.0	0.0	1.1	0.8	0.8	4.9	10.4	27.4	0.0	8.0	12.8	4.2
200	20.2	1.8	1.8	0.8	4.0	0.0	0.6	0.3	1.7	2.1	6.0	11.7	26.5	0.0	7.4	13.5	3.2
220	20.4	1.7	1.6	0.1	3.7	0.0	1.3	0.4	1.6	1.6	4.1	12.3	28.3	0.0	8.0	12.9	3.3
240	20.2	3.2	1.7	0.1	3.9	0.0	0.4	0.3	1.4	1.7	5.1	13.6	26.8	0.0	10.1	11.2	1.4
260	20.9	1.9	2.1	1.3	4.6	0.0	0.0	0.2	0.1	0.1	5.8	12.3	24.7	0.0	12.1	11.0	2.4
280	21.2	2.0	1.6	0.7	3.2	0.0	0.0	0.5	0.0	0.0	5.2	12.4	28.6	0.0	10.0	11.8	2.3
300	22.0	1.7	1.8	0.0	2.4	0.0	0.0	0.6	0.6	0.6	4.8	12.0	29.9	0.0	10.8	11.1	2.2
320	27.7	4.5	2.4	0.0	9.7	0.2	1.0	0.3	4.1	4.1	4.2	6.0	18.2	0.0	8.7	9.1	3.4

Tableau 15 – Minéralogie totale de la carotte 02PC (exprimés en wt. %)(suite).

Depth (cm)	Quartz	Feldspath-K	Plagioclase	Calcite	Dolomite	Pyroxene	Amphibole	Fe-Bearing	Diatoms	Am. Silica	Kaolinite	Chlorite	Illite	Biotite	Smectite	Muscovite	Vermiculite
340	27.8	3.7	2.5	0.4	15.1	0.2	0.5	0.2	0.0	0.0	4.6	11.6	13.0	0.0	8.3	12.1	0.0
350	40.9	4.2	4.8	0.0	2.6	0.0	0.0	0.6	0.1	0.1	4.1	10.9	11.9	0.0	7.9	10.4	1.4
360	20.1	0.5	2.0	0.0	0.7	0.0	0.8	0.0	0.8	3.3	6.9	15.8	25.7	0.0	8.5	13.4	1.9
375	24.1	2.0	1.9	0.0	1.3	0.0	0.6	0.7	0.9	0.9	6.8	14.2	27.9	0.0	6.2	13.2	0.0
380	19.6	0.5	2.4	0.0	0.2	0.0	0.0	0.3	1.1	1.1	6.9	14.8	29.0	0.0	8.6	15.8	0.5
390	26.7	0.4	1.5	0.0	0.5	0.0	0.7	0.0	0.0	0.0	4.6	13.5	27.1	0.0	9.1	14.6	1.1
400	21.1	0.3	2.4	0.0	0.0	0.0	0.0	0.0	0.0	0.0	4.6	13.6	30.3	0.0	14.0	11.7	1.4
420	18.9	0.5	2.1	0.0	0.8	0.0	0.6	0.0	1.8	4.1	4.4	16.5	31.9	0.0	4.6	14.6	0.5
440	21.2	0.4	1.5	0.0	1.1	0.0	0.9	0.2	1.3	1.3	5.9	15.3	29.2	0.0	6.9	15.2	0.8
460	22.7	1.8	2.3	0.0	0.2	0.2	0.4	0.0	0.0	0.0	7.1	10.2	30.2	0.0	14.1	8.7	2.0
480	23.5	2.2	1.7	0.0	0.3	0.0	0.8	0.0	0.7	0.7	6.1	10.7	29.1	0.0	12.9	9.1	2.7
500	24.6	0.9	2.1	0.0	0.3	0.0	0.0	0.2	0.9	0.9	5.9	12.0	27.9	0.0	11.3	12.3	0.9

Tableau 16 – Minéralogie totale de la carotte 05JPC (exprimés en wt. %).

Depth (cm)	Quartz	Feldspath-K	Plagioclase	Calcite	Dolomite	Pyroxene	Amphibole	Fe-Bearing	Diatoms	Am. Silica	Kaolinite	Chlorite	Illite	Biotite	Smectite	Muscovite	Vermiculite
196	15.3	2.4	9.0	0.0	1.0	0.6	2.2	0.1	13.8	16.5	1.0	13.5	8.3	0.1	6.9	14.9	6.2
226	17.3	3.2	10.7	0.0	0.7	0.6	1.3	0.0	13.1	13.1	1.0	12.7	10.3	0.5	7.9	12.4	5.3
299	17.5	4.2	9.3	0.0	1.0	0.0	1.0	0.3	10.8	10.8	1.8	13.1	10.9	0.0	7.0	14.4	5.9
369	17.9	3.7	9.7	0.0	0.9	0.1	1.4	0.2	14.6	14.6	0.6	14.2	6.3	0.5	7.9	14.2	5.0
444	18.0	4.6	8.4	0.0	1.0	0.2	1.4	0.9	12.7	12.7	1.3	14.3	10.1	0.0	7.9	13.7	2.1
516	16.0	2.5	9.5	0.0	1.0	0.2	0.9	0.1	10.2	13.6	0.8	14.6	10.2	0.1	5.8	16.3	5.4
587	17.8	6.0	8.7	0.0	0.8	0.3	0.9	0.3	10.0	10.8	1.2	15.3	8.6	0.0	6.6	16.2	4.2
669	18.5	3.6	8.2	0.0	1.2	0.4	1.9	0.1	7.7	7.7	1.3	13.7	10.3	0.0	8.1	17.2	5.9
736	20.1	3.6	9.3	0.0	0.0	0.9	0.3	0.0	9.0	9.0	0.6	12.8	9.9	0.0	12.7	15.9	4.8
806	18.9	2.9	10.2	0.0	1.2	0.5	1.2	0.1	7.2	7.2	1.0	12.9	13.3	0.0	7.0	16.1	5.0
884	19.2	4.1	9.7	0.0	1.0	0.0	0.9	0.3	5.7	5.7	0.2	15.0	10.3	0.0	8.7	18.9	3.9
949	20.8	3.5	9.0	0.0	1.0	0.0	1.4	0.4	5.2	5.2	0.8	14.8	10.7	0.0	8.8	16.4	4.7
1020	19.8	3.5	9.9	0.0	1.3	0.0	1.2	0.0	5.2	5.2	1.1	14.6	13.6	0.0	7.7	14.7	5.7
1091	19.9	4.7	8.0	0.0	1.3	0.0	1.2	0.0	1.5	1.5	1.7	12.8	10.9	0.0	12.8	17.1	6.4
1165	21.2	2.6	8.7	0.0	1.8	0.0	1.7	0.0	1.5	1.5	1.4	12.4	13.2	0.0	11.3	16.8	5.4
1242	23.6	3.5	8.3	0.0	0.1	0.0	0.8	0.0	0.0	0.0	2.9	11.7	16.0	0.0	10.2	16.5	6.3
1312	23.5	3.6	9.1	0.0	0.4	0.0	0.5	0.0	0.0	0.0	2.4	10.8	17.2	0.0	10.2	16.7	5.5
1335	19.0	3.8	6.7	0.0	1.3	0.0	0.8	0.3	0.0	0.0	2.0	10.6	19.4	0.0	14.6	13.0	7.3
1349	28.1	3.3	7.0	0.0	4.6	0.0	0.4	0.0	0.0	0.0	0.8	11.3	17.1	0.0	9.5	12.5	5.3
1389	29.8	2.0	5.7	0.0	1.0	0.0	0.8	0.0	0.4	0.4	2.9	10.4	21.0	0.0	9.1	13.8	2.7
1410	24.1	4.3	6.5	0.0	3.8	0.0	0.8	0.2	0.0	0.0	2.6	11.2	18.2	0.0	9.5	12.1	6.5
1470	22.3	2.3	7.6	0.0	0.0	0.0	0.8	0.0	0.0	0.0	2.8	12.5	20.7	0.0	10.3	16.8	3.7
1494	21.7	3.8	5.0	0.0	1.0	0.0	0.3	0.3	0.4	0.4	4.4	13.6	19.7	0.0	9.3	16.4	3.3
1532	27.7	3.6	5.6	0.0	0.3	0.0	0.6	0.2	0.3	0.3	3.1	13.4	20.1	0.1	8.6	13.7	2.6
1558	33.6	3.8	5.7	0.0	0.2	0.1	0.0	0.8	0.0	0.0	3.0	12.6	18.8	0.1	7.8	7.4	5.8
1599	39.2	1.9	6.4	0.0	0.0	0.3	0.0	0.2	0.4	0.4	3.5	9.6	18.0	0.0	5.1	11.4	3.7
1614	36.2	4.3	4.5	0.0	0.5	0.0	0.1	0.2	0.3	0.3	4.0	11.4	17.0	0.0	10.5	9.9	0.0
1642	12.0	1.6	7.9	0.4	0.2	0.5	0.7	0.6	21.1	24.4	0.0	10.3	14.2	0.0	10.9	12.9	2.1
1678	15.4	3.2	7.3	0.1	0.1	0.1	0.2	0.0	21.6	22.3	2.1	9.6	14.1	0.0	10.9	12.5	2.1
1701	14.7	1.1	7.8	0.0	0.0	0.0	2.0	0.3	19.6	19.6	1.6	9.9	15.1	0.0	8.9	13.6	4.3

Tableau 17 – Minéralogie totale de la carotte 01JPC (exprimés en wt. %).

Depth (cm)	Quartz	Feldspath-K	Plagioclase	Calcite	Dolomite	Pyroxene	Amphibole	Fe-Bearing	Diatoms	Am. Silica	Kaolinite	Chlorite	Illite	Biotite	Smectite	Muscovite	Vermiculite
5	21.3	3.2	12.4	0.0	0.8	0.0	0.8	0.0	12.3	12.3	1.9	14.9	5.9	0.0	3.1	16.7	5.9
30	20.4	4.6	10.4	0.0	1.5	0.0	2.1	0.0	10.4	10.4	2.4	13.9	6.0	0.2	4.9	17.5	5.6
55	19.2	4.7	10.2	0.0	1.0	0.3	1.6	0.0	10.5	10.5	1.2	14.5	8.6	0.4	5.1	16.5	5.7
86	20.0	3.9	9.9	0.0	1.2	0.1	1.9	0.0	9.5	9.5	1.6	14.2	8.6	0.3	5.2	18.2	4.8
115	18.6	3.3	10.0	0.0	0.6	0.4	1.6	0.0	12.8	12.8	0.8	12.9	11.9	0.0	8.1	13.9	5.1
144	20.5	3.4	10.4	0.0	0.4	0.7	1.1	0.0	10.7	10.7	2.0	13.4	8.3	0.0	6.7	14.6	7.4
172	24.9	5.2	11.5	0.0	1.7	0.0	1.2	0.1	4.1	4.1	3.5	12.2	7.7	0.0	6.9	14.8	5.6
203	23.1	4.2	11.4	0.0	0.7	0.4	1.2	0.1	7.5	7.5	1.6	11.8	10.4	0.0	9.9	13.3	4.3
234	23.5	4.2	12.5	0.0	1.3	0.0	1.2	0.0	4.8	4.8	1.7	12.6	10.2	0.0	8.3	15.0	4.4
255	22.5	4.1	10.5	0.0	1.1	0.0	0.8	0.0	3.3	4.1	1.3	14.1	8.6	0.0	7.7	16.5	8.2
295	23.5	5.0	11.6	0.0	0.5	0.4	0.0	0.0	3.4	3.4	1.3	12.7	8.9	0.0	9.8	16.3	6.1

Tableau 18: Minéralogie des argiles de la carotte 02PC.

Depth (cm)	Illite (%)	Chlorite (%)	Kaolinite (%)	Vermiculite (%)	Chlorite/Smectite (%)
5	55	13	12	19	0
12	66	11	12	6	5
16	63	9	10	11	7
20	67	14	9	10	0
34	61	15	11	11	2
40	64	9	10	17	0
47	61	11	12	7	7
60	67	13	14	2	4
72	66	12	11	7	4
80	69	13	11	3	4
95	66	13	13	8	0
100	64	14	13	2	7
105	60	14	13	12	0
110	67	12	10	8	3
114	67	11	11	7	4
120	59	15	13	12	1
126	61	12	13	11	4
131	60	11	10	18	0
134	62	13	10	15	0
138	59	14	12	14	0
140	67	16	11	3	2
143	63	15	11	12	0
150	66	16	8	10	0
160	62	16	13	9	0
180	65	10	12	13	0
200	58	16	17	4	4
220	57	16	16	10	1
240	60	15	15	2	8
260	54	21	15	11	0
280	66	14	16	2	2
300	57	12	25	6	0
320	52	14	20	14	0
330	49	12	27	12	0
340	51	20	20	9	0
350	57	11	22	9	0
360	64	17	15	3	0
375	64	16	19	1	0
380	60	17	23	1	0
390	68	9	16	7	0
400	65	14	14	6	0
420	67	13	12	8	0
440	61	15	20	4	0
460	58	20	17	4	0
480	55	23	17	5	0
500	56	20	16	8	1

Tableau 19: Minéralogie des argiles de la carotte 05JPC.

Depth (cm)	Illite (%)	Chlorite (%)	Kaolinite (%)	Vermiculite (%)	Chlorite/Smectite (%)
196	49	16	9	27	0
226	46	17	9	29	0
299	42	13	10	35	0
369	32	15	7	46	0
444	38	14	9	39	0
516	40	15	8	37	0
587	34	9	8	41	8
669	38	14	9	39	0
736	38	13	7	43	0
806	69	20	6	5	0
884	55	18	9	19	0
949	41	14	7	38	0
1020	45	16	7	32	0
1091	45	17	6	32	0
1165	63	19	10	8	0
1242	52	15	8	23	2
1312	61	19	12	9	0
1335	58	17	14	11	1
1349	58	14	10	17	0
1389	63	17	10	10	0
1410	44	16	8	32	0
1470	56	14	12	18	0
1494	60	12	12	16	0
1532	62	14	9	8	8
1558	56	20	13	11	0
1599	45	14	12	29	0
1614	32	12	6	31	19
1642	30	10	4	56	0
1678	43	11	5	41	0
1701	52	12	4	32	0

Tableau 20: Minéralogie des argiles de la carotte 01JPC.

Depth (cm)	Illite (%)	Chlorite (%)	Kaolinite (%)	Vermiculite (%)	Chlorite/Smectite (%)
5	29	10	5	25	31
30	42	13	6	7	32
55	44	17	4	9	26
86	27	10	6	41	16
115	36	9	6	7	42
145	30	14	6	50	0
172	45	13	10	33	0
203	35	10	5	7	42
234	43	13	7	11	26
265	36	12	7	15	30
295	34	11	7	17	30

Tableau 21: Provenance des sédiments de la carotte 02PC en utilisant la macro SedUnMixMC (Andrews et Eberl, 2012).

Depth (cm)	Mackenzie River plume	Sands from the Mackenzie River	Banks and Victoria islands	Kara Sea	Total
5	0.7	0.0	0.1	0.1	0.8
12	0.8	0.0	0.1	0.0	0.8
16	0.8	0.0	0.1	0.0	0.8
20	0.8	0.0	0.1	0.0	0.8
34	1.0	0.0	0.1	0.0	1.0
40	0.9	0.0	0.1	0.0	0.9
47	0.9	0.0	0.1	0.0	0.9
60	0.9	0.0	0.1	0.0	0.9
72	0.9	0.0	0.1	0.0	0.9
80	0.8	0.0	0.1	0.0	0.8
95	1.0	0.0	0.1	0.0	1.0
100	0.8	0.0	0.1	0.0	0.8
105	1.0	0.0	0.1	0.0	1.0
114	1.0	0.0	0.1	0.0	1.0
120	0.8	0.0	0.1	0.0	0.9
126	0.9	0.0	0.1	0.0	0.9
131	1.0	0.0	0.1	0.0	1.0
134	1.0	0.0	0.1	0.0	1.0
138	0.7	0.0	0.1	0.1	0.9
140	0.0	0.0	0.7	0.0	0.8
143	0.8	0.0	0.1	0.0	0.9
150	0.7	0.0	0.1	0.0	0.8
160	0.5	0.0	0.4	0.0	1.0
180	0.9	0.0	0.1	0.0	0.9
200	1.0	0.0	0.1	0.0	1.0
220	0.9	0.0	0.1	0.0	0.9
240	1.0	0.0	0.1	0.0	1.0
260	0.9	0.0	0.1	0.0	0.9
280	1.0	0.0	0.1	0.0	1.0
300	1.0	0.0	0.1	0.0	1.0
320	0.5	0.0	0.3	0.1	1.0
330	0.7	0.0	0.2	0.0	0.9
340	0.3	0.1	0.4	0.0	0.9
350	0.4	0.4	0.1	0.0	0.9
360	1.0	0.0	0.1	0.0	1.0
375	1.0	0.0	0.1	0.0	1.0
380	1.0	0.0	0.1	0.0	1.0
390	1.0	0.0	0.1	0.0	1.0
400	1.0	0.0	0.1	0.0	1.0
420	1.0	0.0	0.1	0.0	1.0
440	1.0	0.0	0.1	0.0	1.0
460	1.0	0.0	0.1	0.0	1.0
480	1.0	0.0	0.1	0.0	1.0
500	1.0	0.0	0.1	0.0	1.0

Tableau 22: Provenance des sédiments de la carotte 05JPC en utilisant la macro SedUnMixMC (Andrews et Eberl, 2012).

Depth (cm)	Mackenzie River plume	North Alaska	Banks and Victoria islands	Bering Strait	Eastern Siberian Sea and Laptev Sea	Kara Sea	Total
196	0.2	0.0	0.0	0.3	0.0	0.2	0.7
226	0.3	0.0	0.0	0.4	0.0	0.3	0.9
299	0.3	0.0	0.0	0.4	0.0	0.2	0.9
369	0.1	0.0	0.0	0.5	0.0	0.2	0.8
444	0.3	0.0	0.0	0.4	0.0	0.1	0.8
516	0.3	0.0	0.0	0.5	0.0	0.1	0.9
587	0.3	0.0	0.0	0.5	0.0	0.1	0.8
669	0.3	0.0	0.0	0.4	0.0	0.0	0.8
736	0.3	0.0	0.0	0.5	0.0	0.1	0.8
806	0.4	0.0	0.0	0.5	0.0	0.1	1.0
884	0.3	0.0	0.0	0.5	0.0	0.1	0.9
949	0.3	0.0	0.0	0.5	0.0	0.1	0.9
1020	0.4	0.0	0.0	0.5	0.0	0.1	0.9
1091	0.4	0.0	0.0	0.4	0.0	0.0	0.8
1165	0.4	0.0	0.0	0.5	0.0	0.0	0.9
1242	0.6	0.0	0.0	0.3	0.0	0.0	1.0
1312	0.5	0.0	0.0	0.3	0.2	0.0	0.9
1335	0.5	0.0	0.0	0.3	0.0	0.0	0.8
1349	0.5	0.2	0.0	0.2	0.0	0.0	1.0
1389	0.6	0.2	0.0	0.2	0.0	0.0	1.0
1410	0.6	0.1	0.0	0.2	0.0	0.0	0.9
1470	0.6	0.0	0.0	0.3	0.0	0.0	0.9
1494	0.7	0.0	0.0	0.1	0.0	0.0	0.8
1532	0.7	0.1	0.0	0.2	0.0	0.0	1.0
1558	0.4	0.5	0.0	0.0	0.0	0.0	1.0
1599	0.4	0.6	0.0	0.1	0.0	0.0	1.1
1614	0.3	0.7	0.0	0.0	0.0	0.0	1.0
1642	0.1	0.4	0.0	0.3	0.0	0.1	0.8
1678	0.5	0.0	0.0	0.2	0.0	0.1	0.8
1701	0.5	0.0	0.0	0.2	0.0	0.1	0.8

Tableau 23: Provenance des sédiments de la carotte 01JPC en utilisant la macro SedUnMixMC (Andrews et Eberl, 2012).

Depth (cm)	Mackenzie River plume	North Alaska	Banks and Victoria islands	Bering Strait	Eastern Siberian Sea and Laptev Sea	Kara Sea	Total
5	0.1	0.0	0.0	0.6	0.1	0.2	0.9
30	0.1	0.0	0.0	0.6	0.0	0.2	0.9
55	0.3	0.0	0.0	0.5	0.0	0.1	0.9
86	0.3	0.0	0.0	0.5	0.0	0.1	0.9
115	0.3	0.0	0.0	0.5	0.0	0.1	0.9
144	0.2	0.0	0.0	0.5	0.0	0.1	0.9
172	0.0	0.2	0.0	0.4	0.1	0.2	1.0
203	0.2	0.1	0.0	0.4	0.0	0.3	0.9
234	0.2	0.0	0.0	0.4	0.1	0.2	1.0
255	0.2	0.1	0.0	0.5	0.1	0.2	0.9
295	0.2	0.1	0.0	0.4	0.1	0.1	0.9

RÉFÉRENCES

Aitchison, J., may 1990. Relative variation diagrams for describing patterns of compositional variability. Mathematical Geology 22 (4), 487–511.

Albarède, F., Simonetti, A., Vervoort, J. D., Blichert-Toft, J., Abouchami, W., 1998. A Hf-Nd isotopic correlation in ferromanganese nodules. Geophysical Research Letters 25 (20), 3895–3898.

Ali, S., Stattegger, K., Garbe-Schönberg, D., Frank, M., Kraft, S., Kuhnt, W., 2014. The provenance of Cretaceous to Quaternary sediments in the Tarfaya basin, SW Morocco: Evidence from trace element geochemistry and radiogenic Nd-Sr isotopes. Journal of African Earth Sciences 90, 64–76.

Anderson, L., Abbott, M. B., Finney, B. P., Burns, S. J., 2005. Regional atmospheric circulation change in the North Pacific during the Holocene inferred from lacustrine carbonate oxygen isotopes, Yukon Territory, Canada. Quaternary Research 64 (1), 21–35.

Anderson, L., Berkelhammer, M., Barron, J. A., Steinman, B. A., Finney, B. P., Abbott, M. B., 2016. Lake oxygen isotopes as recorders of North American Rocky Mountain hydroclimate: Holocene patterns and variability at multi-decadal to millennial time scales. Global and Planetary Change 137, 131–148.

Andrews, J. T., 2000. Icebergs and iceberg rafted detritus (IRD) in the North Atlantic: facts and assumptions. Oceanography 13, 100–108.

Andrews, J. T., Bjork, A. A., Eberl, D. D., Jennings, A. E., Verplanck, E. P., 2015. Significant differences in late Quaternary bedrock erosion and transport: East versus West Greenland ˜70°N - evidence from the mineralogy of offshore glacial marine sediments. Journal of Quaternary Science 30 (5), 452–463.

Andrews, J. T., Dunhill, G., 2004. Early to mid-Holocene Atlantic water influx and deglacial meltwater events, Beaufort Sea slope, Arctic Ocean. Quaternary Research 61 (1), 14–21.

Andrews, J. T., Eberl, D. D., 2012. Determination of sediment provenance by unmixing the mineralogy of source-area sediments: The "SedUnMix" program. Marine Geology 291-294, 24–33.

Andrews, J. T., Kristjánsdóttir, G. B., Eberl, D. D., Jennings, A. E., 2013. A quantitative x-ray diffraction inventory of volcaniclastic inputs into the marine sediment archives off Iceland: A contribution to the Volcanoes in the Arctic System programme. Polar Research 32 (1), 1–15.

Andrews, J. T., MacLean, B., 2003. Hudson Strait ice streams: A review of stratigraphy, chronology and links with North Atlantic Heinrich events. Boreas 32 (1), 4–17.

Andrews, J. T., Stein, R., Moros, M., Perner, K., 2016. Late Quaternary changes in sediment composition on the NE Greenland margin (˜73° N) with a focus on the fjords and shelf. Boreas 45 (3), 381–397.

Andrews, J. T., Vogt, C., 2014. Source to sink: Statistical identification of regional variations in the mineralogy of surface sediments in the western Nordic Seas (58°N-75°N; 10°W-40°W). Marine Geology 357, 151–162.

Armstrong-Altrin, J. S., Machain-Castillo, M. L., Rosales-Hoz, L., Carranza-Edwards, A., Sanchez-Cabeza, J.-A., Ruíz-Fernández, A. C., 2015. Provenance and depositional history of continental slope sediments in the Southwestern Gulf of Mexico unraveled by geochemical analysis. Continental Shelf Research 95, 15–26.

Armstrong-Altrin, J. S., Verma, S. P., 2005. Critical evaluation of six tectonic setting discrimination diagrams using geochemical data of Neogene sediments from known tectonic settings. Sedimentary Geology 177 (1-2), 115–129.

Asahara, Y., Takeuchi, F., Nagashima, K., Harada, N., Yamamoto, K., Oguri, K., Tadai, O., 2012. Provenance of terrigenous detritus of the surface sediments in the Bering and Chukchi Seas as derived from Sr and Nd isotopes: Implications for recent climate change in the Arctic regions. Deep-Sea Research Part II: Topical Studies in Oceanography 61-64, 155–171.

Astakhov, A. S., Rujian, W., Crane, K., Ivanov, M. V., Aiguo, G., 2013. Lithochemical classification of the arctic depositional environments (Chukchi Sea) by methods of multivariate statistic. Geochemistry International 51 (4), 269–289.

Barletta, F., St-Onge, G., Channell, J. E., Rochon, A., Polyak, L., Darby, D., 2008. High-resolution paleomagnetic secular variation and relative paleointensity records from the western Canadian Arctic: implication for Holocene stratigraphy and geomagnetic field behaviour. Canadian Journal of Earth Sciences 45 (11), 1265–1281.

Barletta, F., St-Onge, G., Channell, J. E. T., Rochon, A., 2010. Dating of Holocene western Canadian Arctic sediments by matching paleomagnetic secular variation to a geomagnetic field model. Quaternary Science Reviews 29 (17-18), 2315–2324.

Barron, J. A., Anderson, L., 2011. Enhanced Late Holocene ENSO/PDO expression along the margins of the eastern North Pacific. Quaternary International 235 (1-2), 3–12.

Bayon, G., German, C. R., Burton, K. W., Nesbitt, R. W., Rogers, N., 2004. Sedimentary Fe-Mn oxyhydroxides as paleoceanographic archives and the role of aeolian flux in regulating oceanic dissolved REE. Earth and Planetary Science Letters 224 (3-4), 477–492.

Bayon, G., Toucanne, S., Skonieczny, C., André, L., Bermell, S., Cheron, S., Dennielou, B., Etoubleau, J., Freslon, N., Gauchery, T., Germain, Y., Tachikawa, K., Barrat, J. A.,

2015. Rare earth elements and neodymium isotopes in world river sediments revisited 170, 17–38.

Bazhenova, E., 2012. Reconstruction of late Quaternary sedimentary environments at the southern Mendeleev Ridge (Arctic Ocean). Phd thesis, University of Bremen.

Belt, S. T., Vare, L. L., Massé, G., Manners, H. R., Price, J. C., MacLachlan, S. E., Andrews, J. T., Schmidt, S., 2010. Striking similarities in temporal changes to spring sea ice occurrence across the central Canadian Arctic Archipelago over the last 7000 years. Quaternary Science Reviews 29 (25-26), 3489–3504.

Berger, A., Loutre, M. F., 1991. Insolation values for the cliamte of the last 10 million years. Quaternary Science Reviews 10 (1988), 297–317.

Bianchi, G. G., McCave, I. N., 1999. Holocene periodicity in North Atlantic climate and deep-ocean flow south of Iceland. Nature 397, 515–517.

Biscaye, P. E., jul 1965. Mineralogy and Sedimentation of Recent Deep-Sea Clay in the Atlantic Ocean and Adjacent Seas and Oceans. Geological Society of America Bulletin 76 (7), 803–832.

Bischof, J. F., 1997. Mid- to Late Pleistocene Ice Drift in the Western Arctic Ocean: Evidence for a Different Circulation in the Past. Science 277, 74–78.

Bischof, J. F., Darby, D. A., 1999. Quaternary ice transport in the Canadian Arctic and extent of Late Wisconsinan Glaciation in the Queen Elizabeth Islands. Canadian Journal of Earth Sciences 36 (12), 2007–2022.

Blaauw, M., 2010. Methods and code for 'classical' age-modelling of radiocarbon sequences. Quaternary Geochronology 5 (5), 512–518.

Blaauw, M., Christen, A., 2011. Flexible Paleoclimate Age-Depth Models Using an Autoregressive Gamma Process. Bayesian Analysis 6 (3), 457–474.

Blaschek, M., Renssen, H., 2013. The impact of early holocene arctic shelf flooding on climate in an atmosphere-ocean-sea-ice model. Climate of the Past 9 (6), 2651–2667.

Blott, S., Pye, K., 2001. GRADISTAT: A Grain Size Distribution and Statistic Package For the Analysis of UnConsolidated Sediments. Espl 26, 1237–1248.

Boogaart, K. G. V. D., Tolosana-Delgado, R., 2013. Analyzing Compositional Data with R. Springer, Heidelberg-New York-Dodrecht-London.

Bout-Roumazeilles, V., Cortijo, E., Labeyrie, L., Debrabant, P., 1999. Clay mineral evidence of nepheloid layer contributions to the Heinrich layers in the northwest Atlantic. Palaeogeography, Palaeoclimatology, Palaeoecology 146 (1-4), 211–228.

Brabets, T. P., Walvoord, M. A., 2009. Trends in streamflow in the Yukon River Basin from 1944 to 2005 and the influence of the Pacific Decadal Oscillation. Journal of Hydrology 371 (1-4), 108–119.

Brachfeld, S., Barletta, F., St-Onge, G., Darby, D., Ortiz, J. D., 2009. Impact of diagenesis on the environmental magnetic record from a Holocene sedimentary sequence from the Chukchi-Alaskan margin, Arctic Ocean. Global and Planetary Change 68 (1-2), 100–114.

Bringué, M., Rochon, A., 2012. Late Holocene paleoceanography and climate variability over the Mackenzie Slope (Beaufort Sea, Canadian Arctic). Marine Geology 291-294, 83–96.

Broecker, W. S., Andree, M., Wolfli, W., Oeschger, H., Bonani, G., Kennett, J., Peteet, D., 1988. The chronology of the last Deglaciation: Implications to the cause of the Younger Dryas Event. Paleoceanography 3 (1), 1–19.

Bullard, J. E., Baddock, M., Bradwell, T., Crusius, J., Darlington, E., Gaiero, D., Gassó, S., Gisladottir, G., Hodgkins, R., McCulloch, R., McKenna-Neuman, C., Mockford, T., Stewart, H., Thorsteinsson, T., 2016. High-latitude dust in the Earth system. Reviews of Geophysics 54 (2), 447–485.

Burn, C. R., 1997. change during the early Holocene warm interval , western Arctic coast , Canada. Earth 34 (7), 912–925.

Butzin, M., Prange, M., Lohmann, G., jun 2005. Radiocarbon simulations for the glacial ocean: The effects of wind stress, Southern Ocean sea ice and Heinrich events. Earth and Planetary Science Letters 235 (1-2), 45–61.

Campodonico, V. A., Garcoa, M. G., Pasquini, A. I., 2016. The geochemical signature of suspended sediments in the Parana River basin: Implications for provenance, weathering and sedimentary recycling. Catena 143, 201–214.

Carson, M. A., Jasper, J. N., Conly, F. M., 1998. Magnitude and Sources of Sediment Input to the Mackenzie Delta , Northwest Territories , 1974 – 94. Arctic 51 (2), 116 – 124.

Cassano, E. N., Cassano, J. J., 2010. Synoptic forcing of precipitation in the Mackenzie and Yukon River basins. International Journal of Climatology 30 (5), 658–674.

Chan, F. T., MacIsaac, H. J., Bailey, S. A., 2015. Relative importance of vessel hull fouling and ballast water as transport vectors of nonindigenous species to the Canadian Arctic. Canadian Journal of Fisheries and Aquatic Sciences 72 (8), 1230–1242.

Channell, J. E. T., 2002. Geomagnetic excursions and paleointensities in the Matuyama Chron at Ocean Drilling Program Sites 983 and 984 (Iceland Basin). Journal of Geophysical Research 107 (B6), 2114.

Channell, J. E. T., Hodell, D. A., Lehman, B., 1997. Relative geomagnetic paleointensity and δ18O at ODP Site 983 (Gardar Drift, North Atlantic) since 350 ka. Earth and Planetary Science Letters 153 (1-2), 103–118.

Channell, J. E. T., Stoner, J. S., Hodell, D. A., Charles, C. D., 2000. Geomagnetic paleointensity for the last 100 kyr from the sub-antarctic South Atlantic: A tool for inter-hemispheric correlation. Earth and Planetary Science Letters 175 (1-2), 145–160.

Chen, T. Y., Frank, M., Haley, B. a., Gutjahr, M., Spielhagen, R. F., 2012. Variations of North Atlantic inflow to the central Arctic Ocean over the last 14 million years inferred from hafnium and neodymium isotopes. Earth and Planetary Science Letters 353-354, 82–92.

Chen, Z., Gao, A., Liu, Y., Haiqing, S., Shi, X., Yang, Z., 2003. REE geochemistry of surface sediments in the Chukchi Sea. Science in China Series D 46 (6), 603.

Colin, C., Frank, N., Copard, K., Douville, E., sep 2010. Neodymium isotopic composition of deep-sea corals from the NE Atlantic: implications for past hydrological changes during the Holocene. Quaternary Science Reviews 29 (19-20), 2509–2517.

Condron, A., Winsor, P., 2012. Meltwater routing and the Younger Dryas. Proceedings of the National Academy of Sciences 109 (49), 19928–19933.

Corlett, W. B., Pickart, R. S., 2017. The Chukchi slope current. Progress in Oceanography 153, 50–65.

Cornuault, M., Tachikawa, K., Vidal, L., Guihou, A., Siani, G., Deschamps, P., Bassinot, F., Revel, M., mar 2018. Circulation Changes in the Eastern Mediterranean Sea Over the Past 23,000 Years Inferred From Authigenic Nd Isotopic Ratios. Paleoceanography and Paleoclimatology.

Coulter, S. E., Pilcher, J. R., Plunkett, G., Baillie, M., Hall, V. A., Steffensen, J. P., Vinther, B. M., Clausen, H. B., Johnsen, S. J., nov 2012. Holocene tephras highlight complexity of volcanic signals in Greenland ice cores. Journal of Geophysical Research: Atmospheres 117.

Coulthard, R. D., Furze, M. F., Pieńkowski, A. J., Chantel Nixon, F., England, J. H., 2010. New marine ΔR values for Arctic Canada. Quaternary Geochronology 5 (4), 419–434.

Cullers, R. L., 1994. The controls on the major and trace element variation of shales, siltstones, and sandstones of Pennsylvanian-Permian age from uplifted continental blocks in Colorado to platform sediment in Kansas, USA. Geochimica et Cosmochimica Acta 58 (22), 4955–4972.

Dallimore, S. R., Wolfe, S. A., Solomon, S. M., 1996. Influence of ground ice and permafrost on coastal evolution, Richards Island, Beaufort Sea coast, N.W.T. Canadian Journal of Earth Sciences 33 (5), 664–675.

Danielson, S., Curchitser, E., Hedstrom, K., Weingartner, T., Stabeno, P., 2011. On ocean and sea ice modes of variability in the Bering Sea. Journal of Geophysical Research: Oceans 116.

Danielson, S. L., Weingartner, T. J., Hedstrom, K. S., Aagaard, K., Woodgate, R., Curchitser, E., Stabeno, P. J., 2014. Coupled wind-forced controls of the Bering-Chukchi shelf circulation and the Bering Strait throughflow: Ekman transport, continental shelf waves, and variations of the Pacific-Arctic sea surface height gradient. Progress in Oceanography 125, 40–61.

Dankers, P., feb 1981. Relationship between median destructive field and remanent coercive forces for dispersed natural magnetite, titanomagnetite and hematite. Geophysical Journal International 64 (2), 447–461.

Darby, D. A., 2002. Arctic ice export events and their potential impact on global climate during the late Pleistocene. Paleoceanography 17 (2).

Darby, D. A., 2003. Sources of sediment found in sea ice from the western Arctic Ocean, new insights into processes of entrainment and drift patterns. Journal of Geophysical Research 108.

Darby, D. A., Jakobsson, M., Polyak, L., 2005. Icebreaker expedition collects key Arctic seafloor and ice data. Eos, Transactions American Geophysical Union 86 (52), 549.

Darby, D. A., Myers, W. B., Jakobsson, M., Rigor, I., 2011. Modern dirty sea ice characteristics and sources: The role of anchor ice. Journal of Geophysical Research: Oceans 116 (9), 1–18.

Darby, D. A., Ortiz, J., Polyak, L., Lund, S., Jakobsson, M., Woodgate, R. A., 2009. The role of currents and sea ice in both slowly deposited central Arctic and rapidly deposited Chukchi-Alaskan margin sediments. Global and Planetary Change 68 (1-2), 58–72.

Darby, D. A., Ortiz, J. D., Grosch, C. E., Lund, S. P., 2012. 1,500-year cycle in the Arctic Oscillation identified in Holocene Arctic sea-ice drift. Nature Geoscience 5 (12), 897–900.

Darby, D. A., Polyak, L., Bauch, H. a., 2006. Past glacial and interglacial conditions in the Arctic Ocean and marginal seas - a review. Progress in Oceanography 71 (2-4), 129–144.

Darby, D. A., Zimmerman, P., 2008. Ice-rafted detritus events in the Arctic during the last glacial interval, and the timing of the Innuitian and Laurentide ice sheet calving events. Polar Research 27 (2), 114–127.

Darby and Bischof, 2004. A Holocene record of changing Arctic Ocean ice drift analogous to the effects of the Arctic Oscillation. Paleoceanography 19 (1), 1–9.

Day, R., Fuller, M., Schmidt, V., jan 1977. Hysteresis properties of titanomagnetites: Grain-size and compositional dependence. Physics of the Earth and Planetary Interiors 13 (4), 260–267.

de Vernal, A., Hillaire-Marcel, C., Darby, D. A., 2005. Variability of sea ice cover in the Chukchi Sea (western Arctic Ocean) during the Holocene. Paleoceanography 20.

de Vernal, A., Hillaire-Marcel, C., Rochon, A., Fréchette, B., Henry, M., Solignac, S., Bonnet, S., 2013. Dinocyst-based reconstructions of sea ice cover concentration during the Holocene in the Arctic Ocean, the northern North Atlantic Ocean and its adjacent seas. Quaternary Science Reviews 79, 111–121.

de Vernal, A., Rochon, A., 2011. Dinocysts as tracers of sea-surface conditions and sea-ice cover in polar and subpolar environments. IOP Conference Series: Earth and Environmental Science 14.

Debret, M., Sebag, D., Desmet, M., Balsam, W., Copard, Y., Mourier, B., Susperrigui, A. S., Arnaud, F., Bentaleb, I., Chapron, E., Lallier-Vergès, E., Winiarski, T., 2011. Spectrocolorimetric interpretation of sedimentary dynamics: The new "Q7/4 diagram". Earth-Science Reviews 109 (1-2), 1–19.

Dellinger, M., Bouchez, J., Gaillardet, J., Faure, L., Moureau, J., 2017. Tracing weathering regimes using the lithium isotope composition of detrital sediments. Geology 45 (5), 411–414.

Déry, S. J., Wood, E. F., 2005. Decreasing river discharge in northern Canada. Geophysical Research Letters 32 (10), 1–4.

Deschamps, C.-E., Montero-serrano, J.-C., St-Onge, G., 2018a. Sediment provenance changes in the western Arctic Ocean in response to ice- rafting , sea-level and oceanic circulation variations since the last deglaciation. Geochemistry Geophysics Geosystems. URL https://doi.org/10.1029/2017GC007411

Deschamps, C.-E., St-Onge, G., Montero-Serrano, J.-C., Polyak, L., 2018b. Chronostratigraphy and spatial distribution of the Chukchi and Beaufort Sea's magnetic sediments since the last deglaciation. Boreas 47 (2), 544–564.

Dickson, R., Rudels, B., Dye, S., Karcher, M., Meincke, J., Yashayaev, I., 2007. Current estimates of freshwater flux through Arctic and subarctic seas. Progress in Oceanography 73 (3-4), 210–230.

Dietze, E., Hartmann, K., Diekmann, B., IJmker, J., Lehmkuhl, F., Opitz, S., Stauch, G., Wünnemann, B., Borchers, A., 2012. An end-member algorithm for deciphering modern detrital processes from lake sediments of Lake Donggi Cona, NE Tibetan Plateau, China. Sedimentary Geology 243-244, 169–180.

Dietze, E., Wünnemann, B., Hartmann, K., Diekmann, B., Jin, H., Stauch, G., Yang, S., Lehmkuhl, F., 2013. Early to mid-Holocene lake high-stand sediments at Lake Donggi Cona, northeastern Tibetan Plateau, China. Quaternary Research 79 (3), 325–336.

Dong, L., Liu, Y., Shi, X., Polyak, L., Huang, Y., Fang, X., Liu, J., Zou, J., Wang, K., Sun, F., Wang, X., 2017. Sedimentary record from the Canada Basin, Arctic Ocean: implications for late to middle Pleistocene glacial history. Climate of the Past Discussions, 1–60.

Dong, L., Xuefa, S. H. I., Yanguang, L. I. U., Xisheng, F., Zhihua, C., Chunjuan, W., Jianjun, Z. O. U., Yuanhui, H., 2014. Mineralogical study of surface sediments in the western Arctic Ocean and their implications for material sources. Advances in Polar Science 25 (3), 192–203.

Dou, Y., Yang, S., Lim, D.-I., Jung, H.-S., 2015. Provenance discrimination of last deglacial and Holocene sediments in the southwest of Cheju Island, East China Sea. Palaeogeography, Palaeoclimatology, Palaeoecology 422, 25–35.

Du, J., Haley, B. A., Mix, A. C., 2016. Neodymium isotopes in authigenic phases, bottom waters and detrital sediments in the Gulf of Alaska and their implications for paleo-circulation reconstruction. Geochimica et Cosmochimica Acta 193, 14–35.

Dunlop, D. J., 2002a. Theory and application of the Day plot (Mrs/Ms versus Hcr/Hc) 2. Application to data for rocks, sediments, and soils. Journal of Geophysical Research: Solid Earth 107 (B3), EPM 5–1–EPM 5–15.

Dunlop, D. J., 2002b. Theory and application of the Day plot (Mrs/Ms versus Hcr/Hc) 1. Theoretical curves and tests using titanomagnetite data. Journal of Geophysical Research: Solid Earth 107 (B3), EPM 4–1–EPM 4–22.

Durantou, L., Rochon, A., Ledu, D., Massé, G., Schmidt, S., Babin, M., 2012. Quantitative reconstruction of sea-surface conditions over the last 150 yr in the Beaufort Sea based on dinoflagellate cyst assemblages: The role of large-scale atmospheric circulation patterns. Biogeosciences 9 (12), 5391–5406.

Dyke, A., Savelle, J., 2000. Major end moraines of Younger Dryas age on Wollaston Peninsula, Victoria Island, Canadian Arctic: implications for paleoclimate and for formation of hummocky moraine: Discussion. Canadian Journal of Earth Sciences 38 (6), 1003–1006.

Dyke, A. S., 2004. An outline of the deglaciation of North America with emphasis on central and northern Canada. Quaternary Glaciations-Extent and Chronology, Part II: North America 2b, 373–424.

Dyke, A. S., England, J., Reimnitz, E., Jetté, H., 1997. Changes in driftwood delivery to the Canadian Arctic Archipelago: The hypothesis of postglacial oscillations of the transpolar drift. Arctic 50 (1), 1–16.

Eberl, D., 2003. User's guide to RockJock - A program for determining quantitative mineralogy from powder X-ray diffraction data. U.S. Geological Survey Open-File Report 03-78, 1–47.

Eberl, D. D., 2004. Quantitative mineralogy of the Yukon River system: Changes with reach and season, and determining sediment provenance. American Mineralogist 89 (11-12), 1784–1794.

Egozcue, J. J., Pawlowsky-Glahn, V., 2005. Groups of parts and their balances in compositional data analysis. Mathematical Geology 37 (7), 795–828.

El Ouahabi, M., Hubert-Ferrari, A., Fagel, N., 2017. Lacustrine clay mineral assemblages as a proxy for land-use and climate changes over the last 4 kyr: The Amik Lake case study, Southern Turkey. Quaternary International 438 (Part B), 15–29.

England, J. H., Furze, M. F., 2008. New evidence from the western Canadian Arctic Archipelago for the resubmergence of Bering Strait. Quaternary Research 70 (1), 60–67.

Fagel, N., 2007. Clay Minerals, Deep Circulation and Climate. Developments in Marine Geology 1 (07), 139–184.

Fagel, N., Not, C., Gueibe, J., Mattielli, N., Bazhenova, E., 2014. Late Quaternary evolution of sediment provenances in the Central Arctic Ocean: Mineral assemblage, trace element composition and Nd and Pb isotope fingerprints of detrital fraction from the Northern Mendeleev Ridge. Quaternary Science Reviews 92 (2013), 140–154.

Faux, J. F., Belicka, L. L., Rodger Harvey, H., 2011. Organic sources and carbon sequestration in Holocene shelf sediments from the western Arctic Ocean. Continental Shelf Research 31 (11), 1169–1179.

Forest, A., Osborne, P. D., Fortier, L., Sampei, M., Lowings, M. G., 2015. Physical forcings and intense shelf – slope fl uxes of particulate matter in the halocline waters of the Canadian Beaufort Sea during winter. Continental Shelf Research 101, 1–21.

Forest, A., Tremblay, J. É., Gratton, Y., Martin, J., Gagnon, J., Darnis, G., Sampei, M., Fortier, L., Ardyna, M., Gosselin, M., Hattori, H., Nguyen, D., Maranger, R., Vaqué, D., Marrasé, C., Pedrós-Alió, C., Sallon, A., Michel, C., Kellogg, C., Deming, J., Shadwick, E., Thomas, H., Link, H., Archambault, P., Piepenburg, D., 2011. Biogenic carbon flows through the planktonic food web of the Amundsen Gulf (Arctic Ocean): A synthesis of field measurements and inverse modeling analyses. Progress in Oceanography 91 (4), 410–436.

Frank, M., 2002. Radiogenic isotopes: Tracers of past ocean circulation and erosional input. Reviews of Geophysics 40 (1), 1001.

Funk, J. A., 2004. Sediment Accumulation and Diagenesis in the Late Quaternary Equatorial Atlantic Ocean : An Environmental Magnetic and Geochemical Perspective. Ph.d. thesis, Universitat Bremen.

Gajewski, K., 2015. Quantitative reconstruction of Holocene temperatures across the Canadian Arctic and Greenland. Global and Planetary Change 128, 14–23.

Gamboa, A., 2017. Evaluación de la dinámica sedimentaria del margen continental del mar de Beaufort y golfo de Amundsen (Océano Ártico): implicaciones paleoceanográficas y paleoclimáticas durante el Holoceno. Ph.D. thesis, Universidad de Oriente.

Gamboa, A., Montero-Serrano, J.-C., St-Onge, G., Rochon, A., Desiage, P.-A., 2017. Mineralogical, geochemical, andmagnetic signatures of surface sediments fromthe Canadian Beaufort Shelf and Amundsen Gulf (Canadian Arctic). Geochemistry, Geophysics, Geosystems 18 (2), 488–512.

Gardner, J., Dea, W., Vallier, T., 1980. Sedimentology and geochemistry of surface sediments outer continental shelf, southern Bering Sea. Marine Geology 35, 299–329.

Garzanti, E., Andò, S., France-Lanord, C., Vezzoli, G., Censi, P., Galy, V., Najman, Y., 2010. Mineralogical and chemical variability of fluvial sediments. 1. Bedload sand (Ganga-Brahmaputra, Bangladesh). Earth and Planetary Science Letters 299 (3-4), 368–381.

Geiss, C. E., Banerjee, S. K., 2003. A Holocene-Late Pleistocene geomagnetic inclination record from Grandfather Lake, SW Alaska. Geophysical Journal International 153 (2), 497–507.

Gingele, F. X., De Deckker, P., Hillenbrand, C. D., 2004. Late Quaternary terrigenous sediments from the Murray Canyons area, offshore South Australia and their implications for sea level change, palaeoclimate and palaeodrainage of the Murray-Darling Basin. Marine Geology 212 (1-4), 183–197.

Goldstein, S. J., Jacobsen, S. B., 1987. The Nd and Sr isotopic systematics of river water dissolved material : Implications for the sources of Nd and Sr in seawater. Chemical Geology 66 (3-4), 245–272.

Gordeev, V. V., Beeskow, B., Meeresforschung, P.-U. N. D., 2007. Geochemistry of the Ob and Yenisey Estuaries : a comparative study. Tech. rep., AWI-Bremerhaven.

Gordeev, V. V., Rachold, V., Vlasova, I. E., 2004. Geochemical behaviour of major and trace elements in suspended particulate material of the Irtysh river, the main tributary of the Ob river, Siberia. Applied Geochemistry 19 (4), 593–610.

Grootes, P., Stuiver, M., 1997. Oxygen 18/16 variability in Greenland snow and ice with 10-3 to 10-5 year time resolution. Journal of ge 102, 26,455–26,470.

Gutjahr, M., Frank, M., Lippold, J., Halliday, A. N., 2014. Peak Last Glacial weathering intensity on the North American continent recorded by the authigenic Hf isotope composition of North Atlantic deep-sea sediments. Quaternary Science Reviews 99, 97–117.

Gutjahr, M., Frank, M., Stirling, C. H., Klemm, V., van de Flierdt, T., Halliday, A. N., 2007. Reliable extraction of a deepwater trace metal isotope signal from Fe-Mn oxyhydroxide coatings of marine sediments. Chemical Geology 242 (3-4), 351–370.

Gutjahr, M., Hoogakker, B. a. a., Frank, M., McCave, I. N., 2010. Changes in North Atlantic Deep Water strength and bottom water masses during Marine Isotope Stage 3 (45-35kaBP). Quaternary Science Reviews 29 (19-20), 2451–2461.

Hagstrum, J. T., Champion, D. E., 2002. A Holocene paleosecular variation record from 14C-dated volcanic rocks in western North America. Journal of Geophysical Research 107.

Haley, B. A., Frank, M., Spielhagen, R. F., Eisenhauer, A., 2008. Influence of brine formation on Arctic Ocean circulation over the past 15 million years. Nature Geoscience 1 (1), 68–72.

Haley, B. A., Klinkhammer, G. P., McManus, J., 2004. Rare earth elements in pore waters of marine sediments. Geochimica et Cosmochimica Acta 68 (6), 1265–1279.

Haley, B. A., Polyak, L., 2013. Pre-modern Arctic Ocean circulation from surface sediment neodymium isotopes. Geophysical Research Letters 40 (5), 893–897.

Hamilton, T. D., aug 1982. A late Pleistocene glacial chronology for the southern Brooks Range: Stratigraphic record and regional significance. Geological Society of America Bulletin 93 (8), 700–716.

Hamilton, T. D., 1986. Late Cenozoic glaciation of the central Brooks Range. In: Glaciation in Alaska; the geologic record. Alaska Geological Society, pp. 9–50.

Hanslik, D., Jakobsson, M., Backman, J., Björck, S., Sellén, E., O'Regan, M., Fornaciari, E., Skog, G., 2010. Quaternary Arctic Ocean sea ice variations and radiocarbon reservoir age corrections. Quaternary Science Reviews 29 (25-26), 3430–3441.

Harada, N., Katsuki, K., Nakagawa, M., Matsumoto, A., Seki, O., Addison, J. A., Finney, B. P., Sato, M., 2014. Holocene sea surface temperature and sea ice extent in the Okhotsk and Bering Seas. Biogeochemical and physical processes in the Sea of Okhotsk and the linkages to the Pacific Ocean 126, 242–253.

Harrison, J., St-Onge, M., Petrov, O. V., Strelnikov, S., Lopatin, B., Wilson, F., Tella, S., Paul, D., Lynds, T., Shokalsky, S., Hults, C., Bergman, S., Jepsen, H., Solli, A., 2011. Geological map of the Arctic. Geological Survey of Canada Open File 5816.

Henderson, G., 2002. New proxies for paleoclimate. Earth and Planetary Science Letters 203 (1), 1–13.

Héquette, A., Marie-Hélène, R., Hill, P. R., 1995. The effects of the Holocene Sea Level Rise on the Evolution of the Southeastern Coast of the Canadian Beaufort Sea. Journal of Coastal Research 11 (2), 494–507.

Hill, J. C., Driscoll, N. W., 2008. Paleodrainage on the Chukchi shelf reveals sea level history and meltwater discharge. Marine Geology 254 (3-4), 129–151.

Hill, J. C., Driscoll, N. W., 2010. Iceberg discharge to the Chukchi shelf during the Younger Dryas. Quaternary Research 74 (1), 57–62.

Hill, J. C., Driscoll, N. W., Brigham-Grette, J., Donnelly, J. P., Gayes, P. T., Keigwin, L., 2007. New evidence for high discharge to the Chukchi shelf since the Last Glacial Maximum. Quaternary Research 68 (2), 271–279.

Hill, P. R., Héquette, A., Ruz, M.-H., 1993. Holocene sea-level history of the Canadian Beaufort shelf. Canadian Journal of Earth Sciences 30 (1), 103–108.

Hillaire-Marcel, C., De Vernal, A., Polyak, L., Darby, D., 2004. Size-dependent isotopic composition of planktic foraminifers from Chukchi Sea vs. NW Atlantic sediments - Implications for the Holocene paleoceanography of the western Arctic. Quaternary Science Reviews 23 (3-4), 245–260.

Hillaire-Marcel, C., Maccali, J., Not, C., Poirier, A., 2013. Geochemical and isotopic tracers of Arctic sea ice sources and export with special attention to the Younger Dryas interval. Quaternary Science Reviews 79, 184–190.

Hodell, D. A., Mead, G. A., Mueller, P. A., oct 1990. Variation in the strontium isotopic composition of seawater (8 Ma to present) : Implications for chemical weathering rates and dissolved fluxes to the oceans. Chemical Geology: Isotope Geoscience section 80 (4), 291–307.

Hoffmann, S., McManus, J., 2007. Is there a 230Th deficit in Arctic sediments? Earth and Planetary Science Letters 258 (3-4), 516–527.

Hoffmann, S. S., McManus, J. F., Curry, W. B., Brown-Leger, L. S., 2013. Persistent export of 231Pa from the deep central Arctic Ocean over the past 35,000 years. Nature 497, 603–6.

Hofmann, D. I., Fabian, K., 2009. Correcting relative paleointensity records for variations in sediment composition: Results from a South Atlantic stratigraphic network. Earth and Planetary Science Letters 284 (1-2), 34–43.

Hofmann, D. I., Fabian, K., Schmieder, F., Donner, B., Bleil, U., 2005. A stratigraphic network across the Subtropical Front in the central South Atlantic: Multi-parameter correlation of magnetic susceptibility, density, X-ray fluorescence and δ18O records. Earth and Planetary Science Letters 240 (3-4), 694–709.

Holemann, J. A., Schirmacher, M., Kassens, H., Prange, A., 1999. Geochemistry of surficial and ice-rafted sediments from the Laptev Sea (Siberia). Estuarine Coastal and Shelf Science 49 (1), 45–59.

Horikawa, K., Asahara, Y., Yamamoto, K., Okazaki, Y., 2010. Intermediate water formation in the Bering Sea during glacial periods: Evidence from neodymium isotope ratios. Geology 38 (5), 435–438.

Hu, P., Liu, Q., Torrent, J., Barrón, V., Jin, C., 2013. Characterizing and quantifying iron oxides in Chinese loess/paleosols: Implications for pedogenesis. Earth and Planetary Science Letters 369-370, 271–283.

Hutchinson, I., James, T. S., Reimer, P. J., Bornhold, B. D., Clague, J. J., 2004. Marine and limnic radiocarbon reservoir corrections for studies of late- and postglacial environments in Georgia Basin and Puget Lowland, British Columbia, Canada and Washington, USA. Quaternary Research 61 (2), 193–203.

Jackson, S. E., 2001. The Application of Nd:YAG Lasers in LA-ICPMS, in Laser-Ablation-ICPMS in the Earth Sciences: Principles and Applications. In: Laser-Ablation-ICPMS in the Earth Sciences: Principles and Applications. Mineralogical Association of Canada, pp. 29–45.

Jackson, S. E., 2008. LAMTRACE data reduction software for LA-ICP-MS. Mineralogical Association of Canada Short Course Series 40 (40), 305–307.

Jacobsen, S. B., Wasserburg, G., 1980. Sm-Nd isotopic evolution of chondrites. Earth and Planetary Science Letters 50 (1), 139–155.

Jakobsson, M., Pearce, C., Cronin, T. M., Backman, J., Anderson, L. G., Barrientos, N., Björk, G., Coxall, H., De Boer, A., Mayer, L. A., Mörth, C. M., Nilsson, J., Rattray, J. E., Stranne, C., Semiletov, I., O'Regan, M., 2017. Post-glacial flooding of the Bering Land Bridge dated to 11 cal ka BP based on new geophysical and sediment records. Climate of the Past 13 (8), 991–1005.

Jeandel, C., Arsouze, T., Lacan, F., Téchiné, P., Dutay, J. C., 2007. Isotopic Nd compositions and concentrations of the lithogenic inputs into the ocean: A compilation, with an emphasis on the margins. Chemical Geology 239 (1-2), 156–164.

Jombart, T., 2008. Adegenet: A R package for the multivariate analysis of genetic markers. Bioinformatics 24 (11), 1403–1405.

Jung, H. S., Lim, D., Choi, J. Y., Yoo, H. S., Rho, K. C., Lee, H. B., 2012. Rare earth element compositions of core sediments from the shelf of the South Sea, Korea: Their controls and origins. Continental Shelf Research 48, 75–86.

Jutterström, S., Anderson, L. G., mar 2005. The saturation of calcite and aragonite in the Arctic Ocean. Marine Chemistry 94 (1-4), 101–110.

Kalinenko, V. V., 2001. Clay Minerals in Sediments of the Arctic Seas. Lithology and Mineral Resources 36 (4), 362–372.

Katsuki, K., Itaki, T., Khim, B., Uchida, M., Tada, R., 2014. Geophysical Research Letters. Geophysical Research Letters 41 (8), 2892–2898.

Kaufman, D. S., Jensen, B. J. L., Reyes, A. V., Schiff, C. J., Froese, D. G., Pearce, N. J. G., 2012. Late Quaternary tephrostratigraphy, Ahklun Mountains, SW Alaska. Journal of Quaternary Science 27 (4), 344–359.

Keigwin, L. D., Donnelly, J. P., Cook, M. S., Driscoll, N. W., Brigham-Grette, J., 2006. Rapid sea-level rise and Holocene climate in the Chukchi Sea. Geology 34 (10), 861–864.

Khim, B. K., 2003. Two modes of clay-mineral dispersal pathways on the continental shelves of the East Siberian Sea and western Chukchi Sea. Geosciences Journal 7 (3), 253–262.

Kinnard, C., Zdanowicz, C. M., Fisher, D. A., Isaksson, E., de Vernal, A., Thompson, L. G., 2011. Reconstructed changes in Arctic sea ice over the past 1,450 years. Nature 479 (7374), 509–512.

Kirschvink, J. L., 1980. The least-squares line and plane and the analysis of palaeomagnetic data. Geophysical Journal International 62 (3), 699–718.

Kissel, C., Laj, C., Piotrowski, A. M., Goldstein, S. L., Hemming, S. R., 2008. Millennial-scale propagation of Atlantic deep waters to the glacial Southern Ocean. Paleoceanography 23 (2), 1–7.

Kobayashi, D., Yamamoto, M., Irino, T., Nam, S.-I., Park, Y.-H., Harada, N., Nagashima, K., Chikita, K., Saitoh, S.-I., 2016. Distribution of detrital minerals and sediment color in western Arctic Ocean and northern Bering Sea sediments: Changes in the provenance of western Arctic Ocean sediments since the last glacial period. Polar Science 10 (4), 519–531.

Korte, M., Constable, C., 2005. The geomagnetic dipole moment over the last 7000 years—new results from a global model. Earth and Planetary Science Letters 236 (1-2), 348–358.

Korte, M., Constable, C., 2011. Improving geomagnetic field reconstructions for 0-3ka. Physics of the Earth and Planetary Interiors 188 (3-4), 247–259.

Korte, M., Constable, C., Donadini, F., Holme, R., 2011. Reconstructing the Holocene geomagnetic field. Earth and Planetary Science Letters 312 (3-4), 497–505.

Krumm, S., 2006. SediCalc (Free Geological Software).
URL http://www.geol.uni-erlangen.de/sedicalc.

Krylov, A. A., Stein, R., Ermakova, L. A., 2014. Clay minerals as indicators of late quaternary sedimentation constraints in the Mendeleev Rise, Amerasian Basin, Arctic Ocean. Lithology and Mineral Resources 49 (1), 103–116.

Lacan, F., Jeandel, C., 2005. Neodymium isotopes as a new tool for quantifying exchange fluxes at the continent-ocean interface. Earth and Planetary Science Letters 232 (3-4), 245–257.

Lakeman, T. R., Pie, A. J., Nixon, F. C., Furze, M. F. A., Blasco, S., Andrews, J. T., King, E. L., 2018. Collapse of a marine-based ice stream during the early Younger Dryas chronozone , western Canadian Arctic 46 (3), 1–4.

Lambeck, K., Rouby, H., Purcell, A., Sun, Y., Sambridge, M., 2014. Sea level and global ice volumes from the Last Glacial Maximum to the Holocene. Proceedings of the National Academy of Sciences 111 (43), 15296–15303.

Ledu, D., Rochon, A., de Vernal, A., St-Onge, G., 2008. Palynological evidence of Holocene climate change in the eastern Arctic: a possible shift in the Arctic oscillation at the millennial time scale. Canadian Journal of Earth Sciences 45 (11), 1363–1375.

Ledu, D., Rochon, A., de Vernal, A., St-Onge, G., 2010. Holocene paleoceanography of the northwest passage, Canadian Arctic Archipelago. Quaternary Science Reviews 29 (25-26), 3468–3488.

Leite, T. D. F., Escalfoni, R., Da Fonseca, T. C. O., Miekeley, N., 2011. Determination of major, minor and trace elements in rock samples by laser ablation inductively coupled plasma mass spectrometry: Progress in the utilization of borate glasses as targets. Spectrochimica Acta - Part B Atomic Spectroscopy 66 (5), 314–320.

Levi, S., Banerjee, S. K., feb 1976. On the possibility of obtaining relative paleointensities from lake sediments. Earth and Planetary Science Letters 29 (1), 219–226.

Li, C.-F., Guo, J.-H., Yang, Y.-H., Chu, Z.-Y., Wang, X.-C., 2014. Single-step separation scheme and high-precision isotopic ratios analysis of Sr–Nd–Hf in silicate materials. Journal of Analytical Atomic Spectrometry 29 (8), 1467.

Lim, D., Jung, H. S., Choi, J. Y., 2014. REE partitioning in riverine sediments around the Yellow Sea and its importance in shelf sediment provenance. Marine Geology 357, 12–24.

Lisé-Pronovost, A., St-Onge, G., Brachfeld, S., Barletta, F., Darby, D., 2009. Paleomagnetic constraints on the Holocene stratigraphy of the Arctic Alaskan margin. Global and Planetary Change 68 (1-2), 85–99.

Lisé-Pronovost, A., St-Onge, G., Gogorza, C., Haberzettl, T., Jouve, G., Francus, P., Ohlendorf, C., Gebhardt, C., Zolitschka, B., 2015. Rock-magnetic proxies of wind intensity and dust since 51,200 cal BP from lacustrine sediments of Laguna Potrok Aike, southeastern Patagonia. Earth and Planetary Science Letters 411, 72–86.

Liu, Q., Roberts, A. P., Larrasoaña, J. C., Banerjee, S. K., Guyodo, Y., Tauxe, L., Oldfield, F., 2012. Environmental Magnetism : Principles and Applications. Reviews of Geophysics 50.

Liu, Z., Yoshimura, K., Bowen, G. J., Buenning, N. H., Risi, C., Welker, J. M., Yuan, F., 2014. Paired oxygen isotope records reveal modern North American atmospheric dynamics during the Holocene. Nature Communications 5, 1–7.

Lund, S., Keigwin, L., Darby, D., 2016. Character of Holocene paleomagnetic secular variation in the tangent cylinder: Evidence from the Chukchi Sea. Physics of the Earth and Planetary Interiors 256, 49–58.

Maccali, J., 2012. Propriétés géochimiques et isotopiqes des sédiments du détroit de Fram, Océan Arctique. Implications paléocéanographiques et paléoclimatiques. Ph.d thesis, UQAM.

Maccali, J., Hillaire-Marcel, C., Carignan, J., Reisberg, L. C., 2012. Pb isotopes and geochemical monitoring of Arctic sedimentary supplies and water mass export through Fram Strait since the Last Glacial Maximum. Paleoceanography 27 (1).

Maccali, J., Hillaire-Marcel, C., Carignan, J., Reisberg, L. C., 2013. Geochemical signatures of sediments documenting Arctic sea-ice and water mass export through Fram Strait since the Last Glacial Maximum. Quaternary Science Reviews 64, 136–151.

Maccali, J., Hillaire-Marcel, C., Not, C., 2018. Radiogenic isotope (Nd, Pb, Sr) signatures of surface and sea ice-transported sediments from the Arctic Ocean under the present interglacial conditions. Polar Research 37 (1), 1442982.

MacDonald, G. M., Case, R. A., 2005. Variations in the Pacific Decadal Oscillation over the past millennium. Geophysical Research Letters 32 (8), 1–4.

Manley, W., 2002. Postglacial Flooding of the Bering Land Bridge: A Geospatial Animation.

Martinez, N. C., Murray, R. W., Dickens, G. R., Kölling, M., 2009. Discrimination of sources of terrigenous sediment deposited in the central Arctic Ocean through the Cenozoic. Paleoceanography 24 (1).

Martins, V., Rocha, F., Sequeira, C., Martins, P., Santos, J., Dias, J. A., Weber, O., Jouanneau, J. M., Rubio, B., Rey, D., Bernabeu, A., Silva, E., Laut, L., Figueira, R., 2013. Late Holocene climatic oscillations traced by clay mineral assemblages and other palaeoceanographic proxies in Ria de Vigo (NW Spain). Turkish Journal of Earth Sciences 22 (3), 398–413.

März, C., Stratmann, A., Matthiessen, J., Meinhardt, A. K., Eckert, S., Schnetger, B., Vogt, C., Stein, R., Brumsack, H. J., 2011. Manganese-rich brown layers in Arctic Ocean sediments: Composition, formation mechanisms, and diagenetic overprint. Geochimica et Cosmochimica Acta 75 (23), 7668–7687.

Matthiessen, J., Kunz-Pirrung, M., Mudie, P. J., 2000. Freshwater chlorophycean algae in recent marine sediments ofthe Beaufort, Laptev and Kara Seas (Arctic Ocean) as indicators of river runoff. International Journal of Earth Sciences 89 (3), 470–485.

Mazaud, A., dec 2005. User-friendly software for vector analysis of the magnetization of long sediment cores. Geochemistry, Geophysics, Geosystems 6 (12), GC001036.

Mazaud, A., Kissel, C., Laj, C., Sicre, M. A., Michel, E., Turon, J. L., 2007. Variations of the ACC-CDW during MIS3 traced by magnetic grain deposition in midlatitude South Indian Ocean cores: Connections with the northern hemisphere and with central Antarctica. Geochemistry, Geophysics, Geosystems 8 (5), GC001532.

McKay, J. L., De Vernal, A., Hillaire-Marcel, C., Not, C., Polyak, L., Darby, D., 2008. Holocene fluctuations in Arctic sea-ice cover: dinocyst-based reconstructions for the eastern Chukchi Sea. Canadian Journal of Earth Sciences 45 (11), 1377–1397.

McLennan, S., 1993. Weathering and Global Denudation. The Journal of Geology 101 (2), 295–303.

McLennan, S., Taylor, R. S., 2012. The Rare Earth Elements: Fundamentals and Applications. In: Atwood, D. (Ed.), Journal of Chemical Information and Modeling. Wiley, Chichester, Ch. Geology, G, pp. 1–19.

McLennan, S. M., 1989. Rare earth elements in sedimentary rocks; influence of provenance and sedimentary processes. Reviews in Mineralogy and Geochemistry 21 (1), 169–200.

McManus, J. F., Francois, R., Gherardi, J.-M., Keigwin, L. D., Brown-Leger, S., 2004. Collapse and rapid resumption of Atlantic meridional circulation linked to deglacial climate changes. Nature 428 (6985), 834–837.

McNeely, R., Dyke, A., Southon, J. R., 2006. Canadian marine reservoir ages, preliminary data assessment, Open File 5049, 3.

Meier, M. F., Dyurgerov, M. B., Rick, U. K., O'Neel, S., Tad, W. P., Anderson, R. S., Anderson, S. P., Glazovsky, A. F., 2007. Glaciers Dominate Eustatic Sea-Level Rise in the 21st Century. Science 317, 1064–1067.

Meinhardt, A.-K., Pahnke, K., Böning, P., Schnetger, B., Brumsack, H.-J., 2016. Climate change and response in bottom water circulation and sediment provenance in the Central Arctic Ocean since the Last Glacial. Chemical Geology 427, 98–108.

Miller, G. H., Brigham-Grette, J., Alley, R. B., Anderson, L., Bauch, H. A., Douglas, M. S. V., Edwards, M. E., Elias, S. a., Finney, B. P., Fitzpatrick, J. J., Funder, S. V., Herbert, T. D., Hinzman, L. D., Kaufman, D. S., MacDonald, G. M., Polyak, L., Robock, A., Serreze, M. C., Smol, J. P., Spielhagen, R., White, J. W. C., Wolfe, A. P., Wolff, E. W., 2010. Temperature and precipitation history of the Arctic. Quaternary Science Reviews 29 (15-16), 1679–1715.

Millot, R., Gaillardet, J., Dupré, B., Allégre, C. J., 2003. Northern latitude chemical weathering rates: Clues from the Mackenzie River Basin, Canada. Geochimica et Cosmochimica Acta 67 (7), 1305–1329.

Molina-Kescher, M., Frank, M., Hathorne, E. C., 2014. Nd and Sr isotope compositions of different phases of surface sediments in the South Pacific: Extraction of seawater signatures, boundary exchange, and detrital/dust provenance. Geochemistry, Geophysics, Geosystems 15, 3502–3520.

Montero-Serrano, J.-C., Bout-Roumazeilles, V., Sionneau, T., Tribovillard, N., Bory, A., Flower, B. P., Riboulleau, A., Martinez, P., Billy, I., 2010. Changes in precipitation regimes over North America during the Holocene as recorded by mineralogy and geochemistry of Gulf of Mexico sediments. Global and Planetary Change 74 (3-4), 132–143.

Montero-Serrano, J.-C., Bout-Roumazeilles, V., Tribovillard, N., Sionneau, T., Riboulleau, A., Bory, A., Flower, B., 2009. Sedimentary evidence of deglacial megafloods in the northern Gulf of Mexico (Pigmy Basin). Quaternary Science Reviews 28 (27-28), 3333–3347.

Montero-Serrano, J.-C., Deschamps, C.-E., Jaegle, M., 2014. Amundsen Expedition Report: Geology and paleoceanography leg 2a. Tech. rep., ArctiNet, Université Laval.
URL http://www.arcticnet.ulaval.ca/pdf/media/2014{_}Amundsen{_}Expedition{_}Report.pdf

Montero-Serrano, J.-C., Föllmi, K. B., Adatte, T., Spangenberg, J. E., Tribovillard, N., Fantasia, A., Suan, G., 2015. Continental weathering and redox conditions during the early Toarcian Oceanic Anoxic Event in the northwestern Tethys: Insight from the Posidonia Shale section in the Swiss Jura Mountains. Palaeogeography, Palaeoclimatology, Palaeoecology 429, 83–99.

Murton, J. B., Bateman, M. D., Dallimore, S. R., Teller, J. T., Yang, Z., 2010. Identification of Younger Dryas outburst flood path from Lake Agassiz to the Arctic Ocean. Nature 464 (7289), 740–743.

Nagashima, K., Asahara, Y., Takeuchi, F., Harada, N., Toyoda, S., Tada, R., 2012. Contribution of detrital materials from the Yukon River to the continental shelf sediments of the Bering Sea based on the electron spin resonance signal intensity and crystallinity of quartz. Deep-Sea Research Part II: Topical Studies in Oceanography 61-64, 145–154.

Naidu, A., Burrell, D., Wood, D., 1971. Clay Mineral Composition and Geologic Significance of Some Beaufort Sea Sediments. Journal of Sedimentary Petrology 41 (3), 691–694.

Naidu, A., Creager, J., Mowatt, T., 1982. Clay mineral dispersal patterns in the north Bering and Chukchi Seas. Marine Geology 47 (1-2), 1–15.

Naidu, A. S., Mowatt, T. C., 1983. Sources and dispersal patterns of clay minerals in surface sediments from the continental-shelf areas off Alaska. Geological Society of America Bulletin 94 (7), 841–854.

Nesbitt, H. W., 1979. Mobility and fractionation of rare earth elements during weathering of a granodiorite. Nature 279 (5710), 206–210.

Nesbitt, H. W., Young, G. M., 1982. Early Proterozoic climates and plate motions inferred from major element chemistry of lutites. Nature 299 (5885), 715–717.

Not, C., Hillaire-Marcel, C., 2012. Enhanced sea-ice export from the Arctic during the Younger Dryas. Nature Communications 3, 647.

Nowell, G. M., Kempton, P. D., Noble, S. R., Saunders, a. D., Mahoney, J. J., Taylor, R. N., 1998. High-precision Hf isotopic measurements of MORB and OIB by thermal ionization mass-spectrometry: insights into the depleted mantle. Chemical Geology 149, 211–233.

Nürnberg, D., Wollenburg, I., Dethleff, D., Eicken, H., Kassens, H., Letzig, T., Reimnitz, E., Thiede, J., jul 1994. Sediments in Arctic sea ice: Implications for entrainment, transport and release. Marine Geology 119 (3-4), 185–214.

O'Brien, M., Macdonald, R., Melling, H., Iseki, K., 2006. Particle fluxes and geochemistry on the Canadian Beaufort Shelf: Implications for sediment transport and deposition. Continental Shelf Research 26 (1), 41–81.

Okkonen, S. R., Ashjian, C. J., Campbell, R. G., Maslowski, W., Clement-Kinney, J. L., Potter, R., 2009. Intrusion of warm Bering/Chukchi waters onto the shelf in the western Beaufort Sea. Journal of Geophysical Research 114, 1–23.

Ortiz, J. D., Polyak, L., Grebmeier, J. M., Darby, D., Eberl, D. D., Naidu, S., Nof, D., 2009. Provenance of Holocene sediment on the Chukchi-Alaskan margin based on combined diffuse spectral reflectance and quantitative X-Ray Diffraction analysis. Global and Planetary Change 68 (1-2), 73–84.

Overland, J. E., Adams, J. M., Bond, N. A., Climate, J. O. F., Marine, P., Overland, J. E., Adams, J. M., Bond, N. A., Climate, J. O. F., Marine, P., 1999. Decadal Variability of the Aleutian Low and Its Relation to High-Latitude Circulation. Journal of Climate 12 (5), 1542–1548.

Padgham, W. A., Fyson, W. K., 1992. The Slave Province: a distinct Archean craton. Canadian Journal of Earth Sciences 29, 2072–2086.

Paillard, D., Labeyrie, L., Yiou, P., sep 1996. Macintosh Program performs time-series analysis. Eos, Transactions American Geophysical Union 77 (39), 379–379.

Palmer, M. R., Elderfield, H., 1985. Sr isotope composition of sea water over the past 75 Myr. Nature 314 (6011), 526–528.

Patchett, P. J., Embry, A. F., Ross, G. M., Beauchamp, B., Harrison, J. C., Mayr, U., Isachsen, C. E., Rosenberg, E. J., Spence, G. O., 2004. Sedimentary Cover of the Canadian Shield through Mesozoic Time Reflected by Nd Isotopic and Geochemical Results for the Sverdrup Basin, Arctic Canada. The Journal of Geology 112 (1), 39–57.

Pearce, C., Varhelyi, A., Wastegärd, S., Muschitiello, F., Barrientos, N., O'Regan, M., Cronin, T. M., Gemery, L., Semiletov, I., Backman, J., Jakobsson, M., 2017. The 3.6ka Aniakchak tephra in the Arctic Ocean: A constraint on the Holocene radiocarbon reservoir age in the Chukchi Sea. Climate of the Past 13 (4), 303–316.

Pearce, C. R., Jones, M. T., Oelkers, E. H., Pradoux, C., Jeandel, C., 2013. The effect of particulate dissolution on the neodymium (Nd) isotope and Rare Earth Element (REE) composition of seawater. Earth and Planetary Science Letters 369-370, 138–147.

Pearce, N. J. G., Westgate, J. A., Preece, S. J., Eastwood, W. J., Perkins, W. T., 2004. Identification of Aniakchak (Alaska) tephra in Greenland ice core challenges the 1645 BC date for Minoan eruption of Santorini. Geochemistry, Geophysics, Geosystems 5 (3), GC000672.

Peck, J. A., Green, R. R., Shanahan, T., King, J. W., Overpeck, J. T., Scholz, C. a., 2004. A magnetic mineral record of Late Quaternary tropical climate variability from Lake Bosumtwi, Ghana. Palaeogeography, Palaeoclimatology, Palaeoecology 215 (1-2), 37–57.

Peterson, B. J., Holmes, R. M., McClelland, J. W., Vörösmarty, C. J., Lammers, R. B., Shiklomanov, A. I., Shiklomanov, I. A., Rahmstorf, S., 2002. Increasing river discharge to the Arctic Ocean. Science (New York, N.Y.) 298 (5601), 2171–2173.

Petschick, R., 2000. MacDiff 4.2. 5 Manual. Institut für Geologie, Universität Erlangen: Germany.

Phillips, R. L., Grantz, A., 2001. Regional variations in provenance and abundance of ice-rafted clasts in Arctic Ocean sediments: Implications for the configuration of late Quaternary oceanic and atmospheric circulation in the Arctic. Marine Geology 172 (1-2), 91–115.

Pickart, R. S., 2004. Shelfbreak circulation in the Alaskan Beaufort Sea: Mean structure and variability. Journal of Geophysical Research C: Oceans 109 (4), 1–14.

Pickart, R. S., Moore, G. W. K., Torres, D. J., Fratantoni, P. S., Goldsmith, R. A., Yang, J., 2009. Upwelling on the continental slope of the alaskan beaufort sea: Storms, ice, and oceanographic response. Journal of Geophysical Research: Oceans 114 (9), 1–17.

Pickart, R. S., Weingartner, T. J., Pratt, L. J., Zimmermann, S., Torres, D. J., 2005. Flow of winter-transformed Pacific water into the Western Arctic. Deep-Sea Research Part II: Topical Studies in Oceanography 52 (24-26), 3175–3198.

Pizzolato, L., Howell, S. E. L., Derksen, C., Dawson, J., Copland, L., 2014. Changing sea ice conditions and marine transportation activity in Canadian Arctic waters between 1990 and 2012. Climatic Change 123 (2), 161–173.

Poirier, R. K., Cronin, T. M., Briggs, W. M., Lockwood, R., 2012. Central Arctic paleoceanography for the last 50kyr based on ostracode faunal assemblages. Marine Micropaleontology 88-89, 65–76.

Polyak, L., Alley, R. B., Andrews, J. T., Brigham-Grette, J., Cronin, T. M., Darby, D. a., Dyke, A. S., Fitzpatrick, J. J., Funder, S., Holland, M., Jennings, A. E., Miller, G. H., O'Regan, M., Savelle, J., Serreze, M., St. John, K., White, J. W. C., Wolff, E., 2010. History of sea ice in the Arctic. Quaternary Science Reviews 29 (15-16), 1757–1778.

Polyak, L., Belt, S. T., Cabedo-Sanz, P., Yamamoto, M., Park, Y.-H., 2016. Holocene sea-ice conditions and circulation at the Chukchi-Alaskan margin, Arctic Ocean, inferred from biomarker proxies. The Holocene 26 (11), 1–12.

Polyak, L., Bischof, J., Ortiz, J. D., Darby, D. A., Channell, J. E. T., Xuan, C., Kaufman, D. S., Løvlie, R., Schneider, D. A., Eberl, D. D., Adler, R. E., Council, E. A., 2009. Late Quaternary stratigraphy and sedimentation patterns in the western Arctic Ocean. Global and Planetary Change 68 (1-2), 5–17.

Polyak, L., Darby, D. A., Bischof, J. F., Jakobsson, M., 2007. Stratigraphic constraints on late Pleistocene glacial erosion and deglaciation of the Chukchi margin, Arctic Ocean. Quaternary Research 67 (2), 234–245.

Polyakov, I. V., Pnyushkov, A. V., Alkire, M. B., Ashik, I. M., Baumann, T. M., Carmack, E. C., Goszczko, I., Guthrie, J., Ivanov, V. V., Kanzow, T., Krishfield, R., Kwok, R., Sundfjord, A., Morison, J., Rember, R., Yulin, A., apr 2017. Greater role for Atlantic inflows on sea-ice loss in the Eurasian Basin of the Arctic Ocean. Science 356 (6335), 285–291.

Ponomareva, V., Polyak, L., Portnyagin, M., Abbott, P. M., Zelenin, E., Vakhrameeva, P., Garbe-Schönberg, D., 2017. Holocene tephra from the Chukchi-Alaskan margin, Arctic Ocean: Implications for sediment chronostratigraphy and volcanic history. Quaternary Geochronology 45, 85–97.

Porcelli, D., Andersson, P. S., Baskaran, M., Frank, M., Björk, G., Semiletov, I., 2009. The distribution of neodymium isotopes in Arctic Ocean basins. Geochimica et Cosmochimica Acta 73 (9), 2645–2659.

Pourmand, A., Dauphas, N., Ireland, T. J., 2012. A novel extraction chromatography and MC-ICP-MS technique for rapid analysis of REE, Sc and Y: Revising CI-chondrite and Post-Archean Australian Shale (PAAS) abundances. Chemical Geology 291, 38–54.

Prego, R., Caetano, M., Bernardez, P., Brito, P., Ospina-Alvarez, N., Vale, C., 2012. Rare earth elements in coastal sediments of the northern Galician shelf: Influence of geological features. Continental Shelf Research 35, 75–85.

Proshutinsky, A., Ashik, I. M., Dvorkin, E. N., Häkkinen, S., Krishfield, R. A., Peltier, W. R., 2004. Secular sea level change in the Russian sector of the Arctic Ocean. Journal of Geophysical Research: Oceans 109 (C3), 1–19.

Pyne-O'Donnell, S., 2011. The taphonomy of Last Glacial-Interglacial Transition (LGIT) distal volcanic ash in small Scottish lakes. Boreas 40 (1), 131–145.

Rachold, V., 1999. Major, Trace and Rare Earth Element Geochemistry of Suspended Particulate Material of East Siberian Rivers Draining to the Arctic Ocean V. In: Kassens, H., H.A. Bauch, l. Dmitrenko, H. Eicken, H.-W. Hubberten, M. Melles, J. T., Timokhov, L. (Eds.), Land-ocean systems in the Siberian Arctic: Dynamics and history. Springer, Berlin, Ch. Major, tra, pp. 199–222.

Rachold, V., Alabyan, A., Hubberten, H. W., Korotaev, V. N., Zaitsev, A. A., 1996. Sediment transport to the Laptev Sea - Hydrology and geochemistry of the Lena River. Polar Research 15 (2), 183–196.

Rahmstorf, S., 2007. A semi-empirical approach to projecting future sea-level rise. Science 315 (5810), 368–370.

Rasmussen, S. O., Andersen, K. K., Svensson, A. M., Steffensen, J. P., Vinther, B. M., Clausen, H. B., Siggaard-Andersen, M. L., Johnsen, S. J., Larsen, L. B., Dahl-Jensen, D., Bigler, M., Röthlisberger, R., Fischer, H., Goto-Azuma, K., Hansson, M. E., Ruth, U., 2006. A new Greenland ice core chronology for the last glacial termination. Journal of Geophysical Research Atmospheres 111 (6), 1–16.

Reimann, C., Filzmoser, P., Garrett, R. G., Dutter, R., 2008. Statistical Data Analysis Explained. John Wiley & Sons, Ltd, Chichester, UK.

Reimer, P., Bard, E., Bayliss, A., Beck, J., Blackwell, P., Ramsey, C., Buck, C., Cheng, H., Edwards, R., Friedrich, M., Grootes, P., Guilderson, T., Haflidison, H., Hajdas, I., Hatté, C., Heaton, T., Hoffmann, D., Hogg, A., Hughen, K., Kaiser, K., Kromer, B., Manning, S., Niu, M., Reimer, R., Richards, D., Scott, E., Southon, J., Staff, R., Turney, C., Plicht, J., 2013. IntCal13 and Marine13 radiocarbon age calibration curves 0-50,000 years cal BP. Radiocarbon 55 (4), 1869–1887.

Reimnitz, E., Dethleff, D., Nürnberg, D., jul 1994. Contrasts in Arctic shelf sea-ice regimes and some implications: Beaufort Sea versus Laptev Sea. Marine Geology 119 (3-4), 215–225.

Reimnitz, E., Kempema, E. W., Barnes, P. W., 1987. Anchor ice, seabed freezing, and sediment dynamics in shallow Arctic Seas. Journal of Geophysical Research 92 (C13), 14671.

Riboulleau, A., Bout-Roumazeilles, V., Tribovillard, N., Guillot, F., Recourt, P., 2014. Testing provenance diagrams: Lessons from the well-constrained Cariaco Basin. Chemical Geology 389, 91–103.

Richerol, T., Rochon, A., Blasco, S., Scott, D. B., Schell, T. M., Bennett, R. J., 2008. Distribution of dinoflagellate cysts in surface sediments of the Mackenzie Shelf and Amundsen Gulf, Beaufort Sea (Canada). Journal of Marine Systems 74 (3-4), 825–839.

Rickli, J., Frank, M., Baker, A. R., Aciego, S., de Souza, G., Georg, R. B., Halliday, A. N., 2010. Hafnium and neodymium isotopes in surface waters of the eastern Atlantic Ocean: Implications for sources and inputs of trace metals to the ocean. Geochimica et Cosmochimica Acta 74 (2), 540–557.

Rickli, J., Frank, M., Halliday, A. N., 2009. The hafnium-neodymium isotopic composition of Atlantic seawater. Earth and Planetary Science Letters 280 (1-4), 118–127.

Ron, H., Nowaczyk, N. R., Frank, U., Schwab, M. J., Naumann, R., Striewski, B., Agnon, a., 2007. Greigite detected as dominating remanence carrier in Late Pleistocene sediments, Lisan formation, from Lake Kinneret (Sea of Galilee), Israel. Geophysical Journal International 170 (1), 117–131.

Roser, B., Korsch, R., 1988. Provenance signatures of sandstone-mudstone suites determined using discriminant function analysis of major-element data. Chemical Geology 67 (1), 119–139.

Rudels, B., 2012. Arctic Ocean circulation and variability – Advection and external forcing encounter constraints and local processes. Ocean Science 8 (2), 261–286.

Rudels, B., Jones, E. P., Schauer, U., Eriksson, P., 2004. Atlantic Sources of the Arctic Ocean Halocline. Polar Research 23 (2), 181–208.

Sagnotti, L., Macrí, P., Camerlenghi, A., Rebesco, M., 2001. Environmental magnetism of antarctic late pleistocene sediments and interhemispheric correlation of climatic events. Earth and Planetary Science Letters 192 (1), 65–80.

Schell, T. M., Scott, D. B., Rochon, A., Blasco, S., 2008. Late Quaternary paleoceanography and paleo-sea ice conditions in the Mackenzie Trough and Canyon, Beaufort SeaThis article is one of a series of papers published in this Special Issue on the theme Polar Climate Stability Network . Canadian Journal of Earth Sciences 45 (11), 1399–1415.

Schoster, F., Behrends, M., Muller, R., Stein, R., Washner, M., 2000. Modern river discharge and pathways of supplied material in the Eurasian Arctic Ocean: Evidence from mineral assemblagesand major and minor element distribution. International Journal of Earth Sciences 89 (3), 486–495.

Scott, D. B., Schell, T., St-Onge, G., Rochon, A., Blasco, S., 2009. Foraminiferal assemblage changes over the last 15,000 years on the Mackenzie-Beaufort Sea Slope and Amundsen Gulf, Canada: Implications for past sea ice conditions. Paleoceanography 24 (2), 1–20.

Screen, J. A., Francis, J. A., 2016. Contribution of sea-ice loss to Arctic amplification is regulated by Pacific Ocean decadal variability. Nature Climate Change 6, 856–861.

Screen, J. A., Simmonds, I., 2010. The central role of diminishing sea ice in recent Arctic temperature amplification. Nature 464 (7293), 1334–1337.

Serreze, M. C., Holland, M. M., Stroeve, J., 2007. Perspectives on the Arctic's Shrinking Sea-Ice Cover. Science 315 (5818), 1533–1536.

Serreze, M. C., Walsh, J. E., Chapin, F. S., Osterkamp, T., Dyurgerov, M., Romanovsky, V., Oechel, W. C., Morison, J., Zhang, T., Barry, R. G., 2000. Observational evidence of recent change in the northern high-latitude environment. Climatic Change 46 (1-2), 159–207.

Shimada, K., Kamoshida, T., Itoh, M., Nishino, S., Carmack, E., McLaughlin, F., Zimmermann, S., Proshutinsky, A., 2006. Pacific Ocean inflow: Influence on catastrophic reduction of sea ice cover in the Arctic Ocean. Geophysical Research Letters 33 (8), 3–6.

Sikes, E. L., Samson, C. R., Guilderson, T. P., Howard, W. R., 2000. Old radiocarbon ages in the southwest Pacific Ocean during the last glacial period and deglaciation. Nature 303, 555–559.

Simon, Q., St-Onge, G., Hillaire-Marcel, C., 2012. Late Quaternary chronostratigraphic framework of deep Baffin Bay glaciomarine sediments from high-resolution paleomagnetic data. Geochemistry, Geophysics, Geosystems 13 (1), 1–24.

Snowball, I., Sandgren, P., 2004. Geomagnetic field intensity changes in Sweden between 9000 and 450 cal BP: extending the record of "archaeomagnetic jerks" by means of lake sediments and the pseudo-Thellier technique. Earth and Planetary Science Letters 227 (3-4), 361–376.

Song, Y. H., Choi, M. S., 2009. REE geochemistry of fine-grained sediments from major rivers around the Yellow Sea. Chemical Geology 266 (3-4), 337–351.

Spielhagen, R. F., Werner, K., Sørensen, S. A., Zamelczyk, K., Kandiano, E., Budeus, G., Husum, K., Marchitto, T. M., Hald, M., 2011. Enhanced modern heat transfer to the Arctic by warm Atlantic Water. Science (New York, N.Y.) 331 (6016), 450–453.

St-Onge, G., Long, B. F., 2009. CAT-scan analysis of sedimentary sequences: An ultrahigh-resolution paleoclimatic tool. Engineering Geology 103 (3-4), 127–133.

St-Onge, G., Mulder, T., Francus, P., Long, B., 2007. Chapter Two Continuous Physical Properties of Cored Marine Sediments. In: Hillaire-Marcel, C., de Vernal, A. (Eds.), Developments in Marine Geology, Proxies in Late Cenozoic Paleoceanography 1. Elsevier, Amsterdam, pp. 63–98.

St-Onge, G., Stoner, J., 2011. Paleomagnetism Near the North Magnetic Pole: A Unique Vantage Point for Understanding the Dynamics of the Geomagnetic Field and Its Secular Variations. Oceanography 24 (3), 42–50.

St-Onge, G., Stoner, J. S., Hillaire-Marcel, C., 2003. Holocene paleomagnetic records from the St. Lawrence Estuary, eastern Canada: Centennial- to millennial-scale geomagnetic modulation of cosmogenic isotopes. Earth and Planetary Science Letters 209 (1-2), 113–130.

Stein, R., 2008. Arctic Ocean Sediments: Processes, Proxies, and Paleoenvironment: Processes, Proxies, and Paleoenvironment. In: Developments in Marine Geology. Vol. 2. Elsevier, Amsterdam, p. 592.

Stein, R., Fahl, K., Schade, I., Manerung, A., Wassmuth, S., Niessen, F., Nam, S. I., 2017. Holocene variability in sea ice cover, primary production, and Pacific-Water inflow and climate change in the Chukchi and East Siberian Seas (Arctic Ocean). Journal of Quaternary Science 32 (3), 362–379.

Stichel, T., Frank, M., Rickli, J., Haley, B. A., 2012. The hafnium and neodymium isotope composition of seawater in the Atlantic sector of the Southern Ocean. Earth and Planetary Science Letters 317-318, 282–294.

Stokes, C. R., Clark, C. D., Darby, D. A., Hodgson, D. A., 2005. Late Pleistocene ice export events into the Arctic Ocean from the M'Clure Strait Ice Stream, Canadian Arctic Archipelago. Global and Planetary Change 49 (3-4), 139–162.

Stokes, C. R., Clark, C. D., Storrar, R., 2009. Major changes in ice stream dynamics during deglaciation of the north-western margin of the Laurentide Ice Sheet. Quaternary Science Reviews 28 (7-8), 721–738.

Stokes, C. R., Clark, C. D., Winsborrow, C. M., 2006. Subglacial bedform evidence for a major palaeo-ice stream and its retreat phases in Amundsen Gulf, Canadian Arctic Archipelago. Journal of Quaternary Science 21 (4), 399–412.

Stokes, C. R., Tarasov, L., 2010. Ice streaming in the Laurentide Ice Sheet: A first comparison between data-calibrated numerical model output and geological evidence. Geophysical Research Letters 37 (1), 1–5.

Stoner, J. S., Channell, J. E. T., Hillaire-Marcel, C., Kissel, C., 2000. Geomagnetic paleointensity and environmental record from Labrador Sea core MD95-2024: Global marine sediment and ice core chronostratigraphy for the last 110 kyr. Earth and Planetary Science Letters 183 (1-2), 161–177.

Stoner, J. S., St-Onge, G., 2007. Paleoceanography: Reversals, Excursions, Paleointensity, and Secular Variation. In: Hillaire-Marcel, C., de Vernal, A. (Eds.), Developments in Marine Geology, Proxies in Late Cenozoic Paleoceanography 1, elsevier Edition. Amsterdam, pp. 63–98.

Stumpf, R., 2011. Late Quaternary variability of hydrography and weathering inputs on the SW Iberian shelf from clay minerals and the radiogenic isotopes of neodymium, strontium and lead. Ph.D. thesis, Christian-Albrechts.

Tachikawa, K., 2003. Neodymium budget in the modern ocean and paleo-oceanographic implications. Journal of Geophysical Research 108 (C8), 3254.

Tachikawa, K., Jeandel, C., Vangriesheim, A., Dupré, B., 1999. Distribution of rare earth elements and neodymium isotopes in suspended particles of the tropical Atlantic Ocean (EUMELI site). Deep-Sea Research Part I: Oceanographic Research Papers 46 (5), 733–755.

Tanaka, T., Togashi, S., Kamioka, H., Amakawa, H., Kagami, H., Hamamoto, T., Yuhara, M., Orihashi, Y., Yoneda, S., Shimizu, H., Kunimaru, T., Takahashi, K., Yanagi, T., Nakano, T., Fujimaki, H., Shinjo, R., Asahara, Y., Tanimizu, M., Dragusanu, C., 2000. JNdi-1: A neodymium isotopic reference in consistency with LaJolla neodymium. Chemical Geology 168 (3-4), 279–281.

Tarasov, L., Peltier, W., 2005. Arctic freshwater forcing of the Younger Dryas cold reversal. Nature 435, 662–665.

Tauxe, L., 1993. Sedimentary records of relative paleointensity of the geomagnetic field: Theory and practice. Reviews of Geophysics 31 (3), 319.

Tauxe, L., Mullender, T. A. T., Pick, T., 1996. Potbellies, wasp-waists, and superparamagnetism in magnetic hysteresis. Journal of Geophysical Research 101 (B1), 571.

Tauxe, L., Pick, T., Kok, Y. S., nov 1995. Relative paleointensity in sediments: A Pseudo-Thellier Approach. Geophysical Research Letters 22 (21), 2885–2888.

Tauxe, L., Yamazaki, T., 2007. 5.13 Paleointensities. In: G. Schubert (Ed.), Treatise on Geophysics, vol. 5, Magnetism. Elsevier, Amsterdam, pp. 510–563.

Taylor, S. R. ., McClennan, S. M., 1985. The continental crust: Its composition and evolution. John Wiley & Sons Ltd, Oxford.

Taylor, S. R., McLennan, S. M., Armstrong, R. L., Tarney, J., may 1981. The Composition and Evolution of the Continental Crust: Rare Earth Element Evidence from Sedimentary Rocks. Philosophical Transactions of the Royal Society A: Mathematical, Physical and Engineering Sciences 301 (1461), 381–399.

Thió-Henestrosa, S., Martín-Fernández, J. A., 2005. Dealing with Compositional Data: The Freeware CoDaPack. Mathematical Geology 37 (7), 773–793.

Thompson, D., Wallace, J., 1998. The Arctic Oscillation in the wintertime geopotential height and temperature fields. Geophysical Research Letters 25 (9), 1297–1300.

Tremblay, L. B., Mysak, L. A., Dyke, A. S., 1997. Evidence from driftwood records for century-to-millennial scale variations of the high latitude atmospheric circulation during the Holocene. Geophysical Research Letters 24 (16), 2027–2030.

Trenberth, K. E., Hurrell, J. W., 1994. Decadal atmospheric-ocean variations in the Pacific. Climate Dynamics 9, 303–319.

van de Flierdt, T., Robinson, L. F., Adkins, J. F., 2010. Deep-sea coral aragonite as a recorder for the neodymium isotopic composition of seawater. Geochimica et Cosmochimica Acta 74 (21), 6014–6032.

Van Den Boogaart, G., Tolosana-Delgado, R., 2008. "compositions": A unified R package to analyze compositional data. Computers and Geosciences 34 (4), 320–338.

Venuti, A., Florindo, F., Caburlotto, A., Hounslow, M. W., Hillenbrand, C. D., Strada, E., Talarico, F. M., Cavallo, A., 2011. Late Quaternary sediments from deep-sea sediment drifts on the Antarctic Peninsula Pacific margin: Climatic control on provenance of minerals. Journal of Geophysical Research: Solid Earth 116 (6), 1–18.

Verma, S. P., Armstrong-Altrin, J. S., 2013. New multi-dimensional diagrams for tectonic discrimination of siliciclastic sediments and their application to Precambrian basins. Chemical Geology 355, 117–133.

Vervoort, J. D., Patchett, P. J., Blichert-toft, J., Albare, F., 1999. Relationships between Lu – Hf and Sm – Nd isotopic systems in the global sedimentary system. Earth and Planetary Science Letters 168, 79–99.

Vihma, T., 2014. Effects of Arctic Sea Ice Decline on Weather and Climate: A Review. Surveys in Geophysics 35 (5), 1175–1214.

Viscosi-Shirley, C., Mammone, K., Pisias, N., Dymond, J., 2003a. Clay mineralogy and multi-element chemistry of surface sediments on the Siberian-Arctic shelf: Implications for sediment provenance and grain size sorting. Continental Shelf Research 23 (11-13), 1175–1200.

Viscosi-Shirley, C., Pisias, N., Mammone, K., 2003b. Sediment source strength, transport pathways and accumulation patterns on the Siberian-Arctic's Chukchi and Laptev shelves. Continental Shelf Research 23 (11-13), 1201–1225.

Vogt, C., 1997. Regional and temporal variations of mineral assemblages in Arctic Ocean sediments as climatic indicator during glacial/ interglacial changes. Ph.D. thesis, Alfred Wegener Insitute.

Von Eynatten, H., Tolosana-Delgado, R., Karius, V., 2012. Sediment generation in modern glacial settings: Grain-size and source-rock control on sediment composition. Sedimentary Geology 280, 80–92.

Von Eynatten, H., Tolosana-Delgado, R., Karius, V., Bachmann, K., Caracciolo, L., 2016. Sediment generation in humid Mediterranean setting: Grain-size and source-rock control on sediment geochemistry and mineralogy (Sila Massif, Calabria). Sedimentary Geology 336, 68–80.

Wagner, A., Lohmann, G., Prange, M., 2011. Arctic river discharge trends since 7ka BP. Global and Planetary Change 79 (1-2), 48–60.

Wahsner, M., Müller, C., Stein, R., Ivanov, G., Levitan, M., Shelekhova, E., Tarasov, G., 1999. Clay-mineral distribution in surface sediments of the Eurasian Arctic Ocean and continental margin as indicator for source areas and transport pathways - a synthesis. Boreas 28 (1), 215–233.

Wanner, H., Beer, J., Bütikofer, J., Crowley, T. J., Cubasch, U., Flückiger, J., Goosse, H., Grosjean, M., Joos, F., Kaplan, J. O., Küttel, M., Müller, S. A., Prentice, I. C., Solomina, O., Stocker, T. F., Tarasov, P., Wagner, M., Widmann, M., 2008. Mid- to Late Holocene climate change: an overview. Quaternary Science Reviews 27 (19-20), 1791–1828.

Wegner, C., Bennett, K. E., Vernal, A. D., Forwick, M., Fritz, M., Heikkila, M., Ła, M., Lantuit, H., Laska, M., Moskalik, M., Regan, M. O., Rachold, V., Vonk, J. E., Werner, K., Pawłowska, J., Promin, A., 2015. Variability in transport of terrigenous material on the shelves and the deep Arctic Ocean during the Holocene ¨ , 7. Polar Research 34 (1), 1–19.

Weingartner, T., Aagaard, K., Woodgate, R., Danielson, S., Sasaki, Y., Cavalieri, D., 2005. Circulation on the north central Chukchi Sea shelf. Deep Sea Research Part II: Topical Studies in Oceanography 52 (24-26), 3150–3174.

Weis, D., Kieffer, B., Maerschalk, C., Barling, J., De Jong, J., Williams, G. A., Hanano, D., Pretorius, W., Mattielli, N., Scoates, J. S., Goolaerts, A., Friedman, R. M., Mahoney, J. B., 2006. High-precision isotopic characterization of USGS reference materials by TIMS and MC-ICP-MS. Geochemistry, Geophysics, Geosystems 7 (8).

Weltje, G. J., may 1997. End-member modeling of compositional data: Numerical-statistical algorithms for solving the explicit mixing problem. Mathematical Geology 29 (4), 503–549.

Weltje, G. J., Von Eynatten, H., 2004. Quantitative provenance analysis of sediments: Review and outlook. Sedimentary Geology 171 (1-4), 1–11.

Wickert, A. D., 2016. Reconstruction of North American drainage basins and river discharge since the Last Glacial Maximum. Earth Surface Dynamics 4 (4), 831–869.

Woodgate, R. A., 2013. Arctic Ocean Circulation: Going Around At the Top Of the World. The Nature Education Knowledge Project 4 (8), 1–12.

Woodgate, R. A., Aagaard, K., Swift, J. H., Falkner, K. K., Smethie, W. M., 2005. Pacific ventilation of the Arctic Ocean's lower halocline by upwelling and diapycnal mixing over the continental margin. Geophysical Research Letters 32 (18), 1–5.

Woodgate, R. A., Weingartner, T. J., Lindsay, R., 2012. Observed increases in Bering Strait oceanic fluxes from the Pacific to the Arctic from 2001 to 2011 and their impacts on the Arctic Ocean water column. Geophysical Research Letters 39 (24), 2–7.

Wu, W., Zheng, H., Xu, S., Yang, J., Liu, W., 2013. Trace element geochemistry of riverbed and suspended sediments in the upper Yangtze River. Journal of Geochemical Exploration 124, 67–78.

Xuan, C., Channell, J. E. T., feb 2010. Origin of apparent magnetic excursions in deep-sea sediments from Mendeleev-Alpha Ridge, Arctic Ocean. Geochemistry, Geophysics, Geosystems 11 (2).

Yamamoto, M., Nam, S. I., Polyak, L., Kobayashi, D., Suzuki, K., Irino, T., Shimada, K., 2017. Holocene dynamics in the Bering Strait inflow to the Arctic and the Beaufort Gyre circulation based on sedimentary records from the Chukchi Sea. Climate of the Past 13 (9), 1111–1127.

Yeloff, D., Bennett, K. D., Blaauw, M., Mauquoy, D., Sillasoo, Ü., van der Plicht, J., van Geel, B., 2006. High precision 14C dating of Holocene peat deposits: A comparison of Bayesian calibration and wiggle-matching approaches. Quaternary Geochronology 1 (3), 222–235.

Zijderveld, J. D. A., 1967. A. C. Demagnetization of Rocks: Analysis of Results. In: Elsevier (Ed.), Methods in Palaeomagnetism, collinson, Edition. New York, pp. 254–286.

Zimmermann, B., Porcelli, D., Frank, M., Andersson, P. S., Baskaran, M., Lee, D. C., Halliday, A. N., 2009a. Hafnium isotopes in Arctic Ocean water. Geochimica et Cosmochimica Acta 73 (11), 3218–3233.

Zimmermann, B., Porcelli, D., Frank, M., Rickli, J., Lee, D. C., Halliday, A. N., 2009b. The hafnium isotope composition of Pacific Ocean water. Geochimica et Cosmochimica Acta 73 (1), 91–101.